

ELECTRON TUNNELING THROUGH PHENYLENE BRIDGES

Thesis by

RANDY VILLAHERMOSA

In Partial Fulfillment of the Requirements

for the Degree of

DOCTOR of PHILOSOPHY

California Institute of Technology

Pasadena, California

2002

(Defended May 29th, 2002)

©2002

Randy Villahermosa

All Rights Reserved

ACKNOWLEDGMENTS

There is no better Dynamic Duo than my research advisor Harry Gray and my mentor, Jay Winkler. Harry kept his word, never letting things get dull in (or out of) lab. Between the gay karaoke bar, one too many parties, "12 months of Harry Gray", and the occasional discussion on science between sips of fine Kentucky whiskey, Harry made it all fun. Jay doesn't let on, but I know he likes me, and I like him! Jay deserves a special nod of gratitude for always trying to make me a little more accurate. Harry and Jay showed me how science should be done.

A very special thank you for Mary. She was my Suga' Mama and kept me well supplied in creature comforts and overstocked with support, patience, and fun.

I have been fortunate enough to work with some of the best colleagues, all of whom have made invaluable contributions to this thesis. Adrian Ponce and Susan Pasco were a tremendous help in getting this project started. Thanks goes to Gary Mines (of ethynyl-"G" fame) for use of his quencher and name. I want to give a special thanks to Peter Green and Bob Becker for their contributions and support of the mass spectrometry work; Peter's insight and skills made a huge impact on this thesis. I am in debt to Pratip Bhattacharya for the NMR's of anything with a metal and to Larry Henling and Mike Day for the crystal structure. Special thanks to Mike Hill for stimulating conversations about the world around us. Chris Chang's synthetic advice and enthusiasm were both extremely appreciated. I would also like to thank Nate Lewis and Michael Freund for use of their lab space and allowing me to overstay my welcome. The support staff at Caltech, Tom Dunn, Steve Gould, Chris Smith, Dian Buchness, Pat Anderson, Rick Jackson, and Catherine May, has been excellent. I want to give a special thanks to Rick Gerhart for his glassblowing work. While at Caltech I've had the pleasure of working with some exceptional undergraduates: Josh Brown, Liviu Mirica, Bryan Tiedemann, and Sina Yeganeh. In their own ways, they have made my time at Caltech interesting.

I want to save my last acknowledgment for the members of the Gray group. Far too numerous to mention, the impressions they left on me will be burned into my psyche forever.

ABSTRACT

A series of donor-bridge-acceptor (D-B-A) complexes, $[(bpy)_2Ru(bpy-(XY)_n-G)](PF_6)_2$ (where $n = 2$ to 5 , $bpy = 2,2'$ -bipyridine, $XY = 2,5$ -xylene, and G is 3-ethynyl-4-methoxy- N,N -dimethylaniline; abbreviated $[Ru-(XY)_n-G]^{2+}$), were designed, synthesized, and characterized to study electron tunneling through phenylene bridges. $[Ru-(XY)_n-G]^{2+}$ is a versatile D-B-A scaffold that exhibits a strong correlation between xylene conformation and electron transfer properties.

$[Ru-(XY)_n-G](PF_6)_2$ was assembled from three components in a convergent process. Stepwise oligomer growth produced the well-defined bridging ligand, $bpy-(XY)_n$; bipyridine was regioselectively functionalized with a xylene oligomer through multiple cycles of palladium-catalyzed cross-couplings. The donor, synthesized separately, was joined to $bpy-(XY)_n$ using an alkyne linkage. Metalation with a $(bpy)_2Ru$ fragment finished assembly of the D-B-A complex. The D-B-A series was analyzed with mass spectrometry and NMR.

Spectroscopic, electrochemical, and spectroelectrochemical characterizations of $[Ru-(XY)_n-G]^{2+}$ indicate no significant electronic or chemical difference among the members of the series. UV-visible absorption spectra, with a metal to ligand charge transfer (MLCT) band maximum of 460 nm, resemble the model complexes $[Ru(bpy)_3]^{2+}$ and $[Ru-XY-TMS]^{2+}$ (where TMS = trimethylsilyl). Representative cyclic voltammograms

of $[\text{Ru}-(\text{XY})_3-\text{G}]^{2+}$ contain reversible redox couples for $\text{Ru}^{\text{II/III}}$ and $\text{G}^{0/+}$, with potentials of 1.24 and 0.59 V (vs. Ag/AgCl). Spectroelectrochemical traces, displaying loss of MLCT intensity and increased absorption centered at 520 nm, indicate the formation of $[\text{Ru}^{\text{III}}-(\text{XY})_n-\text{G}^+]^{4+}$.

The flash-quench technique was used to measure the electron transfer rates for $[\text{Ru}^{\text{III}}-(\text{XY})_n-\text{G}]^{3+} \rightarrow [\text{Ru}^{\text{II}}-(\text{XY})_n-\text{G}^+]^{3+}$. The rates, $9.0 \pm 0.3 \times 10^6$, $2 \pm 1 \times 10^5$, and $6 \pm 1 \times 10^3$ for $n = 3$ through 5, have a strong dependence on donor-acceptor distance. Estimates of the donor-acceptor distance were used to determine a distance decay constant, β , of 0.84 \AA^{-1} . The typical β -value for electron tunneling through phenylenes is 0.4 \AA^{-1} . The unusually high β -value for $[\text{Ru}-(\text{XY})_n-\text{G}]^{2+}$ is attributed to near-orthogonal dihedral angles between adjacent xylene rings. UV-visible spectra, cyclic voltammograms, and structural information, from molecular modeling calculations and a crystal structure, all support a near-orthogonal twist angle.

The versatility of $[\text{Ru}-(\text{XY})_n-\text{G}]^{2+}$ as a molecular scaffold was demonstrated in studies on electron transfer reactions in nanocrystalline TiO_2 solar cells. Modified to incorporate a terminal carboxyl group, $[\text{Ru}-(\text{XY})_n-\text{BA}]^{2+}$ (where BA = 4-ethynyl-benzoic acid) was synthesized and used as a TiO_2 solar cell dye. Utilizing the flash-quench method, the second-order rate constant for dye regeneration with I^- ($[\text{Ru}^{\text{III}}-(\text{XY})_n-\text{BA}]^{3+} \rightarrow [\text{Ru}-(\text{XY})_n-\text{BA}]^{2+}$) in homogenous fluid solution was $1.5 \times 10^{10} \text{ M}^{-1}\text{s}^{-1}$ for all three dyes in the series $n=0$ to 2.

TABLE of CONTENTS

Acknowledgments	iii
Abstract	iv
List of Figures, Tables, and Schemes	xii
List of Synthesized Compounds	xvii
Thesis Overview	1

Chapter 1. Introduction and Background

1.1 Electron Transfer Reactions	4
1.2 Electron Transfer Theory	5
1.3 Tunneling Energy Effects	6

Chapter 2. Design and Synthesis of Phenylene Donor-Bridge-Acceptor Complexes

Introduction

2.1 Donor-Bridge-Acceptor Complexes	9
2.2 Design of Donor-Bridge-Acceptor Complexes	10
2.3 D-B-A Scaffold – $[\text{Ru}(\text{XY})_n\text{-R}]^{2+}$	12

Results and Discussion

2.4 Target D-B-A complex – $[\text{Ru}(\text{XY})_n\text{-G}]^{2+}$	17
2.5 Applications of Palladium-Catalyzed Cross-Coupling Reactions.....	18
2.6 Retrosynthetic Analysis and Synthetic Route to $[\text{Ru}(\text{XY})_n\text{-G}]^{2+}$	23
2.7 Synthesis of Xylene Oligomers	23
2.8 Methods for Oligomer and D-B-A Characterization	27
2.9 Synthesis of Bipyridine-Xylene Oligomer Ligands	29
2.10 Synthesis of Ethynyl-G	31
2.11 $[\text{Ru}(\text{XY})_n\text{-G}]^{2+}$ Assembly	32

Methods and Materials

2.12 Reagents	36
2.13 Instrumentation	37
2.14 Flash GC-MS	37
2.15 Sample Preparation	37

Experimental

2.16 General Procedures	38
Suzuki Cross-Coupling General Method A	38
Suzuki Cross-Coupling General Method B	39
Sonogashira Cross-Coupling General Method	40
Deprotection/Iodination General Method	40
Ruthenium Metalation General Method	40
2.17 Synthetic Procedures	42
TMS-XY-Br	42
TMS-XY-B(OH) ₂	43
BR-XY-I	43
TMS-(XY) ₂ -TMS	44
TMS-(XY) ₂ -Br	44
I-(XY) ₂ -I	45
H-(XY) ₂ -H	45
TMS-(XY) ₃ -TMS	45
3-bromo-4-methoxyaniline	46
4-methoxy-3-(trimethylsilylethynyl-aniline)	46
TMS-ethynyl-G	47
Ethynyl-G	47
Bpy-XY-TMS	47
Bpy-XY-I	48
Bpy-(XY) ₂ -TMS	48
Bpy-(XY) ₂ -I	48
Bpy-(XY) ₂ -G	49
[Ru-(XY) ₂ -G](PF ₆) ₂	49
Bpy-(XY) ₃ -TMS	49
Bpy-(XY) ₃ -I	50
Bpy-(XY) ₃ -G	50
[Ru-(XY) ₃ -G](PF ₆) ₂	50

Bpy-(XY) ₄ -TMS	51
Bpy-(XY) ₄ -I	51
Bpy-(XY) ₄ -G	52
[Ru-(XY) ₄ -G](PF ₆) ₂	52
Bpy-(XY) ₅ -TMS	52
Bpy-(XY) ₅ -I	53
Bpy-(XY) ₅ -G	53
[Ru-(XY) ₅ -G](PF ₆) ₂	53

Chapter 3. Characterization of [Ru-(XY)_n-G]²⁺ and Related Compounds

Introduction

3.1 Characterizations	56
-----------------------------	----

Experimental

3.2 Reagents	59
3.3 Instrumentation and Experimental Procedures	59
3.4 Synthesis	61
[Ru-XY-TMS](PF ₆) ₂	61

Results and Discussion

3.5 [Ru-XY-TMS] ²⁺	62
3.6 [Ru-XY-TMS] ²⁺ UV-visible Absorption Spectrum	62
3.7 [Ru-XY-TMS] ²⁺ Electrochemistry	63
3.8 [Ru-XY-TMS] ²⁺ Spectroelectrochemistry	64
3.9 [Ru-XY-TMS] ²⁺ Photophysics	64
3.10 TMS-Ethynyl-G UV-visible Absorption Spectrum	66
3.11 TMS-Ethynyl-G Electrochemistry and Spectroelectrochemistry	66
3.12 [Ru-(XY) _n -G] ²⁺ NMR Spectra	67
3.13 [Ru-(XY) _n -G] ²⁺ Mass Spectra	68
3.14 [Ru-(XY) _n -G] ²⁺ UV-visible Absorption Spectra	69
3.15 [Ru-(XY) ₃ -G] ²⁺ Electrochemistry and Spectroelectrochemistry	71
3.16 [Ru-(XY) _n -G] ²⁺ Photophysics	71

Conclusion	73
------------------	----

Figures and Tables	75
--------------------------	----

Chapter 4. Electron Transfer Properties of $[\text{Ru}-(\text{XY})_n-\text{G}]^{2+}$

Introduction

4.1 $[\text{Ru}-(\text{XY})_n-\text{G}]^{2+}$ D-B-A Complex	117
4.2 Relevant Electron Transfer Reactions	119

Materials and Methods

4.3 Materials and Sample Preparation	122
$[\text{MV}](\text{PF}_6)_2$	123
4.4 Instrumentation	123
4.5 Experimental Procedures	124
4.6 Data Analysis	125
4.7 Excited State Lifetimes and Stern-Volmer Analysis	126
4.8 Flash Quench and Instrument Limitations	127

Results

4.9 Estimating k_{ET} for $[\text{Ru}-(\text{XY})_2-\text{G}]^{2+}$	131
4.10 Electron Transfer of $[\text{Ru}-(\text{XY})_2-\text{G}]^{2+}$ with low Quencher Concentrations	132
4.11 Electron Transfer of $[\text{Ru}-(\text{XY})_2-\text{G}]^{2+}$ with High Quencher Concentrations	136
4.12 Electron Transfer of $[\text{Ru}-(\text{XY})_3-\text{G}]^{2+}$, General Considerations	146
4.13 Electron Transfer Reactions of $[\text{Ru}-(\text{XY})_3-\text{G}]^{2+}$	146
4.14 Electron Transfer Kinetics of $[\text{Ru}-(\text{XY})_3-\text{G}]^{2+}$	149
4.15 $[\text{Ru}-(\text{XY})_3-\text{G}]^{2+}$ Flash-Quench Transient Difference Spectra	149
4.16 $[\text{Ru}-(\text{XY})_4-\text{G}]^{2+}$ Electron Transfer Kinetics	162
4.17 $[\text{Ru}-(\text{XY})_4-\text{G}]^{2+}$ Transient Difference Spectra	163
4.18 $[\text{Ru}-(\text{XY})_5-\text{G}]^{2+}$ Electron Transfer–Experimental Methods and Analysis	169
4.19 $[\text{Ru}-(\text{XY})_5-\text{G}]^{2+}$ Electron Transfer kinetics	172

Discussion

4.20 $[\text{Ru}-(\text{XY})_n-\text{G}]^{2+}$ Electron Transfer Kinetics Summary	176
4.21 Experimental Considerations for determining β	178
4.22 Donor-Acceptor Distances	179
4.23 Electron Transfer Distance Decay Constant – β	181
4.24 Conformational Effects on Electron Transfer	183

Conclusion	200
-------------------------	-----

Chapter 5. Synthesis, Characterization, and Electron Transfer Reactions of Nanocrystalline TiO₂ Solar Cell Dyes – [Ru-(XY)_n-BA]²⁺

Introduction

5.1 Nanocrystalline TiO ₂ Solar Cells	202
5.2 Electron Transfer Reactions in Nanocrystalline TiO ₂ Solar Cells	203
5.3 Application of [Ru-(XY) _n -BA] ²⁺ to Studying TiO ₂ Solar Cells	204

Experimental

5.4 Methods and Materials	205
5.5 Synthetic Procedures	205
4-TMS-BA	205
4-Ethynyl-BA	206
Bpy-(XY) ₀ -BA	206
[Ru-(XY) ₀ -BA](PF ₆) ₂	206
Bpy-(XY) ₁ -BA	207
[Ru-(XY) ₁ -BA](PF ₆) ₂	207
Bpy-(XY) ₂ -BA	207
[Ru-(XY) ₂ -BA](PF ₆) ₂	208

Results and Discussion

5.6 Synthesis of [Ru-(XY) _n -BA] ²⁺	209
5.7 UV-Visible Absorption Spectra of [Ru-(XY) _n -BA] ²⁺	211
5.8 Electrochemistry of [Ru-(XY) _n -BA] ²⁺	212
5.9 Photophysics of [Ru-(XY) _n -BA] ²⁺	212
5.10 Regeneration of [Ru-(XY) _n -BA] ²⁺ with Iodide	212

Conclusion	215
-------------------------	-----

Figures and Tables	216
---------------------------------	-----

Appendix A. Custom Glassware – Low Temperature Addition Funnel	229
Appendix B. Optically Transparent Thin Layer (OTTL) Spectroelectrochemical Cell ..	232
Appendix C. Nanosecond Laser Flash Photolysis	234
Appendix D. Spectroscopic Handles	236
Methyl Viologen (MV^{2+}) Spectra	
$[Ru-(XY)_n-G]^{2+}$ Handles	
TMS-ethynyl-G Handles	
References	242

FIGURES, TABLES, and SCHEMES

Chapter 2. Design and Synthesis of Phenylene Donor-Bridge-Acceptor Complexes

Figures

2.1 Donor-Bridge-Acceptor Scaffold	12
2.2 Donors for $[\text{Ru}^{\text{II}}-(\text{XY})_n-\text{R}]^{2+}$	15
2.3 Electron Transfer D-B-A Complex $[\text{Ru}-(\text{XY})_n-\text{G}]^{2+}$	16
2.4 Retrosynthetic Analysis of $[\text{Ru}-(\text{XY})_n-\text{G}]^{2+}$	18
2.5 Phenylboronic Anhydride Trimer	28
2.6 Bpy- $(\text{XY})_n-\text{R}$	29
2.7 Ethynyl-G	31

Tables

2.1 Synthesized Xylene Oligomers	26
--	----

Schemes

2.1 General Synthetic Route to $[\text{Ru}-(\text{XY})_n-\text{G}]^{2+}$	20
--	----

Chapter 3. Characterization of $[\text{Ru}-(\text{XY})_n-\text{G}]^{2+}$ and Related Compounds

Figures

3.1 D-B-A Complex $[\text{Ru}-(\text{XY})_n-\text{G}]^{2+}$ and Model Compounds	58
3.2 $[\text{Ru}-\text{XY}-\text{TMS}]^{2+}$ UV-visible Absorption Spectrum	76
3.3 $[\text{Ru}-\text{XY}-\text{TMS}]^{2+}$ Cyclic Voltammogram	77
3.4 Expanded $[\text{Ru}-\text{XY}-\text{TMS}]^{2+}$ Cyclic Voltammogram	78
3.5 $[\text{Ru}-\text{XY}-\text{TMS}]^{2+}$ Spectroelectrochemical Traces	79
3.6 $[\text{Ru}-\text{XY}-\text{TMS}]^{2+}$ $\text{Ru}^{\text{III/II}}$ Difference Spectrum	80
3.7 $[\text{Ru}(\text{bpy})_3]^{2+}$ Spectroelectrochemical Traces	81
3.8 $[\text{Ru}(\text{bpy})_3]^{2+}$ $\text{Ru}^{\text{III/II}}$ Difference Spectrum	82
3.9 $[\text{Ru}-\text{XY}-\text{TMS}]^{2+}$ Excited State Luminescence Decay	83
3.10 $[\text{Ru}-\text{XY}-\text{TMS}]^{2+}$ Excited State Difference Spectrum (low concentration)	84

3.11 [Ru-XY-TMS] ²⁺ Excited State Difference Spectrum (high concentration)	85
3.12 TMS-Ethynyl-G UV-visible Absorption Spectrum	86
3.13 TMS-Ethynyl-G Cyclic Voltammogram	87
3.14 Expanded TMS-Ethynyl-G Cyclic Voltammogram	88
3.15 TMS-Ethynyl-G Spectroelectrochemical Traces	89
3.16 TMS-Ethynyl-G ⁺ /TMS-Ethynyl-G Difference Spectrum	90
3.17 [Ru-XY-TMS] ²⁺ NMR Spectrum	91
3.18 [Ru-(XY) ₂ -G] ²⁺ NMR Spectrum	92
3.19 [Ru-(XY) ₃ -G] ²⁺ NMR Spectrum	93
3.20 [Ru-(XY) ₄ -G] ²⁺ NMR Spectrum	94
3.21 Calculated Isotope Patterns	95
3.22 [Ru-(XY) ₂ -G] ²⁺ ESI Mass Spectrum	96
3.23 Detailed View of [Ru-(XY) ₂ -G] ²⁺ ESI Mass Spectrum	97
3.24 [Ru-(XY) ₃ -G] ²⁺ ESI Mass Spectrum	98
3.25 Detailed View of [Ru-(XY) ₃ -G] ²⁺ ESI Mass Spectrum	99
3.26 [Ru-(XY) ₄ -G] ²⁺ ESI Mass Spectrum	100
3.27 Detailed View of [Ru-(XY) ₄ -G] ²⁺ ESI Mass Spectrum	101
3.28 [Ru-(XY) ₅ -G] ²⁺ ESI Mass Spectrum	102
3.29 Detailed View of [Ru-(XY) ₅ -G] ²⁺ ESI Mass Spectrum	103
3.30 [Ru-(XY) _n -G] ²⁺ UV-visible Absorption Spectra	104
3.31 [Ru-(XY) ₃ -G] ²⁺ UV-visible Absorption Spectrum	105
3.32 UV-visible Absorption Spectra Comparison of Ruthenium Polypyridyl Complexes	106
3.33 [Ru-(XY) ₃ -G] ²⁺ Cyclic Voltammogram (Ru ^{II/III})	107
3.34 [Ru-(XY) ₃ -G] ²⁺ Cyclic Voltammogram (G ^{0/+})	108
3.35 [Ru-(XY) ₃ -G] ²⁺ Spectroelectrochemical Traces	109
3.36 [Ru ^{III} -(XY) ₃ -G ⁺]/[Ru-(XY) ₃ -G] ²⁺ Difference Spectrum	110
3.37 [Ru-(XY) _n -G] ²⁺ Excited State Luminescence Decay	111
3.38 [Ru-(XY) ₂ -G] ²⁺ Excited State Difference Spectrum	112

Tables

3.1 Summary of UV-visible Absorption Spectra	113
3.2 Summary of Redox Potentials	114
3.3 Summary of Excited State Lifetimes	115

Chapter 4. Electron Transfer Properties of $[\text{Ru}-(\text{XY})_n-\text{G}]^{2+}$

Figures

4.1 Electron Transfer Reaction Schematic	130
4.2 Estimated $[\text{Ru}-(\text{XY})_2-\text{G}]^{2+}$ Electron Transfer Rates	137
4.3 Stern-Volmer Analysis of $[\text{Ru}-(\text{XY})_2-\text{G}]^{2+}$	138
4.4 Transient Absorption of $[\text{Ru}-(\text{XY})_2-\text{G}]^{2+}$ with 5 mM MV^{2+}	139
4.5 Transient Difference Spectra of $[\text{Ru}-(\text{XY})_2-\text{G}]^{2+}$ with 5 mM MV^{2+}	140
4.6 Comparison of $[\text{Ru}-(\text{XY})_2-\text{G}]^{2+}$ Transient Difference Spectra	141
4.7 Comparison of MV^+ and $[\text{Ru}-(\text{XY})_2-\text{G}]^{2+}$ Transient Spectra	142
4.8 Transient Absorption Spectra of $[\text{Ru}-(\text{XY})_2-\text{G}]^{2+}$ with MV^{2+} at 460 nm	143
4.9 Transient Absorption Spectra of $[\text{Ru}-(\text{XY})_2-\text{G}]^{2+}$ with MV^{2+} at 500 nm	144
4.10 Stern-Volmer Analysis of $[\text{Ru}-(\text{XY})_3-\text{G}]^{2+}$ Quenching by MV^{2+}	151
4.11 $[\text{Ru}-(\text{XY})_2-\text{G}]^{2+}$ Quencher Concentration Dependent Transient Absorption Traces	152
4.12 $[\text{Ru}-(\text{XY})_3-\text{G}]^{2+}$ Quencher Concentration Dependent Transient Absorption	157
4.13 $[\text{Ru}-(\text{XY})_3-\text{G}]^{2+}$ Transient Absorption Traces under Flash-Quench Conditions	158
4.14 $[\text{Ru}-(\text{XY})_3-\text{G}]^{2+}$ Flash-Quench Transient Difference Spectra	159
4.15 Comparison of $[\text{Ru}-(\text{XY})_3-\text{G}]^{2+}$ Electron Transfer Product and MV^+	160
4.16 Upper and Lower Limit for $[\text{Ru}-(\text{XY})_3-\text{G}]^{2+}$	161
4.17 Stern-Volmer Analysis of $[\text{Ru}-(\text{XY})_4-\text{G}]^{2+}$ Quenching with MV^{2+}	165
4.18 $[\text{Ru}-(\text{XY})_4-\text{G}]^{2+}$ Transient Absorption under Flash-Quench Conditions	166
4.19 $[\text{Ru}-(\text{XY})_4-\text{G}]^{2+}$ Transient Difference Spectra under Flash-Quench Conditions	167
4.20 Comparison of MV^+ to $[\text{Ru}-(\text{XY})_4-\text{G}]^{2+}$ Electron Transfer Products	168
4.21 $[\text{Ru}-(\text{XY})_5-\text{G}]^{2+}$ Transient Absorption Spectra under Flash-Quench Conditions	174
4.22 Concentration Dependence of $[\text{Ru}-(\text{XY})_5-\text{G}]^{2+}$ Rates	175
4.23 Limits of $[\text{Ru}-(\text{XY})_n-\text{G}]^{2+}$ Electron Transfer Rates	188
4.24 Electron Tunneling Pathways	189
4.25 Tunneling Segments	190
4.26 $[\text{Ru}-(\text{XY})_n-\text{G}]^{2+}$ Electron Tunneling Pathways	192
4.27 $[\text{Ru}-(\text{XY})_n-\text{G}]^{2+}$ β -Plots	194
4.28 Closest Approach Distance, r_o'	196
4.29 Distance Dependence of $[\text{Ru}-(\text{XY})_5-\text{G}]^{2+}$ Electron Transfer Rates (β -Plot)	198
4.30 TMS-(XY) ₂ -TMS X-ray Crystal Structure	199

Tables

4.1 Observed Kinetics for $[\text{Ru}-(\text{XY})_2-\text{G}]^{2+}$ Under Flash-Quench Conditions	145
4.2 $[\text{Ru}-(\text{XY})_3-\text{G}]^{2+}$ Electron Transfer Kinetics under Flash-Quench Conditions ($k_{\text{ET}} > k_{\text{q}}'$) .	153
4.3 $[\text{Ru}-(\text{XY})_3-\text{G}]^{2+}$ Electron Transfer Kinetics under Flash-Quench Conditions ($k_{\text{ET}} < k_{\text{q}}'$) .	154
4.4 $[\text{Ru}-(\text{XY})_n-\text{G}]^{2+}$ Electron Transfer Rates	187
4.5 Tunneling Segment Lengths	191
4.6 Electron Tunneling Distances	193
4.7 $[\text{Ru}-(\text{XY})_n-\text{G}]^{2+}$ Close Contact Electron Transfer Rates	195
4.8 $[\text{Ru}-(\text{XY})_n-\text{G}]^{2+}$ Closest Approach Distance, r_0'	197

Schemes

4.1 Flash Quench	120
4.2 $[\text{Ru}-(\text{XY})_3-\text{G}]^{2+}$ Electron Transfer Reactions under Flash-Quench Conditions	155
4.3 Kinetic Analysis of the Electron Transfer Mechanism for $[\text{Ru}-(\text{XY})_3-\text{G}]^{2+}$	156
4.4 $[\text{Ru}-(\text{XY})_4-\text{G}]^{2+}$ Electron Transfer Reactions Under Flash-Quench Conditions	169

Chapter 5. Synthesis, Characterization, and Electron Transfer Reactions of Nanocrystalline TiO_2 Solar Cell Dyes – $[\text{Ru}-(\text{XY})_n-\text{BA}]^{2+}$

Figures

5.1 Schematic of Nanocrystalline TiO_2 Solar Cells	217
5.2 Electron Transfer Reactions of Nanocrystalline TiO_2 Solar Cells	218
5.3 $[\text{Ru}-(\text{XY})_n-\text{BA}]^{2+}$	219
5.4 $[\text{Ru}-(\text{XY})_n-\text{BA}]^{2+}$ Bound to TiO_2	220
5.5 $[\text{Ru}-(\text{XY})_n-\text{BA}]^{2+}$ UV-visible Absorption Spectra	221
5.6 $[\text{Ru}-(\text{XY})_0-\text{BA}]^{2+}$ Cyclic Voltammogram ($\text{Ru}^{\text{II/III}}$)	222
5.7 $[\text{Ru}-(\text{XY})_n-\text{BA}]^{2+}$ Excited State Lifetimes	223
5.8 $[\text{Ru}-(\text{XY})_n-\text{BA}]^{2+}$ Regeneration with Iodide	224
5.9 $[\text{Ru}-(\text{XY})_n-\text{BA}]^{2+}$ Regeneration with Iodide Pseudo – First-Order Plots	225

Tables

5.1 Summary of $[\text{Ru}-(\text{XY})_n\text{-BA}]^{2+}$ UV-Visible Absorption Spectra	226
5.2 Summary of $[\text{Ru}-(\text{XY})_n\text{-BA}]^{2+}$ Redox Potentials	227
5.3 Summary of $[\text{Ru}-(\text{XY})_n\text{-BA}]^{2+}$ Excited State Lifetimes	228

Schemes

5.1 General Synthetic Route to $[\text{Ru}-(\text{XY})_n\text{-BA}]^{2+}$	210
5.2 Dye Regeneration in Homogenous Fluid Solution.....	213

Appendix A. Custom Glassware – Low Temperature Addition Funnel

Figure A.1 Addition Funnel Schematic	231
--	-----

Appendix B. Optically Transparent Thin Layer Spectroelectrochemical Cell

Figure B.1 OTTL Cell Schematic	233
--------------------------------------	-----

Appendix C. Nanosecond Laser Flash Photolysis

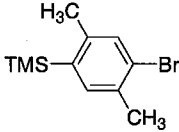
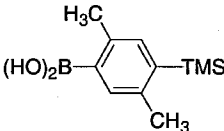
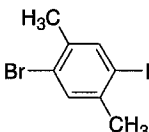
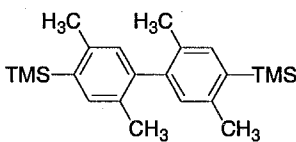
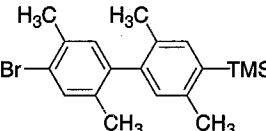
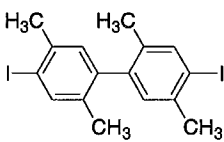
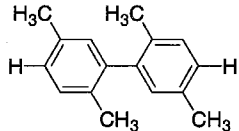
Figure C.1 Laser Flash Photolysis Instrument Schematic	235
--	-----

Appendix D. Spectroscopic Handles

Figure D.1 Methyl Viologen (MV^{2+}) Spectroelectrochemical Traces	237
Figure D.2 Methyl Viologen Cation (MV^+) UV-visible Absorption	238
Figure D.3 $\text{MV}^+ - \text{MV}^{2+}$ Difference Spectrum	239
Figure D.4 Methyl Viologen (MV) Spectroelectrochemical Traces	240
Table D.1 Spectroscopic Handles	241

SYNTHESIZED COMPOUNDS

The following table is a summary of all the compounds synthesized as part of this thesis.

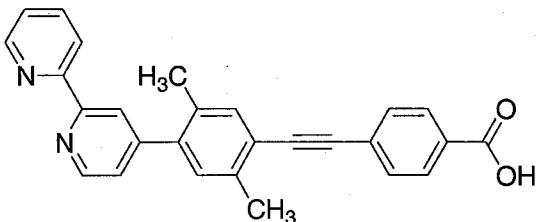
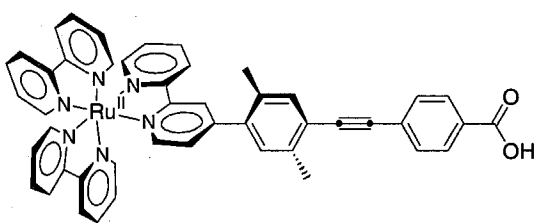
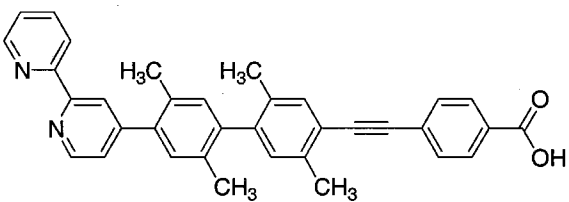
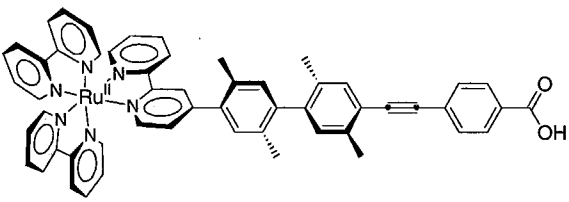
Abbreviation	Structure	Name
TMS-XY-Br		1-bromo-2,5-dimethyl-4-trimethylsilylbenzene
TMS-XY-B(OH) ₂		2,5-dimethyl-4-trimethylsilylphenylboronic acid
Br-XY-I		1-bromo-4-iodo-2,5-dimethylbenzene
TMS-(XY) ₂ -TMS		2,2',5,5'-tetramethyl-4,4'-di(trimethylsilyl)-1,1'-biphenyl
TMS-(XY) ₂ -Br		2,2',5,5'-tetramethyl-4-trimethylsilyl,4'-bromo-1,1'-biphenyl
I-(XY) ₂ -I		4,4'-diiodo,2,2',5,5'-tetramethyl-1,1'-biphenyl
H-(XY) ₂ -H		2,2',5,5'-tetramethyl-1,1'-biphenyl

Abbreviation	Structure	Name
TMS-(XY) ₃ -TMS		2,2',2'',5,5',5''-hexamethyl-4,4''-di(trimethylsilyl)-1,1':4',1''-terphenyl
		3-bromo-4-methoxyaniline
		4-methoxy-3-(trimethylsilylethynyl)-aniline
TMS-Ethynyl-G		4-methoxy-3-(trimethylsilylethynyl)-N,N-dimethylaniline
Ethynyl-G		3-ethynyl-4-methoxy-N,N-dimethylaniline
Bpy-XY-TMS		4-(2,5-dimethyl-4-trimethylsilylphenyl)-2,2'-bipyridine
Bpy-XY-I		4-(2,5-dimethyl-4-iodophenyl)-2,2'-bipyridine
Bpy-(XY) ₂ -TMS		4-(4'-trimethylsilyl-2,2',5,5'-tetramethyl-1,1'-biphenyl-4-yl)-2,2'-bipyridine

Abbreviation	Structure	Name
Bpy-(XY) ₂ -I		4-(4'-iodo-2,2',5,5'-tetramethyl-1,1'-biphenyl-4-yl)-2,2'-bipyridine
Bpy-(XY) ₂ -G		4-(4'-(3-ethynyl-4-methoxy-N,N-dimethylaniline)-2,2',5,5'-tetramethyl-1,1'-biphenyl-4-yl)-2,2'-bipyridine
[Ru-(XY) ₂ -G] ²⁺		[(bpy) ₂ Ru ^{II} (bpy-(XY) ₂ -G)](PF ₆) ₂
Bpy-(XY) ₃ -TMS		4-(4''-trimethylsilyl-2,2',2'',5,5',5''-hexamethyl-1,1':4,1''-terphenyl-4-yl)-2,2'-bipyridine
Bpy-(XY) ₃ -I		4-(4''-iodo-2,2',2'',5,5',5''-hexamethyl-1,1':4,1''-terphenyl-4-yl)-2,2'-bipyridine
Bpy-(XY) ₃ -G		4-(4''-(3-ethynyl-4-methoxy-N,N-dimethylaniline)-2,2',2'',5,5',5''-hexamethyl-1,1':4,1''-terphenyl-4-yl)-2,2'-bipyridine
[Ru-(XY) ₃ -G] ²⁺		[(bpy) ₂ Ru ^{II} (bpy-(XY) ₃ -G)](PF ₆) ₂

Abbreviation	Structure	Name
Bpy-(XY) ₄ -TMS		4-(4'''-trimethylsilyl-2,2',2'',2''',5,5',5'',5'''-octamethyl-1,1':4',1'':4'',1'''-quaterphenyl-4-yl)-2,2'-bipyridine
Bpy-(XY) ₄ -I		4-(4'''-iodo-2,2',2'',2''',5,5',5'',5'''-octamethyl-1,1':4',1'':4'',1'''-quaterphenyl-4-yl)-2,2'-bipyridine
Bpy-(XY) ₄ -G		4-(4'''-(3-ethynyl-4-methoxy-N,N-dimethylaniline)-2,2',2'',2''',5,5',5'',5'''-octamethyl-1,1':4',1'':4'',1'''-quaterphenyl-4-yl)-2,2'-bipyridine
[Ru-(XY) ₄ -G] ²⁺		[(bpy) ₂ Ru ^{II} (bpy-(XY) ₄ -G)](PF ₆) ₂
Bpy-(XY) ₅ -TMS		4-(4''''-trimethylsilyl-2,2',2'',2''',2''',5,5',5'',5''',5''''-decamethyl-1,1':4',1'':4'',1''':4''',4''''-pentaphenyl-4-yl)-2,2'-bipyridine
Bpy-(XY) ₅ -I		4-(4'''-iodo-2,2',2'',2''',2''',5,5',5'',5''',5''''-decamethyl-1,1':4',1'':4'',1''':4''',4''''-pentaphenyl-4-yl)-2,2'-bipyridine
Bpy-(XY) ₅ -G		4-(4'''-(3-ethynyl-4-methoxy-N,N-dimethylaniline)-2,2',2'',2''',2''',5,5',5'',5''',5''''-decamethyl-1,1':4',1'':4'',1''':4''',4''''-pentaphenyl-4-yl)-2,2'-bipyridine

Abbreviation	Structure	Name
$[\text{Ru}-(\text{XY})_5-\text{G}]^{2+}$		$[(\text{bpy})_2\text{Ru}^{\text{II}}(\text{bpy}-(\text{XY})_5-\text{G})](\text{PF}_6)_2$
$[\text{Ru}(\text{bpy})_3](\text{PF}_6)_2$		
$[\text{Ru}-\text{XY}-\text{TMS}]^{2+}$		$[(\text{bpy})_2\text{Ru}(\text{bpy}-\text{XY}-\text{TMS})](\text{PF}_6)_2$
$[\text{MV}](\text{PF}_6)_2$		1,1'-dimethyl-4,4'- bipyridinium dihexafluorophosphate
4-TMS-BA		4-trimethylsilyl-ethynyl-benzoic acid
4-Ethynyl-BA		4-ethynyl-benzoic acid
$\text{Bpy}-(\text{XY})_0-\text{BA}$		4-(4'-ethynyl-benzoic acid)-2,2'- bipyridine
$[\text{Ru}-(\text{XY})_0-\text{BA}]^{2+}$		$[(\text{bpy})_2\text{Ru}^{\text{II}}(\text{bpy}-(\text{XY})_0-\text{BA})](\text{PF}_6)_2$

Abbreviation	Structure	Name
Bpy-(XY) ₁ -BA		4-(2,5-dimethyl-4-(4-ethynylbenzoic acid)-2,2'-bipyridine
[Ru-(XY) ₁ -BA] ²⁺		[(bpy) ₂ Ru ^{II} (bpy-(XY) ₁ -BA)](PF ₆) ₂
Bpy-(XY) ₂ -BA		4-(4'-(4-ethynylbenzoic acid)-2,2',5,5'-tetramethyl-1,1'-biphenyl-4-yl)-2,2'-bipyridine
[Ru-(XY) ₂ -BA] ²⁺		[(bpy) ₂ Ru ^{II} (bpy-(XY) ₂ -BA)](PF ₆) ₂

THESIS OVERVIEW

A series of donor-bridge-acceptor (D-B-A) complexes consisting of a ruthenium polypyridyl acceptor, variable-length xylene bridge (XY), and 3-ethynyl-4-methoxy-N,N-dimethylaniline (G) as the donor, $[(bpy)_2Ru(bpy-(XY)_n-G)](PF_6)_2$ (where $n = 2$ to 5 ; abbreviated $[Ru-(XY)_n-G]^{2+}$), were designed, synthesized, and characterized to carry out electron transfer studies. $[Ru-(XY)_n-G]^{2+}$ is the first in a series of D-B-A complexes for evaluating tunneling energy effects¹⁻⁴ on long-range electron-transfer reactions.⁵⁻²⁹

Experimental electron-transfer studies of $[Ru-(XY)_n-G]^{2+}$ reveal a strong relationship between the conformational structure of the bridge and the distance decay constant, β .

Chapter 2 discusses the design and synthesis of $[Ru-(XY)_n-G]^{2+}$ and related compounds. The design requirements for D-B-A complexes and a general synthetic approach are included in the first part of the chapter. Specific details of the synthetic

schemes and experimental details are described for the successful synthesis of $[\text{Ru}(\text{XY})_n\text{-G}]^{2+}$ as well. This series of D-B-A complexes required extensive use of multi-step synthetic methods. Palladium-catalyzed cross-coupling reactions³⁰⁻³⁴ and protecting group strategies were major elements in the synthesis.

Chapter 3 contains UV-visible absorption, electrochemical, spectroelectrochemical, NMR, mass spectrometry, and photophysical characterizations of $[\text{Ru}(\text{XY})_n\text{-G}]^{2+}$, its components, and related compounds. The characterizations have a dual purpose. The first is to identify spectroscopic handles that will be useful in carrying out electron-transfer studies. The second is to probe the properties of $[\text{Ru}(\text{XY})_n\text{-G}]^{2+}$. All of the characterizations consistently suggest that the physical properties of $[\text{Ru}(\text{XY})_n\text{-G}]^{2+}$ do not vary significantly from the basic $[\text{Ru}(\text{bpy})_3]^{2+}$ complex.

Chapter 4 discusses, in detail, the use of time-resolved spectroscopy to monitor electron-transfer reactions involving $[\text{Ru}(\text{XY})_n\text{-G}]^{2+}$ and to measure the associated rate constants. Analysis of the tunneling distances between the donor and acceptor is included to construct a plot of electron-transfer rates versus distance. The slope of this plot is the electron transfer distance decay constant, β . Comparisons of $[\text{Ru}(\text{XY})_n\text{-G}]^{2+}$ with similar compounds reported in the literature reveal a strong relationship between the structure of the xylene bridge and β .

Chapter 5 illustrates the use of $[\text{Ru}(\text{XY})_n\text{-G}]^{2+}$ -like complexes for studying interfacial electron transfer at a liquid-semiconductor junction. Dyes for use in nanocrystalline TiO_2 solar cells were synthesized by exchanging the aromatic amine donor, G, with a benzoic acid (BA) group to produce $[\text{Ru}(\text{XY})_n\text{-BA}]^{2+}$. Synthesis, characterization, and solution phase electron-transfer reactions are discussed in this chapter.

Chapter 1

INTRODUCTION and BACKGROUND

INTRODUCTION

1.1 Electron-Transfer Reactions

Electron transfers form an important class of reactions that play a vital role in many chemical processes.^{35,36} Experimental studies of electron-transfer reactions are all based on the broad foundation created by Marcus Theory.^{37,38} This thesis focuses on experimental studies of electron-transfer reactions mediated by substituted phenylene oligomers. The general approach is to incorporate oligomers into donor-bridge-acceptor (D-B-A) complexes. The oligomers act as molecular wires,³⁹⁻⁴⁴ directing and mediating the transfer of electrons between donor and acceptor. Results in this thesis on electron-transfer studies of $[\text{Ru}-(\text{XY})_n-\text{G}]^{2+}$ lay the foundation for addressing tunneling energy effects, highlight bridge conformational effects, and give a general picture of electron tunneling through substituted-phenylene bridges. Creating a set of D-B-A complexes with known electron transfer properties has applications in the

development of novel materials for nanotechnology,⁴⁵⁻⁴⁸ molecular electronics,^{36,44,49-76} and solar energy conversion.^{77,78}

Throughout this thesis, "electron tunneling" refers to a class of electron transfer reactions. Electron tunneling^{16,18,79} uses an intervening medium to facilitate charge transfers. Typically, electron-tunneling reactions occur over long distances ($> 10 \text{ \AA}$) and are non-adiabatic. The D-B-A complexes studied in this thesis meet those criteria and fall under the category of electron tunneling.

1.2 Electron-Transfer Theory

Marcus Theory^{37,38} and associated derivations have proven extremely invaluable for the study of many chemical systems that incorporate electron-transfer reactions.³⁵ The basis of Marcus Theory relates the electron transfer rate constant, k_{ET} , to free energy driving force, ΔG° , and reorganizational energy (λ).⁸⁰⁻⁸²

$$k_{\text{ET}} = v_{\text{N}} \kappa_{\text{E}} \exp\left(\frac{-(\Delta G^\circ + \lambda)^2}{4\lambda RT}\right) \quad (1.1)$$

where v_{N} is a nuclear frequency factor and κ_{E} is an electronic factor.

Electron-transfer reactions occurring over long distances or between a weakly coupled donor and acceptor typically fall within the non-adiabatic regime; the reactants form the transition state many times before proceeding on to products. Introduction of quantum mechanical terms, to account for donor-acceptor coupling in these cases, yields the semiclassical electron-transfer equation,

$$k_{\text{ET}} = \left(\frac{4\pi^3}{h^2 \lambda k_B T} \right)^{\frac{1}{2}} H_{AB}^2 \exp \left(-\frac{(\Delta G^\circ + \lambda)^2}{4\lambda k_B T} \right) \quad (1.2)$$

In expression 1.2, H_{AB} is the electronic tunneling matrix element⁸³ between the donor and acceptor.

1.3 Tunneling Energy Effects

The energy of the ($D + A$) and ($D^+ + A^-$) states at the transition-state configuration is known as the tunneling energy. It has been predicted that tuning the energy difference, $\Delta\epsilon$, between the one-electron reduced or one-electron oxidized bridge states and the tunneling energy can significantly affect the rates of electron transfer, especially at long distances.^{1,84-91} McConnell's superexchange mode⁹²⁻⁹⁵ is useful for describing the electronic coupling between a donor and acceptor, spanned by a bridge of repeating units. The model relates the electronic-coupling matrix element, H_{AB} , to the coupling between the donor and bridge, h_{Db} , between individual bridge units, h_b , and between the bridge and acceptor, h_{bA} .

$$H_{AB} = \frac{h_{Db}}{\Delta\epsilon} \left(\frac{h_b}{\Delta\epsilon} \right)^{n-1} h_{bA} \quad (1.3)$$

Furthermore, the model predicts a relationship between the distance decay constant, β , the length of a bridge unit, α , and $\Delta\epsilon$.

$$\beta = \left(\frac{2}{\alpha} \right) \ln \left(\frac{h_b}{\Delta \epsilon} \right) \quad (1.4)$$

From equation 1.4, the superexchange model establishes an inverse relationship between electron transfer rates and $\Delta \epsilon$; decreasing the energy gap between the bridge states and the tunneling energy will yield a smaller β and more efficient electron transfer.

Chapter 2

DESIGN and SYNTHESIS of PHENYLENE DONOR-BRIDGE-ACCEPTOR COMPLEXES

INTRODUCTION

2.1 Donor-Bridge-Acceptor Complexes

Donor-bridge-acceptor (D-B-A) complexes are a versatile class of compounds.²⁻
^{13,35,96-111} Mechanism elucidation, ¹¹²⁻¹¹⁴ biological charge transport, ^{16-29,115-124} funda-
 mental electron transfer,²⁻⁴ solar-energy conversion,¹²⁵⁻¹²⁸ and nanotechnology^{46-48,51} are
 just some of the applications. D-B-A complexes are complicated species that are the
 product of sophisticated design and technically challenging syntheses. D-B-A complexes
 should be thought of more as molecular machines than merely as molecules. They are
 designed for a specific function or purpose, and must conform to many synthetic,
 experimental, and technical criteria.

This thesis discusses the electron-transfer properties of molecular wires based on
 substituted phenylene oligomers. The approach is to incorporate the oligomers as
 bridges into a series of D-B-A complexes. In this chapter the design philosophy and
 synthetic methods and routes used to construct the D-B-A complexes will be discussed.
 The target D-B-A complexes are deceptively simple looking but required challenging

multistep syntheses. New methods for characterizing the intermediates and products were also necessary.

2.2 Design of Donor-Bridge-Acceptor Complexes

D-B-A complexes are in many ways the molecular equivalent of a machine. They are often large assemblies, incorporating different components that serve specific roles. They are designed to fulfill a specific function under a stringent set of criteria. The philosophy behind the design of D-B-A complexes is to create a molecule that performs a specific task, is stable under the experimental conditions, is characterizable, and has design flexibility to accommodate changes to a study's parameters or goals with minimal effort. The last point highlights the notion that D-B-A complexes are molecular scaffolds, on which parts can be added or changed as needed.

D-B-A complexes for use in electron transfer studies have several criteria. The donor and acceptor must undergo a thermodynamically downhill electron-transfer reaction. Therefore, the donor should have a lower redox potential than the acceptor. The electron transfer reaction for this study is intramolecular, so the donor and acceptor must be covalently attached to either side of the phenylene bridge. The flash-quench method¹²⁹ was used to carry out the electron transfer study. The D-B-A complexes must comply with the requirements for the flash quench (sufficient excited state lifetime, efficient quenching, etc.) and must not undergo any dark reactions. To measure kinetics, the course of the reaction must be followed at any given time point; therefore, there must be a method for experimentally monitoring the consumption of reactants and formation of products. The D-B-A complex should also be stable through multiple redox cycles.

In addition to the general design requirements placed on D-B-A complexes for electron-transfer studies, there are criteria specific to this report. The additional parameters pertain to probing tunneling energy effects and measuring distance-dependent electron-transfer rates. The one-electron oxidation potential of the bridge should be higher than the acceptor's and the reduction potential should be lower than the donor's. This is to avoid the bridge oxidation or reduction during the electron-transfer reaction. The goal is to study an electron tunneling reaction; oxidation or reduction of the bridge would lead to a hopping mechanism rather than tunneling.

RESULTS and DISCUSSION

2.3 D-B-A Scaffold – $[\text{Ru}-(\text{XY})_n\text{-R}]^{2+}$

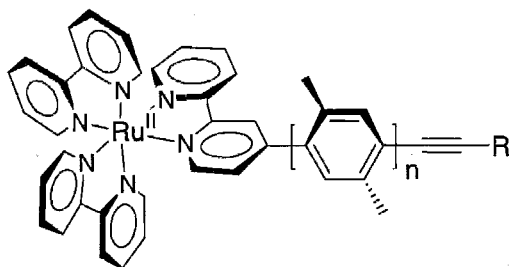


Figure 2.1 Donor-Bridge-Acceptor Scaffold

The D-B-A scaffold is based on a transition metal, polypyridyl framework (Figure 2.1) that incorporates a bridging phenylene ligand, and can accommodate a variety of donors or terminal functional groups (R). Transition-metal polypyridyl

complexes ($M = \text{Ru, Os, Re, etc.}$) have been proven, in numerous studies, to be a good choice for use in donor-bridge-acceptor complexes.^{5,6,8-10,100} Varying the transition metal is a convenient way to vary the tunneling energy as well. Polypyridyl complexes also have convenient spectroscopic handles for monitoring reaction progress. Several donors were synthesized and studied (Figure 2.2) including the inorganic complex $\text{Ru}^{\text{II}}(\text{NH}_3)_5\text{Py}'$ (where Py' is the attachment point to the phenylene bridge via an alkyne linkage), the organometallic compound ferrocene, and an organic aromatic amine, 3-ethynyl-4-methoxyphenyl-*N,N*-dimethylamine (ethynyl-G). The donor and acceptor are linked to the bridge through C-C covalent bonds that will hold the assembly together through multiple redox cycles.

To probe tunneling energy effects on electron transfer reactions, it was important to have bridge state energies that remain constant with distance. Highly conjugated molecular wires, such as phenylethynylenes or vinyl oligomers, are very efficient electron transfer media.¹³⁰⁻¹³³ The energy of the one-electron oxidized or reduced states changes readily with distance, however, judging by the absorption spectra and redox potentials of the monomer versus higher order oligomers.^{130,134} On the other extreme, the energy of aliphatic bridges, such as straight chain alkanes, is relatively insensitive with length. The flexibility of aliphatic bridges creates a distribution of distances, complicating the determination of β . Furthermore, the bridge energies are rather high, making them experimentally infeasible for tunneling energy studies.

Phenylene oligomers have the best combination of stable bridge state energy and structural rigidity. The twist angle between adjacent monomers (typically 22 to 50°)¹³⁵⁻¹³⁸ decreases electronic coupling, thus stabilizing the bridge energies.¹⁰¹

Phenylene oligomers are rigid with high rotational barriers (20-30 kcal)¹³⁹ for substituted

phenylenes. Phenylenes are notoriously insoluble and the addition of a large, planar bipyridine ring only increases the likelihood of precipitation. Once metalated, the dication ruthenium complex would impart solubility to the oligomer. Oligomer synthetic methods are too harsh for metal complexes preventing metalation until the last step.

Substituting the benzene rings with methyl groups greatly enhances solubility over plain phenylenes.¹³⁹ It is a common approach to add alkyl groups to an oligomer's center ring.^{140,141} Such an approach could cause variability in the bridge states due to a lack of structural consistency. A better approach is to use a xylene oligomer bridge. Functionalizing each ring with methyl groups, using 2,5-dimethylbenzene as the monomer, produces an oligomer that is soluble in a wide range of organic solvents.

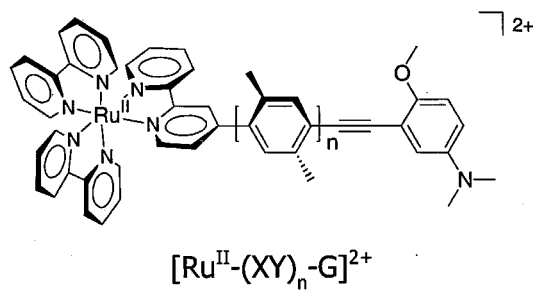
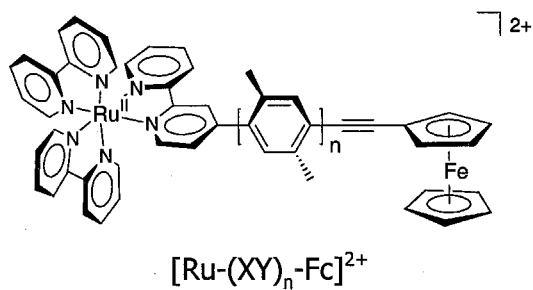
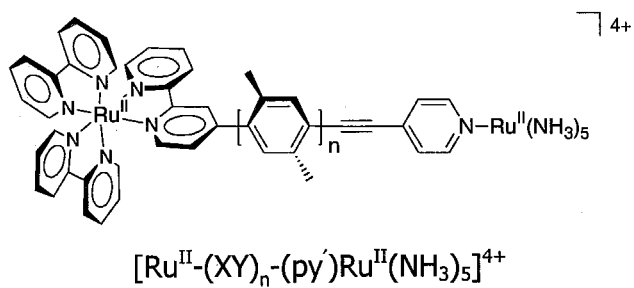


Figure 2.2 Donors for $[\text{Ru}-(\text{XY})_n-\text{R}]^{2+}$

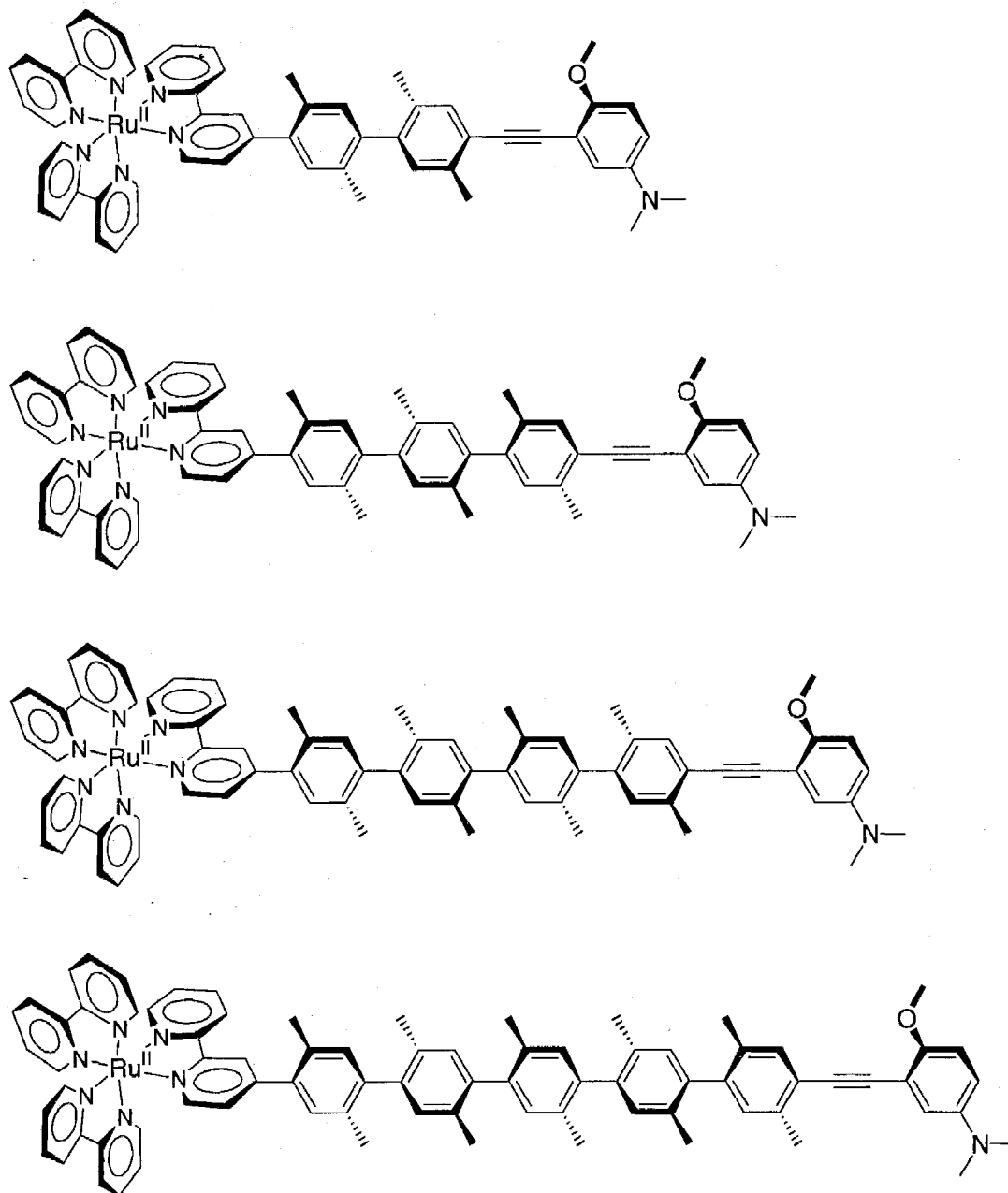


Figure 2.3 [Ru(XY)_n-G]²⁺ D-B-A Electron Transfer Complexes

2.4 Target D-B-A Complex – $[\text{Ru}-(\text{XY})_n\text{-G}]^{2+}$

The target series of D-B-A complexes (Figure 2.3) was constructed with 2 to 5 xylene rings. The oxidative flash-quench method begins with an excited-state quenching reaction; the starting state, $[\text{Ru}^{\text{II}}-(\text{XY})_n\text{-G}]^{2+}$, is oxidized to $[\text{Ru}^{\text{III}}-(\text{XY})_n\text{-G}]^{3+}$.

Ruthenium polypyridyl complexes have sufficiently long-lived excited-state lifetimes for the flash-quench method. The oxidation $\text{Ru}^{\text{II}} \rightarrow \text{Ru}^{\text{III}}$ and reverse reaction $\text{Ru}^{\text{III}} \rightarrow \text{Ru}^{\text{II}}$ are reversible and readily monitored spectroscopically. The spectroscopic and electron transfer properties of ruthenium polypyridyl complexes are also well understood.¹⁴² All of these factors dictate the ruthenium component act as the acceptor.

The choice of donor was not as straightforward as the acceptor or bridge. Choosing a ruthenium polypyridyl complex as the acceptor constrained the list of potential candidates. The donor needed to have an oxidation potential less than the $\text{Ru}^{\text{II/III}}$ couple (1.6 V vs. NHE). The first choice, $\text{Ru}^{\text{II}}(\text{NH}_3)_5\text{Py}'$, had good spectroscopic handles and the appropriate redox potential. Under actual experimental conditions, it suffered from a general lack of stability and the $\text{Ru}(\text{NH}_3)_5$ core apparently photolyzed off during flash quench experiments. Ferrocene was far more stable and exhibited good redox properties but lacked good spectroscopic handles.

After further investigation, aromatic amines were deemed good choices for donors. Their redox potentials are tunable with the addition of ring substituents. The neutral and radical cation species have good spectroscopic signatures. Using proper handling and care, they are relatively stable and can tolerate repeated irradiation during

electron transfer experiments. 3-ethynyl-4-methoxy-N,N-dimethylaniline (ethynyl-G) was chosen as the donor for the D-B-A complexes. The parent compound, 4-methoxy-N,N-dimethylaniline reductively quenches $^*[Ru(bpy)_3]^{2+}$, making it an ideal donor for the D-B-A complexes.¹⁴³⁻¹⁴⁶ The use of an acetylene linkage ensures a strong covalent bond with the phenylene bridge.

2.5 Retrosynthetic Analysis and Synthetic Route to $[Ru-(XY)_n-G]^{2+}$

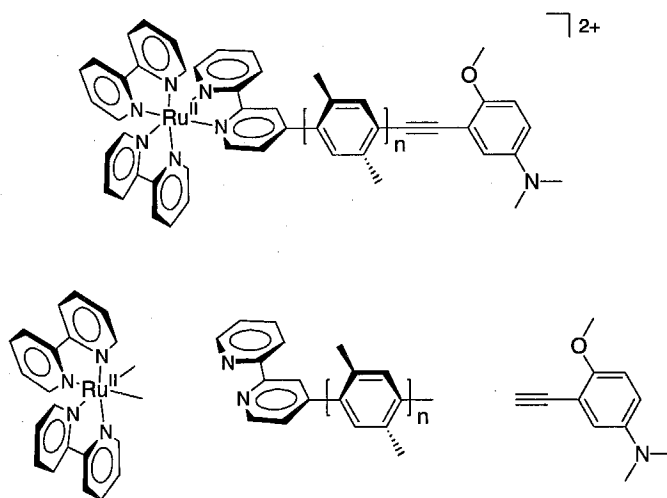


Figure 2.4 Retrosynthetic Analysis of $[Ru-(XY)_n-G]^{2+}$

The retrosynthetic analysis of $[Ru-(XY)_n-G]^{2+}$ (Figure 2.4) guides the development of a synthetic strategy that involves constructing the donor, bridge, and

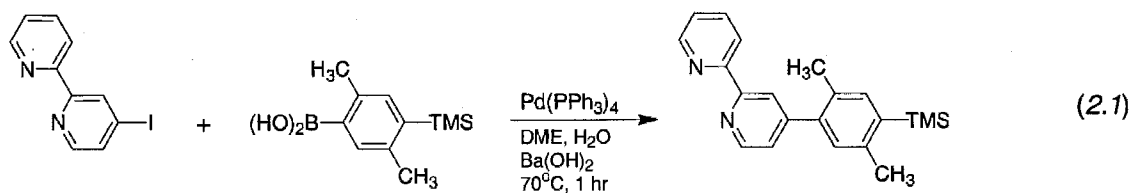
acceptor separately before assembling them to form $[\text{Ru}-(\text{XY})_n-\text{G}]^{2+}$. Through compartmental-izing the synthesis, changes to any of the parts do not require the entire assembly to be constructed from scratch. The ruthenium precursor is commercially available as $[\text{Ru}(\text{bpy})_2\text{Cl}_2]\text{Cl}_2$, and readily undergoes substitution reactions with the oligomer-functionalized bipyridine ligand. The oligomer will be synthesized in a stepwise approach, working from bipyridine out. While divergent/convergent strategies^{130,147} are more efficient, the D-B-A complex oligomer is asymmetric; any advantages in speed of the divergent/convergent approach are negated by loss of regioselectivity. Total control over functionality in the para positions of the oligomers is only achievable through stepwise growth. The donor is synthesized separately from the other components and added to the oligomer ligand. The bridge-donor assembly is then joined to the ruthenium complex to form a completed D-B-A complex (Scheme 2.1).

SCHEME 2.1

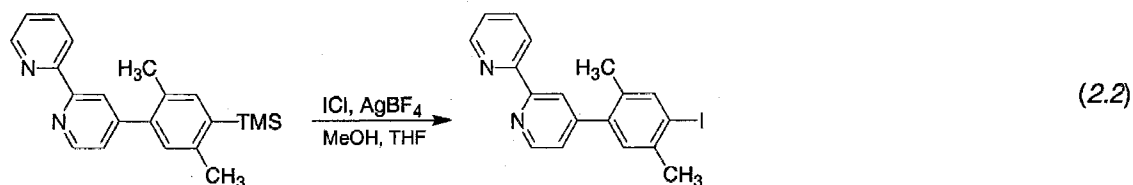
part 1 of 3

General Synthetic Route to $[\text{Ru}(\text{XY})_n\text{-G}]^{2+}$
Bridging Ligand

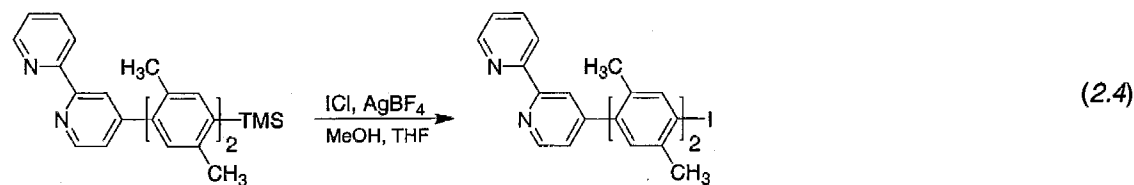
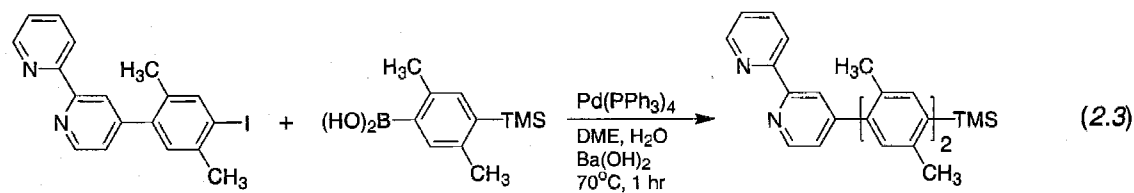
Initial cross-coupling



Deprotection and Halogenation



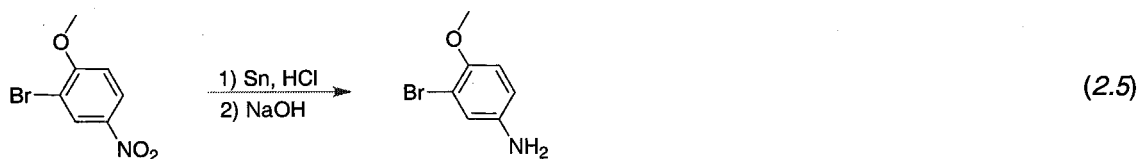
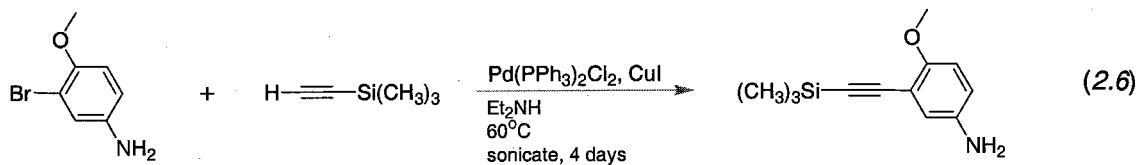
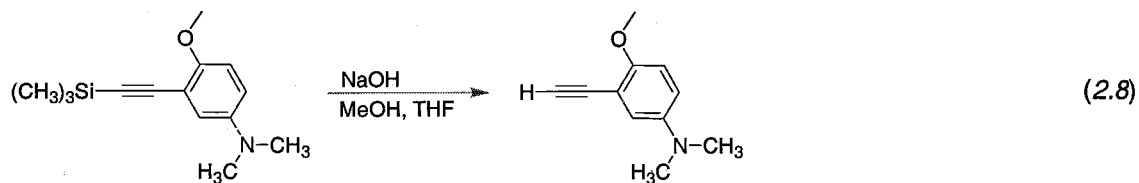
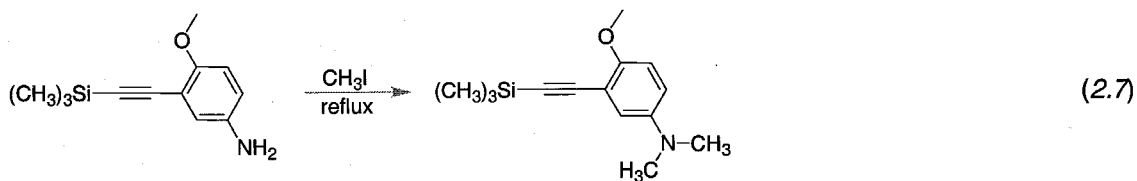
Oligomer-Extending Coupling Cycles



SCHEME 2.1

part 2 of 3

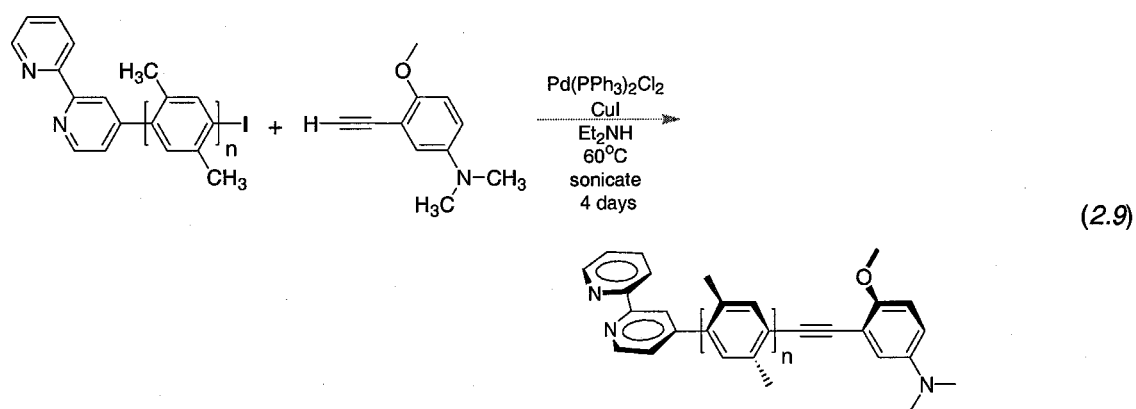
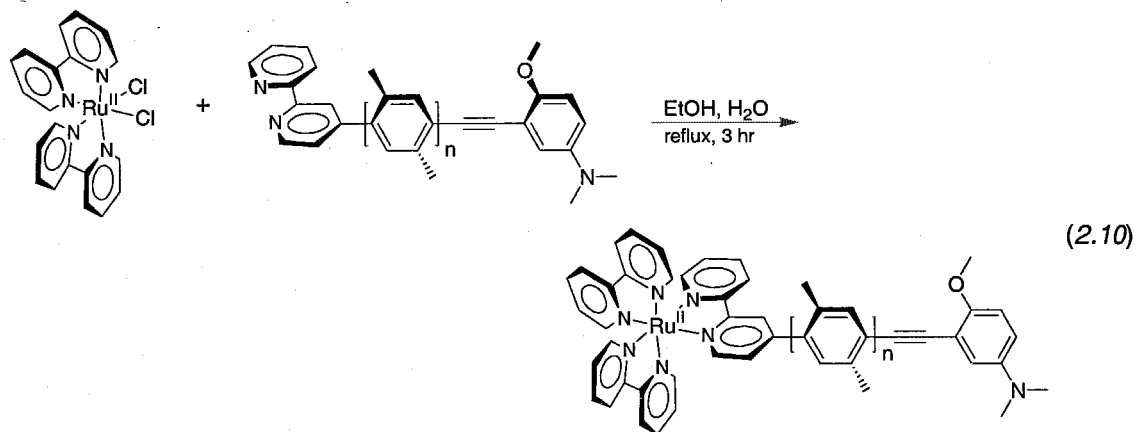
General Synthetic Route to $[\text{Ru}-(\text{XY})_n-\text{G}]^{2+}$
Donor Synthesis

Reduction*Addition of Bridge Linkage**Methylation and Deprotection*

SCHEME 2.1

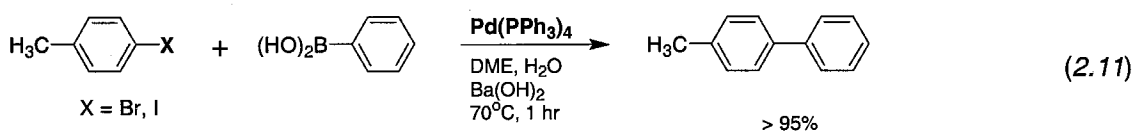
part 3 of 3

General Synthetic Route to $[\text{Ru}(\text{XY})_n\text{-G}]^{2+}$
D-B-A Assembly

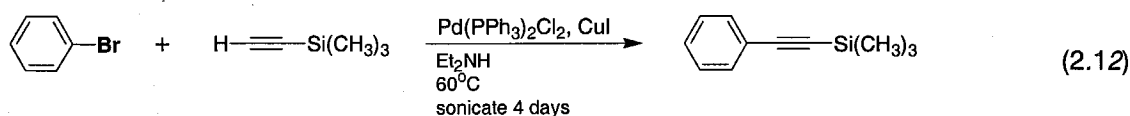
Bridge-Donor Assembly*Final Assembly*

2.6 Application of Palladium-Catalyzed Cross-Coupling Reactions

The synthesis of the bridging ligand, donor, and bridge-donor assembly relies heavily on palladium-catalyzed cross-coupling reactions.³⁰⁻³⁴ While there are several types, Suzuki^{148,149} and Sonogashira¹⁵⁰ proved the most useful. Suzuki cross-coupling reactions form carbon-carbon bonds between aryl halides and aryl boronic acids (Reaction 2.11).



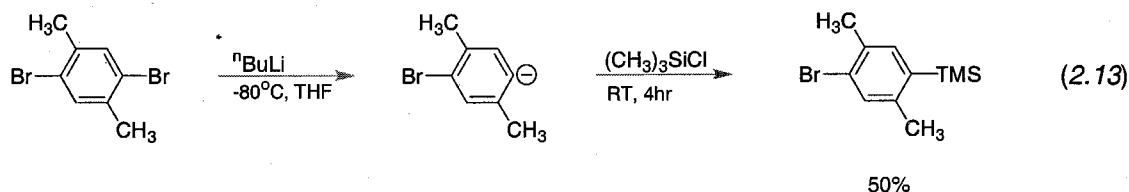
Suzuki reactions are useful because they tolerate sterically hindered substrates,¹⁵¹ such as the ortho-substituted phenyl monomers incorporated in $[\text{Ru}(\text{XY})_n\text{-G}]^{2+}$. The other type of cross-coupling reaction, Sonogashira, is a convenient method for introducing donors to the assembly (Reaction 2.12). Utilizing a Pd^{II} catalyst, this type of cross-coupling forms C–C bonds between aromatic halides and alkynes.



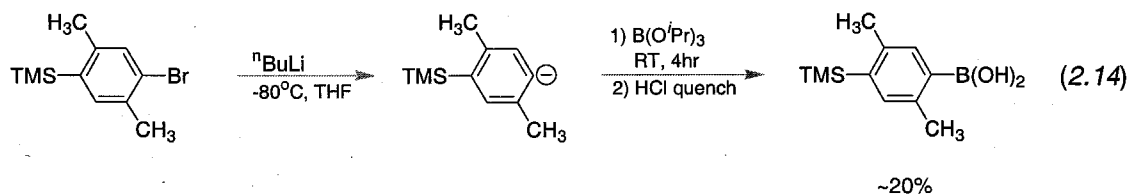
2.7 Synthesis of Xylene Oligomers

The oligomers comprising the bridge are synthesized using Suzuki cross-coupling chemistry. The required precursors are an arylhalide and a phenylboronic acid. The stepwise approach to synthesizing the oligomers requires a protection scheme to

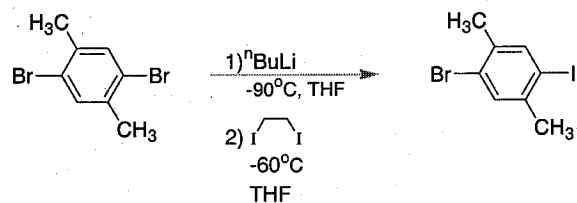
prevent unwanted coupling reactions. Dibromoxylene was protected by treatment with butyllithium followed by addition of trimethylsilyl chloride (Reaction 2.13).



Vacuum distillation resulted in a 50% isolated yield of 99% pure TMS protected bromoxylene (TMS-XY-Br). The arylboronic acid precursor (TMS-XY-B(OH)₂) was synthesized from TMS-XY-Br through dehalogenation with butyllithium, addition of triisopropylborate, followed by acid workup (Reaction 2.14). It was important to have pure TMS-XY-Br to obtain appreciable amounts of arylboronic acid. The product of Reaction 2.14 was often isolated as a trianhydride (section 2.8 Figure 2.5).



Several oligomers and oligomer derivatives were synthesized (Table 2.1) utilizing the precursors TMS-XY-Br and TMS-XY-B(OH)₂, under Suzuki cross-coupling conditions. Reacting dibromoxylene with ⁿBuLi followed by 1,2-diiodoethane afforded the precursor Br-XY-I (Reaction 2.15).¹⁵²

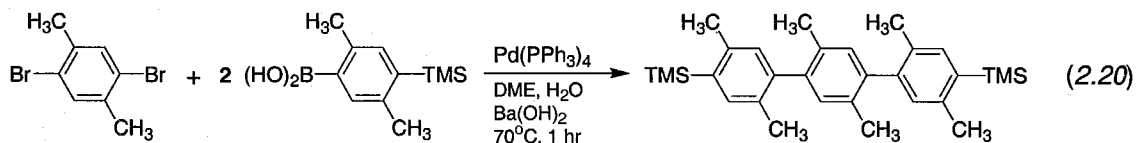
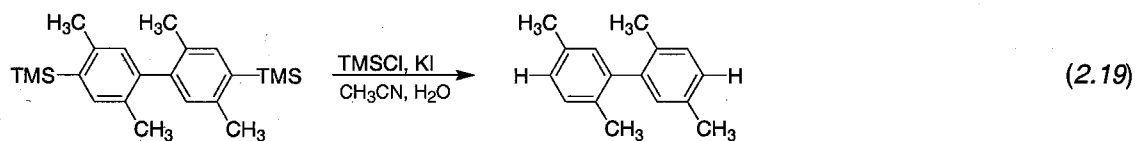
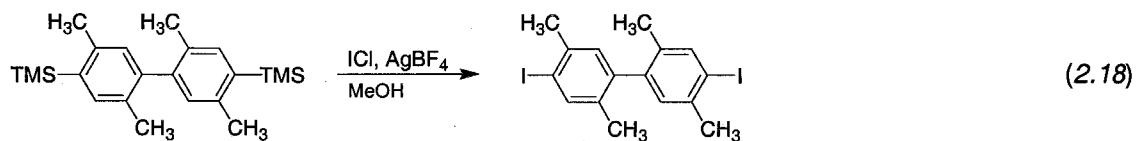
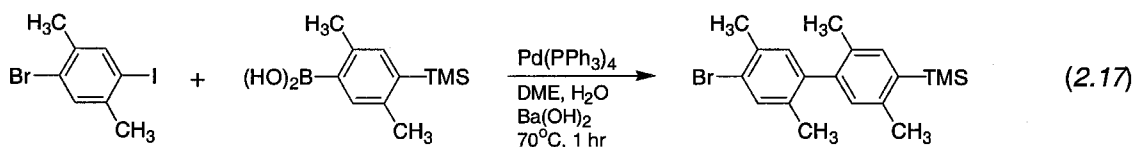
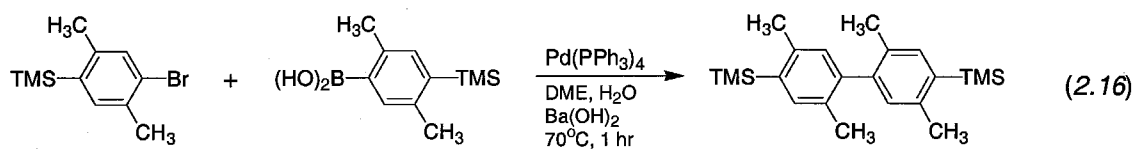


(2.15)

The deprotection step is quantitative and selective for TMS-protected aromatics.

Asymmetric oligomers, such as $\text{Br}-(\text{XY})_2\text{-TMS}$, were synthesized by taking advantage of the greater reactivity of iodo- over bromo- aromatic substrates. It was difficult to avoid producing the trimer, $\text{TMS}-(\text{XY})_3\text{-TMS}$, however, and careful control over reagent concentrations was necessary.

TABLE 2.1 – Synthesized Xylene Oligomers



2.8 Methods for Oligomer and D-B-A Characterization

The highly symmetrical nature of the xylene oligomers, lack of distinctive functional groups, and the size of the D-B-A assemblies made characterization difficult. NMR spectrometry was a less efficient method for monitoring reaction progress and identifying products. A multitude of peaks, all within the aromatic region or methyl region, proved difficult to resolve. Numerous background aromatic resonances from the catalyst and, in the case of the D-B-A assembly, protons on the ancillary bpy ligands further mitigated the usefulness of NMR techniques.

Fortunately, each chemical transformation involved additions or changes that could be detected, distinguished, and identified using mass spectrometry. In the case of precursors, xylene oligomers, and smaller ($n < 3$) bpy-xylene ligands, a new coupled gas chromatography mass spectrometry (referred to as Flash GC-MS) technique was developed. Typical gas chromatography columns are long (25 m or greater) and contain a relatively thick layer of a silica stationary phase. The new technique uses standard GC-MS equipment but with a shorter column (3 to 10 m) and a thinner stationary phase. The effective range of this new technique was only limited by the range of the mass spectrometer (1000 m/z).

Much larger compounds, with relatively high boiling points ($> 200\text{ }^{\circ}\text{C}$) could be separated and their mass spectra analyzed in one third of the time. Using traditional GC-MS conditions, it would not be possible to analyze most of the xylene oligomer and all of the bipyridine ligands in this thesis. The phenylboronic anhydride trimer (Figure 2.5), which has a molecular weight of 612.45 g, was not detected by NMR but readily observed in the mass spectrum. A separate, softer ionization technique, atmospheric

pressure chemical ionization (APCI), proved useful for compounds with m/z 's greater than 1000.

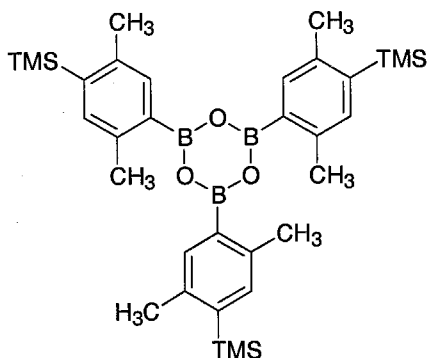
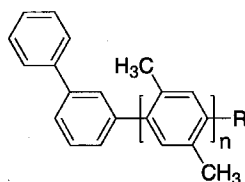


Figure 2.5 Phenylboronic Anhydride Trimer

Mass spectrometry does not just provide mass to charge (m/z) ratios; careful analysis of the isotope patterns can reveal or confirm the identity of a compound. This was particularly useful in characterizing the $[\text{Ru}-(\text{XY})_n\text{-G}]^{2+}$ ions. The method of choice for charged species is electrospray ionization mass spectrometry (ESI). The high resolution of the ESI instrument gives detailed isotope patterns. By calculating isotope patterns and m/z 's, it was possible to distinguish between reactants, product, and decomposition products. Furthermore, the m/z ratio was used to determine the charge of the complexes, ruling out the formation of dimers, or high-order D-B-A complexes. While care must be used when relying on mass spectrometry data to identify compounds, it proved to be the most useful and efficient technique for characterizing $[\text{Ru}-(\text{XY})_n\text{-G}]^{2+}$.

2.9 Synthesis of Bipyridine-Xylene Oligomer Ligands

The starting reagent, 4-iodo-2,2'-bipyridine (bpy-I), was synthesized in four steps, on a large scale (20 g) from literature procedures.¹⁵³ The synthesis of the bipyridine-xylene oligomer series, bpy-(XY)_n-R (where n = 1 to 5; Figure 2.6), is based on a repeating cycle of two reactions (Scheme 2.1, part 1).

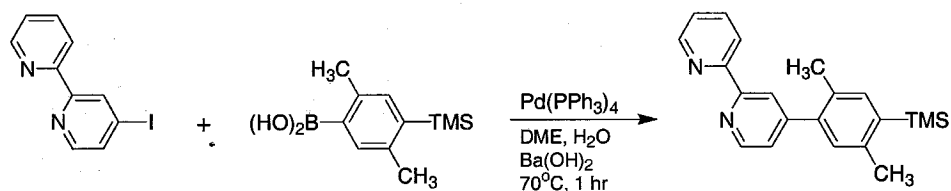


n = 1 to 5
R: I, TMS

Figure 2.6 bpy-(XY)_n-R

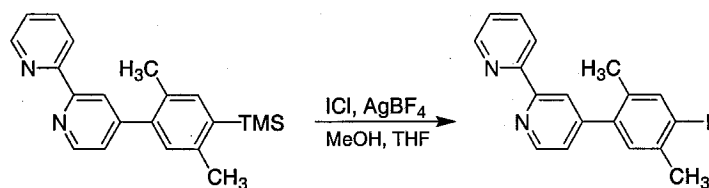
Purification was achieved using silica gel chromatography with a relatively polar mobile phase. It was necessary to ensure the cross-coupling and deprotection steps proceeded quantitatively. While it was possible to remove reaction impurities, it proved extremely difficult to separate product from starting compounds. Mass spectrometry was used to monitor the course of the reactions to ensure that all of the reactants had been consumed.

The initial coupling reaction (Scheme 2.1, Reaction 2.1),



was under Suzuki conditions using tetrakis Pd^0 as the catalyst. Ba(OH)_2 was required as the base to facilitate the cross-coupling reaction with a sterically hindered boronic acid. The use of Na_2CO_3 as the base resulted in no detectable cross-coupling product.

One pot deprotection and iodination prepared the substrate for the next round of coupling reactions (Scheme 2.1, Reaction 2.2).



The product of reaction 2.2, bpy-XY-I, could then undergo the same cross-coupling as shown in reaction 2.1. Theoretically, the cycle to extend the length of the oligomer could continue indefinitely, but in practice synthesizing ligands greater than $n = 3$ was challenging. The reactions consumed all of the reactant but the final isolated yields were anywhere from 50 to 80% per reaction. Less than unity yields had a tremendously detrimental effect on the yield of longer oligomers. The synthesis of bpy-(XY)₅-I took ten steps (not including precursors); assuming an 80% yield per step, the final isolated yield of pen tamer ligand would be 10%.

2.10 Synthesis of Ethynyl-G

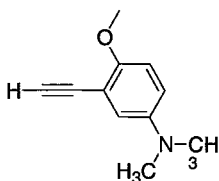
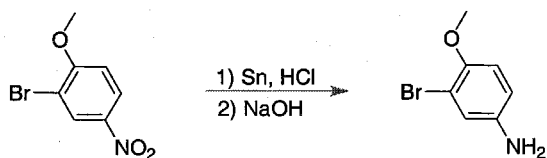
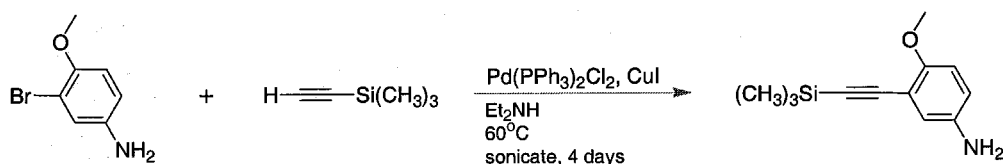


Figure 2.7 Ethynyl-Gary

The harsh conditions required to produce boronic acids and low yields severely limited the use of Suzuki conditions to attach the donor to $\text{bpy}-(\text{XY})_n\text{-I}$. Therefore, a different strategy, based on Sonogashira cross-coupling chemistry was used. The donor, 4-methoxy-N,N-dimethylaniline, would be functionalized with an alkyne. This was accomplished by making the aromatic halide precursor through standard reduction of a nitroanisole precursor.¹⁵⁴ Commercially available 3-bromo-4-methoxy-nitrobenzene was reduced to a mixture of free-base, 3-bromo-4-methoxyaniline, and the HCl salt.



The mixture of free-base and salt was not separated for the subsequent step. The alkyne was added via a Sonogashira cross-coupling reaction with TMS protected acetylene (Scheme 2.1, Reaction 2.6).

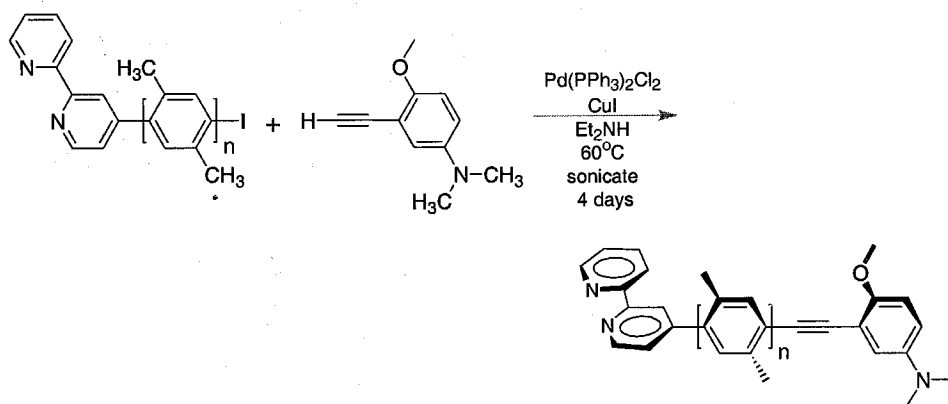


Cross-coupling the highly deactivated amine substrate proved difficult. After four days of sonication at 60°C , all of the substrate was consumed and a considerable amount of palladium black was produced in the process (judging by a fine black precipitate).

Methylation of the amine would typically yield a mixture of the N,N-dimethyl derivative and the quaternary, tetramethyl amine iodide salt. The mixture was carried on to the deprotection of the TMS group using base. The last step exchanged the TMS group for hydrogen and free-based the amine salt to give the final donor, ethynyl-G (Figure 2.7).

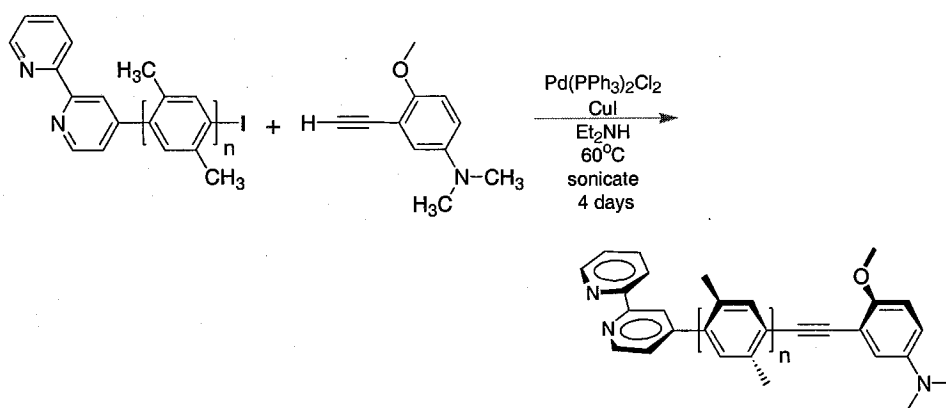
2.11 $[\text{Ru}-(\text{XY})_n-\text{G}]^{2+}$ Assembly

The assembly of $[\text{Ru}-(\text{XY})_n-\text{G}]^{2+}$ occurred in two steps. The first involved a Sonogashira cross-coupling reaction to attach the donor, ethynyl-G, to the bpy-xylene oligomer bridge (Scheme 2.1, Reaction 2.9).



This step followed the same conditions used in reaction 2.6 to make ethynyl-G.

Reaction times for reaction 2.9 extended from a few hours to several days as the bpy-xylene oligomer got longer. Purification followed the same protocol as used with the bpy-xylene oligomers. Once the donor was attached to the bridge, to make bpy-(XY)_n-G, the second step was performed (Scheme 2.1, Reaction 2.10).



Metalation of $\text{bpy}-(\text{XY})_n\text{-G}$ to form $[\text{Ru}-(\text{XY})_n\text{-G}]^{2+}$ was done under standard ligand substitution conditions.^{8,9,12,97,155} The product of reaction 2.10, $[\text{Ru}-(\text{XY})_n\text{-G}]\text{Cl}_2$, was metathesized to the hexafluorophosphate salt for solubility in organic solvents. For the longer complexes ($n = 4$ and 5), the intermediates, $\text{bpy}-(\text{XY})_n\text{-TMS}$, $\text{bpy}-(\text{XY})_n\text{-I}$, and $\text{bpy}-(\text{XY})_n\text{-G}$ were difficult to isolate as pure compounds. A different approach was taken, using the metalation reaction as a purification method. Each reaction prior to metalation was carried out until no starting compound remained, then purified to remove any bipyridine derivatives other than $\text{bpy}-(\text{XY})_n\text{-G}$. The semi-crude ligand was metalated and the complex purified.

Purification of ruthenium polypyridyl complexes is challenging. Traditional organic synthetic methods, such as silica gel chromatography, are not typically used because of difficulties dealing with charged species. Combinations of recrystallization, alumina, and ion-exchange chromatography are typically used to purify metal complexes. $[\text{Ru}-(\text{XY})_n\text{-G}]^{2+}$ bound tightly to cationic ion-exchange resin and an anionic stationary phase gave unsatisfactory results. Recrystallization only yields satisfactory results when good quality microcrystalline or crystalline precipitates are formed. Even then, co-crystallization of impurities is possible.

Based on work by Sauvage,¹⁵⁵ it was possible to use regular, normal-phase silica gel. A special mobile phase gradient was used, starting with 100% acetonitrile and ending with a solution of 20% H_2O in acetonitrile. Depending on the experimental conditions and $[\text{Ru}-(\text{XY})_n\text{-G}]^{2+}$ complex ($n = 3$ and 4), this solvent system was sufficient to elute the product without tailing or streaking. If a strong gradient was required, 1:20:80 to 5:20:80 saturated aqueous potassium nitrate:water:acetonitrile was used. Judging by the numerous bands that eluted from the column, utilizing typical

recrystallization protocols on $[\text{Ru}(\text{XY})_n\text{-G}]^{2+}$ would not provide satisfactory results. For example, a sample of $[\text{Ru}(\text{XY})_5\text{-G}]\text{Cl}_2$ that was metathesized to the PF_6 salt, washed with copious amounts of water, followed by recrystallization, was subjected to the silica gel purification protocol. No less than six bands were collected from the column, of which three contained ruthenium complexes. The product was the only fraction to emit orange-red light under long-wavelength UV irradiation.

Purified $[\text{Ru}(\text{XY})_n\text{-G}]^{2+}$ was characterized with spectroscopy, electrochemistry, photophysical measurements, NMR spectrometry, and mass spectrometry. All of these methods gave results consistent with the structure and expected properties of $[\text{Ru}(\text{XY})_n\text{-G}]^{2+}$. The mass spectra were particularly useful, as the distinctive isotope patterns of ruthenium complexes, combined with a large number of carbons and nitrogens from the ligands, made identification of the purified D-B-A complex unambiguous.

MATERIALS and METHODS

2.12 Reagents

All reagents were used as received unless otherwise noted. Commercially available metal complexes and palladium catalyst were purchased from Strem. Most of the commercially available organic compounds were purchased from Aldrich with a few from Acros, Baker, TCI, and VWR. Solvents for synthesis, analysis, and purification were from EM Science. NMR solvents were purchased from Cambridge Isotope Lab and contained no tetramethylsilane (TMS). When noted, dimethyl ether, ethyl ether, and THF were purified by distilling from sodium benzophenone ketal. EM Science's Dri-Solve low-moisture DME and THF were also used. 3-bromo-4-methoxyanisole was purchased from Lancaster. Argon was purified with an oxygen scrubber (Oxyclear) and dried over molecular sieves. 4-iodobipyridine was synthesized from a literature procedure.¹⁵³

2.13 Instrumentation

Mass spectrometry was performed on either a gas chromatography-mass spectrometer (HP), an atmospheric pressure chemical ionization (APCI) instrument (Agilent 1100 series), or an electrospray ionization spectrometer (Finnigan LCQ). NMR spectra were collected on a 300 or 600 MHz Bruker magnet.

2.14 Flash GC-MS

A new GC-MS method was developed to facilitate the analysis and characterization of high-boiling point, large molecular weight molecules. A standard HP-1 column was shortened to only 8 m. The shorter length, in combination with a relatively thin stationary phase, allowed large, typically "sticky" molecules, such as xylene oligomers or bpy-xylene ligands, to be separated. A typical run took less than ten minutes, one-third the time using traditional methods. It was found that a three m long column (Quadrex) also achieved impressive results. Clean baselines, well-resolved peaks, and good mass spectra were typical results from this method. The biggest limiting factor was the mass spectrometer, which had a maximum m/z of 1000.

2.15 Sample Preparation

Mass spectrometry samples were typically made in dichloromethane, using a 5 μL sample volume. ESI samples were typically made in acetonitrile with concentrations of less than 1 μM . Most NMR samples of organic compounds were done in CDCl_2 , while metal complexes, including $[\text{Ru}(\text{XY})_n\text{-G}]^{2+}$, were in CD_3CN . All of the samples were made fresh and, when appropriate, bubble degassed with dry argon.

EXPERIMENTAL

2.16 General Procedures

The following are general synthetic, purification, and analytic procedures referred to in the experimental section. The addition of large volumes of air- and/or water-sensitive reagents (such as $n\text{BuLi}$ or TMSCl) was facilitated by using the low-temperature addition funnel in appendix A.

Suzuki Cross-Coupling General Method A – A two neck-round bottom flask, fitted with a reflux condenser (with an oil bubbler connected on the other end) and a rubber septum, was charged with arylhalide substrate, DME (0.17 M solution of substrate), arylboronic acid (1.1 equiv.), $\text{Ba}(\text{OH})_2 \cdot 8\text{H}_2\text{O}$ (1.5 equiv.) and a magnetic stir bar. The solution and reaction vessel were degassed for 5 minutes by bubbling dry, oxygen-free argon gas through the solution with a needle. $\text{Pd}(\text{PPh}_3)_4$ (5% mol. equiv.) was added to the reaction mixture and the solution was degassed for another 5 minutes. Degassed H_2O (56 equiv.) was then added with a syringe. The mixture was heated to 70°C and

the reaction progress monitored by TLC, GC-MS, or APCI. After all of the substrate was consumed (1 to 24 hrs), the reaction mixture was filtered through Celite. The Celite was washed with CH_2Cl_2 and the combined filtrates were extracted with CH_2Cl_2 . The organic layers were combined and dried over anhydrous MgSO_4 . The solvent was removed via rotary evaporation. The crude solid was loaded onto a normal-phase silica gel column and the fractions were checked by TLC, GC-MS, or APCI. Further purification, if needed, was done by slow-evaporation recrystallization.

Suzuki Cross-Coupling General Method B – A two neck-round bottom flask, fitted with a reflux condenser (with a oil bubbler connected on the other end) and a rubber septum, was charged with arylhalide substrate, DME (0.17 M solution of substrate), arylboronic acid (2.2 equiv.), $\text{Ba}(\text{OH})_2 \cdot 8\text{H}_2\text{O}$ (1.5 equiv.) and a magnetic stir bar. The solution and reaction vessel were degassed for 5 minutes by bubbling dry, oxygen free argon gas through a needle. $\text{Pd}(\text{PPh}_3)_4$ (10% mol. equiv.) was added to the reaction mixture and the solution was degassed for another 5 minutes. Degassed H_2O (112 equiv.) was then added with a syringe. The mixture was heated to 70°C and the reaction progress monitored by TLC, GC-MS, or APCI. After all of the substrate was consumed (1 hour to 24 hours), the reaction mixture was filtered through Celite. The Celite was washed with CH_2Cl_2 and the combined filtrates were extracted with CH_2Cl_2 . The organic layers were combined and dried over anhydrous MgSO_4 . The solvent was removed via rotary evaporation. The crude solid was loaded onto a normal-phase silica gel column and the fractions were checked by TLC, GC-MS, or APCI. Further purification, if needed, was done by slow-evaporation recrystallization.

Sonogashira Cross-Coupling General Method – A thick-walled Schlenk tube was charged with diethylaniline and an aromatic halide substrate. The tube was bubble degassed with dry, oxygen free argon. Under a blanket of argon, $\text{Pd}(\text{PPh}_3)_2\text{Cl}_2$ (5 mol % typical) and CuI (10 mol % typical) were added to the tube. The ethynyl derivative was added, the tube sealed, placed in a sonicator, and heated to 60°C . The reaction was monitored by GC-MS or APCI and the reaction was stopped when all of the substrate was consumed. The reaction mixture was concentrated to a residue via rotary evaporation. The crude product was loaded onto a silica gel column with CH_2Cl_2 for purification.

Deprotection/Iodination General Method – A round bottom flask, containing a 3:2 mixture of $\text{MeOH}:\text{THF}$, was charged with TMS protected substrate. The solution was cooled to 0°C in an ice bath and solid AgBF_4 (1.2 equiv.) was added under a blanket of argon. ICl (1.2 equiv.) was then added dropwise with a syringe and the reaction mixture stirred for 2 hours. The reaction was warmed to room temperature and filtered over Celite. The Celite was washed with CH_2Cl_2 , and the combined filtrates were then washed with aqueous $\text{Na}_2\text{S}_2\text{O}_3$ (10% weight/volume) and dried over MgSO_4 . The solvent was removed with rotary evaporation and the crude solid purified on a silica gel column and/or with slow-evaporation recrystallization.

Ruthenium Metalation General Method – The $\text{bpy}-(\text{XY})_n\text{-G}$ ligand was added to a round bottom flask fitted with a reflux condenser and stir bar. The ligand was dissolved in a solvent mixture of 1:5 $\text{CHCl}_3:\text{EtOH}$ and degassed with argon. $(\text{bpy})_2\text{RuCl}_2$ (1.2 equiv) was added and the solution heated to reflux. After the ligand was con-

sumed, the solvent was removed via rotary evaporation to yield a dark residue. The crude material was loaded onto a normal-phase silica gel column with a mixture of acetonitrile and CH_2Cl_2 . The product was eluted using the following gradient: The column was first washed with acetonitrile to remove any organic compounds. This was followed by a gradient of 5 to 20% water in acetonitrile, in 1 column-volume steps. Several column-volumes of 20% water in acetonitrile were used until no more bands were eluted. The final product was eluted with a gradient starting at 0:20:80 up to 5:20:80 saturated aqueous $\text{KNO}_3\text{:H}_2\text{O:CH}_3\text{CN}$. The product band could be detected on the column by observing orange-red emission under long-wavelength UV excitation. The product fractions were collected off the column as a mixture of the dichloride and dinitrate salts. The solvent was removed via rotary evaporation to produce a red residue. The residue was dissolved in a minimal amount of water and treated with a saturated solution of NH_4PF_6 to produce the ruthenium hexafluorophosphate salt as a red solid. The precipitate was collected on a sintered glass frit, washed with copious amounts of water, and dried in a vacuum oven at 30°C overnight. The product was then stored in the dark, under argon in a Schlenk tube.

2.17 Synthetic Procedures

TMS-XY-Br (1-bromo-2,5-dimethyl-4-trimethylsilylbenzene) – A one liter three-neck flask was charged with 500 mL of THF (freshly distilled) and 20 g (75.8 mmol) of 1,4-dibromo-2,5-dimethylbenzene. A magnetic stir bar was added and the flask was sealed with a thermometer, a glass tube for inert gas, and a septum in each neck. A needle attached to a bubbler was added through the septum. The solution was cooled to -78°C (dry ice/acetone) and bubble degassed for 15 minutes while stirring. $n\text{BuLi}$ (1.1 equiv; 52.1 mL of a 1.6 M solution in hexanes) was added dropwise via a syringe, or the addition funnel in appendix A, over 40 minutes producing a clear lime-green solution. The reaction was stirred for 4 hours at -78°C , during which time a white precipitate formed. TMSCl (1.1 equiv) was then added dropwise with a syringe over 10 minutes. The solution was stirred and slowly warmed to room temperature over 12 hours. The reaction was quenched with 200 mL of H_2O . CH_2Cl_2 was then added to aid in separating the layers. The aqueous phase was extracted with CH_2Cl_2 (3 x 100 mL) and the combined organic extracts were dried over anhydrous MgSO_4 . Rotary evaporation yielded a thick yellow oil which was purified by reduced-pressure distillation (400 mTorr) at 66°C . (17g, 88%) ^1H NMR (300 MHz, CD_2Cl_2) δ 7.32 (s, 1H), 7.28 (s, 1H), 2.38 (s, 3H), 2.34 (s, 3H), 0.291 (s, 9H); ^{13}C NMR (75 MHz, CD_2Cl_2) δ 143.3, 138.3, 137.2, 134.4, 133.6, 126.4, 22.6, 22.4, 0.34; MS (CI) $[\text{M}]^+$ 256, 258 (calc. 256, 258); $[\text{M} - \text{CH}_3]^+$ 241, 243 (calc. 241, 243) m/z.

TMS-XY-B(OH)₂ (2,5-dimethyl-4-trimethylsilyl-phenylboronic acid) – A 500 mL 3-neck flask containing 20 g (77.7 mmol) of TMS-XY-Br, 250 mL of THF (freshly distilled), and a stir bar was sealed with a septum, argon gas tube, an oil bubbler (via a syringe needle in the septum), and a thermometer. The reaction flask was cooled to -78°C (dry ice/acetone) and bubble degassed for 15 minutes. 1.1 equivalents of $^n\text{BuLi}$ (53.4 mL of a 1.6 M solution in hexanes) was placed in a Schlenk flask and cooled to -78°C . The $^n\text{BuLi}$ was then added dropwise over 20 minutes with a cannula. The solution was stirred for 45 minutes before adding 1.75 equivalents of $\text{B}(\text{O}-i\text{Pr})_3$ dropwise over 5 minutes. The white turbid solution was then warmed to room temperature over an hour. The reaction was quenched with 110 mL of 3 M HCl. CH_2Cl_2 (200 mL) was added and the organic layer was separated. The aqueous phase was extracted with CH_2Cl_2 (3 x 100 mL) and the combined organic extracts were washed with H_2O (2 x 100 mL). The organic phase was dried over anhydrous MgSO_4 and the solvent was removed with rotary evaporation. The crude solid was purified by recrystallizing from a 1:1 mixture of ethyl acetate:hexanes through slow evaporation. A white solid was collected on a Buchner funnel and washed with cold EtOAc. (7.4g, 43%) ^1H NMR (300 MHz, CD_2Cl_2) δ 7.9 (s, 1H), 7.4 (s, 1H), 2.8 (s, 3H), 2.5 (s, 3H), 0.35 (s, 9H); MS (CI) $[\text{M} - 2\text{H}]^+$ 219 (calc. 222.1) m/z.

Br-XY-I (1-bromo-4-iodo-2,5-dimethylbenzene) – 20 g of 1,4-dibromo-2,5-dimethylbenzene was added to 300 mL of THF (distilled) and degassed with argon. 47 mL of $^n\text{BuLi}$ (1 equiv., 1.6 M solution in hexanes) was added over 20 minutes at -90°C (methanol, liquid nitrogen bath). The reaction was stirred for 10 minutes and then added, via cannula over 45 minutes, to a solution of 1,2-diiodoethane (1.064

equiv.), in 125 mL of THF cooled to -60°C (EtOH, dry ice bath). The solution was stirred for 30 minutes and then warmed to room temperature. 200 mL of CH_2Cl_2 were added and the reaction mixture washed with H_2O (3 x 150 mL). The aqueous extracts were further extracted with CH_2Cl_2 (3 x 50 mL) and the combined organic extracts were dried over anhydrous MgSO_4 . The solvent was removed with rotary evaporation and the crude solid was purified with silica gel chromatography (10:1 hexanes:ethyl acetate) followed by slow evaporation from methanol in 50% isolated yield. (5.2g, 21%) ^1H NMR (300 MHz, CD_2Cl_2) δ 7.7 (s, 1H), 7.4 (s, 1H), 2.4 (s, 3H), 2.3 (s, 3H); MS (CI) $[\text{M}]^+$ m/z.

TMS-(XY)₂-TMS (2,2',5,5'-tetramethyl-4,4'-di(trimethylsilyl)-1,1'-biphenyl) – Using the Suzuki cross-coupling general method A, TMS-XY-Br (4.1 mmol) and TMS-XY-B(OH)₂, the reaction was heated for 4 hours. The crude product was purified with 10:1 hexanes:ethyl acetate to afford a white solid. (765 mg, 53%) ^1H NMR (300 MHz, CD_2Cl_2) δ 7.3 (s, 2H), 6.9 (s, 2H), 2.4 (s, 6H), 2.0 (s, 6H), 0.36 (s, 9H); ^{13}C NMR (75 MHz, CD_2Cl_2) δ 142.7, 140.8, 137.1, 136.3, 132, 130, 22.6, 19.4; MS (CI) $[\text{M}]^+$ 354 (calc. 354.2), $[\text{M} - \text{CH}_3]^+$ 339 (calc. 339.2) m/z.

TMS-(XY)₂-Br (2,2',5,5'-tetramethyl-4-trimethylsilyl,4'-bromo-1,1'-biphenyl) – Using the Suzuki cross-coupling general method A, Br-XY-I (2mmol) and TMS-XY-B(OH)₂, the reaction was heated overnight. The crude product was purified on silica gel with hexanes to produce a white powder. MS (CI) $[\text{M}]^+$ 360, 362 (calc. 360.1, 362.1), 345, 347 (calc. 345.1, 347.1) m/z.

I-(XY)₂-I (4,4'-diiodo,2,2',5,5'-tetramethyl-1,1'-biphenyl) – Following the general deprotection/iodination method, 250 mg (1.41 mmol) of TMS-(XY)₂-TMS was reacted for 90 minutes. The crude product was purified with silica gel column chromatography (10:1 hexanes:ethyl acetate) followed by recrystallization. ¹H NMR (300 MHz, CD₂Cl₂) δ 7.7 (s, 2H), 6.9 (s, 2H), 2.4 (s, 6H), 2.0 (s, 6H); MS (CI) [M]⁺ 462 (calc. 461.9) m/z.

H-(XY)₂-H (2,2',5,5'-tetramethyl-1,1'-biphenyl) – 50 mg (0.14 mmol) of TMS-(XY)₂-TMS was added to a round bottom flask containing 3 mL of CH₂Cl₂ and 2 mL of CH₃CN. 47.5 mg (2 equiv.) of KI was added under a blanket of argon. 40 μL (2 equiv.) of TMSCl was added dropwise with a syringe and the reaction stirred at room temperature for 2 hours. The reaction mixture was added to an aqueous solution of NaHCO₃. The organic layers were extracted with Et₂O and dried over MgSO₄. The solvent was removed with rotary evaporation and the crude product was purified with a silica gel column using 20:1 hexanes:ethyl acetate to yield a white solid. ¹H NMR (300 MHz, CD₂Cl₂) δ 7.13 (d, 2H), 7.04 (d, 2H), 6.89 (s, 2H) 2.32 (s, 6H), 1.99 (s, 6H); ¹³C NMR (75 MHz, CD₂Cl₂) δ 142, 135.3, 133, 130.5, 130, 128, 21, 19; MS (CI) [M]⁺ 210 (calc. 210.1), 195 (calc. 195.1) m/z.

TMS-(XY)₃-TMS (2,2',2'',5,5',5''-hexamethyl-4,4''-di(trimethylsilyl)-1,1':4',1''-terphenyl) The general Suzuki cross-coupling method B was utilized with 1,4-dibromo,2,5-dimethylbenzene (0.227 mmol) and TMS-XY-B(OH)₂. The reaction was stirred for 12 hours and the crude product was purified on a silica gel column with 10:1 hexanes:ethyl acetate. MS (CI) [M]⁺ 458 (calc. 458.3), 443 (calc. 443.3) m/z.

3-bromo-4-methoxyaniline – Concentrated HCl (4.8 equiv. of a 12 M solution) was dropwise added to a round bottom flask containing 3-bromo-4-methoxynitrobenzene (21.5 mmol) and Sn metal (1.5 equiv.). The flask was fitted with a condenser and the solution heated to reflux for 3 hours. The reaction mixture was cooled to room temperature and then neutralized to a pH of 7 with aqueous NaOH. The mixture was then extracted with CH₂Cl₂ (3 x 100 mL) and the combined organics dried over anhydrous MgSO₄. The solvent was removed with rotary evaporation and the crude residue was purified on a silica gel column with 1:1 hexanes:ethyl acetate to yield a yellow solid consisting of a mixture of the freebase (89%) and the HCl salt (11%). (4.5 g, 60%) ¹H NMR (300 MHz, CD₂Cl₂) δ 6.9 (d, 1H), 6.7 (d, 1H), 6.6 (dd, 1H), 3.8 (s, 3H), 3.5 (s, 2H); MS (CI) [M]⁺ 201, 203 (calc. 201.0, 203.0), [M - CH₃]⁺ 186, 188 (calc. 186, 188) m/z.

4-methoxy-3-trimethylsilylethynyl-aniline – The general Sonogashira cross-coupling method was used with 3-bromo-4-methoxyaniline (4.95 mmol), trimethylsilylacetylene (10 equiv.), Pd(PPh₃)₂Cl₂ (5 mol %) and CuI (10 mol %) to produce crude product in 4 days of sonication. After removing the solvent, the crude residue was loaded onto a silica gel column with a minimal amount of CH₂Cl₂. The product was eluted with 3:2 hexanes:ethyl acetate to produce a light yellow-brown solid (2.2g, 74%) ¹H NMR (300 MHz, CD₂Cl₂) δ 6.74 (d, 1H), 6.7 (d, 1H), 6.64 (dd, 1H), 3.8 (s, 3H), 3.5 (s, 2H), 0.24 (s, 9H); MS (CI) [M]⁺ 219 (calc. 219.1), [M - CH₃]⁺ 204 (calc. 204.1) m/z.

TMS-ethynyl-G (4-methoxy-3-trimethylsilylethynyl-N,N-dimethylaniline) – To a round-bottom flask fitted with a reflux condenser was added 4-methoxy-3-trimethylsilylethynyl-aniline (3.7 mmol, 800 mg) and 40 mL of iodomethane (solvent). The solution was covered with a blanket of argon and heated to reflux for 2 days. The solvent was removed *in vacuo* and the crude reaction mixture was taken up in CH₂Cl₂ and filtered. The solvent was removed via rotary evaporation and loaded onto a silica gel column. The product was eluted with a mixture of 3:2 hexanes:ethyl acetate to produce a yellowish-brown solid (124 mg, 14%) ¹H NMR (300 MHz, CD₂Cl₂) δ 6.78 (m, 3H), 3.79 (s, 3H), 2.85 (s, 6H), 0.25 (s, 9H); MS (CI) [M]⁺ 247 (calc. 247.1), 232 (calc. 232.1) m/z.

Ethynyl-G (3-ethynyl-4-methoxy-N,N-dimethylaniline) – 4-methoxy-3-trimethylsilylethynyl-N,N-dimethylaniline (0.15 mmol) was dissolved in a solvent mixture of 1:1.4 THF:MeOH (3 mL:4.2 mL) and bubble degassed with argon. A solution of 5N NaOH (1.8 equiv.) was added dropwise with a syringe. The reaction mixture was stirred at room temperature for 4 hours. 5 mL of H₂O was added to the reaction mixture and the organics extracted with CH₂Cl₂ (3 x 50 mL). The solvent was removed with rotary evaporation and the crude product purified with a silica gel column using 3:2 hexanes:ethyl acetate as the eluant to yield a yellowish-brown solid. (18 mg, 69%) ¹H NMR (600 MHz, CD₃CN) δ 6.91 (d, 1H), 6.86 (d, 1H), 6.82 (dd, 1H), 3.78 (s, 3H), 2.84 (s, 6H); MS (CI) [M]⁺ 175 (calc. 175.1), 160 (calc. 160.1) m/z.

bpy-XY-TMS (4-(2,5-dimethyl-4-trimethylsilylphenyl)-2,2'-bipyridine) – General Suzuki cross-coupling method A was used with 4-iodobipyridine (3.55 mmol), TMS-XY-B(OH)₂,

and a reaction time of 3 hours. The crude reaction mixture was purified with a mobile phase of 50:3 CH₂Cl₂: MeOH on a normal-phase silica gel column. (1.5 g, 64%) MS (CI) [M - H]⁺ 331 (calc. 331), [M - CH₃]⁺ 317 (calc. 317) m/z.

bpy-XY-I (4-(2,5-dimethyl-4-iodophenyl)-2,2'-bipyridine) – Using the general deprotection/iodination method with bpy-XY-TMS (3 mmol) substrate, the reaction was worked-up after 24 hours of stirring at 0°C. The crude product was purified with a silica gel column using 50:3 CH₂Cl₂: MeOH. (0.80 g, 46%) ¹H NMR (300 MHz, CD₂Cl₂) δ 8.7 (d, 1H), 8.65 (dd, 1H), 8.49 (d, 1H), 8.4 (d, 1H), 7.85 (triplet of doublets, 1H), 7.79 (s, 1H), 7.35 (triplet of doublets, 1H), 7.27 (dd, 1H), 7.18 (s, 1H) 2.44 (s, 3H), 2.24 (s, 3H); MS (CI) [M - H]⁺ 385 (calc. 385) m/z.

bpy-(XY)₂-TMS (4-(4'-trimethylsilyl-2,2',5,5'-tetramethyl-1,1'-biphenyl-4-yl)-2,2'-bipyridine) – General Suzuki cross-coupling method A was used with bpy-XY-I (5.18 mmol), TMS-XY-B(OH)₂, and a reaction time of 3 hours. The crude reaction mixture was purified with a mobile phase of 50:3 CH₂Cl₂: MeOH on a normal-phase silica gel column. (3.52g, 63%) ¹H NMR (300 MHz, CD₂Cl₂) δ 8.7 (dd, 1H), 8.65 (doublet of triplets, 1H), 8.5 (doublet of triplets, 2H), 7.85 (triplet of doublets, 1H), 7.35 (m, 3H), 7.2 (s, 1H), 7.05 (s, 1H), 6.95 (s, 1H), 2.44 (s, 3H), 2.31 (s, 3H), 2.07 (s, 6H); MS (CI) [M]⁺ 436 (calc. 436.2), [M - CH₃]⁺ 421 (calc. 421.2) m/z.

bpy-(XY)₂-I (4-(4'-iodo-2,2',5,5'-tetramethyl-1,1'-biphenyl-4-yl)-2,2'-bipyridine) – Using the general deprotection/iodination method with bpy-(XY)₂-TMS (2.3 mmol) substrate, the reaction was worked-up after 24 hours of stirring at 0°C. The crude

product was purified with a silica gel column using 50:3 CH₂Cl₂: MeOH. MS (CI) [M]⁺ 489 (calc. 490.1) m/z.

bpy-(XY)₂-G (4-(4'-(3-ethynyl-4-methoxy-N,N-dimethylaniline)-2,2',5,5'-tetramethyl-1,1'-biphenyl-4-yl)-2,2'-bipyridine) – The general Sonogashira cross-coupling method was used with bpy-(XY)₂-I (0.1 mmol), 3-ethynyl-4-methoxy-N,N-dimethylaniline (1.1 equiv.), 10 mL of Et₂NH₂, Pd(PPh₃)₂Cl₂ (5 mol %), and CuI (10 mol %). The reaction was sonicated at room temperature for 24 hours. The crude reaction residue was loaded onto a silica gel column and eluted with 50:3 CH₂Cl₂:MeOH. (34 mg, 63%) MS (ESI) [M+H]⁺ 538.3 (calc. 538.3) m/z.

[Ru-(XY)₂-G](PF₆)₂ ([bpy)₂Ru^{II}(bpy-(XY)₂-G](PF₆)₂) – Using the general ruthenium metalation method, bpy-(XY)₂-G (0.07 mmol), Ru(bpy)Cl₂ (1.2 equiv), 15 mL EtOH, and 3 mL of CHCl₃ were gently refluxed overnight. The product was purified on silica gel and collected with a mixture of 2.5:20:80 saturated aqueous KNO₃:H₂O:CH₃CN as the final eluant. Concentrating and metathesizing to the hexafluorophosphate salt produced a red solid. (26 mg, 32%) ¹H NMR (600 MHz, CD₃CN) δ 6.9 – 8.7 (m, 30H), 3.87 (s, 3H), 2.96 (s, 6H), 2.51 (s, 3H), 2.35 (s, 3H), 2.09 (s, 3H), 2.05 (s, 3H); MS (ESI) [M - PF₆]⁺ 1096.3 (calc. 1096.3) m/z.

bpy-(XY)₃-TMS (4-(4''-trimethylsilyl-2,2',2'',5,5',5''-hexamethyl-1,1':4',1''-terphenyl-4-yl)-2,2'-bipyridine) – General Suzuki cross-coupling method A was used with bpy-(XY)₂-I (2.04 mmol), TMS-XY-B(OH)₂, and a reaction time of 6 hours. The crude reaction mixture was purified with a mobile phase of 50:3 CH₂Cl₂: MeOH on a normal-phase

silica gel column. (1.9 g, 57%) ^1H NMR (300 MHz, CD_2Cl_2) δ 8.7 (d, 1H), 8.48 (doublet of triplets 2H), 7.86 (triplet of doublets, 1H), 7.37 (m, 2H), 7.36 (s, 1H), 7.24 (s, 1H), 7.11 (d, 2H), 7.02 (s, 1H), 6.99 (s, 1H), 6.96 (d, 1H), 2.45 (s, 3H), 2.34 (s, 3H), 2.13 (d, 3H), 2.08 (m, 6H), 2.06 (s, 3H), 0.36 (s, 9H); MS (CI) $[\text{M}]^+$ 540 (calc. 540.3), $[\text{M} - \text{CH}_3]^+$ 525 (calc. 525.3) m/z.

bpy-(XY)₃-I (4-(4''-iodo-2,2',2'',5,5',5''-hexamethyl-1,1':4',1''-terphenyl-4-yl)-2,2'-bipyridine) – Using the general deprotection/iodination method with bpy-(XY)₃-TMS (1.85 mmol) substrate, the reaction was worked-up after 24 hours of stirring at 0°C. The crude product was purified with a silica gel column using 50:3 CH_2Cl_2 : MeOH. (2g, 95%) MS (CI) $[\text{M}]^+$ 594 (calc. 594.2) m/z.

bpy-(XY)₃-G (4-(4''-(3-ethynyl-4-methoxy-N,N-dimethylaniline)-2,2',2'',5,5',5''-hexamethyl-1,1':4',1''-terphenyl-4-yl)-2,2'-bipyridine) – The general Sonogashira cross-coupling method was used with bpy-(XY)₃-I (0.1 mmol), 3-ethynyl-4-methoxy-N,N-dimethylaniline (1 equiv.), 5 mL of Et_2NH_2 , $\text{Pd}(\text{PPh}_3)_2\text{Cl}_2$ (5 mol %), and CuI (10 mol %). The reaction was sonicated at 60°C for 24 hours. The crude reaction residue was loaded onto a silica gel column and eluted with 50:3 CH_2Cl_2 :MeOH. (13.7 mg, 21%) ^1H NMR (300 MHz, CD_3CN) δ 8.7 (dd, 2H), 8.5 (d, 1H), 7.9 (triplet of doublets, 1H), 7.1 (m, 12H), 3.86 (s, 3H), 2.89 (s, 6H), 2.53 (s, 3H), 2.34 (s, 3H), 2.09 (overlapping doublets, 12H); MS (CI) $[\text{M}]^+$ 641 (calc. 641.3), 626 (calc. 626.3) m/z.

[Ru-(XY)₃-G](PF₆)₂ ($[(\text{bpy})_2\text{Ru}^{\text{II}}(\text{bpy}-(\text{XY})_3\text{-G})(\text{PF}_6)_2]$) – Using the general ruthenium metalation method, bpy-(XY)₃-G (0.023 mmol), $\text{Ru}(\text{bpy})\text{Cl}_2$ (1.2 equiv), 10 mL EtOH, and

2 mL of CHCl_3 were gently refluxed overnight. The product was purified on silica gel and collected with a mixture of 20:80 $\text{H}_2\text{O}:\text{CH}_3\text{CN}$ as the final eluant. Concentrating and metathesizing to the hexafluorophosphate salt produced a red solid. (16.9 mg, 54%) ^1H NMR (300 MHz, CD_3CN) δ 8.6 (m, 8H), 8.1 (m, 5H), 7.8 (m, 6H), 7.5 (m, 8H), 7.1 (m, 5H), 3.9 (s, 3H), 2.9 (s, 6H), 2.5 (s, 3H), 2.4 (s, 3H), 2.1 (m, 12H); MS (ESI) $[\text{M} - 2(\text{PF}_6)]^{2+}$ 527.7 (calc. 527.7) m/z.

bpy-(XY)₄-TMS (4-(4'''-trimethylsilyl-2,2',2'',5,5',5'',5'''-octamethyl-1,1':4',1'':4'',1'''-quaterphenyl-4-yl)-2,2'-bipyridine) – General Suzuki cross-coupling method A was used with bpy-(XY)₃-I (3.36 mmol), TMS-XY-B(OH)₂, and a reaction time of 2 days. The crude reaction mixture was purified with a mobile phase of 50:3 CH_2Cl_2 : MeOH on a normal-phase silica gel column. (1.3 g, 60%) ^1H NMR (300 MHz, CD_2Cl_2) δ 8.72 (dd, 1H), 8.67 (doublet of triplets, 1H), 8.5 (m, 2H), 7.86 (triplet of doublets, 1H), 7.35 (m, 3H), 7.25 (s, 1H), 7.14 (d, 1H), 7.07 (m, 3H), 6.96 (m, 2H) 2.45 (s, 3H), 2.35 (s, 3H), 2.15 (d, 3H), 2.11 (m, 12H), 2.06 (s, 3H) 0.37 (s, 9H); MS (CI) $[\text{M}]^+$ 644 (calc. 644.4), 629 (calc. 629.3) m/z.

bpy-(XY)₄-I (4-(4'''-iodo-2,2',2'',5,5',5'',5'''-octamethyl-1,1':4',1'':4'',1'''-quaterphenyl-4-yl)-2,2'-bipyridine) – Using the general deprotection/iodination method with bpy-(XY)₄-TMS (2 mmol) substrate, the reaction was worked-up after 24 hours of stirring at 0°C. The crude product was purified with a silica gel column using 50:3 CH_2Cl_2 : MeOH. (0.89 g, 64%) ^1H NMR (300 MHz, CD_2Cl_2) δ 8.85 (d, 1H), 8.8 (doublet of triplets, 1H), 8.5 (d, 1H), 8.4 (d, 1H), 8 (triplet of doublets, 1H), 7.75 (s, 1H), 7.6 (dd, 1H), 7.5 (triplet of doublets, 1H), 7.3 (s, 1H), 7.2 (d, 1H), 7.05 (m, 4),

δ 7.8 (s, 1H), 2.45 (s, 3H), 2.40 (s, 3H), 2.1 (d, 3H), 2.15 (d, 9H), 2.1 (d, 6H) ; MS (ESI) $[M]^+$ 699.2 (calc. 699.2) m/z.

bpy-(XY)₄-G (4-(4'''-(3-ethynyl-4-methoxy-N,N-dimethylaniline)-2,2',2'',2''',5,5',5'',5'''-octamethyl-1,1':4',1'':4'',1'''-quaterphenyl-4-yl)-2,2'-bipyridine) – The general Sonogashira cross-coupling method was used with bpy-(XY)₄-I (0.04 mmol), 3-ethynyl-4-methoxy-N,N-dimethylaniline (1.1 equiv.), 10 mL of Et₂NH₂, 5 mL toluene, 5 mL CH₂Cl₂ (for substrate solubility), Pd(PPh₃)₂Cl₂ (5 mol %), and CuI (10 mol %). The reaction was sonicated at 60°C for 24 hours. The crude reaction residue was loaded onto a silica gel column and eluted with 50:3 CH₂Cl₂:MeOH. (21.2 mg, 73%) MS (ESI) $[M+H]^+$ 746.3 (calc. 746.4) m/z.

[Ru-(XY)₄-G](PF₆)₂ ([bpy]₂Ru^{II}(bpy-(XY)₄-G)(PF₆)₂) – Using the general ruthenium metalation method, bpy-(XY)₄-G (0.032 mmol), Ru(bpy)Cl₂ (1.2 equiv), 10 mL EtOH, 6 mL of CHCl₃, 2 mL MeOH, and 3 mL CH₂Cl₂ were gently refluxed overnight. The product was purified on silica gel and collected with a mixture of 10:80 H₂O:CH₃CN as the final eluant. Concentrating and metathesizing to the hexafluorophosphate salt produced a red solid. (4 mg, 10%) ¹H NMR (600 MHz, CD₃CN) δ 7.8 (m, 34H), 3.8 (s, 3H), 2.9 (s, 6H), 2.5 (s, 3H), 2.4 (s, 3H) 2.1 (m, 18H); MS (ESI) $[M - 2(PF_6)]^{2+}$ 579.7 (calc. 579.7) m/z.

bpy-(XY)₅-TMS (4-(4''''-trimethylsilyl-2,2',2'',2''',2''''-5,5',5'',5''',5''''-decamethyl-1,1':4',1'':4'',1''':4''',4''''-pentaphenyl-4-yl)-2,2'-bipyridine) – General Suzuki cross-coupling method A was used with bpy-(XY)₄-I (0.430 mmol), TMS-XY-B(OH)₂, and a reaction time of 1 day. The crude reaction mixture was purified with a mobile phase of

50:3 CH₂Cl₂: MeOH on a normal-phase silica gel column. MS (ESI) [M + H]⁺ 749.5 (calc. 749.4) m/z.

bpy-(XY)₅-I (4-(4'''-iodo-2,2',2'',2''',2''',5,5',5'',5''',5''''-decamethyl-1,1':4',1'':4'',1''':4''',4''''-pentaphenyl-4-yl)-2,2'-bipyridine) – Using the general deprotection/iodination method with bpy-(XY)₅-TMS (0.423 mmol) substrate, the reaction was worked-up after 24 hours of stirring at 0°C. The crude product was purified with a silica gel column using 50:3 CH₂Cl₂: MeOH. (100 mg, 60%) MS (CI) [M]⁺ 803.2 (calc. 803.3) m/z.

bpy-(XY)₅-G (4-(4'''-(3-ethynyl-4-methoxy-N,N-dimethylaniline)-2,2',2'',2''',2''',5,5',5'',5''',5''''-decamethyl-1,1':4',1'':4'',1''':4''',4''''-pentaphenyl-4-yl)-2,2'-bipyridine) – The general Sonogashira cross-coupling method was used with bpy-(XY)₅-I (0.03 mmol), 4-methoxy-3-ethynyl-N,N-dimethylaniline (1.1 equiv.), 10 mL of Et₂NH₂, 5 mL toluene, 5 mL CH₂Cl₂ (for substrate solubility), Pd(PPh₃)₂Cl₂ (5 mol %), and CuI (10 mol %). The reaction was sonicated at 60°C for 24 hours. The crude reaction residue was loaded onto a silica gel column and eluted with 50:3 CH₂Cl₂:MeOH. MS (CI) [M]⁺ 850.4 (calc. 850.5) m/z.

[Ru-(XY)₅-G](PF₆)₂ ([bpy]₂Ru^{II}(bpy-(XY)₅-G)(PF₆)₂) – Using the general ruthenium metalation method, bpy-(XY)₅-G (0.03 mmol), Ru(bpy)Cl₂ (1.2 equiv), 10 mL EtOH, and 6 mL of CHCl₃ were gently refluxed overnight. The product was purified on silica gel and collected with a mixture of 2.5:20:80 saturated aqueous KNO₃:H₂O:CH₃CN as the

final eluant. Concentrating and metathesizing to the hexafluorophosphate salt produced a red solid. (2.9 mg, ~10%) ^1H NMR (600 MHz, CD_2Cl_2) δ 6.8 – 8.8 (m, 36H), 2 – 4 (m, 39H); MS (CI) $[\text{M} - 2(\text{PF}_6)]^{2+}$ 631.7 (calc. 631.8) m/z.

Chapter 3

CHARACTERIZATION of $[\text{Ru}-(\text{XY})_n\text{-G}]^{2+}$ and RELATED COMPOUNDS

INTRODUCTION

3.1 Characterizations

This chapter contains spectroscopic, electrochemical, spectroelectrochemical, NMR, mass spectrometry, and photophysical characterizations of $[\text{Ru}(\text{XY})_n\text{-G}]^{2+}$ and its model compounds $[\text{Ru-XY-TMS}]^{2+}$ ($[(\text{bpy})_2\text{Ru}(\text{bpy-XY-TMS})](\text{PF}_6)_2$) and TMS-ethynyl-G (Figure 3.1). These methods yield a picture of the electronic and chemical properties of the D-B-A complexes. The trends in absorption spectra, redox potentials, and excited-state lifetimes yield information about changes in electronic coupling between donor and acceptor as the bridge is lengthened.

Measuring electron-transfer reaction kinetics requires monitoring reactant consumption and product formation. This is not possible without prior knowledge of the spectroscopic features of the reactants and products. Steady-state absorption spectra reveal key electronic transitions that can be used as spectroscopic handles for reaction progress. Changes in band shape and position of the electronic transitions, as a function of donor-bridge separation, indicate the extent of electronic coupling. Measuring

redox potentials ensures the flash quench process will proceed as planned. Electrochemical oxidation/reduction cycles test the stability of $[\text{Ru}-(\text{XY})_n-\text{G}]^{2+}$. Trends in redox potential yield information about electronic coupling.

Steady-state absorption spectroscopy and electrochemistry can be combined to carryout extremely useful spectroelectrochemical measurements. There are many possible electron transfer reactions that can occur with $[\text{Ru}-(\text{XY})_n-\text{G}]^{2+}$. The flash-quench method allows us to partially control which electron transfer process occurs. Using spectroelectrochemistry, the spectral changes during the quenching reaction, electron-transfer reaction of interest, and back reaction, can be predicted and spectroscopic handles identified.

Model complexes are important for interpreting the spectroscopic and electrochemical data from $[\text{Ru}-(\text{XY})_n-\text{G}]^{2+}$. Recording the model's steady-state absorption spectrum, redox potentials, and excited-state lifetimes form a good baseline to compare with $[\text{Ru}-(\text{XY})_n-\text{G}]^{2+}$. Besides modeling the electronic and chemical properties of the assembly, $[\text{Ru}-(\text{XY})_n-\text{G}]^{2+}$, they can also be used to mimic the electron transfer reaction. Intermediates in the synthesis of $[\text{Ru}-(\text{XY})_n-\text{G}]^{2+}$ were chosen to represent the donor and acceptor as individual components.

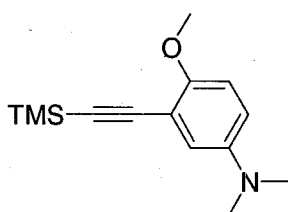
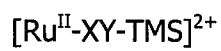
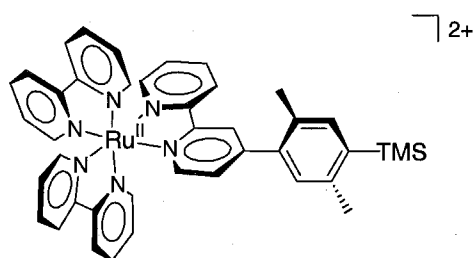
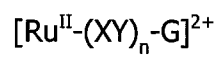
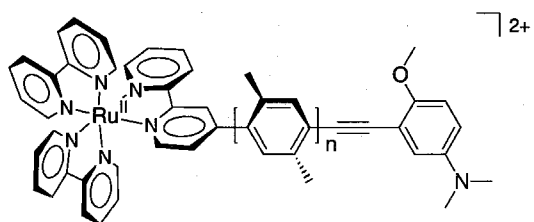


Figure 3.1 D-B-A complex $[\text{Ru}^{\text{II}}-(\text{XY})_n-\text{G}]^{2+}$ and model compounds

EXPERIMENTAL

3.2 Reagents

The solvents for sample preparation were commercially available (Burdick & Jackson) and of the highest quality and with low water content. The solvents were used as received from freshly opened bottles. Tetrabutyl ammonium hexafluorophosphate (TBAH) electrolyte was purchased from BaChem and used as received.

3.3 Instrumentation and Experimental Procedures

Steady-state absorption spectra were recorded with a diode-array spectrometer (HP 8452a). Absorption measurements were made using a 1 cm pathlength quartz cuvette at room temperature. The spectra were corrected with a spectrum of neat solvent or air. Typically, the samples had a concentration between 10 to 30 μM and were prepared the same day of the experiment.

Electrochemical measurements were performed with a CH Instruments analyzer. The experiments were performed in a custom-made three-arm cell containing a working

compartment, a reference arm connected to the working compartment with a Pt-wire Luggin Capillary, and an auxiliary electrode arm sealed to the working compartment with a fine glass frit. Unless otherwise specified, the electrolyte was 0.1 M tetrabutyl ammonium hexafluorophosphate in acetonitrile. The cell was sealed and the sample bubble degassed with argon. Experiments were carried out under a blanket of argon. Glassy carbon was used as the working electrode, an aqueous Ag/AgCl electrode acted as reference, and the auxiliary electrode was a piece of platinum wire. The working electrode was polished with alumina and sonicated before use. Samples were stirred between experiments with a magnetic stir bar.

Spectroelectrochemical experiments were performed using a custom made optically transparent thin layer (OTTL) cell (appendix B). The cell was made from a modified infrared spectroscopy flow cell. Gold minigrid was used as the working and counter electrodes. The optical windows were made of organic-solvent resistant CaF_2 . A thin layer of sample was created between the two windows using a Teflon space (50 to 100 microns wide). The reference electrode was placed in the sample inlet. Care was taken to make sure there was no sample movement through the flow cell during the experiments. The sample and OTTL cell were degassed prior to taking data. The OTTL cell replaced the sample holder in the UV-visible spectrometer. Spectroelectrochemistry spectra were collected by performing bulk electrolysis at a given potential. Spectra were recorded at regular intervals until less than 5% of the original current was passed to the working electrode.

Luminescent decay and transient absorption spectra were recorded with a nanosecond time-resolved flash photolysis instrument as described in section 4.4. Samples were prepared in acetonitrile in the concentration range of 10 to 30 μM .

Samples were degassed with four freeze-pump-thaw cycles, and back-filled with dry, oxygen-free argon gas.

3.4 Synthesis

[Ru-XY-TMS](PF₆)₂ ([((bpy)₂Ru(bpy-XY-TMS))](PF₆)₂, where bpy-XY-TMS is 4-(2,5-dimethyl-4-trimethylsilylphenyl)-2,2'-bipyridine) – This model metal complex was synthesized using the general ruthenium metalation method (2.16). Bpy-XY-TMS (0.075 mmol) was reacted with Ru(bpy)₂Cl₂ (1 equiv.) overnight. The product was purified on silica gel and collected with a mixture of 5:20:80 saturated aqueous KNO₃:H₂O:CH₃CN as the final eluant. Concentrating and metathesizing to the hexafluorophosphate salt produced a red solid. (37 mg, 47%) ¹H NMR (600 MHz, CD₃CN) δ 8.55 (m, 7H), 8.1 (m, 5H), 7.8 (m, 5H), 7.44 (m, 7H), 7.2 (s, 1H) 2.49 (s, 3H), 2.33 (s, 3H); MS (ESI) [M - PF₆]⁺ (calc.) m/z.

TMS-ethynyl-G (4-methoxy-3-trimethylsilylethynyl-N,N-dimethylaniline) – The synthesis of this compound is detailed in section 2.17.

Ethynyl-G (3-ethynyl-4-methoxy-N,N-dimethylaniline) – The synthesis of this compound is detailed in section 2.17.

RESULTS and DISCUSSION

3.5 [Ru-XY-TMS]²⁺

The model complex [Ru-XY-TMS]²⁺ serves as the baseline for understanding how the xylene bridge and amine donor affect the metal center in [Ru-(XY)_n-G]²⁺. The xylene-functionalized bipyridine ligand of [Ru-XY-TMS]²⁺ better mimics [Ru-(XY)_n-G]²⁺ than plain [Ru(bpy)₃]²⁺. Comparisons of [Ru-XY-TMS]²⁺ with [Ru(bpy)₃]²⁺ isolate the effect of the xylene bridge on the metal center, however. Perturbations to ruthenium's electronic structure in [Ru-(XY)_n-G]²⁺ will be apparent from comparisons of UV-visible absorption spectra, redox potentials, and excited-state lifetimes with [Ru-XY-TMS]²⁺.

3.6 [Ru-XY-TMS]²⁺ UV-Visible Absorption Spectrum

The steady-state UV-visible absorption spectrum (Figure 3.2, Table 3.1) of [Ru-XY-TMS]²⁺, in acetonitrile, exhibits the typical bands for a ruthenium polypyridyl complex. A $\pi \rightarrow \pi^*$ transition for the three bipyridine ligands is observed at a λ_{max} of

288 nm ($\epsilon = 87,800 \text{ M}^{-1}\text{cm}^{-1}$). The metal to ligand charge transfer band (MLCT), which corresponds to an excited state configuration of Ru^{III} and a reduced ligand, is typically found in the region of 400 to 500 nm. The band exhibits the characteristic "double hump" and has a λ_{max} of 450 nm ($\epsilon = 17,600 \text{ M}^{-1}\text{cm}^{-1}$). When compared to $[\text{Ru}(\text{bpy})_3]^{2+}$, the presence and position of the ligand and MLCT bands are identical (Figure 3.2, inset). $[\text{Ru-XY-TMS}]^{2+}$ does have larger extinction coefficients than $[\text{Ru}(\text{bpy})_3]^{2+}$, however. For comparison, the experimentally determined extinction coefficient for $[\text{Ru}(\text{bpy})_3]^{2+}$ at 288 nm is $67,600 \text{ M}^{-1} \text{ cm}^{-1}$ and at 450 nm is $12,600 \text{ M}^{-1}\text{cm}^{-1}$. $[\text{Ru-XY-TMS}]^{2+}$ also has a small shoulder at 325 nm that is not present with $[\text{Ru}(\text{bpy})_3]^{2+}$, and is likely attributed to bpy-XY-TMS.

3.7 $[\text{Ru-XY-TMS}]^{2+}$ Electrochemistry

The cyclic voltammogram for $[\text{Ru-XY-TMS}]^{2+}$ (Figure 3.3, Table 3.2) in acetonitrile shows a clean, reversible one-electron process for the redox couple, $\text{Ru}^{\text{II/III}}$. The couple has a potential of 1.32 V (vs. Ag/AgCl) with a peak separation, ΔE_p , of 73 mV; that is within experimental error of the theoretical value of 60 mV. The cyclic voltammogram of $[\text{Ru}(\text{bpy})_3]^{2+}$ (taken under the same conditions) has a $\text{Ru}^{\text{II/III}}$ couple of 1.33 V ($\Delta E_p = 64 \text{ mV}$) vs. Ag/AgCl. A cyclic voltammogram with an expanded potential window (Figure 3.4) exhibits three additional reversible couples corresponding to reduction of the three bipyridine ligands ($\text{bpy}^{0/-}$). The redox potentials are -1.29 ($\Delta E_p = 78 \text{ mV}$), -1.48 ($\Delta E_p = 60 \text{ mV}$), -1.72 ($\Delta E_p = 78 \text{ mV}$) and do not deviate from the values for $[\text{Ru}(\text{bpy})_3]^{2+}$ (-1.28, -1.48, -1.73 V vs. Ag/AgCl). The irreversible anodic peak at 2.22 V is not present in the $[\text{Ru}(\text{bpy})_3]^{2+}$ cyclic voltammogram and is assigned to xylene

oxidation. A peak at 0 V, also absent from $[\text{Ru}(\text{bpy})_3]^{2+}$, is presumably the matching cathodic peak for xylene. The redox potentials for $\text{Ru}^{\text{I/III}}$ and the bipyridine ligands of $[\text{Ru-XY-TMS}]^{2+}$ show no deviation from $[\text{Ru}(\text{bpy})_3]^{2+}$. Within the sensitivity of cyclic voltammetry, there is no effect of having a xylene ring on the bipyridine ligand. There are additional peaks that are unique to $[\text{Ru-XY-TMS}]^{2+}$ arising from the ligand bpy-XY-TMS.

3.8 $[\text{Ru-XY-TMS}]^{2+}$ Spectroelectrochemistry

Spectroelectrochemistry (0.1 M TBAH in acetonitrile) of $[\text{Ru-XY-TMS}]^{2+}$ was performed in the potential region where ruthenium is oxidized, $\text{Ru}^{\text{II}} \rightarrow \text{Ru}^{\text{III}}$ (Figure 3.5 and 3.6). The oxidation was reversible and upon reduction at 0 V ($\text{Ru}^{\text{III}} \rightarrow \text{Ru}^{\text{II}}$), the initial spectrum was recovered. When compared to $[\text{Ru}(\text{bpy})_3]^{2+}$ (Figure 3.7 and 3.8), $[\text{Ru-XY-TMS}]^{2+}$ has essentially the same features. Both exhibit a bleach in the region of 450 nm corresponding to loss of MLCT intensity. The intensity loss at 288 nm ($\pi \rightarrow \pi^*$ band) is observed for both compounds as well. The characteristic growth of a peak at 320 nm observed for $[\text{Ru}(\text{bpy})_3]^{2+}$ is present in the $[\text{Ru-XY-TMS}]^{2+}$ spectra, but the increase is far less intense. The differences between $[\text{Ru-XY-TMS}]^{2+}$ and $[\text{Ru}(\text{bpy})_3]^{2+}$ are attributed to the xylene ring and appear to have a minimal effect on the metal center.

3.9 $[\text{Ru-XY-TMS}]^{2+}$ Photophysics

The excited state lifetime of $[\text{Ru-XY-TMS}]^{2+}$, τ_o , was measured using time-resolved luminescence decay spectroscopy (Figure 3.9, Table 3.3). A 44.5 μM sample had a lifetime of 618 ns, while a sample roughly half the concentration (24.5 μM) had a

lifetime of 909 ns. In the low concentration limit, it is expected that the excited lifetimes should not vary with concentration. Solvent impurities or differences in oxygen levels could cause variations in lifetime measurements between samples. Since both samples were prepared using the same procedures and solvent, the concentration dependent lifetimes are due to self-quenching. The lifetime of the lower concentration $[\text{Ru-XY-TMS}]^{2+}$ sample matches $[\text{Ru}(\text{bpy})_3]^{2+}$ and, therefore, is a better representation of the intrinsic lifetime.

Transient absorption spectroscopy was used to collect single-wavelength, ΔOD versus time profiles of the low concentration $[\text{Ru-XY-TMS}]^{2+}$ sample. Taken at many wavelengths between 300 and 560 nm, difference spectra were generated at various time points between 0 ns (laser excitation) and 2 μs (Figure 3.10). Difference spectra for the high concentration $[\text{Ru-XY-TMS}]^{2+}$ sample (Figure 3.11) essentially have the same features as the low concentration sample, with the exception of residual absorption red of 480 nm.

The difference spectra correspond to the spectral evolution of the excited-state species decaying to the ground state. The features include a band at 365 and 525 nm, corresponding to a bipyridine radical cation. This is consistent with the expected structure of $^*[\text{Ru-XY-TMS}]^{2+}$; the excited states of transition metal polypyridyl complexes can be written as a combination of M^{III} and $\text{bpy}^{\cdot+}$. The other assigned feature is a bleach of the MLCT band at 450 nm, again consistent with an M^{III} excited-state. The lifetime measurements and transient difference spectra indicate $[\text{Ru-XY-TMS}]^{2+}$ has the same excited-state properties as $[\text{Ru}(\text{bpy})_3]^{2+}$.

3.10 TMS-Ethynyl-G UV-Visible Absorption Spectrum

Just as $[\text{Ru-XY-TMS}]^{2+}$ served as a good model for the acceptor, TMS-ethynyl-G is directly related to the donor of $[\text{Ru-(XY)}_n\text{-G}]^{2+}$. The UV-visible absorption spectrum of TMS-ethynyl-G (Figure 3.12) exhibits a band centered at 344 nm ($\epsilon = 4.3 \times 10^3 \text{ M}^{-1}\text{cm}^{-1}$) assigned to a $\pi \rightarrow \pi^*$ transition. The absorption spectrum indicates that neutral TMS-ethynyl-G does not interfere with ruthenium's MLCT spectroscopic handle at 450 nm.

3.11 TMS-Ethynyl-G Electrochemistry & Spectroelectrochemistry

Electrochemical experiments were undertaken to explore the redox properties of TMS-ethynyl-G. The electron-transfer reaction involves oxidation of the aromatic amine in $[\text{Ru-(XY)}_n\text{-G}]^{2+}$ to a radical cation. Cyclic voltammograms of TMS-ethynyl-G (Figure 3.13) were recorded at positive potentials. The traces show a reversible couple at 0.683 Volts ($\Delta E_p = 79 \text{ mV}$) vs. Ag/AgCl, corresponding to the oxidation of TMS-ethynyl-G ($\text{G} \rightarrow \text{G}^+$). Scanning further positive (Figure 3.14) reveals an irreversible couple with an anodic peak potential of 1.6 V vs. Ag/AgCl. The corresponding cathodic peak appears at 0.310 V vs. Ag/AgCl. The irreversible couple is likely the formation of the TMS-ethynyl- G^{2+} dication ($\text{G}^+ \rightarrow \text{G}^{2+}$); oxidized forms of aromatic amines are prone to decomposition^{144,146}. Scan rate studies of the second oxidation indicate that a rate of 10 V/s is not sufficient to avoid an irreversible couple.

Combining bulk electrolysis and UV-visible absorption spectroscopy produced the spectroelectrochemical traces and difference spectrum in Figure 3.15 and 3.16.

TMS-ethynyl-G was oxidized in a spectroelectrochemical cell at a potential of 1 V (vs. Ag/AgCl). The absorption spectra were recorded over time and then converted to

extinction coefficients. Formation of TMS-ethynyl- G^+ leads to a bleach of the band at 344 nm and formation of a band centered at 520 nm ($\epsilon = 1.8 \times 10^3 \text{ M}^{-1}\text{cm}^{-1}$). This spectrum is in good agreement with photochemical generated 4-methoxy-N,N-dimethylaniline.^{144,146} The spectrum recorded at the end of the electrolysis (signified by less than 5% of the initial current being passed to the cell) likely includes contribution from the oxidized decomposition product. The rate of electrolysis is relatively slow (approximately 1 – 5 minutes), thereby allowing decomposition to occur.

3.12 $[\text{Ru}-(\text{XY})_n-G]^{2+}$ NMR Spectra

NMR spectra of the series $[\text{Ru}-(\text{XY})_n-G]^{2+}$ were recorded on a 600 MHz spectrometer (Figure 3.17 to 3.20). Insufficient quantities of $[\text{Ru}-(\text{XY})_n-G]^{2+}$ and the complexity of the chemical shifts yielded relatively low-resolution spectra. Nonetheless, the observed resonances and integrations were consistent with the expected structure of $[\text{Ru}-(\text{XY})_n-G]^{2+}$. The spectra can be divided into two distinct regions. The ancillary bipyridine ligands, the functionalized bipyridine, the xylene rings, and the donor all have aromatic resonances clustered in the region from 7 ppm to 9 ppm. The large number of aromatic resonances makes resolving and assigning the peaks difficult. At least some of the xylene aromatic singlets can be observed in the spectra however.

The second region is between 2 and 4 ppm, where methyl resonances of the xylene bridge and the donor are found. The methoxy and methylated amine resonances are easily discerned at ~ 4 ppm and ~ 3 ppm, respectively. While some methyl group singlets are observable, many peaks overlap to form an unresolvable peak cluster. Comparison of $[\text{Ru}-(\text{XY})_n-G]^{2+}$ NMR spectra to $[\text{Ru-XY-TMS}]^{2+}$ and TMS-ethynyl-G confirms the assignment of the donor's methyl resonances.

3.13 [Ru-(XY)_n-G]²⁺ Mass Spectra

Mass spectrometry proved invaluable to the identification and characterization of [Ru-(XY)_n-G]²⁺. The complexity of the NMR spectra made analysis difficult, and combined with the lack of material, necessitated the use of alternative characterization methods. Electrospray ionization (ESI) was utilized to obtain mass spectra of [Ru-(XY)_n-G]²⁺. ESI is a relatively soft ionization method that produces very few mass fragments. Fragments containing [Ru-(XY)_n-G]²⁺ and a PF₆⁻ counterion were not uncommon and sometimes comprised the main mass peak.

Ruthenium has a rich and unique isotope pattern, making identification of ruthenium-containing fragments straightforward. The high abundance of carbon and nitrogen create even more unique patterns due to contributions from [M+1] intensity. Figure 3.21 illustrates the changes in the isotope pattern when ligands are added to a ruthenium fragment. The plots were generated by calculating the theoretical distribution using IsoPro[®].¹⁵⁶ The plots were then normalized to the most abundant mass peak (denoted *m*₀) using the following equation,

$$\Omega = \frac{m - m_0}{z} \quad (1)$$

where Ω is the normalized mass and *m* is the observed mass peak.

Inclusion of a significant amount of C¹³ from organic groups greatly increases the M+1 ($\Omega = 1$) intensity for [Ru-XY-TMS]²⁺. [Ru-(XY)₃-G]²⁺, with 35 more carbons from the

xylene bridge and donor, has an even more intense M+1 peak. In all, contributions from the metal, ancillary ligands, bridge, and donor combine to form a unique isotope fingerprint for the $[\text{Ru}-(\text{XY})_n-\text{G}]^{2+}$ series.

The electrospray ionization mass spectra of $[\text{Ru}-(\text{XY})_n-\text{G}]^{2+}$ are shown in Figures 3.22 through 3.29. The samples were measured in acetonitrile using positive mode detection. In each case, the main mass peak matched the calculated value. A more detailed view of the isotope pattern for the main peak was obtained using the instrument's "zoom scan" mode. This feature yields a higher resolution m/z spectrum with clearly defined isotope patterns. The experimentally recorded isotope patterns were overlaid with calculated ones. For each complex, good agreement between the experimental and the calculated was observed. In the case of $[\text{Ru}-(\text{XY})_4-\text{G}]^{2+}$, there is a slight discrepancy between the experimental and calculated main peak m/z in the expanded view (Figure 3.26). The higher resolution "zoom scan" spectrum (Figure 3.27) shows good agreement with the calculated values, however.

3.14 $[\text{Ru}-(\text{XY})_n-\text{G}]^{2+}$ UV-visible Absorption Spectra

There are three main spectral features in the UV-visible absorption spectra of the $[\text{Ru}-(\text{XY})_n-\text{G}]^{2+}$ series (Figure 3.30 and 3.31). A band at 288 nm corresponds to the $\pi \rightarrow \pi^*$ transition of the bipyridine ligands. There is broad absorption from 300 to 400 nm due to the xylene bridge and aromatic amine donor. The last feature is the MLCT band centered at 450 nm. Along the series ($n = 2$ to 5), the absorption spectra essentially remain unchanged as the length between the donor and acceptor increases. There is no shift in the MLCT band as a function of donor-acceptor distance. This would suggest that the electronic coupling between the donor and acceptor is weak. Strong

coupling would result in a blue shift of MLCT band as the bridge increased in length. The longer-length bridges would have weaker electronic interactions causing a blue-shift of the MLCT bands. Furthermore, comparison of the $[\text{Ru}-(\text{XY})_n-\text{G}]^{2+}$ series with $[\text{Ru}-\text{XY}-\text{TMS}]^{2+}$ shows no difference in the position of the MLCT band. Any perturbation to the metal center from extending the xylene bridge and adding a donor is negligible. Interestingly, there is extra absorption at 500 nm for $[\text{Ru}-(\text{XY})_2-\text{G}]^{2+}$ and $[\text{Ru}-(\text{XY})_4-\text{G}]^{2+}$; this may be related to the number of monomers being odd or even.

Comparing $[\text{Ru}(\text{bpy})_3]^{2+}$, $[\text{Ru}-\text{XY}-\text{TMS}]^{2+}$, and $[\text{Ru}-(\text{XY})_n-\text{G}]^{2+}$ is useful for illuminating the effect of the xylene bridge and aromatic amine donor. Starting with $[\text{Ru}(\text{bpy})_3]^{2+}$, adding a single xylene ring to a bipyridine ligand gives $[\text{Ru}-\text{XY}-\text{TMS}]^{2+}$. Adding additional xylene rings, to make an oligomer bridge, and adding an aromatic amine give $[\text{Ru}-(\text{XY})_n-\text{G}]^{2+}$. Any perturbations from the base $[\text{Ru}(\text{bpy})_3]^{2+}$ absorption spectrum will be evident in the absorption band around 290 nm ($\pi \rightarrow \pi^*$), the MLCT band at 450 nm and any broad absorption between those markers.

There is no difference in the position of the 288 nm bpy band between $[\text{Ru}(\text{bpy})_3]^{2+}$, $[\text{Ru}-\text{XY}-\text{TMS}]^{2+}$, and $[\text{Ru}-(\text{XY})_n-\text{G}]^{2+}$ (Figure 3.32). The same is true for the MLCT band, where the shape and position of the characteristic "double hump" does not change among the three compounds. The only significant difference is in the absorption between the bpy and MLCT bands. In this region, the xylene rings and aromatic amine absorb. Closer to the 288 nm band, the xylene bridge has some absorption as well. Therefore, $[\text{Ru}-\text{XY}-\text{TMS}]^{2+}$ is expected to have increased absorption around 320 nm but lacks any significant absorption increase between 320 and 400 nm, when compared to $[\text{Ru}(\text{bpy})_3]^{2+}$. The additional organic functionality in $[\text{Ru}-(\text{XY})_n-\text{G}]^{2+}$ should lead to

increased absorption between the bpy and MLCT band. All of these predictions are consistent with the observed spectra.

3.15 [Ru-(XY)₃-G]²⁺ Electrochemistry and Spectroelectrochemistry

The cyclic voltammogram of [Ru-(XY)₃-G]²⁺, expected to be representative of the [Ru-(XY)_n-G]²⁺ series, has a reversible couple at 1.24 V (vs. Ag/AgCl) assigned to the redox couple Ru^{II/III} (Figure 3.33). An additional redox couple (Figure 3.34) is observed separately at 0.591 V (vs. Ag/AgCl), corresponding to G → G⁺. Bulk electrolysis of [Ru-(XY)₃-G]²⁺ to [Ru^{III}-(XY)₃-G⁺]⁴⁺ was carried out while recording spectral changes (Figure 3.35 and 3.36). The spectroelectrochemical traces show loss of absorption at the MLCT band, corresponding to Ru^{II} → Ru^{III}. This is matched by a broad absorption increase at 520 nm, indicative of G → G⁺ oxidation. The spectral changes are consistent with formation of [Ru^{III}-(XY)₃-G⁺]⁴⁺. Reduction back to [Ru-(XY)₃-G]²⁺, after the spectroelectrochemistry experiments were complete, shows the process was reversible.

3.16 [Ru-(XY)_n-G]²⁺ Photophysics

The excited-state, *[Ru-(XY)_n-G]²⁺, was characterized using time-resolved spectroscopy. The luminescence decay traces for [Ru-(XY)_n-G]²⁺ (Figure 3.37) were measured in deaerated acetonitrile solution, in the absence of quencher. With the exception of [Ru-(XY)₂-G]²⁺, the series members (n = 3 to 5) have the same excited state lifetime (Table 3.3), with an average value of 1.05 μs. The lifetimes were determined from fitting the luminescence decay traces with a monoexponential decay function. The lifetime of [Ru-(XY)₂-G]²⁺ (760 ns) is not significantly shorter than the rest of the [Ru-(XY)_n-G]²⁺ series to attribute the difference to a specific chemical or

structural factor. The transient difference spectra of $^*[Ru-(XY)_2-G]^{2+}$ decaying to the ground state (Figure 3.38) show all of the expected features. An initial absorption increase at 365 and 520 nm (broad) is indicative of bipyridine radical cation formation. The initial bleach at 450 nm indicates oxidation from $Ru^{II} \rightarrow Ru^{III}$. This is consistent with an MLCT excited state that involves oxidation of the metal center and reduction of a ligand.

CONCLUSION

Characterization of the D-B-A complex $[\text{Ru}-(\text{XY})_n-\text{G}]^{2+}$ and its associated components and model complexes has a dual purpose. The first is to identify spectroscopic handles that will be useful in carrying out electron-transfer studies (appendix D, Table D.1). The second is to understand the electronic and chemical properties of $[\text{Ru}-(\text{XY})_n-\text{G}]^{2+}$. Based on UV-visible absorption, electrochemical, spectroelectrochemical, and photophysical characterizations, there is no significant difference between $[\text{Ru}(\text{bpy})_3]^{2+}$, $[\text{Ru}-\text{XY}-\text{TMS}]^{2+}$, and the $[\text{Ru}-(\text{XY})_n-\text{G}]^{2+}$ series. The absorption spectra are the same, the potentials do not shift, and the excited state lifetimes are also essentially identical.

The lack of any significant difference in the physical properties of $[\text{Ru}-\text{XY}-\text{TMS}]^{2+}$ versus $[\text{Ru}(\text{bpy})_3]^{2+}$ suggests that there is no perturbation to the ruthenium chromophore from the presence of a xylene functionalized bipyridine ligand. Likewise, the presence of an extended xylene bridge and donor does not affect the metal center in $[\text{Ru}-(\text{XY})_n-\text{G}]^{2+}$. All of this data indicates weak electronic communication between the

ruthenium and aromatic amine. This can be rationalized by a twist angle between the bipyridine ligand and xylene bridge, and between adjacent xylene rings that is larger than the typical value of 22 to 55°. ¹³⁵⁻¹³⁸ This has significant consequences for the xylene-bridge mediated electron tunneling reactions in $[\text{Ru}-(\text{XY})_n-\text{G}]^{2+}$. It can be predicted from the characterizations of $[\text{Ru}-(\text{XY})_n-\text{G}]^{2+}$ that the distance decay constant, β , for electron transfer is going to be higher than typical values for similar phenylene D-B-A complexes.

FIGURES and TABLES

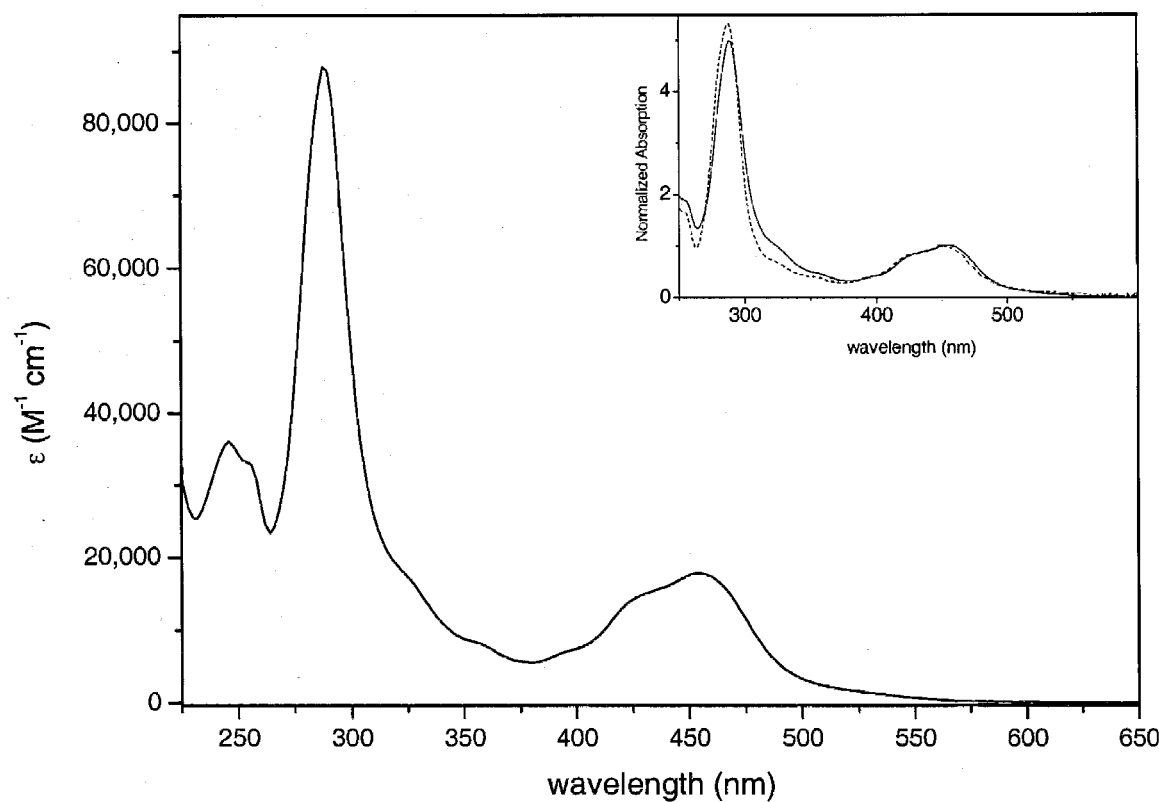


FIGURE 3.2 – $[\text{Ru-XY-TMS}]^{2+}$ UV-visible Absorption Spectrum

The UV-visible absorption of $[\text{Ru-XY-TMS}]^{2+}$ was taken in acetonitrile.

(Inset) Overlay of $[\text{Ru-XY-TMS}]^{2+}$ absorption spectrum (—) and $[\text{Ru}(\text{bpy})_3]^{2+}$ (---) (normalized).

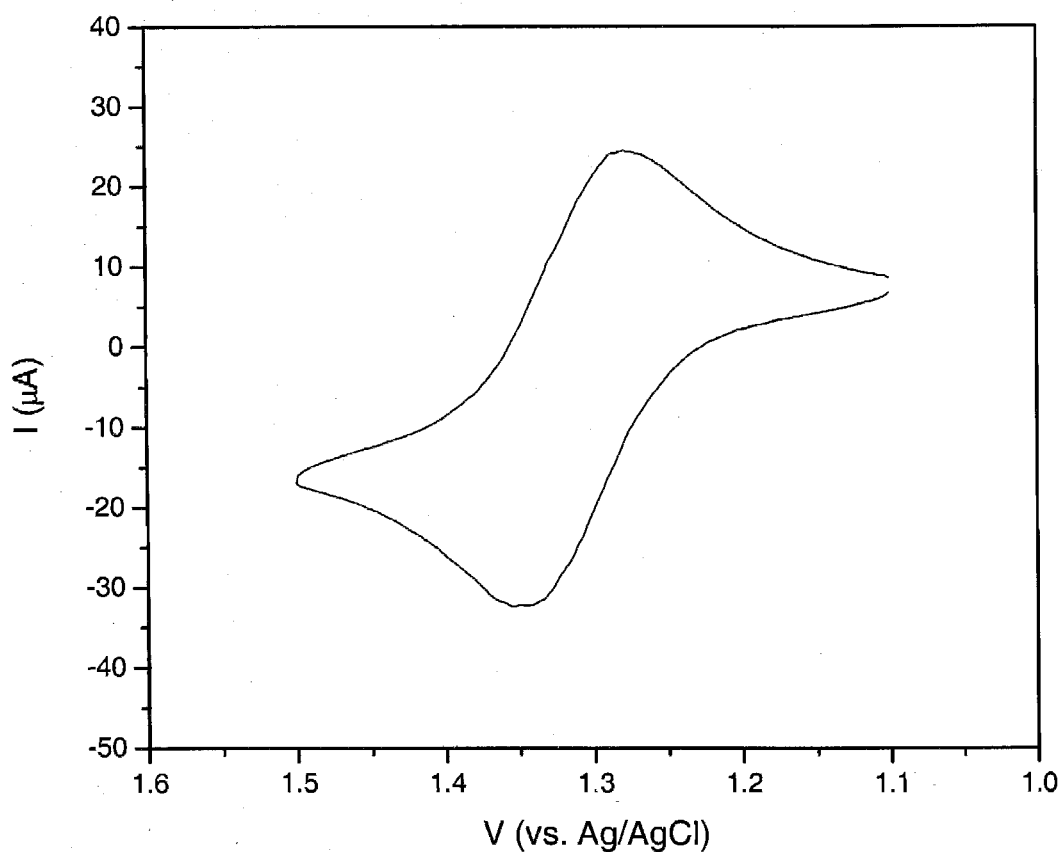


FIGURE 3.3 – $[\text{Ru-XY-TMS}]^{2+}$ Cyclic Voltammogram

The cyclic voltammogram of $[\text{Ru-XY-TMS}]^{2+}$, taken in the region of the $\text{Ru}^{\text{II/III}}$ couple, shows one reversible couple with a potential of 1.32 V (vs. Ag/AgCl) and peak separation of 73 mV.

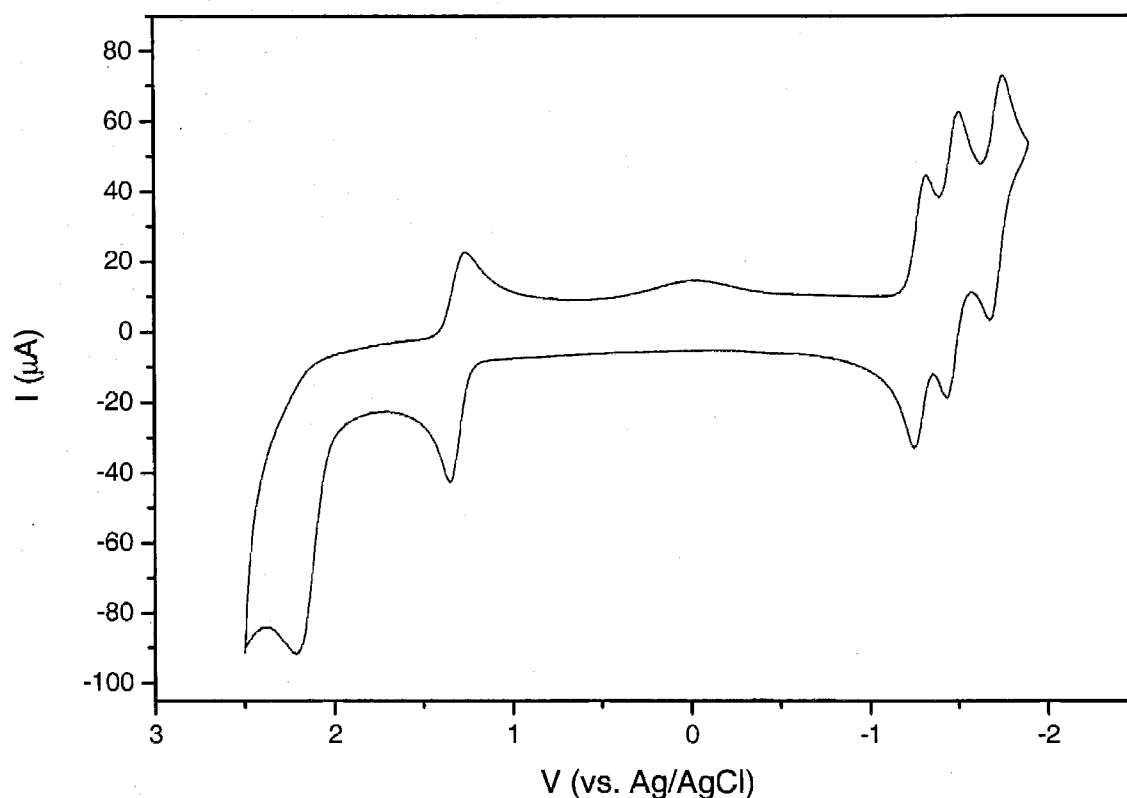


FIGURE 3.4 – Expanded $[\text{Ru-XY-TMS}]^{2+}$ Cyclic Voltammogram

The cyclic voltammogram of $[\text{Ru-XY-TMS}]^{2+}$ shows three distinct couples for the reduction of the bipyridine ligands (-1.29 ($\Delta E_p = 0.078$), -1.48, ($\Delta E_p = 0.06$), -1.72 ($\Delta E_p = 0.078$) vs. Ag/AgCl). The $\text{Ru}^{\text{II/III}}$ couple has a potential of 1.31 V ($\Delta E_p = 0.086$) vs. Ag/AgCl. The anodic peak at 2.22 V (vs. Ag/AgCl) is assigned to the irreversible oxidation of $\text{XY} \rightarrow \text{XY}^+$. The corresponding cathodic peak is found at 0 V.

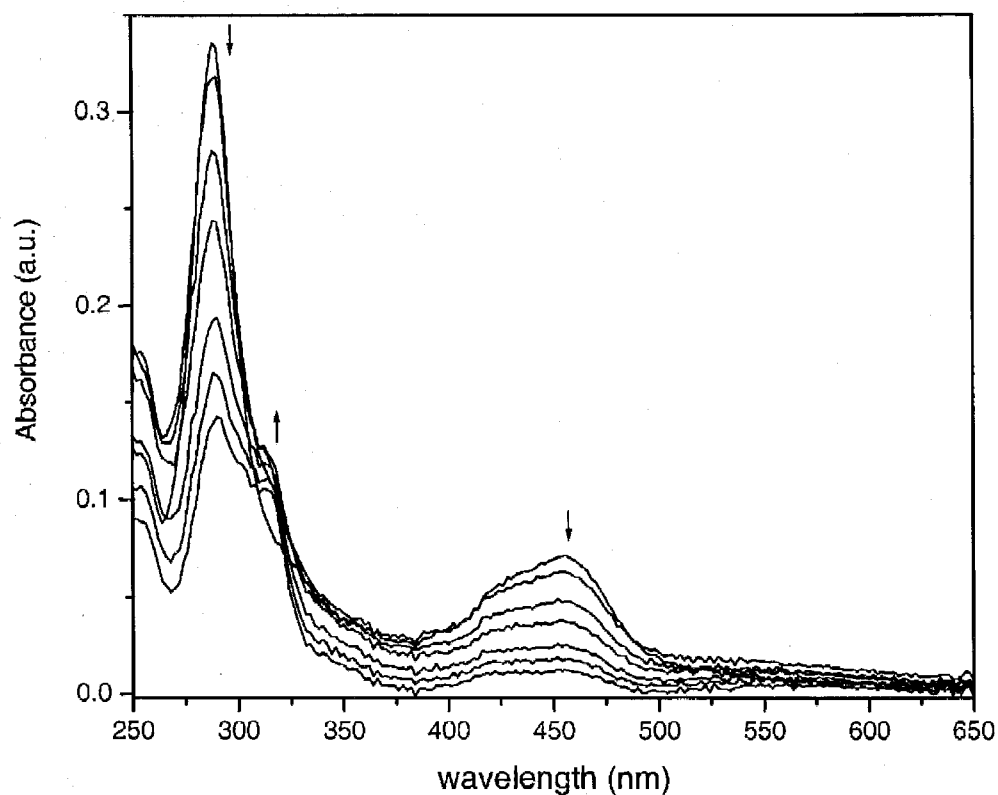


FIGURE 3.5 – $[\text{Ru-XY-TMS}]^{2+}$ Spectroelectrochemical Traces

UV-visible absorption traces taken during the bulk electrolysis of $[\text{Ru-XY-TMS}]^{2+}$ corresponding to $\text{Ru}^{\text{II}} \rightarrow \text{Ru}^{\text{III}}$. Arrows indicate direction of spectral changes upon ruthenium oxidation.

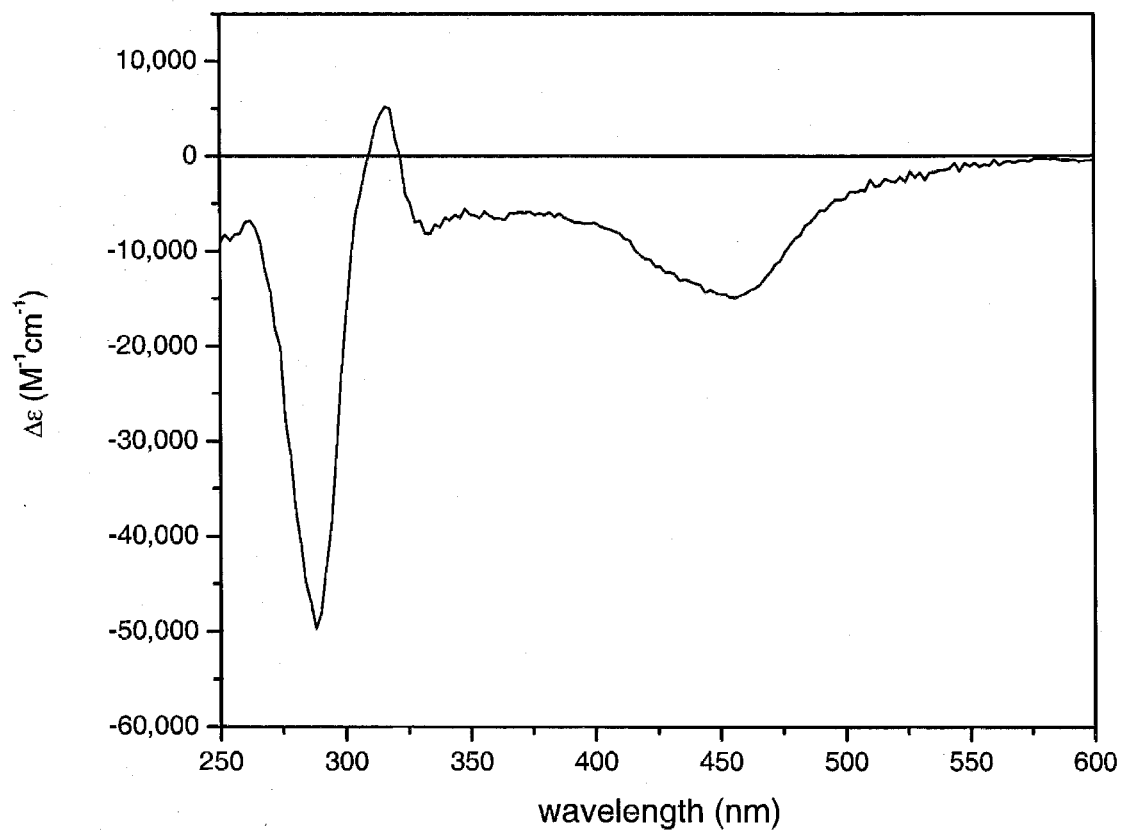


FIGURE 3.6 – $[\text{Ru-XY-TMS}]^{2+}$ $\text{Ru}^{\text{III/II}}$ Difference Spectrum

Difference spectrum of $[\text{Ru-XY-TMS}]^{2+}$ for the $\text{Ru}^{\text{II}} \rightarrow \text{Ru}^{\text{III}}$ transition. The difference spectrum was generated from the spectroelectrochemical data in Figure 3.5 and by assuming that the oxidation to Ru^{III} was complete.

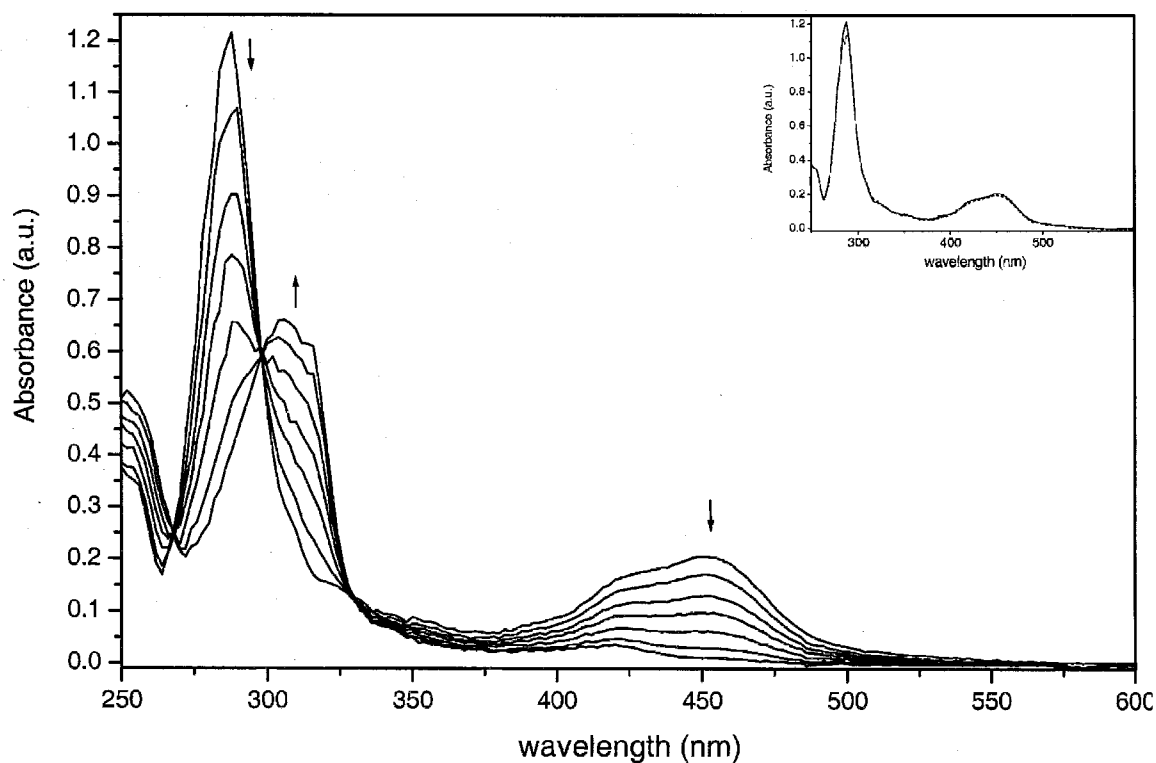


FIGURE 3.7 – $[\text{Ru}(\text{bpy})_3]^{2+}$ Spectroelectrochemical Traces

UV-visible absorption traces during the bulk electrolysis of $[\text{Ru}(\text{bpy})_3]^{2+}$ corresponding to $\text{Ru}^{\text{II}} \rightarrow \text{Ru}^{\text{III}}$. Arrows indicate direction of spectral changes upon ruthenium oxidation.

(Inset) Initial UV-visible spectrum of $[\text{Ru}^{\text{II}}(\text{bpy})_3]^{2+}$ before electrolysis (—), overlaid with the spectrum after electrolysis and subsequent reduction at 0 V ($\text{Ru}^{\text{II}} \rightarrow \text{Ru}^{\text{III}} \rightarrow \text{Ru}^{\text{II}}$) (----). The inset indicates the oxidation, ($\text{Ru}^{\text{II}} \rightarrow \text{Ru}^{\text{III}}$), is fully reversible.

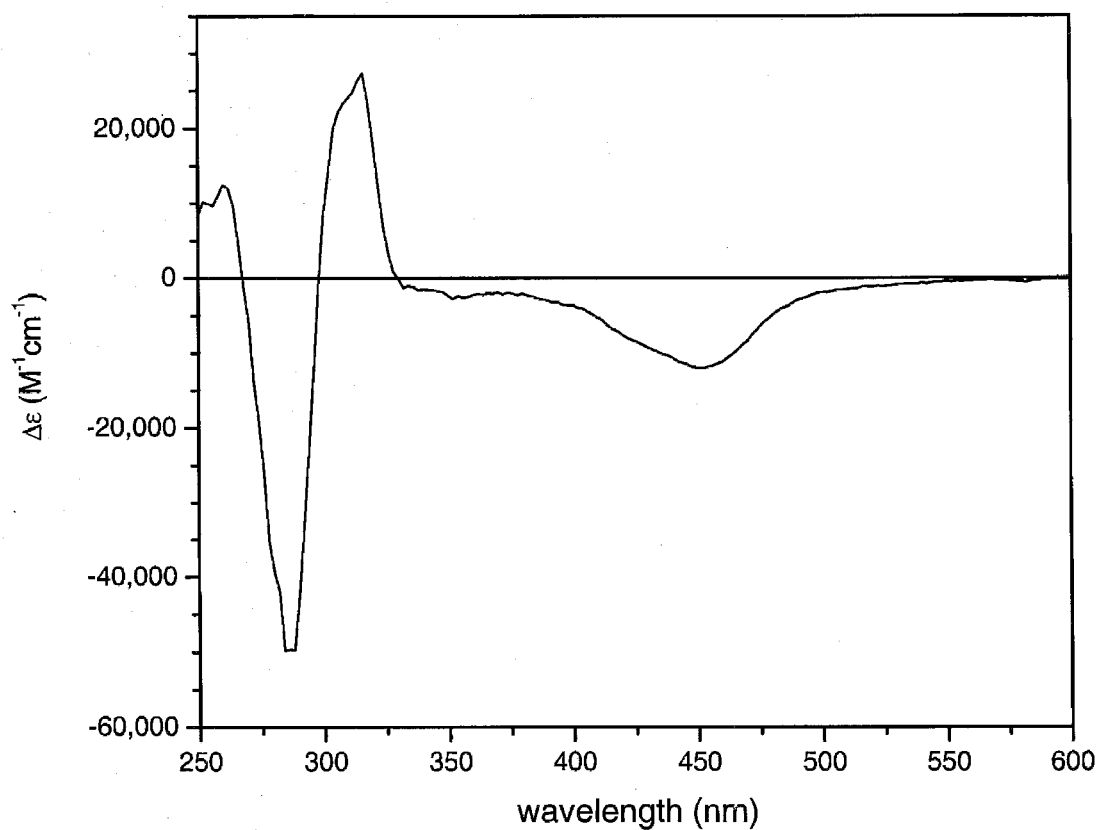


FIGURE 3.8 – $[\text{Ru}(\text{bpy})_3]^{2+}$ $\text{Ru}^{\text{III/II}}$ Difference Spectrum

Difference spectrum of $[\text{Ru}(\text{bpy})_3]^{2+}$ for the $\text{Ru}^{\text{II}} \rightarrow \text{Ru}^{\text{III}}$ transition. The difference spectrum was generated from the spectroelectrochemical data in Figure 3.7 and by assuming that the oxidation to Ru^{III} was complete.

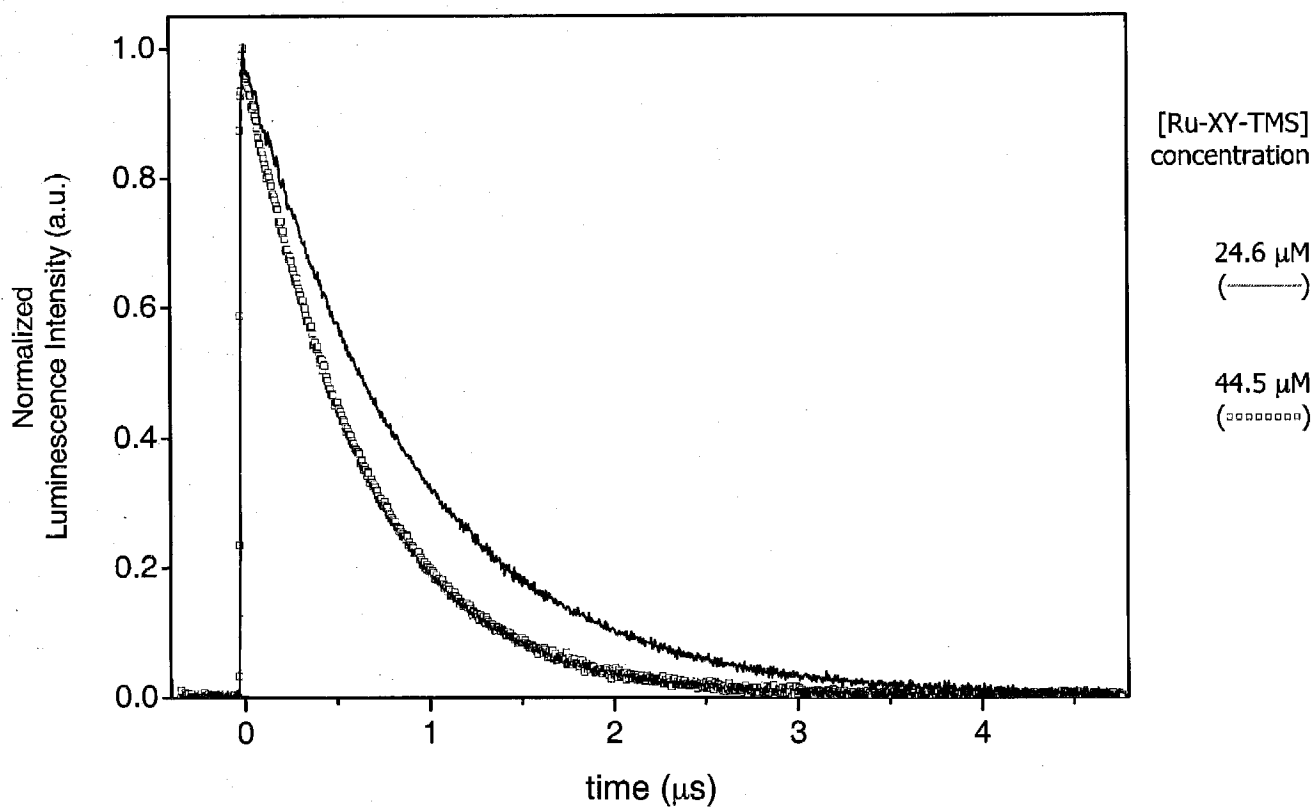


FIGURE 3.9 – $[\text{Ru-XY-TMS}]^{2+}$ Excited State Luminescence Decay

The excited state luminescence decay profiles for a 24.6 and 44.5 μM sample of $[\text{Ru-XY-TMS}]^{2+}$ (acetonitrile). The traces were fit to monoexponential functions to yield a rate constant of $1.1 \times 10^6 \text{ s}^{-1}$ (909 ns) and $1.6 \times 10^6 \text{ s}^{-1}$ (618 ns) for the 24.6 μM and 44.5 μM samples, respectively.

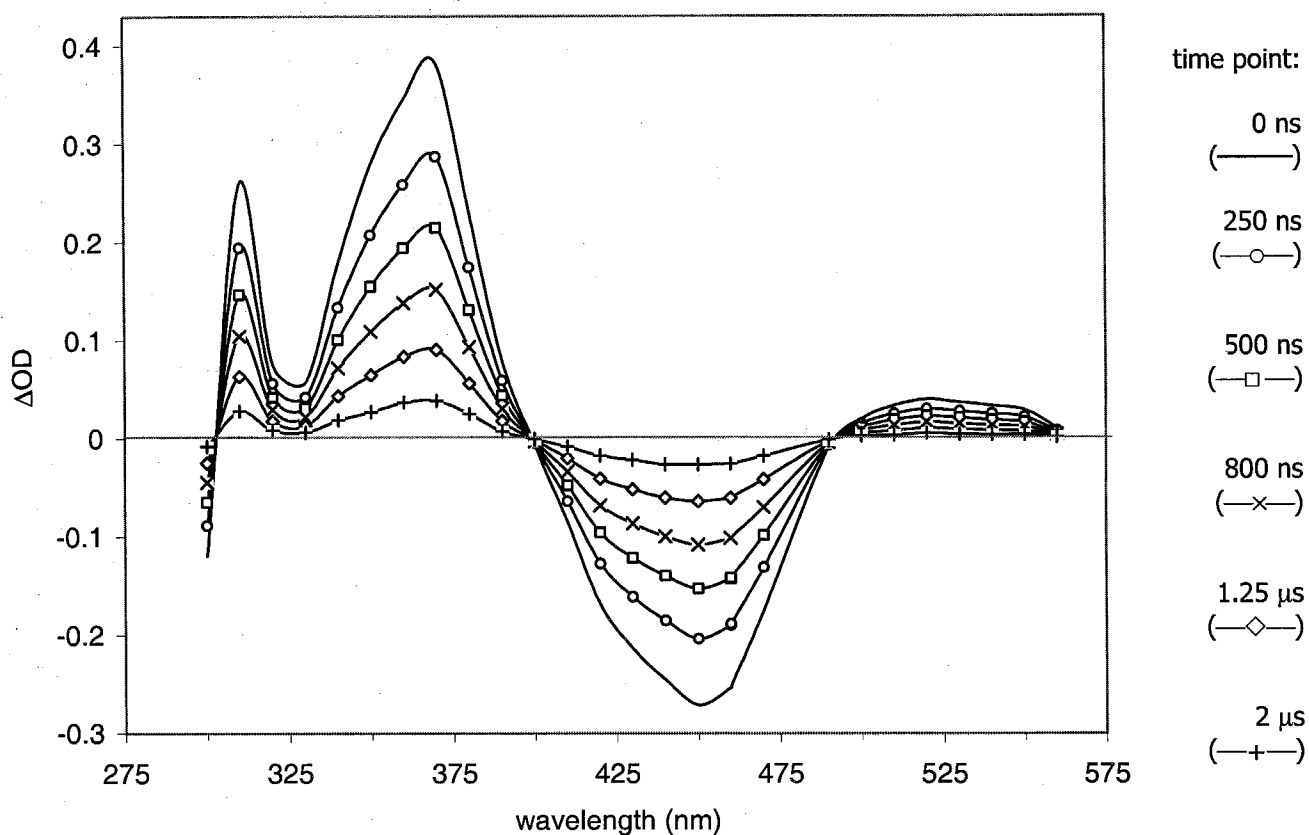


FIGURE 3.10 – $[\text{Ru-XY-TMS}]^{2+}$ Excited State Difference Spectrum (low concentration)

Transient difference spectra of a $24.5 \mu\text{M}$ sample of $[\text{Ru-XY-TMS}]^{2+}$ (low concentration). Time zero is the arrival of the laser pulse. The spectral features include formation of the bipyridine radical anion at 365 nm and 525 nm, and the bleach of the MLCT band at 450 nm.

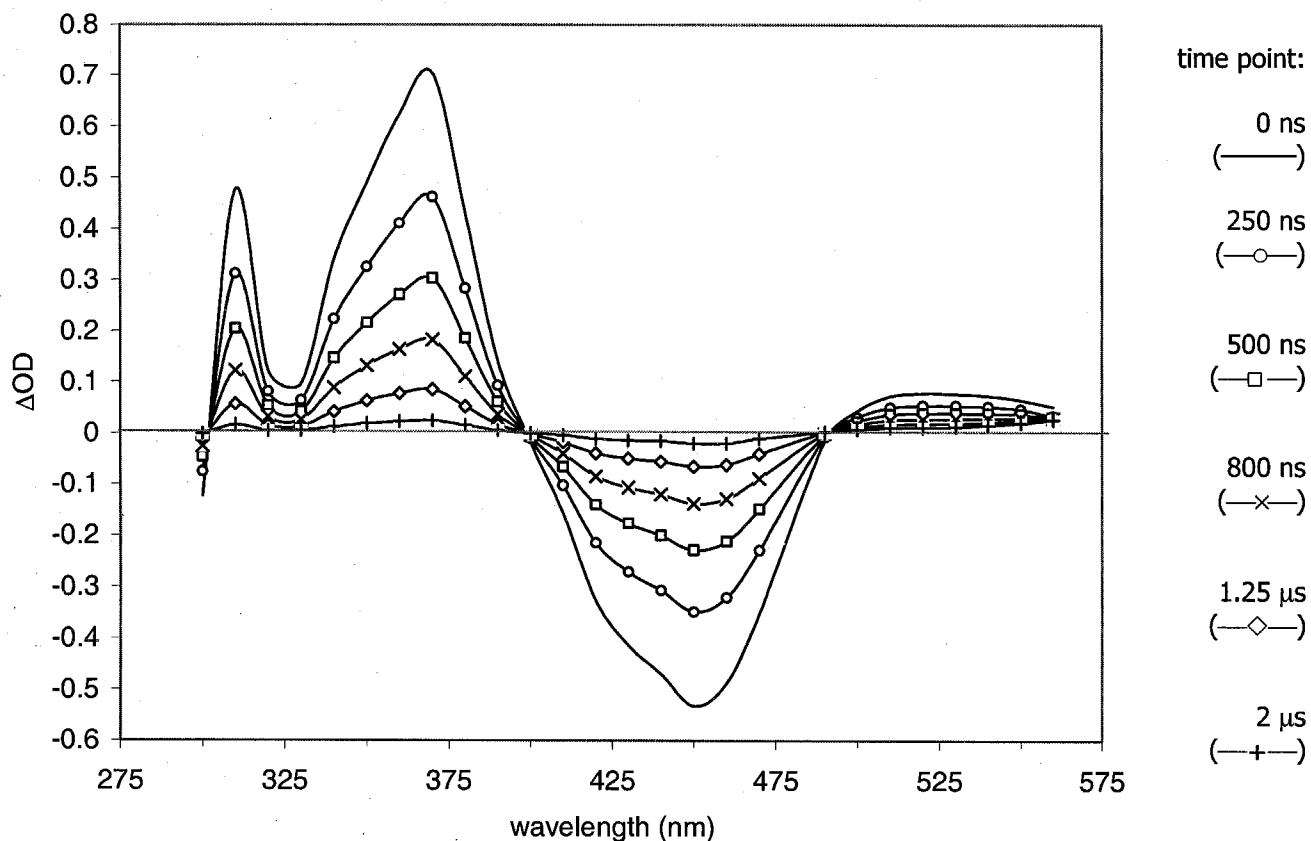


FIGURE 3.11 – $[\text{Ru-XY-TMS}]^{2+}$ Excited State Difference Spectrum (high concentration)

Transient difference spectra of a $44.5 \mu\text{M}$ sample of $[\text{Ru-XY-TMS}]^{2+}$ (low concentration). Time zero is the arrival of the laser pulse. The same spectral features observed in the low concentration sample (Figure 3.10) are found in these traces. Formation of the bipyridine radical anion at 365 nm and 525 nm, and the bleach of the MLCT band at 450 nm are both observed.

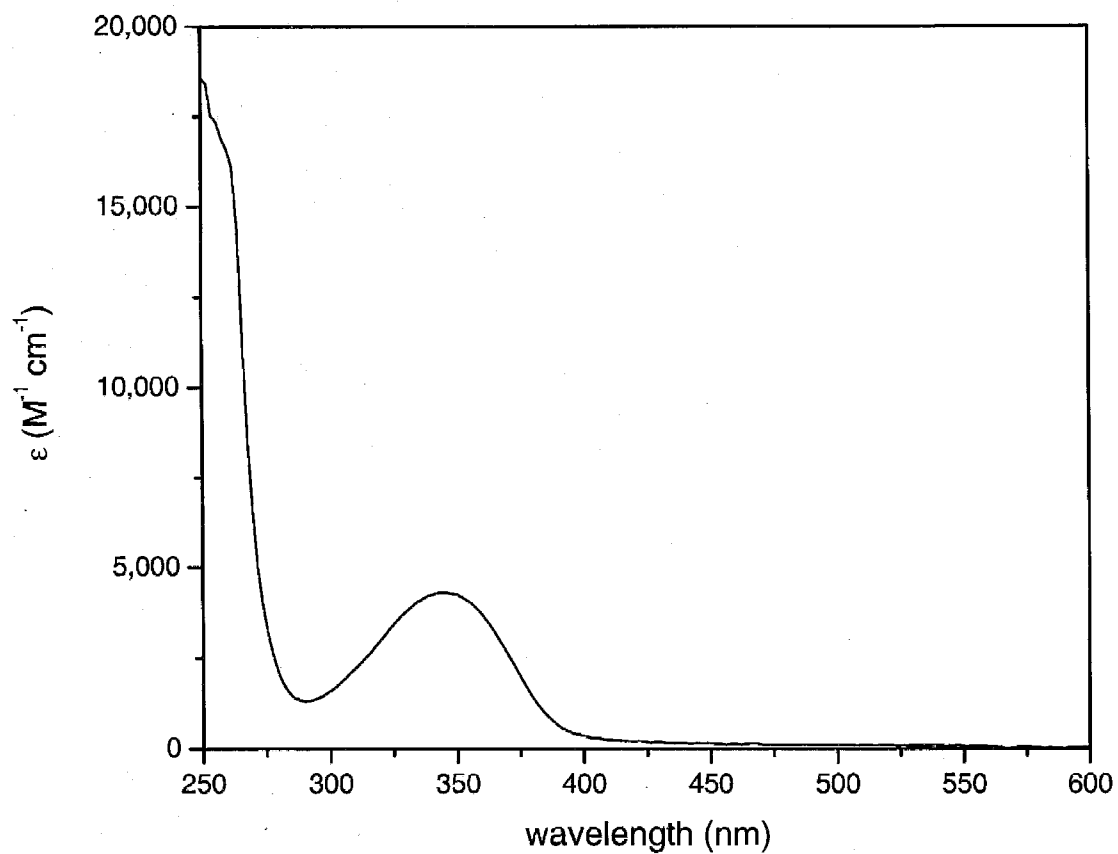


FIGURE 3.12 – TMS-Ethynyl-G UV-visible Absorption Spectrum

The UV-visible spectrum of TMS-ethynyl-G in acetonitrile exhibits a band at 344 nm assigned to a $\pi \rightarrow \pi^*$ transition.

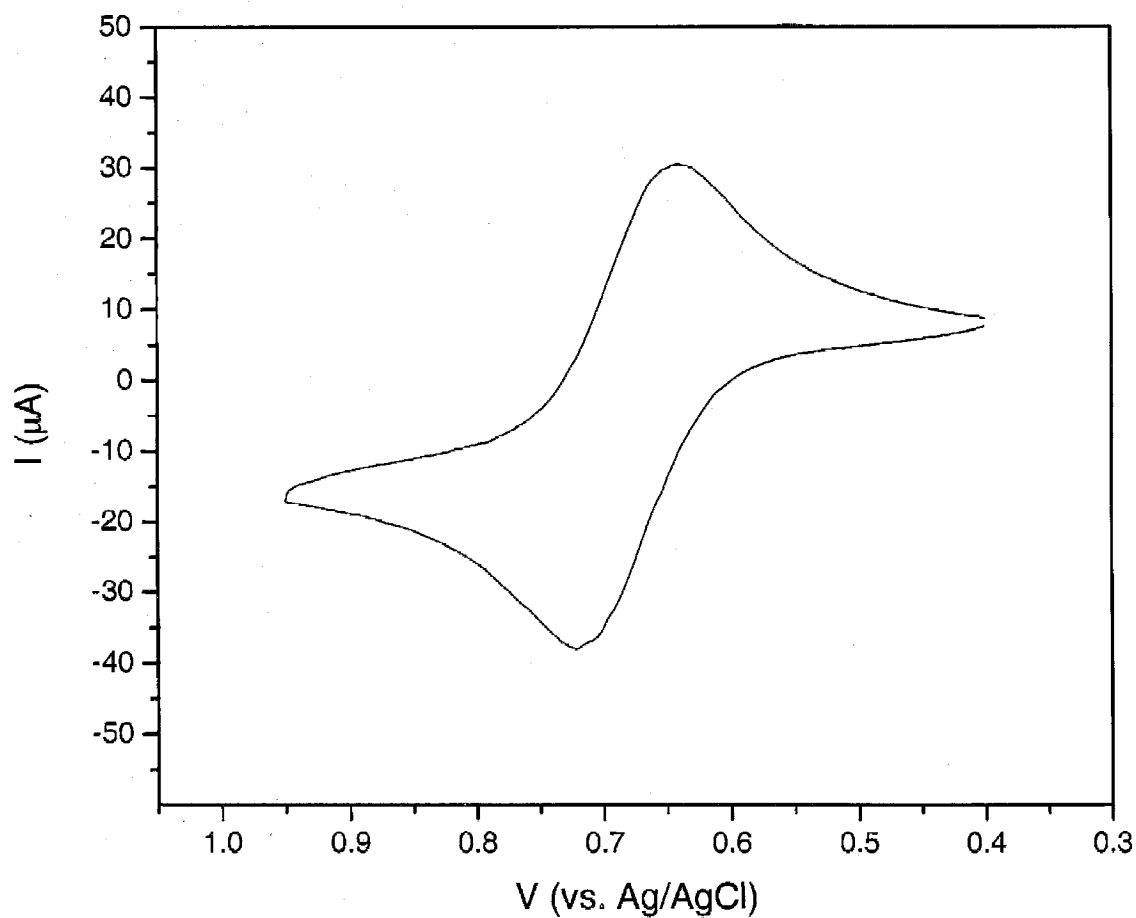


FIGURE 3.13 – TMS-Ethynyl-G Cyclic Voltammogram

The cyclic voltammogram of TMS-ethynyl-G, in the region of the $G^{0/+}$ couple, has a potential of 0.683 V (vs. Ag/AgCl) and peak separation of 79 mV. The scan rate was 0.25 V/s.

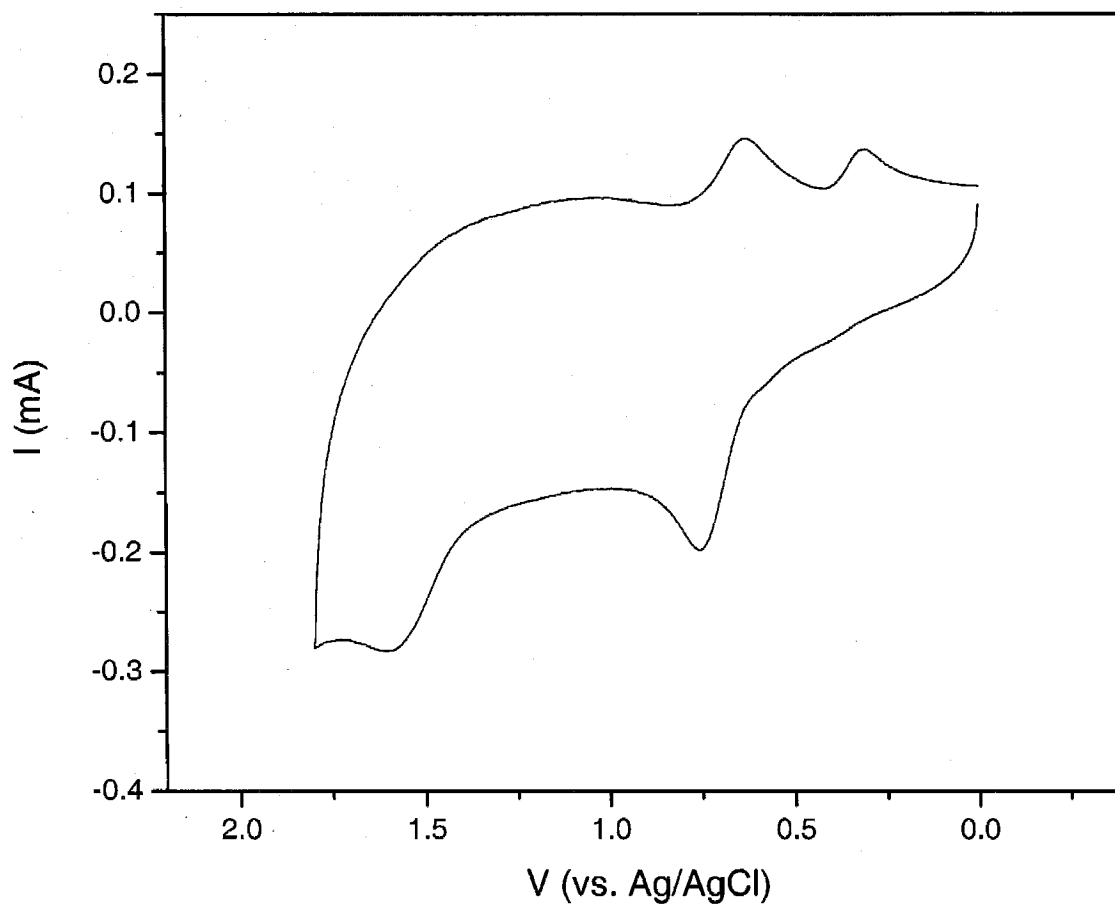


FIGURE 3.14 – Expanded TMS-Ethynyl-G Cyclic Voltammogram

The expanded cyclic voltammogram of TMS-ethynyl-G shows a reversible couple at 0.683 V (vs. Ag/AgCl) and an irreversible anodic peak at 1.6V and the corresponding cathodic peak at 0.31 V (vs. Ag/AgCl).

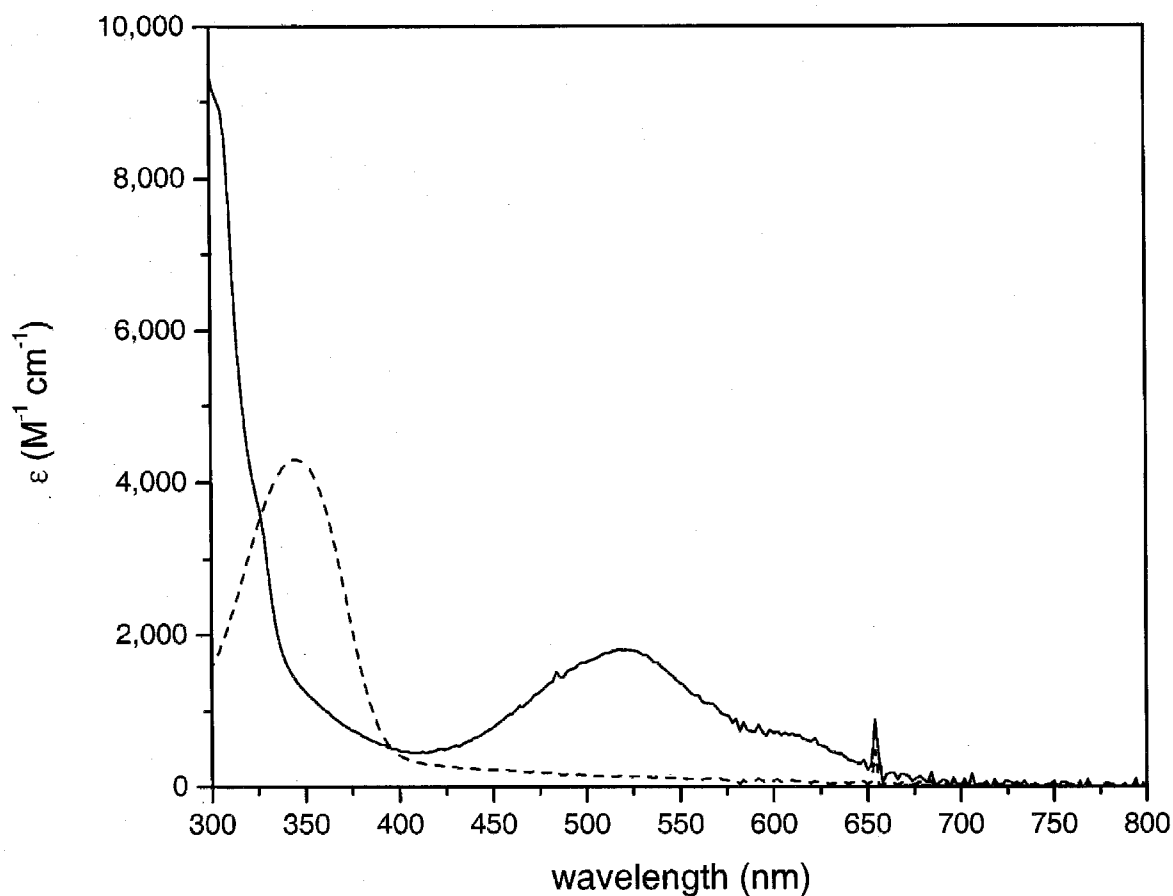


FIGURE 3.15 – TMS-Ethynyl-G Spectroelectrochemical Traces

UV-visible absorption traces during the bulk electrolysis of TMS-ethynyl-G corresponding to $G^0 \rightarrow G^+$. The broken line represents the neutral starting state, while the solid line is the spectrum after bulk electrolysis at 1 V (vs. Ag/AgCl). (The spike at ~650 nm is an instrument artifact.)

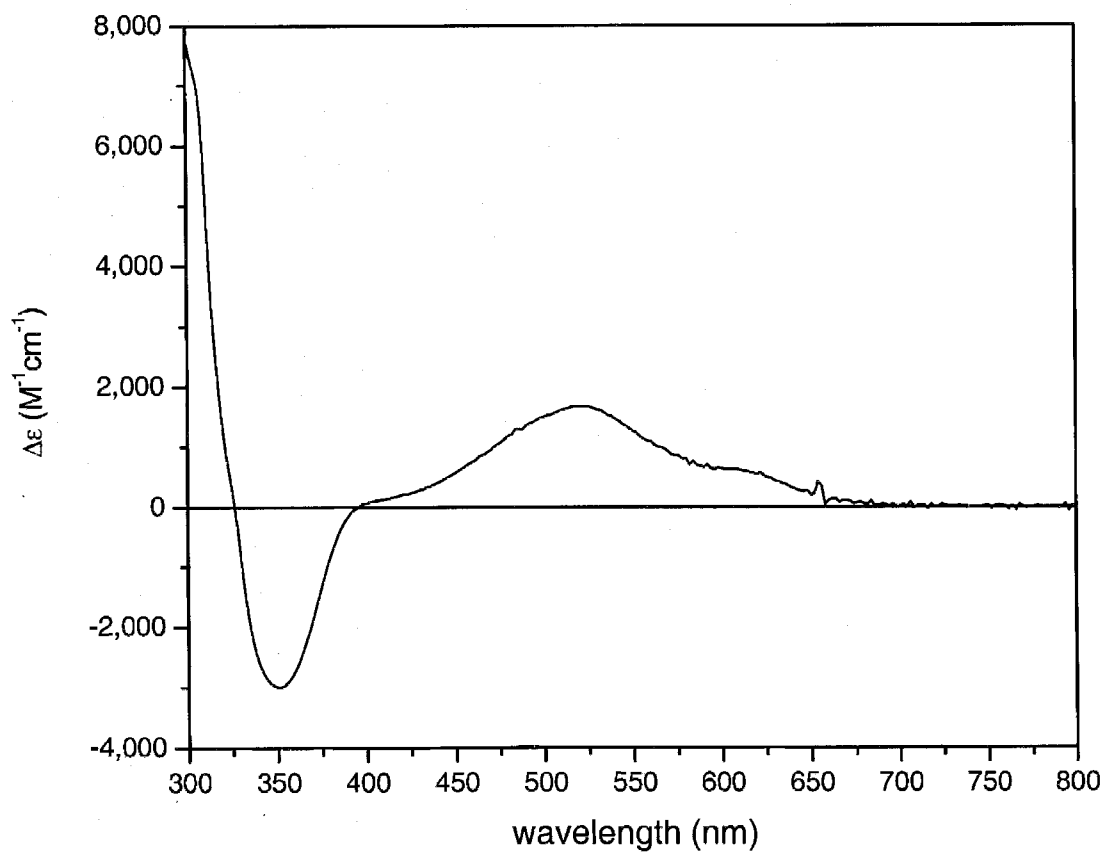


FIGURE 3.16 – TMS-Ethynyl-G⁺/TMS-Ethynyl-G
Difference Spectrum

Difference spectrum of TMS-Ethynyl-G for the G⁺→G⁺ redox states. The difference spectrum was generated from the spectroelectrochemical data in Figure 3.15 and by assuming that the oxidation to G⁺ was complete.

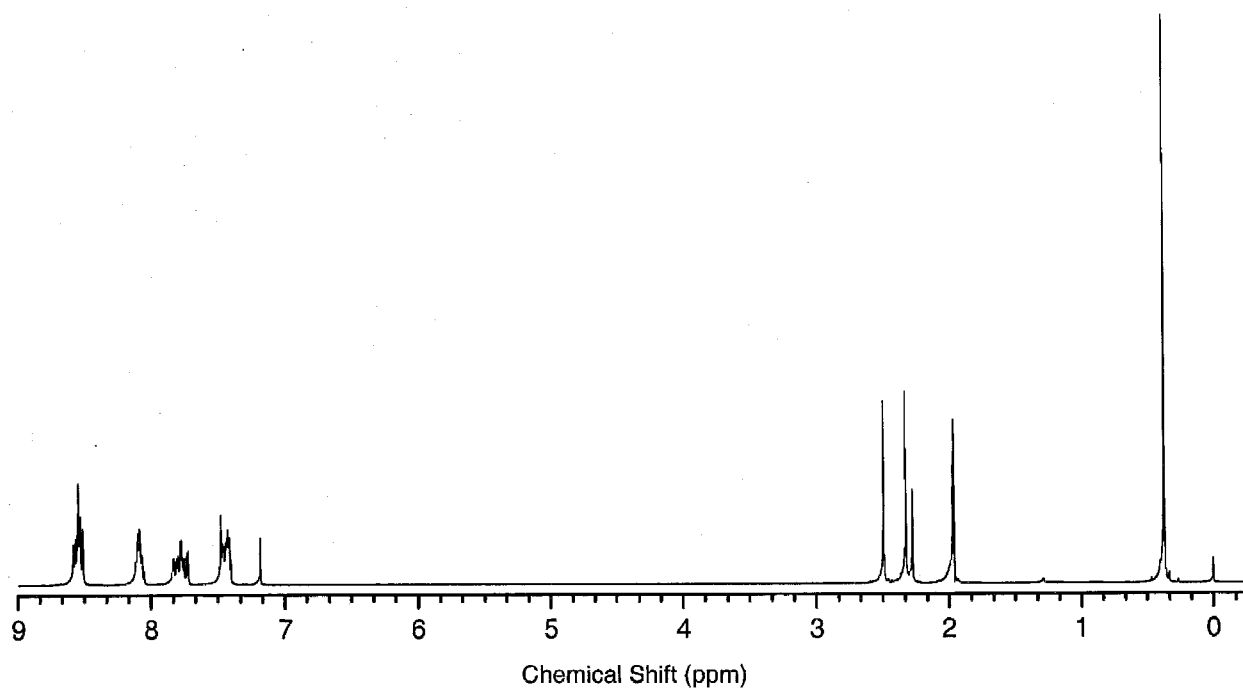


FIGURE 3.17 - $[\text{Ru-XY-TMS}]^{2+}$ NMR Spectrum

The samples were recorded in CD_3CN with a 600 MHz spectrometer and referenced to tetramethylsilane (added to sample).

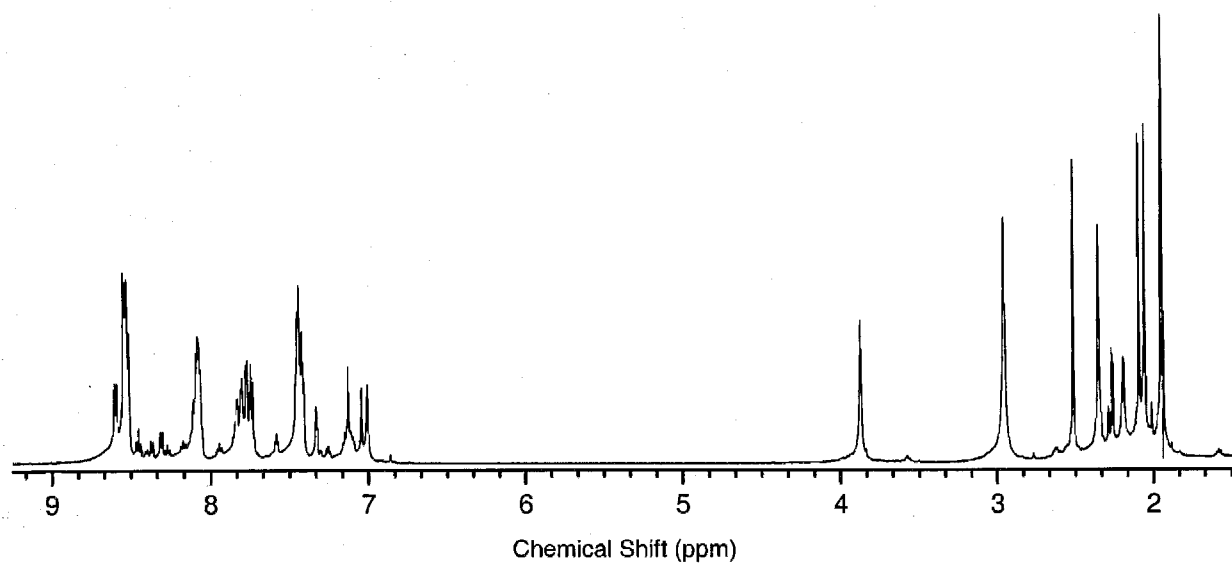


FIGURE 3.18 – $[\text{Ru}-(\text{XY})_2\text{-G}]^{2+}$ NMR Spectrum

The samples were recorded in CD_3CN with a 600 MHz spectrometer and referenced to tetramethylsilane (added to sample).

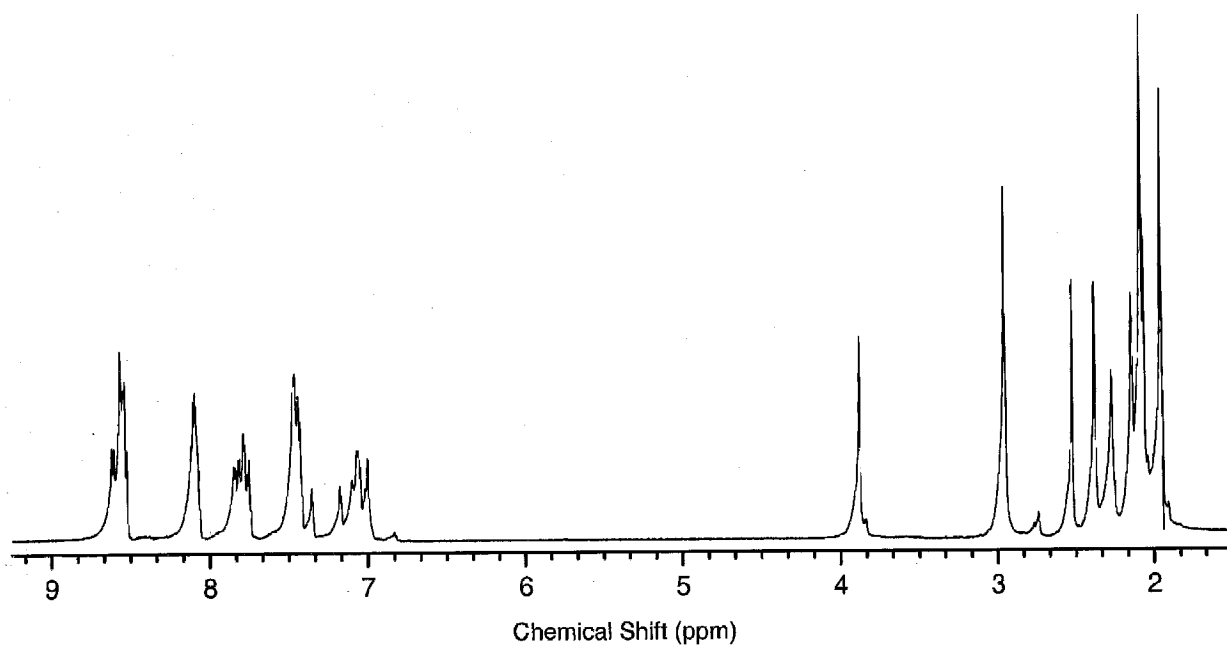


FIGURE 3.19 – $[\text{Ru}-(\text{XY})_3\text{-G}]^{2+}$ NMR Spectrum

The samples were recorded in CD_3CN with a 600 MHz spectrometer and referenced to tetramethylsilane (added to sample).

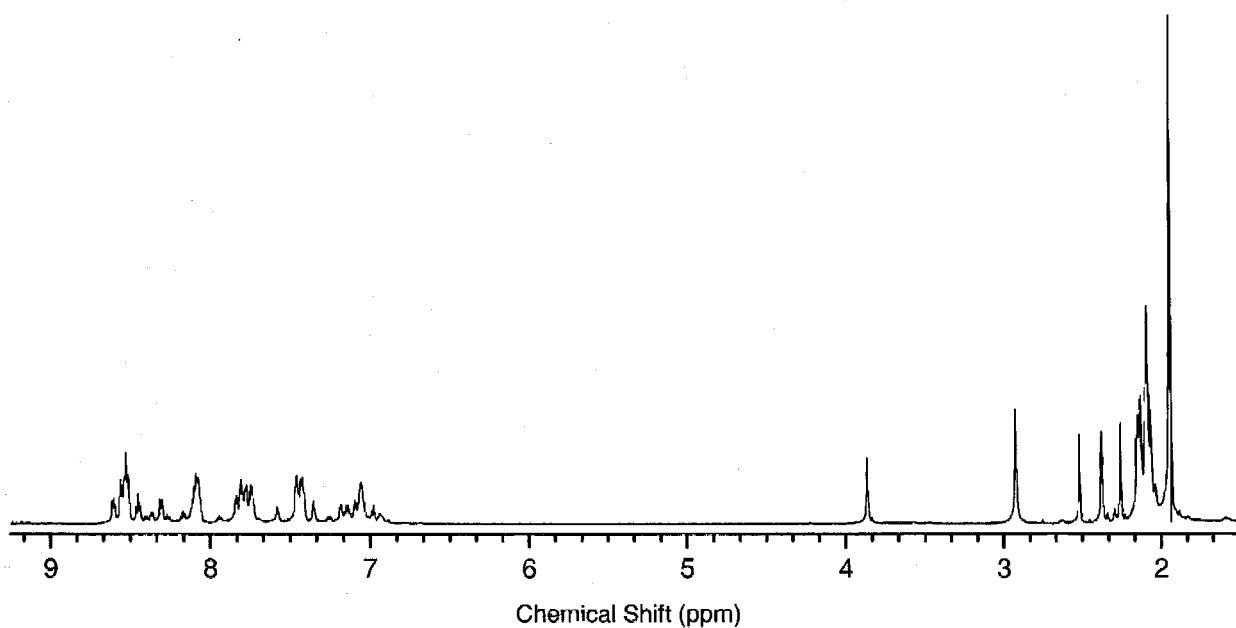


FIGURE 3.20 – $[\text{Ru}(\text{XY})_4\text{-G}]^{2+}$ NMR Spectrum

The samples were recorded in CD_3CN with a 600 MHz spectrometer and referenced to tetramethylsilane (added to sample).

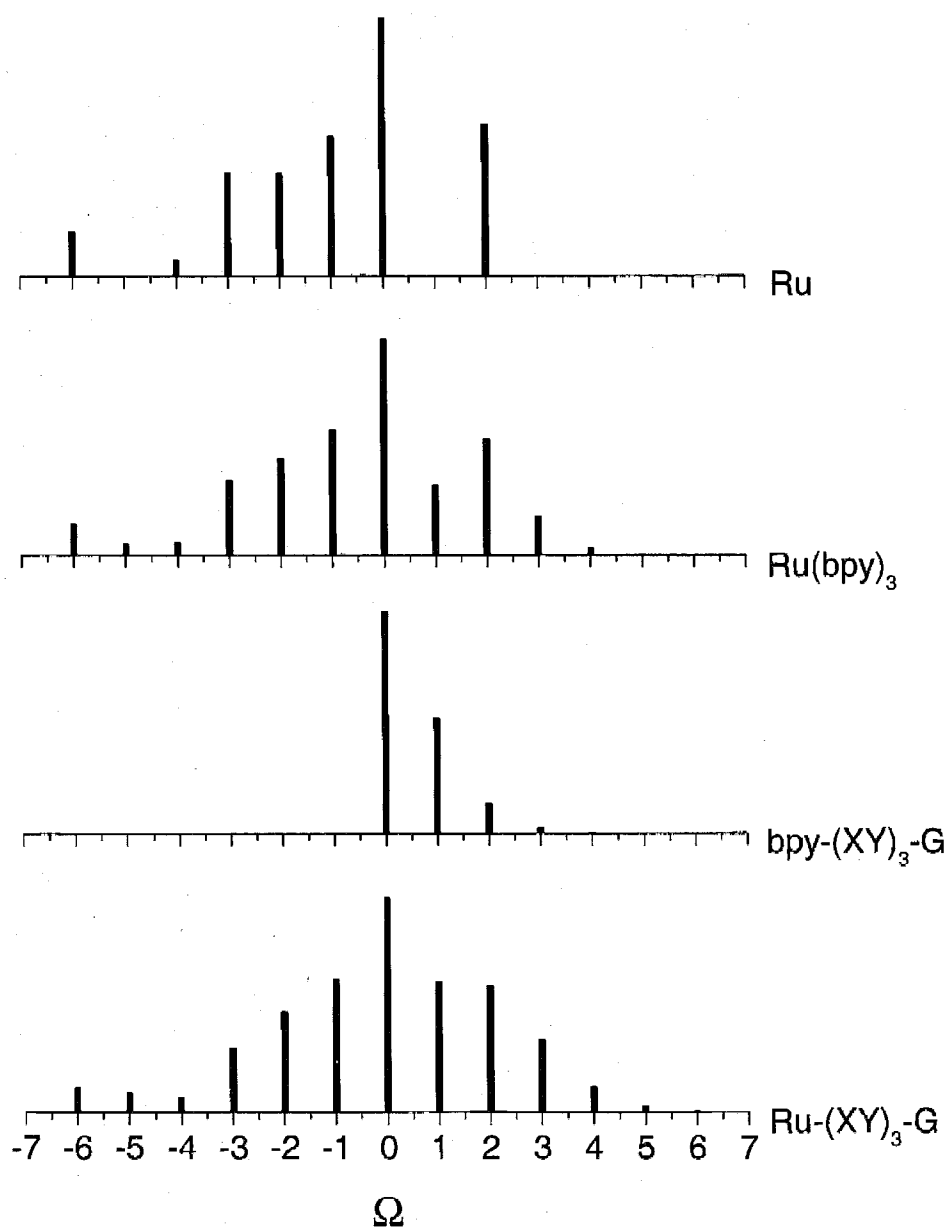


FIGURE 3.21 – Calculated Isotope Patterns

The calculated isotope patterns show the progression from free ruthenium metal to the D-B-A complex, $[\text{Ru}-(\text{XY})_3\text{-G}]^{2+}$. Ω is a normalized m/z ratio that resets the most abundant peak to zero (see section 3.13 for details).

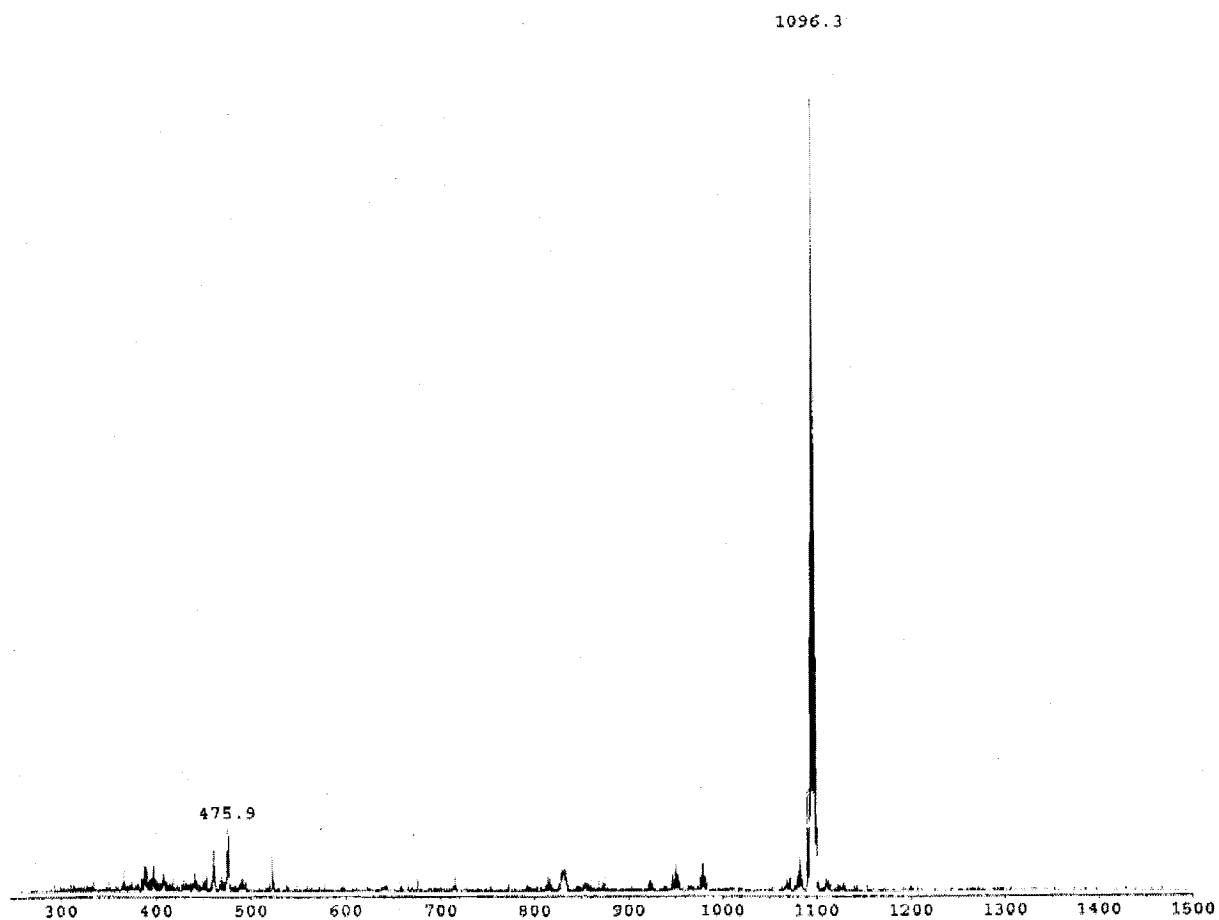


FIGURE 3.22 – $[\text{Ru}(\text{XY})_2\text{-G}]^{2+}$ ESI Mass Spectrum

ESI mass spectrum of $[\text{Ru}(\text{XY})_2\text{-G}]^{2+}$ in acetonitrile with positive ion detection. The main peak at 1096.3 m/z is assigned to $[\text{Ru}(\text{XY})_2\text{-G}](\text{PF}_6)^+$ (calc. 1096.3) and the peak at 475.9 is the dication, $[\text{Ru}(\text{XY})_2\text{-G}]^{2+}$.

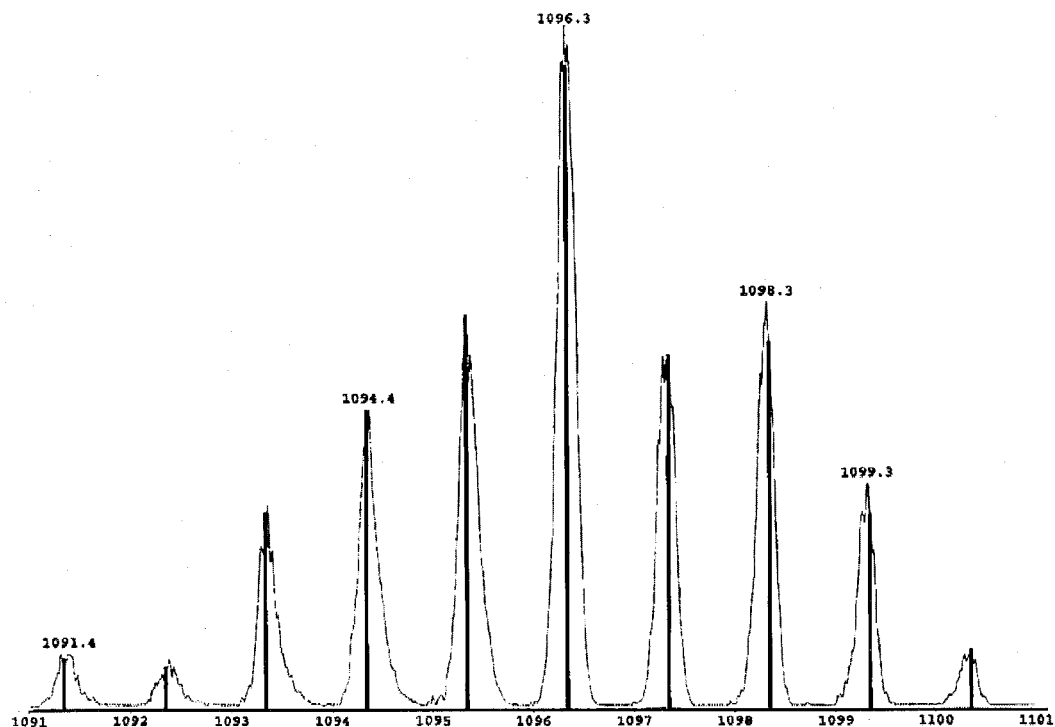


FIGURE 3.23 – Detailed View of $[\text{Ru}-(\text{XY})_2-\text{G}]^{2+}$ ESI Mass Spectrum

Expanded view of 1096.3 m/z peak of the $[\text{Ru}-(\text{XY})_2-\text{G}](\text{PF}_6)^{2+}$ ESI spectrum in Figure 3.22. The spectrum is overlaid with the calculated isotope pattern (solid bars).

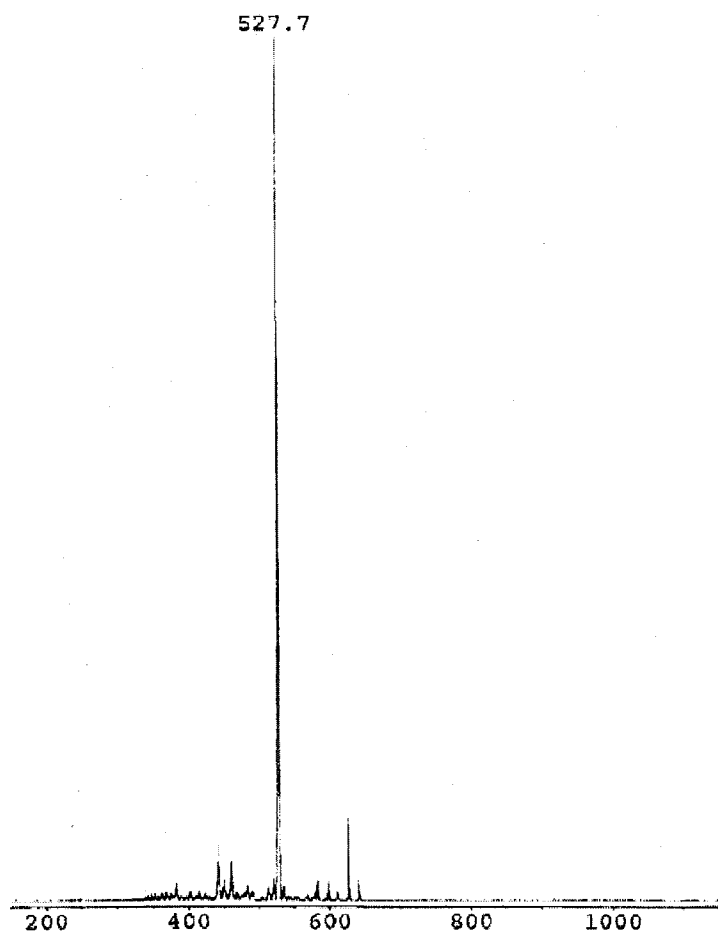


FIGURE 3.24 – $[\text{Ru}-(\text{XY})_3\text{-G}]^{2+}$ ESI Mass Spectrum

ESI mass spectrum of $[\text{Ru}-(\text{XY})_3\text{-G}]^{2+}$ in acetonitrile under positive ion detection. The main peak at 527.7 m/z is assigned to $[\text{Ru}-(\text{XY})_3\text{-G}]^{2+}$ (calc. 527.7).

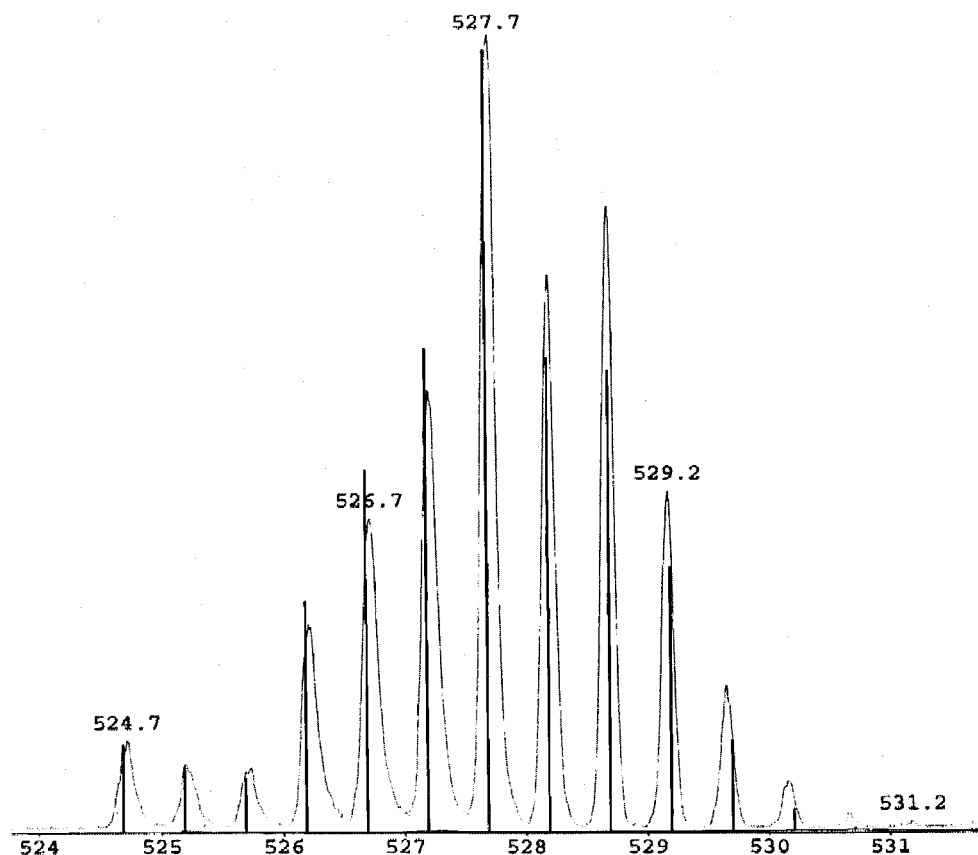


FIGURE 3.25 – Detailed View of $[\text{Ru}(\text{XY})_3\text{-G}]^{2+}$ ESI Mass Spectrum

Expanded view of 527.7 m/z peak of the $[\text{Ru}(\text{XY})_3\text{-G}]^{2+}$ ESI spectrum in Figure 3.24. The spectrum is overlaid with the calculated isotope pattern (solid bars).

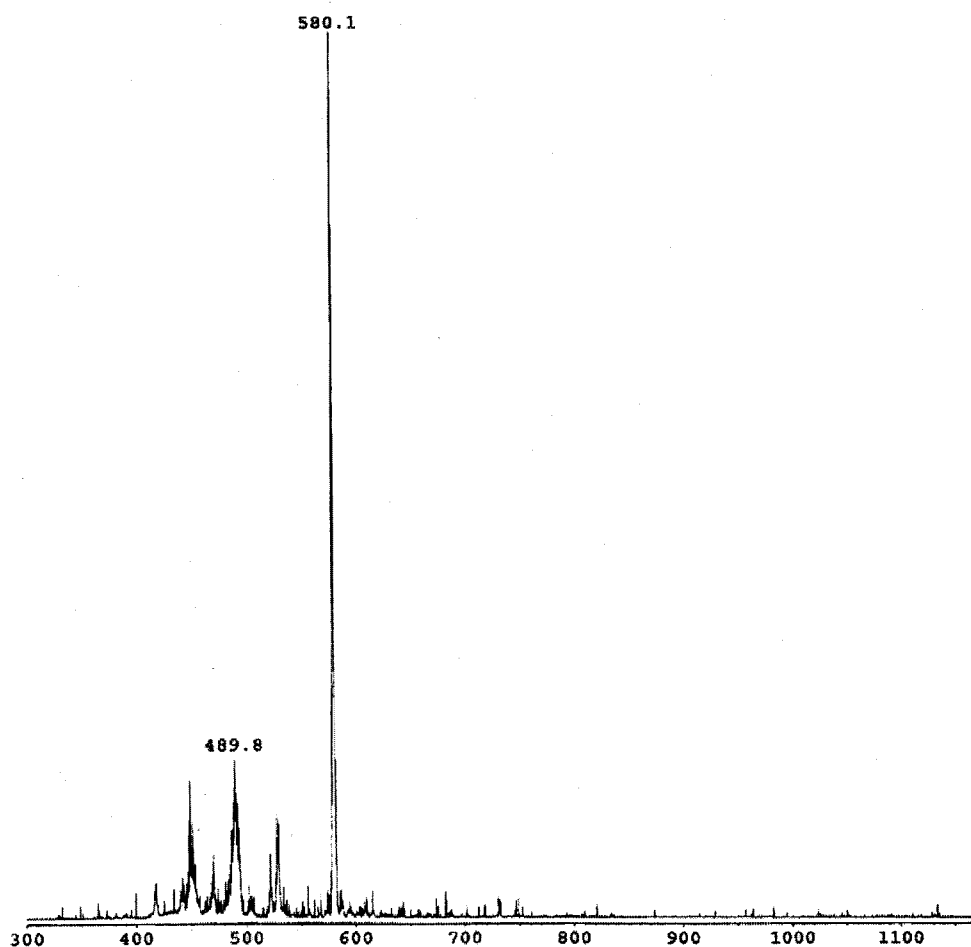


FIGURE 3.26 – $[\text{Ru}-(\text{XY})_4\text{-G}]^{2+}$ ESI Mass Spectrum

ESI mass spectrum of $[\text{Ru}-(\text{XY})_4\text{-G}]^{2+}$ in acetonitrile under positive ion detection. The main peak at 580.1 m/z is assigned to $[\text{Ru}-(\text{XY})_4\text{-G}]^{2+}$ (calc. 579.7). The peak at 489.8 m/z is $[\text{Ru}(\text{bpy})_2\text{Cl}_2]$ plus a proton.

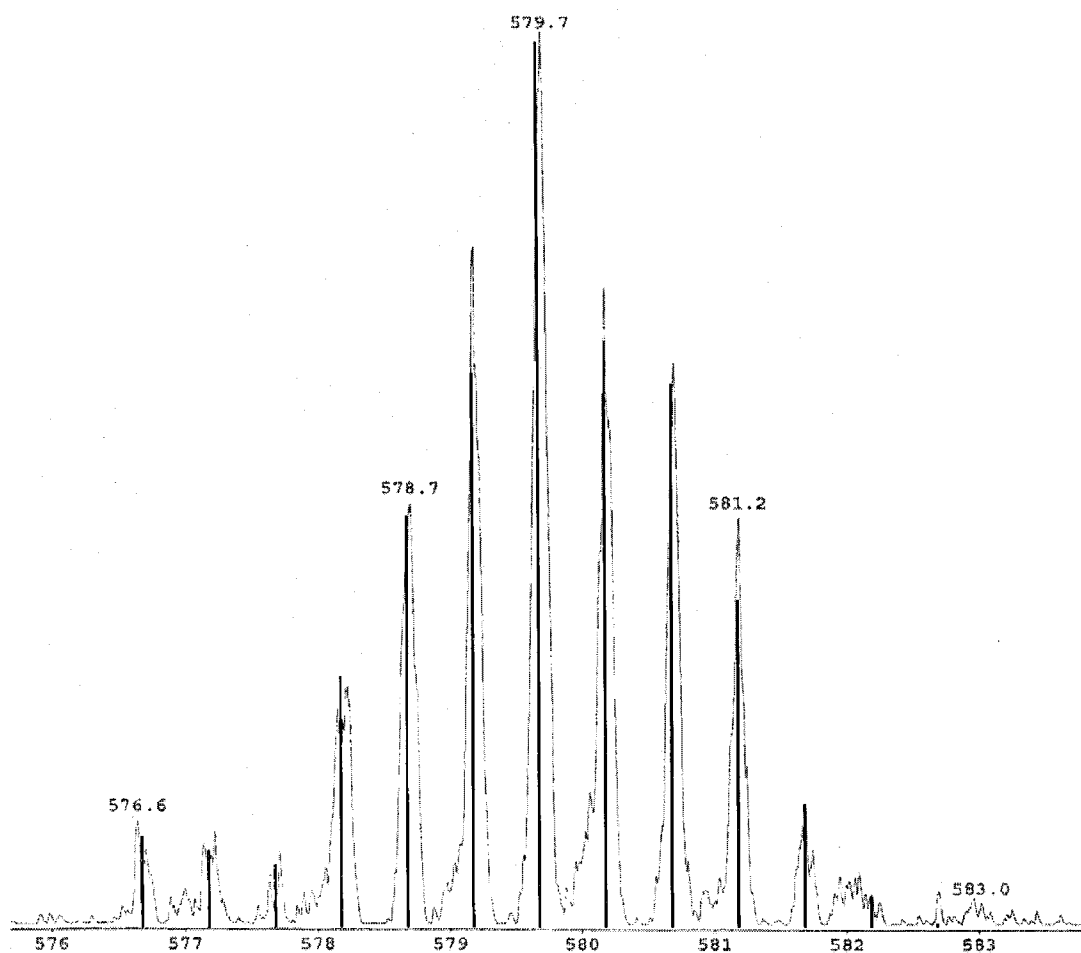


FIGURE 3.27 – Detailed View of $[\text{Ru}(\text{XY})_4\text{-G}]^{2+}$ ESI Mass Spectrum

Expanded view of 580.1 m/z peak of the $[\text{Ru}(\text{XY})_4\text{-G}]^{2+}$ ESI spectrum in Figure 3.26. Using the "zoom scan" mode of the spectrometer a higher resolution spectrum is possible. The spectrum is overlaid with the calculated isotope pattern (solid bars).

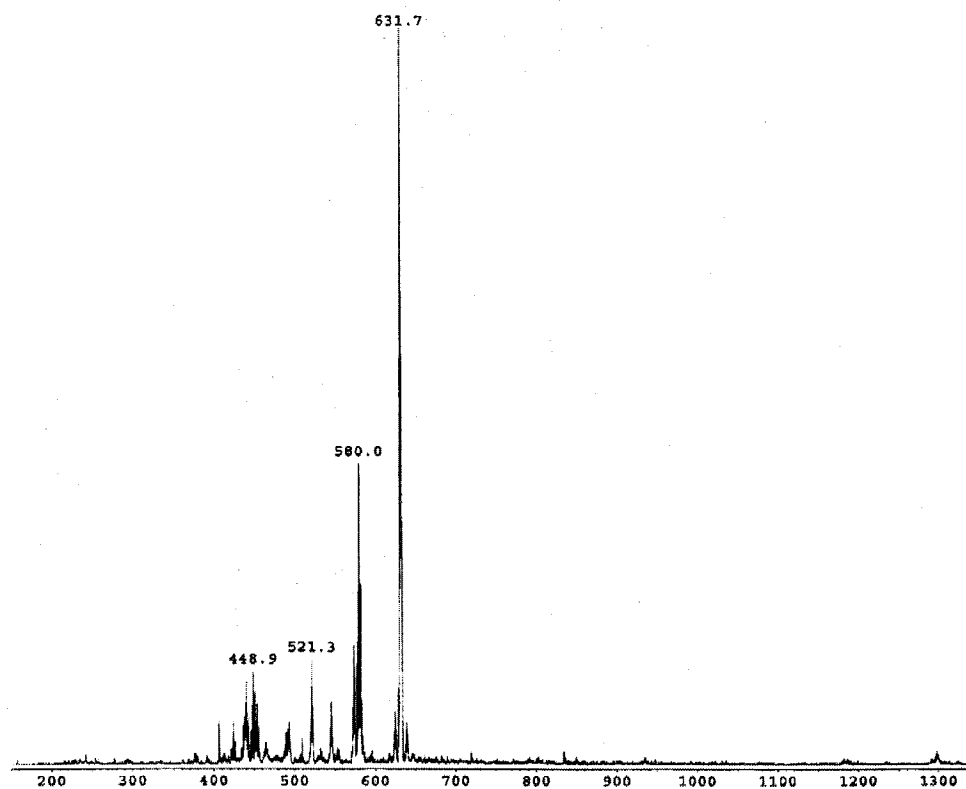


FIGURE 3.28 – $[\text{Ru}(\text{XY})_5\text{-G}]^{2+}$ ESI Mass Spectrum

ESI mass spectrum of $[\text{Ru}(\text{XY})_5\text{-G}]^{2+}$ in acetonitrile under positive ion detection. The main peak at 631.7 m/z is assigned to $[\text{Ru}(\text{XY})_5\text{-G}]^{2+}$ (calc. 631.8).

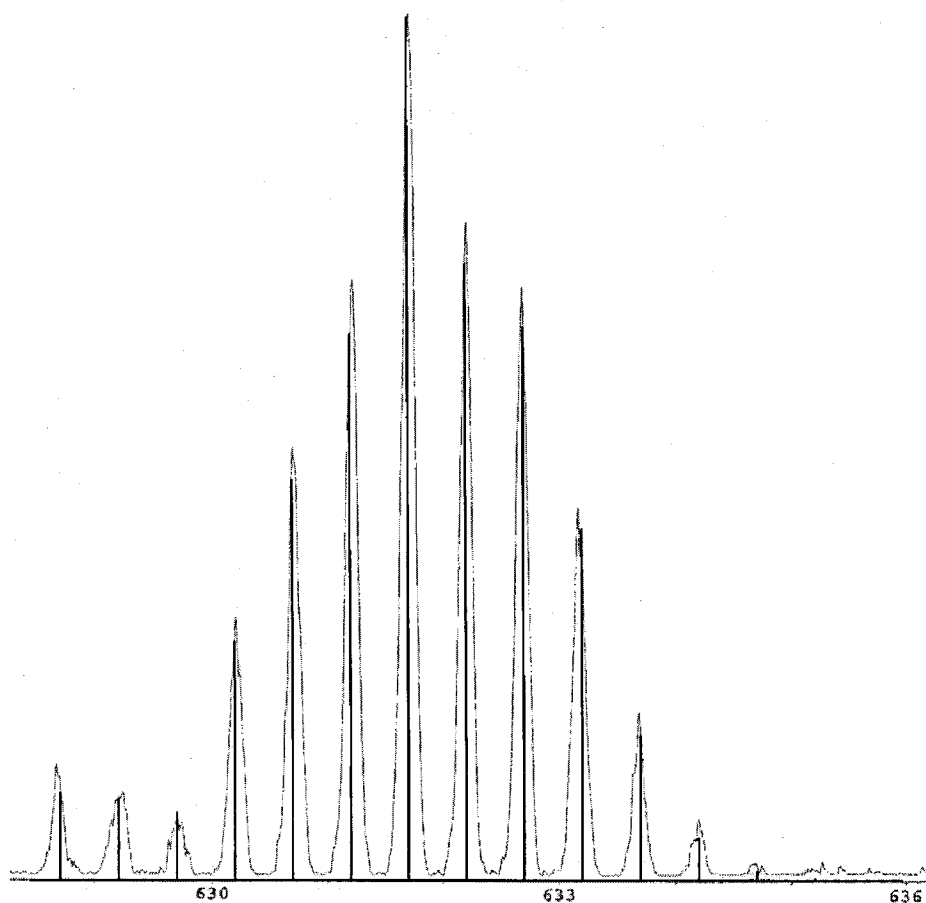


FIGURE 3.29 – Detailed View of $[\text{Ru}-(\text{XY})_5\text{-G}]^{2+}$ ESI Mass Spectrum

Expanded view of 631.7 m/z peak of the $[\text{Ru}-(\text{XY})_5\text{-G}]^{2+}$ ESI spectrum in Figure 3.28. The spectrum is overlaid with the calculated isotope pattern (solid bars).

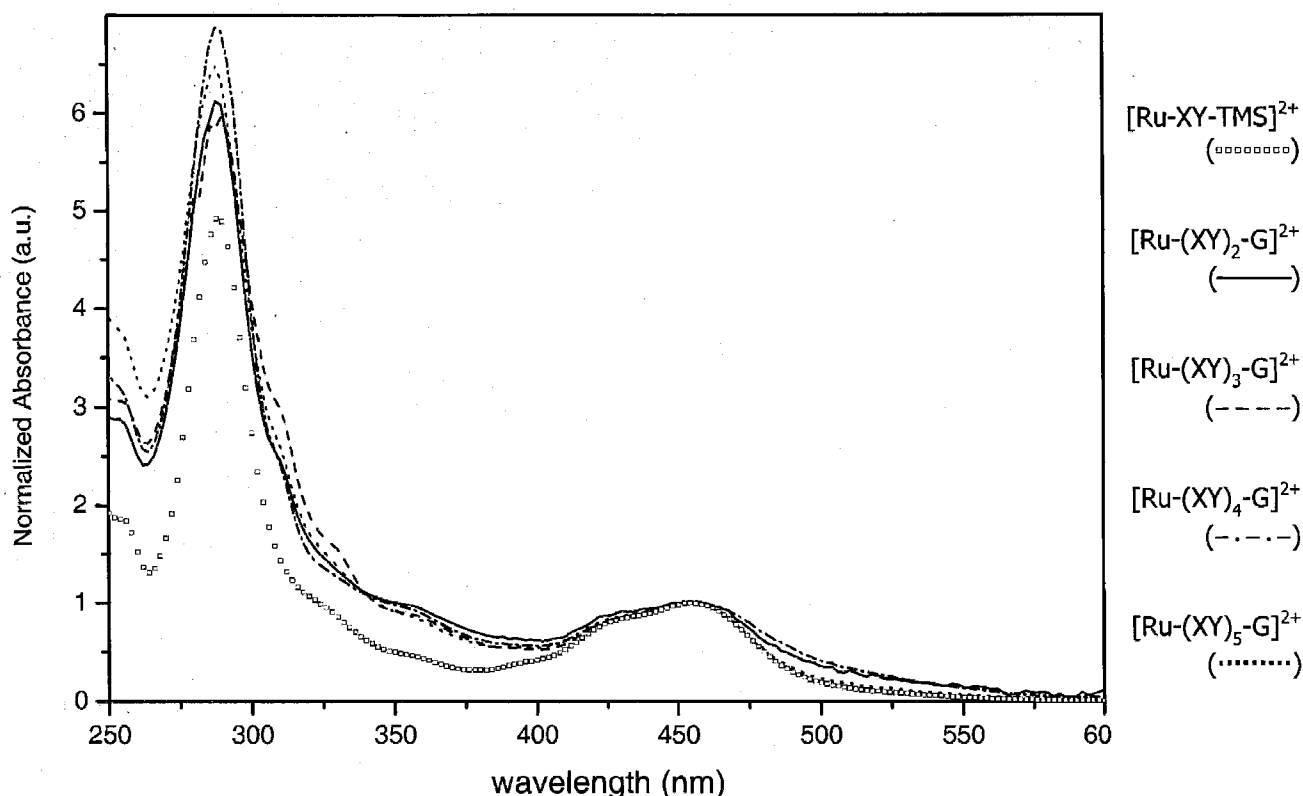


FIGURE 3.30 – $[\text{Ru}-(\text{XY})_n\text{-G}]^{2+}$ UV-Visible Absorption Spectra

The UV-visible absorption spectra of $[\text{Ru}-(\text{XY})_n\text{-G}]^{2+}$ (where $n = 2$ to 5) were taken in acetonitrile, with $[\text{Ru-XY-TMS}]^{2+}$ included for comparison. The traces were normalized at 454 nm. Two major features are the $\pi \rightarrow \pi^*$ transition at 288 nm and the metal to ligand charge transfer (MLCT) band at 450 nm.

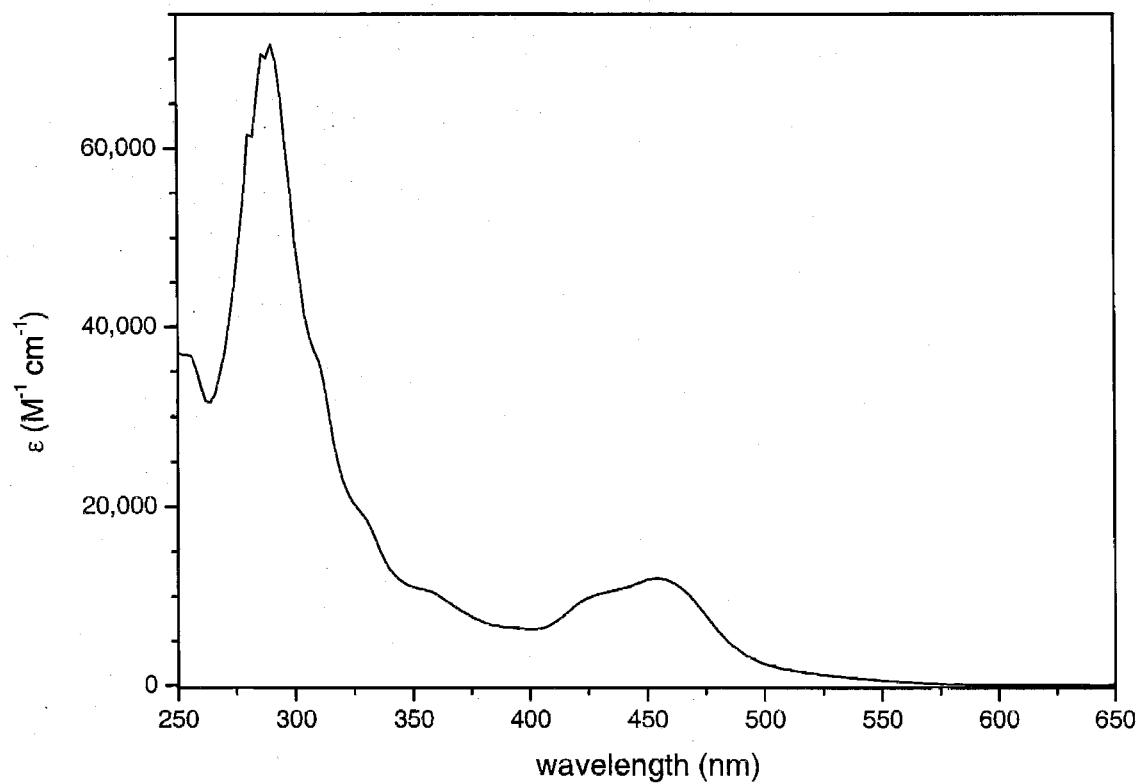


FIGURE 3.31 – $[\text{Ru}-(\text{XY})_3\text{-G}]^{2+}$ UV-Visible Absorption Spectrum

Representative of the series $[\text{Ru}-(\text{XY})_n\text{-G}]^{2+}$, the spectrum of $[\text{Ru}-(\text{XY})_3\text{-G}]^{2+}$ exhibits the expected $\pi \rightarrow \pi^*$ (288 nm) and MLCT (450 nm) bands typical of ruthenium polypyridyl complexes.

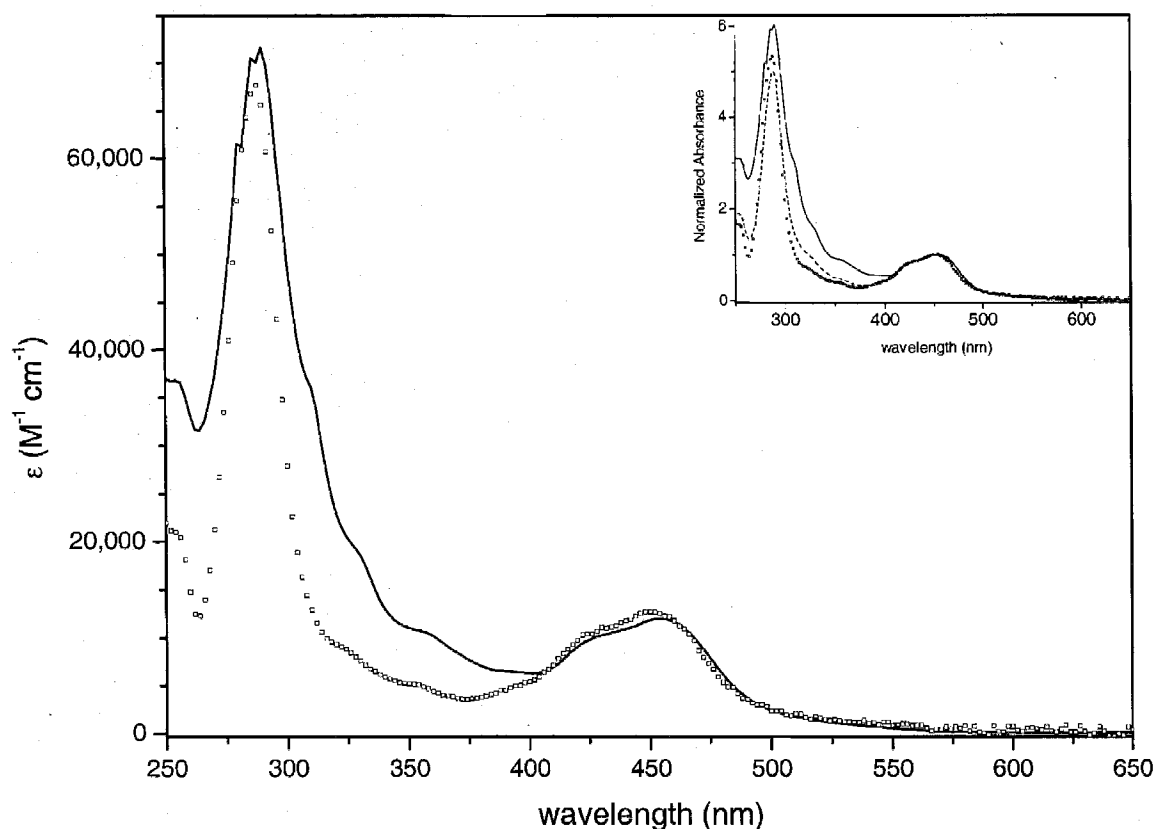


FIGURE 3.32 – UV-visible Absorption Spectra Comparison of Ruthenium Polypyridyl Complexes

The comparison between the absorption spectrum of $[\text{Ru}(\text{XY})_3\text{-G}]^{2+}$ (—) and $[\text{Ru}(\text{bpy})_3]^{2+}$ (•••••) shows no difference in the MLCT bands. There is increased absorption for $[\text{Ru}(\text{XY})_3\text{-G}]^{2+}$ between 290 and 400 nm due to the xylene bridge and aromatic amine donor.

(Inset) Normalized comparison of $[\text{Ru}(\text{XY})_3\text{-G}]^{2+}$ (—), $[\text{Ru}(\text{bpy})_3]^{2+}$ (•••••), and $[\text{Ru-XY-TMS}]^{2+}$ (---). $[\text{Ru-XY-TMS}]^{2+}$ has intermediate absorption in the region of 350 nm due to the presence of a xylene ring, relative to $[\text{Ru}(\text{bpy})_3]^{2+}$, but lack of a full bridge and donor, when compared to $[\text{Ru}(\text{XY})_3\text{-G}]^{2+}$.

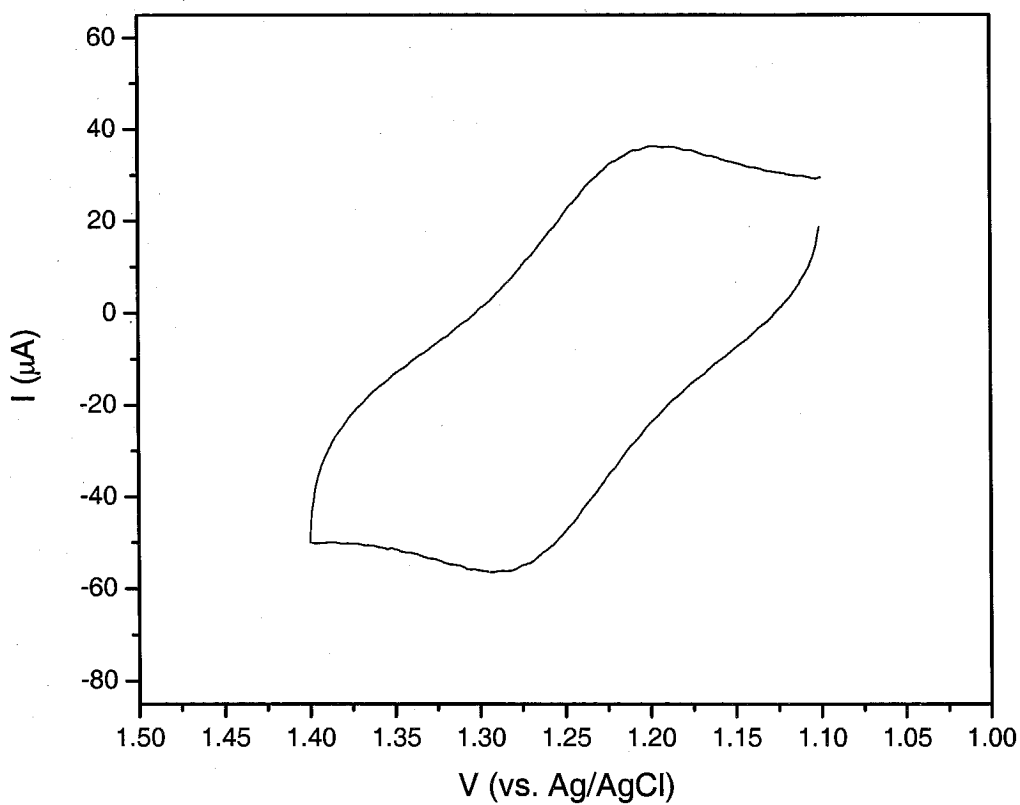


FIGURE 3.33 – $[\text{Ru}(\text{XY})_3\text{-G}]^{2+}$ Cyclic Voltammogram ($\text{Ru}^{\text{II/III}}$)

The cyclic voltammogram of $[\text{Ru}(\text{XY})_3\text{-G}]^{2+}$ shows a reversible redox couple for $\text{Ru}^{\text{II/III}}$. The potential is 1.24 V (vs. Ag/AgCl) with a peak separation of 80 mV.

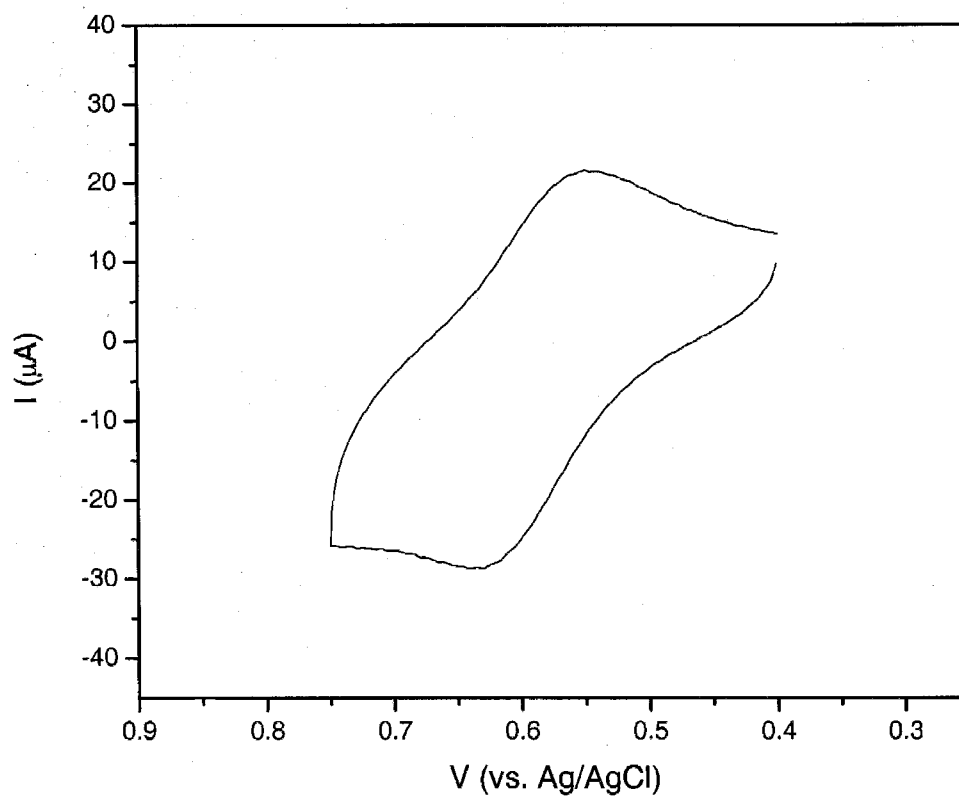


FIGURE 3.34 – $[\text{Ru}-(\text{XY})_3\text{-G}]^{2+}$ Cyclic Voltammogram ($\text{G}^{0/+}$)

The cyclic voltammogram of $[\text{Ru}-(\text{XY})_3\text{-G}]^{2+}$ at lower positive potentials shows a reversible redox couple for $\text{G}^{0/+}$. The potential is 0.591 V (vs. Ag/AgCl) with a peak separation of 90 mV.

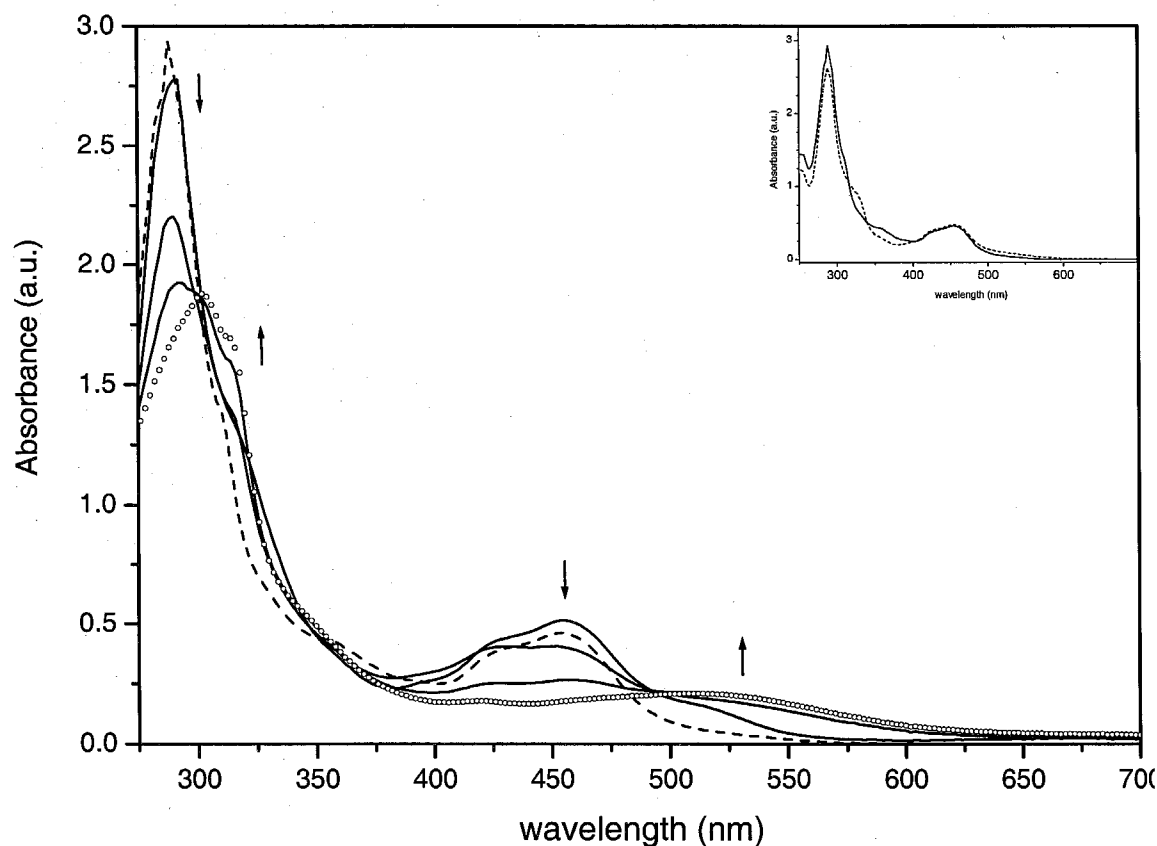


FIGURE 3.35 – $[\text{Ru}(\text{XY})_3\text{-G}]^{2+}$ Spectroelectrochemical Traces

UV-visible absorption spectra were taken of $[\text{Ru}(\text{XY})_3\text{-G}]^{2+}$ during bulk electrolysis to form $[\text{Ru}^{\text{III}}(\text{XY})_3\text{-G}^+]^{4+}$. The initial trace (---) shows loss of intensity in the MLCT band (450 nm) corresponding to $\text{Ru}^{\text{II}} \rightarrow \text{Ru}^{\text{III}}$. Concomitant absorption increase, centered at 520 nm, is due to $\text{G} \rightarrow \text{G}^+$. The final trace (.....) corresponds to $[\text{Ru}^{\text{III}}(\text{XY})_3\text{-G}^+]^{4+}$.

(Inset) The bulk electrolysis to form $[\text{Ru}^{\text{III}}(\text{XY})_3\text{-G}^+]^{4+}$ was reversible judging by the comparison of the absorption spectra before electrolysis (—) and after reduction back to $[\text{Ru}^{\text{II}}(\text{XY})_3\text{-G}]^{2+}$ (----).

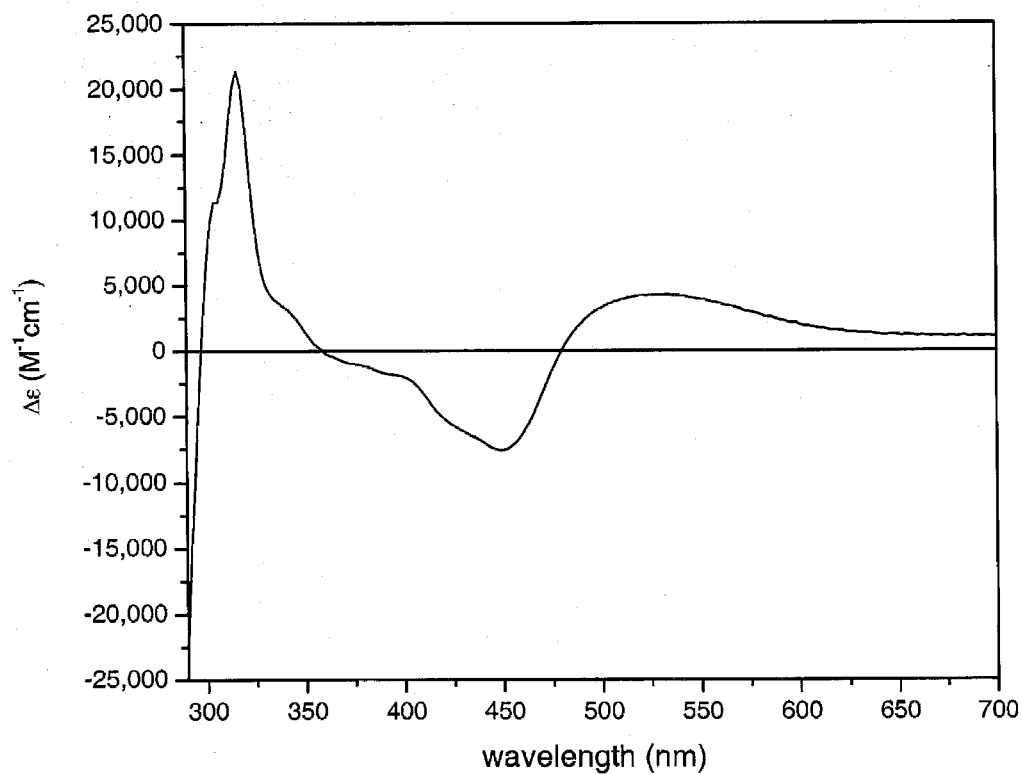


FIGURE 3.36 – $[\text{Ru}^{\text{III}}-(\text{XY})_3-\text{G}^+]^{4+}/[\text{Ru}^{\text{II}}-(\text{XY})_3-\text{G}]^{2+}$
Difference Spectrum

Difference spectrum of $[\text{Ru}^{\text{III}}-(\text{XY})_3-\text{G}^+]^{4+}/[\text{Ru}^{\text{II}}-(\text{XY})_3-\text{G}]^{2+}$ calculated from the spectro-electrochemical data in Figure 3.35.

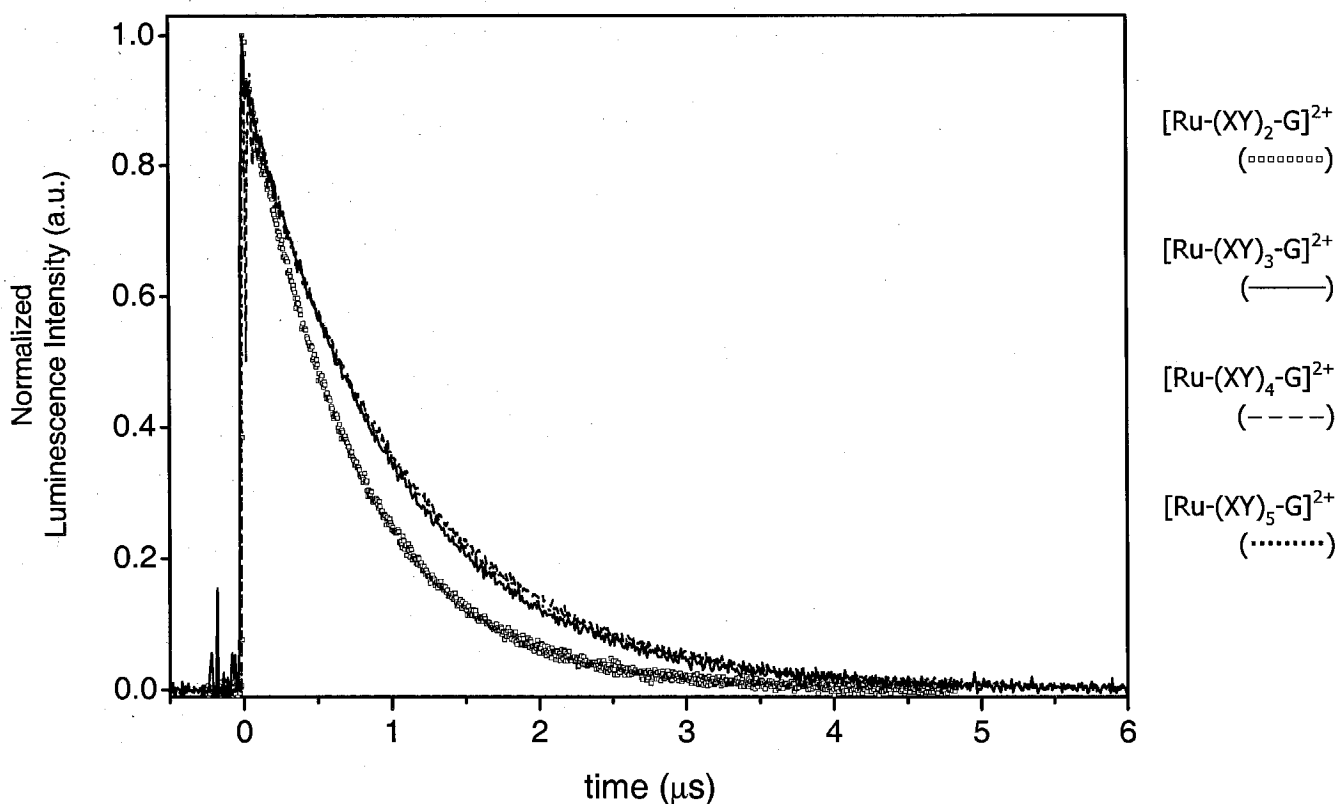


FIGURE 3.37 – $[\text{Ru}-(\text{XY})_n-\text{G}]^{2+}$ Excited State Luminescence Decay

Excited state luminescence decay of $^*[\text{Ru}-(\text{XY})_n-\text{G}]^{2+}$ in deaerated acetonitrile solutions. Lifetimes were determined from fits to monoexponential decay functions. With the exception of $[\text{Ru}-(\text{XY})_2-\text{G}]^{2+}$, the series has essentially the same excited state lifetime, with an average value of $1.05 \mu\text{s}$ (for $n = 3$ to 5). The lifetime of $[\text{Ru}-(\text{XY})_2-\text{G}]^{2+}$ was 760 ns , based on monoexponential fits to the decay traces.

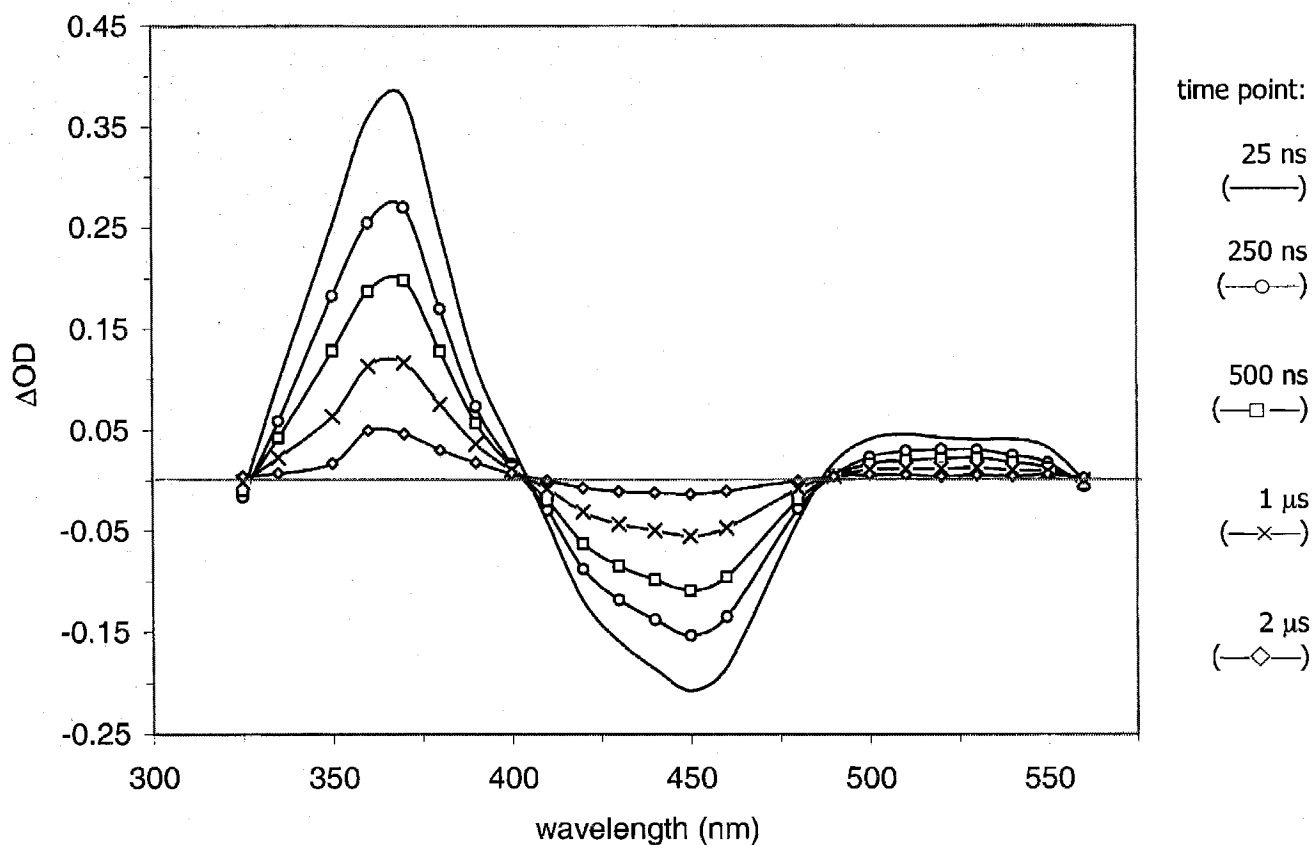


FIGURE 3.38 – $[\text{Ru}-(\text{XY})_2\text{-G}]^{2+}$ Excited State Difference Spectrum

Transient absorption difference spectra of $[\text{Ru}-(\text{XY})_2\text{-G}]^{2+}$ generated from single-wavelength measurements. The spectral changes are consistent with the structure of $^*[\text{Ru}-(\text{XY})_2\text{-G}]^{2+}$. Those features include an increase at 365 nm and a broad increase from 500 nm to 550 nm corresponding to a bipyridine radical anion. The bleach at 450 nm is consistent with loss of MLCT intensity from oxidation of ruthenium ($\text{Ru}^{\text{II}} \rightarrow \text{Ru}^{\text{III}}$).

TABLE 3.1 – Summary of UV-Visible Absorption Spectra

compound	Ru MLCT nm (epsilon M ⁻¹ cm ⁻¹)	$\pi \rightarrow \pi^*$ nm (epsilon M ⁻¹ cm ⁻¹)
[Ru ^{II} (bpy) ₃] ²⁺	450 (12,600)	288 (67,600)
[Ru ^{II} -XY-TMS] ²⁺	450 (17,600)	288 (87,000)
TMS-ethynyl-G	NA	344 (4,300)
[Ru ^{II} -(XY) ₂ -G] ²⁺	450	288
[Ru ^{II} -(XY) ₃ -G] ²⁺	450 (11,850)	288 (70,050)
[Ru ^{II} -(XY) ₄ -G] ²⁺	450	288
[Ru ^{II} -(XY) ₅ -G] ²⁺	450	288

TABLE 3.2 – Summary of Redox Potentials

Compound	$\text{Ru}^{\text{II/III}} \text{E}^{\circ} (\Delta\text{E}_p)$ (V) ^a	$\text{G}^{0/+} \text{E}^{\circ}$ (V) ^a	$\text{XY}^{0/+} \text{E}^{\circ}$ (V) ^a	$\text{bpy}^{0/-} \text{E}^{\circ}$ (V) ^a
$[\text{Ru}(\text{bpy})_3]^{2+}$	1.33 (0.068)	NA	NA	-1.28 (0.063) -1.48 (0.084) -1.73 (0.111)
$[\text{Ru-XY-TMS}]^{2+}$	1.32 (0.073)	NA	2.22 ^b	-1.29 (0.078) -1.48 (0.06) -1.72 (0.078)
TMS-ethynyl-G	NA	0.683 (0.079)	NA	NA
$[\text{Ru-(XY)}_3\text{-G}]^{2+}$	1.24 (0.080)	0.591 (0.090)		

^avs Ag/AgCl^b irreversible

TABLE 3.3 – Summary of Excited State Lifetimes

compound	τ_0 (ns) ^a
[Ru(bpy) ₃] ²⁺	909
[Ru-XY-TMS] ²⁺	909
[Ru-(XY) ₂ -G] ²⁺	760
[Ru-(XY) ₃ -G] ²⁺	1,021
[Ru-(XY) ₄ -G] ²⁺	1,069
[Ru-(XY) ₅ -G] ²⁺	1,055

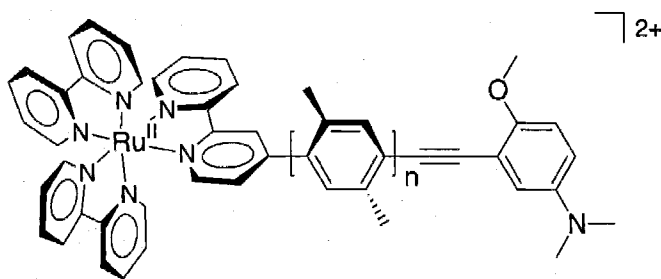
^a Measured in deaerated acetonitrile.

Chapter 4

ELECTRON TRANSFER PROPERTIES of $[\text{Ru}-(\text{XY})_n\text{-G}]^{2+}$

INTRODUCTION

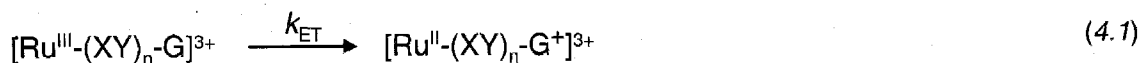
4.1 $[\text{Ru}(\text{XY})_n\text{-G}]^{2+}$ D-B-A Complex



$[\text{Ru}^{\text{II}}(\text{XY})_n\text{-G}]^{2+}$ D-B-A complexes

The donor-bridge-acceptor complexes $[\text{Ru}(\text{XY})_n\text{-G}]^{2+}$ (where $n = 2$ to 5) were designed to measure electron transfer rates mediated by xylene bridges. The rates of

interest stem from a ground state, intramolecular electron transfer reaction (equation 4.1).



Utilizing the flash-quench method¹²⁹ and time-resolved transient absorption spectroscopy, the rate constant k_{ET} was measured. The effect of donor-acceptor separation, r , on k_{ET} was used to evaluate the electron tunneling efficiency of substitute phenylene oligomers.

Studying the electron transfer reactions of $[\text{Ru}-(\text{XY})_n-\text{G}]^{2+}$ and measuring the rates for bridge-mediated electron transfer are important for assessing the role of tunneling energy on long-range electron transfer. Knowing the efficiency of electron transfer through substituted phenyl rings is also important for the rational design of molecular materials with applications in nanotechnology.^{43,46-48,52,54,157} $[\text{Ru}-(\text{XY})_n-\text{G}]^{2+}$ is an excellent donor-bridge-acceptor system and scaffold for future studies on the role of bridge mediated electron transfer.

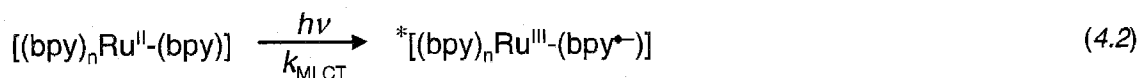
$[\text{Ru}-(\text{XY})_n-\text{G}]^{2+}$ satisfies the experimental design and technical criteria to study the kinetics and mechanism of oligoxylene-mediated electron transfer. The complex consists of a donor, G (3-ethynyl-4-methoxy-N,N-dimethylaniline), and an acceptor, $(\text{bpy})_2\text{Ru}(\text{bpy}')$ [where bpy' is the donor-capped bridging ligand, $\text{bpy}-(\text{XY})_n-\text{G}$], that are redox active within the workable range of the solvent used, acetonitrile. Furthermore, the redox potentials of the donor, 1.6 V (vs. N.H.E.), and the acceptor, 0.9 V (vs. N.H.E.), are such that the electron transfer reaction described in equation 4.1 is favored. The rate of reactant, $[\text{Ru}^{\text{III}}-(\text{XY})_n-\text{G}]^{3+}$, consumption and product, $[\text{Ru}^{\text{II}}-(\text{XY})_n-\text{G}^+]^{3+}$,

formation can be measured spectroscopically. The bridge consists of xylene oligomers, satisfying the requirement of constant bridge state energy. Lastly, $[\text{Ru}-(\text{XY})_n-\text{G}]^{2+}$ is fully amenable to the flash quench and is stable through multiple redox cycles.

In this chapter, the electron transfer rate constant, k_{ET} for $[\text{Ru}-(\text{XY})_n-\text{G}]^{2+}$ (where $n = 3$ to 5) will be provided, along with a discussion of the experimental details of measuring the rate constant for each complex. The electron transfer rates are then compiled to determine the exponential distance decay constant, β . The distance between the donor and acceptor is required to complete the β -analysis; approaches to determining the donor-acceptor separation, r , will also be discussed.

4.2 Relevant Electron Transfer Reactions

There are many electron transfer reactions that can occur with $[\text{Ru}-(\text{XY})_n-\text{G}]^{2+}$ under flash-quench conditions. The formation of a metal-to-ligand charge transfer (MLCT) state (equation 4.2) can be considered an electron transfer reaction between the metal center and ligand.



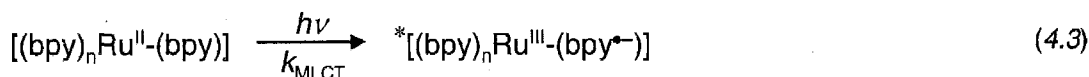
The flash-quench method, outlined in Scheme 4.1, was utilized to measure k_{ET} . The flash quench begins with excitation from 10 ns pulses of 480 nm light to produce the ³MLCT excited state ${}^*[\text{Ru}-(\text{XY})_n-\text{G}]^{2+}$ (equation 4.3). The excited state is then

deactivated by a quencher through a bimolecular electron transfer reaction to produce the flash-quench product, $[\text{Ru}^{\text{III}}-(\text{XY})_n-\text{G}]^{3+}$ (equation 4.4). This is followed by the ground state, intramolecular electron transfer reaction, represented by k_{ET} (equation 4.1). The quenching reaction (equation 4.4) and the quencher recombination reaction (equation 4.5) are the upper and lower time limits for k_{ET} (equation 4.1).

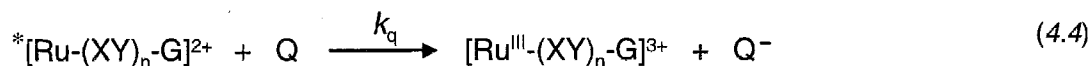
Scheme 4.1

Flash Quench

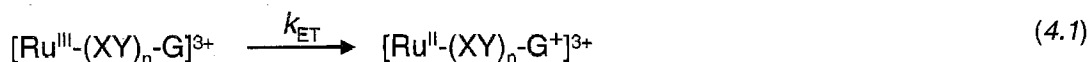
Excited state formation via excitation into the MLCT band,



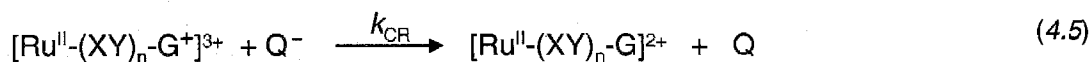
Excited state quenching,



Bridge mediated, intramolecular electron transfer,

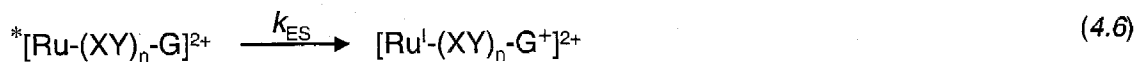


Quencher charge recombination,

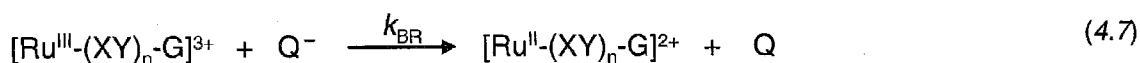


There are several competing electron transfer reactions that interfere with the bridge-mediated reaction (equation 4.1). Isolating these reactions is challenging and

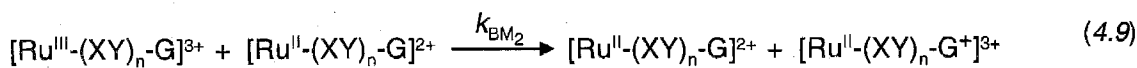
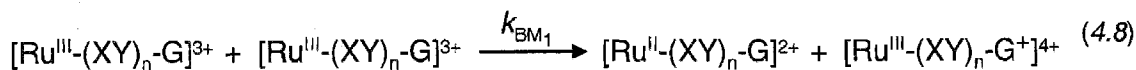
necessary. If the donor and acceptor are electronically well-coupled, which is a possibility when the donor-acceptor span is short, excited state deactivation can occur through intramolecular electron transfer,



Charge recombination between the quenching reaction product, $[\text{Ru}^{\text{III}}-(\text{XY})_n-\text{G}]^{3+}$, and reduced quencher can compete if k_{ET} is slow.



Reactions between $[\text{Ru}^{\text{III}}-(\text{XY})_n-\text{G}]^{3+}$ and itself or $[\text{Ru}^{\text{II}}-(\text{XY})_n-\text{G}]^{2+}$ also complicate the determination of k_{ET} (equation 4.8 and 4.9)



The extent to which the nonproductive reactions (equation 4.6 through 4.9) interfere with measuring k_{ET} depends on the donor-acceptor distance. Reaction 4.6 is only an issue for complexes with relatively short donor-acceptor separations. In practice, reaction 4.7 does not become a significant interference until substantial

concentrations of quencher ($> 100 \text{ mM MV}^{2+}$ with 10 to $30 \text{ }\mu\text{M}$ $[\text{Ru}-(\text{XY})_n\text{-G}]^{2+}$) are present and only if k_{ET} is relatively slow ($< 1 \times 10^5 \text{ s}^{-1}$). Kinetic modeling has shown that reaction 4.8 is a negligible process. Reaction 4.9 does pose a problem for complexes that have a slow k_{ET} . Figure 4.1 displays a schematic of all the electron transfer reactions described in this chapter. The extent that reaction 4.6 through 4.9 interfere with measuring k_{ET} will be discussed in detail for each complex. Figure 4.1 is a schematic of all the relevant electron transfer reactions discussed in this section.

MATERIALS and METHODS

4.3 Materials and Sample Preparation

The electron transfer studies were done in acetonitrile (Burdick & Jackson brand). The solvent was used as received from freshly open bottles. The spectroscopic and kinetic studies were performed in a custom made cell designed for inert or reduced pressure work. The cell consisted of a quartz cuvette (nominal pathlength of 1 cm) attached to a small reservoir with an intervening Teflon stopcock. Samples were prepared in approximately 2 mL of solvent with $[\text{Ru}-(\text{XY})_n\text{-G}]^{2+}$ concentrations between 10 and $30 \text{ }\mu\text{M}$. The samples were deaerated, using a Schlenk line, via four freeze-pump-thaw cycles and back-filled with dry, oxygen-free argon gas.

The cuvette arm was isolated, via the stopcock, from the reservoir arm. Solid quencher was introduced into the reservoir arm and deaerated with four pump/argon back-fill cycles. The stopcock isolating the sample solution was then opened and the two sides mixed without introducing any oxygen and with minimal change in the sample's total volume. $[\text{MV}](\text{PF}_6)_2$,^{142,145,158-162} referred to as MV^{2+} , was the quencher; the dichloride salt is not readily soluble in acetonitrile to levels necessary for flash-quench experiments.

$[\text{MV}](\text{PF}_6)_2$ - (1,1'-dimethyl-4,4'-bipyridinium dihexafluorophosphate; methyl viologen; MV^{2+}) The quencher, MV^{2+} , was prepared from the commercially available dichloride salt (Aldrich – 98%, used as received). A saturated aqueous solution of methyl viologen dichloride was treated with a saturated aqueous solution of ammonium hexafluorophosphate (NH_4PF_6 ; Aldrich, used as received). The solution was cooled at 0 °C for 15 minutes before a white precipitate was collected on a Buchner funnel. The fine white solid was then washed with H_2O and dried in a vacuum oven at 35 °C overnight. $[\text{MV}](\text{PF}_6)_2$ was stored in a Schlenk tube under an argon atmosphere. Care was taken not to expose the solid to air for prolonged periods of time as decomposition to a hard white solid, insoluble in acetonitrile, would result.

4.4 Instrumentation

Steady-state UV-visible absorption measurements were carried out using a diode array spectrometer (HP 8452a). Time-resolved spectroscopy experiments were performed on a custom-made flash photolysis instrument.¹⁶³ Samples were excited with 1 to 4 mJ pulses, 10 ns duration, of 480 nm light. The pulses were generated from an

OPO (Spectra-Physics MOPO) pumped by a frequency-tripled YAG (Spectra-Physics Quanta Ray) laser. Samples were probed with white light produced from an arc lamp ran in either continuous mode or pulsed to generate a order of magnitude more light for approximately 500 μ s.

The optics were arranged such that the excitation and probe beams were co-linear. Probe light was directed to a PMT detector, through a monochromator using 1:1 imaging. The current from the PMT was converted to voltage, amplified (custom made amplifier, bandwidth 200 MHz), and collected by a transient digitizer operating at 200 MHz and capable of 10 bit analog-to-digital conversions. The digitized data, processed by a computer, was referenced to the probe signal in the absence of excitation (blank cycle), to produce a transient absorption trace of ΔOD versus time or a luminescence decay trace (with no referencing) of intensity versus time.

4.5 Experimental Procedures

The experiments were performed at ambient temperature (~ 22 $^{\circ}\text{C}$). All samples were less than a day old, and most were prepared immediately prior to performing experiments. The samples were checked for decomposition and lack of reversibility by taking a UV-visible spectrum (from 190 to 820 nm) before and after laser measurements. Decomposition would be evident from changes in the spectrum, while a build-up of MV^+ would be indicative of a new reversible system. Unless otherwise noted, there was no difference in the absorption spectrum before and after the experiments.

Data taken at some wavelengths had artifacts from stray laser light and/or sample luminescence. When necessary, these artifacts were removed via raw signal subtraction: Immediately after collecting a transient absorption trace and without

changing any of the instrument or experimental settings, a luminescence decay profile was recorded. The decay profile is due to stray laser light and/or sample luminescence, which does not vary substantially from shot to shot or between data collection sets. The raw voltages recorded from the decay profile were then subtracted from the transient absorption voltages. The ratio of the corrected absorption voltages to the blank was then converted to ΔOD 's.

4.6 Data Analysis

Unless otherwise noted, the luminescence decay and transient absorption traces were analyzed by fitting to a series of exponential decay functions of the form,

monoexponential

$$y(t) = c_0 + c_1 e^{-k_1 t} \quad (4.10)$$

biexponential

$$y(t) = c_0 + c_1 e^{-k_1 t} + c_2 e^{-k_2 t} \quad (4.11)$$

three exponentials,

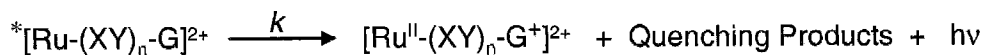
$$y(t) = c_0 + c_1 e^{-k_1 t} + c_2 e^{-k_2 t} + c_3 e^{-k_3 t} \quad (4.12)$$

The fits were optimized using a least-squares regression method. The functions in equations 4.10 through 4.12 are valid so long as the data being fit is composed of one or more first-order processes, represented by rate constant k_n (where $n = 1$ to 3).

When this is not the case, such as when bimolecular charge recombination reactions contribute significantly to the observed signal (i.e., equation 4.5), then other methods for determining rate constants are necessary, and will be discussed where appropriate.

4.7 Excited State Lifetimes and Stern-Volmer Analysis

Excited state lifetimes were determined from time-resolved luminescence decay measurements using the previously described flash photolysis instrument. Fitting the decay profiles to a monoexponential function (equation 4.10) yields a rate constant equal to the sum of radiative, k_r , nonradiative, k_{nr} , and quenching, k_q , rate constants (equation 4.13; decay pathways due to decomposition, self-quenching, or excited-state chemistry are considered negligible and ignored). The term, k_{lum_0} , is given to the luminescence decay rate constant in the absence of quencher, and k_{lum} with quencher (equation 4.14 and 4.15).



$$k = k_r + k_{nr} + k_q \quad (4.13)$$

$$k_{lum_0} = k \quad \text{when } [Q] = 0 \quad (4.14)$$

$$k_{lum} = k \quad \text{when } [Q] > 0 \quad (4.15)$$

Under pseudo-first-order conditions, k_{lum} can be related to k_q via equation 4.16,

$$\text{when } [Q] > 0, \quad k_{lum} = k_q' = k_q[Q]_0 \quad (4.16)$$

The mechanism and kinetics of the quenching process in the flash-quench method are aptly described by Stern-Volmer relationships.¹⁶⁴ A Stern-Volmer analysis, in

which the quenching rate constant k_q is determined, is a useful diagnostic for the flash-quench method. Deviations from Scheme 4.1 will be evident from a Stern-Volmer plot of τ_o/τ versus quencher concentration. τ_o , the excited state lifetime in the absence of quencher, and τ , the lifetime with a known amount of quencher present in solution, is the reciprocal of the luminescence decay constants, k_{lum_o} and k_{lum} , respectively. A Stern-Volmer plot can be fit to a linear function that yields a slope proportional to k_q ,

$$\tau_o/\tau = (k_q/k_{lum_o})[Q] + 1 \quad (4.17)$$

Good agreement of the experimentally determined k_q with published values is another check of the flash-quench method. For MV^{2+} in acetonitrile solution, k_q ranges from $6.8 \times 10^9 \text{ M}^{-1} \text{ s}^{-1}$ to $2.8 \times 10^9 \text{ M}^{-1} \text{ s}^{-1}$.^{142,145,159-162,164}

4.8 Flash Quench and Instrument Limitations

The ability to measure fast electron transfer rate constants ($> 1 \times 10^8 \text{ s}^{-1}$) is hampered by the instrument response of the flash photolysis setup, previously described in the experimental section, and the inherent limits of the flash-quench method. The electronics of the instrument have a bandwidth of 200 MHz, giving a maximum time response of 5 ns. YAG-OPO laser pulses have a full width half maximum (FWHM) of approximately 10 ns, placing an upper limit on the reaction time constant that can be measured. An instrument with a faster response could be used (such as a picosecond

laser coupled to streak camera detection) but does not solve the speed limitations associated with the flash-quench method.

The flash quench is limited, on the fast timescale, to the quenching reaction (equation 4.4). Excited-state quenching is a bimolecular process that is limited by diffusion, quencher concentration, and k_q . The choice of quencher depends on several factors, including cage escape yields, spectral overlap of the oxidized and reduced states with other species in solution, solubility, and stability. Several quenchers were tested, including methyl viologen, ruthenium^{III} hexaamine, tetracyanomethane, 1,4-benzoquinone, tetracyanquinodimethane, tetrachlorobenzoquinone, duroquinone, and bianthrone. Methyl viologen (MV^{2+}) proved to be the only quencher that met all of the stated criteria. Spectroelectrochemical traces and difference spectra for $MV^{2+} \rightarrow MV^+$ are provided in appendix D.

While the solubility of $[MV](PF_6)_2$ in acetonitrile is relatively good, concentrations above 100 mM are problematic for measuring k_{ET} . An observed k_{lum} of $1 \times 10^8 \text{ s}^{-1}$ is possible (assuming $k_q = 1 \times 10^9 \text{ M}^{-1} \text{ s}^{-1}$) but is possibly too slow to measure k_{ET} for the shortest complex ($n=2$). This limitation notwithstanding, higher concentrations of MV^{2+} would likely cause spectroscopic interference due to the rapid back reactions (equation 4.5 and 4.7; increasing the rate of the quenching reaction also increases the rate of the back reactions). Transient absorption traces that exhibit normal flash-quench behavior ($k_{ET} < k_q'$) fit well to biexponential functions. Samples where $k_{ET} \geq k_q'$ have transient absorption traces that can be fit by a single exponential function, where $k_{obs} = k_q'$ rather than k_{ET} . In these cases, it is important to examine the dependence of k_{obs} , the observed rate constant, on the quencher concentration.

Measuring slow k_{ET} rates ($< 1 \times 10^4 \text{ s}^{-1}$) also proves problematic due to interference from bimolecular reactions between the flash-quench product, $[\text{Ru}^{\text{III}}-(\text{XY})_n\text{-G}]^{3+}$, and $[\text{Ru}^{\text{II}}-(\text{XY})_n\text{-G}]^{2+}$ (k_{BM2} , equation 4.9). The typical concentration range for this study is 10 to 30 μM in $[\text{Ru}-(\text{XY})_n\text{-G}]^{2+}$; intermolecular reactions can compete with k_{ET} for complexes with large donor-acceptor separation. In these cases, to determine k_{ET} , the dependence of k_{obs} on $[\text{Ru}-(\text{XY})_n\text{-G}]^{2+}$ concentration must be measured.

Whether the limitations of the flash-quench method or the instrumentation are an issue for measuring k_{ET} depends on a number of factors, including the distance spanning the donor and acceptor, the electron-transfer distance decay constant (β), the reorganizational energy (λ), and the free-energy driving force (ΔG). Careful analysis of the luminescence decay and transient absorption traces can reveal whether k_{obs} is related to k_{ET} or some other competing reaction.

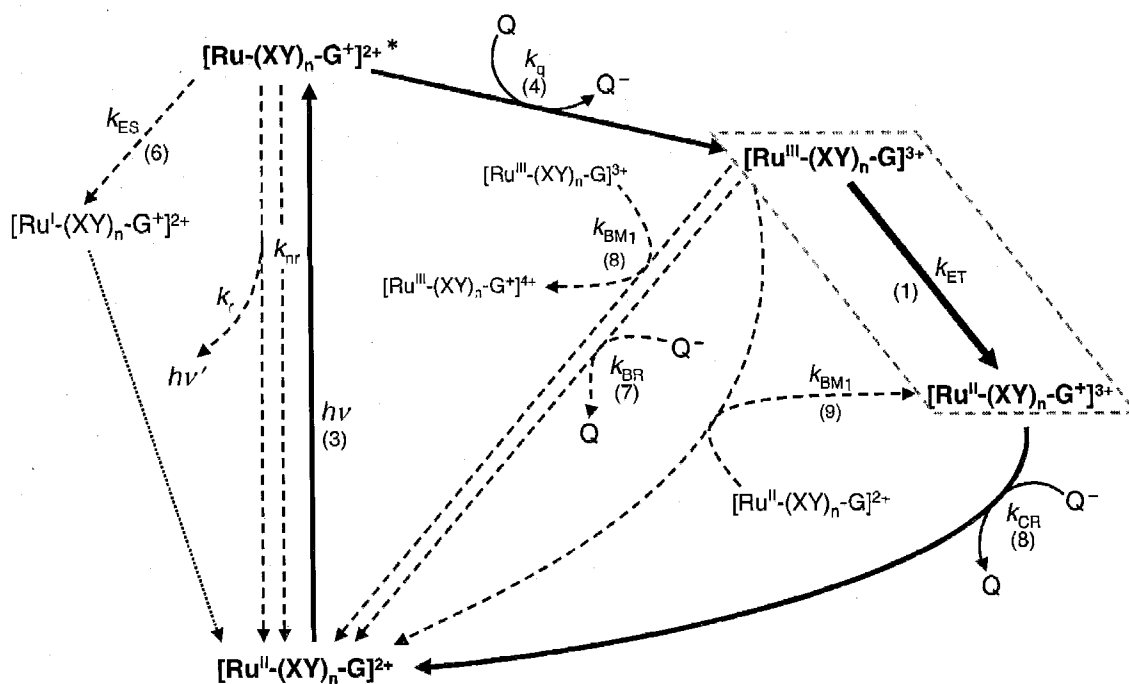


FIGURE 4.1 – Electron Transfer Reaction Schematic

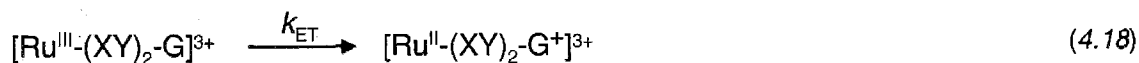
Schematic of the electron transfer reactions and related process involved in determining k_{ET} for $[Ru-(XY)_n-G]^{2+}$ using the flash-quench method. The reaction sequence starts with excitation of the resting state, $[Ru^{II}-(XY)_n-G]^{2+}$ (3), followed by quenching (4), subsequent ground state intramolecular electron transfer (1), and charge recombination (8) to restore the system to the starting state.

Major flash-quench reactions (—), nonproductive competing reactions (---), reactions that occur but not mentioned in text (.....); numbers in parentheses refer to equations in the text.

RESULTS

4.9 Estimating k_{ET} for $[Ru-(XY)_2-G]^{2+}$

There are several methods for estimating the ground state, intramolecular electron transfer rate constant, k_{ET} , for $[Ru-(XY)_2-G]^{2+}$ ($G \rightarrow Ru^{III}$; equation 4.18).



One method relies on equation 4.19 to estimate k_{ET} by attenuating k_0 , the close contact electron transfer rate constant, by an exponential term that involves β , the distance decay constant, and the distance between the donor and acceptor, r ,

$$k_{ET} = k_0 e^{-\beta r} \quad (4.19)$$

Reasonable estimates for k_0 (10^{14} to 10^{15} s^{-1}) and the typical β -value for phenylene bridges of 0.4 \AA^{-1} ¹⁶⁵ can be used for equation 4.19. Donor-acceptor distances were estimated using molecular modeling calculations. The edge of the donor was assumed to be the three-carbon of the aromatic ring. If the acceptor is localized on the metal, calculations yield a range for r of 13 to 15 \AA . This gives an estimated k_{ET} of $2 \times 10^9 \text{ s}^{-1}$; this rate constant is fast enough to compete with the quenching process, necessitating a quencher concentration dependence study on k_{obs} .

4.10 Electron Transfer of $[\text{Ru}(\text{XY})_2\text{-G}]^{2+}$ (Low Quencher Concentrations)

The flash-quench method was utilized in an attempt to measure k_{ET} for $[\text{Ru}(\text{XY})_2\text{-G}]^{2+}$ (Scheme 4.1). Since the estimated k_{ET} was on the same order as the upper experimental limit, it was important to measure the kinetics at low and high quencher concentrations. 5 mM of MV^{2+} quencher produced an observed luminescence decay rate constant, k_{lum} , of $4 \times 10^6 \text{ s}^{-1}$ (200 ns), representing a factor of 4 shorter lifetime over τ_0 . On the high end, samples with 80 mM of MV^{2+} yielded a k_{lum} of $8 \times 10^7 \text{ s}^{-1}$ (12.5 ns), or a factor of 64 shorter lifetime than an unquenched sample.

Stern-Volmer analysis of $[\text{Ru}(\text{XY})_2\text{-G}]^{2+}$ quenching with MV^{2+} (Figure 4.3) yielded a k_q of $1.1 \times 10^9 \text{ M}^{-1} \text{ s}^{-1}$; the good agreement with the literature value indicates no unusual interactions between the quencher and ruthenium excited state. Furthermore, the lack of irregularities in the linearity or the slope of the Stern-Volmer plot further suggests the flash quench is proceeding as outlined in Scheme 4.1.

The electron transfer kinetics were measured using single-wavelength time-resolved spectroscopy. Figure 4.4 shows the normalized transient absorption traces at 460 nm and 500 nm for $[\text{Ru}-(\text{XY})_2-\text{G}]^{2+}$ with 5 mM MV^{2+} . From spectroelectrochemical characterizations, we know the trace at 460 nm corresponds to changes in the MLCT region, and is diagnostic of ruthenium oxidation state changes. The trace at 500 nm is a spectroscopic handle for the formation of product, $[\text{Ru}^{\text{II}}-(\text{XY})_n-\text{G}^+]^{3+}$.

The large bleach at time zero observed in the 460 nm trace corresponds to formation of the $^*[\text{Ru}-(\text{XY})_2-\text{G}]^{2+}$. The bleach is due to a loss of absorbance in the MLCT band, as indicated by the model complexes $[\text{Ru}-\text{XY}-\text{TMS}]^{2+}$ and $[\text{Ru}(\text{bpy})_3]^{2+}$. The formation of the excited-state is also evident from the trace at 500 nm, where an absorption increase is observed. This is consistent with the transient traces and difference spectrum of $[\text{Ru}-(\text{XY})_2-\text{G}]^{2+}$ in the absence of quencher.

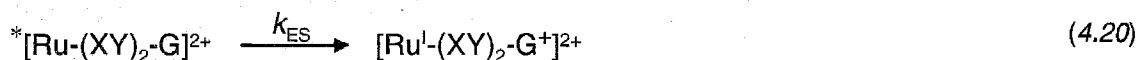
The observed signal at 460 nm can be fit with a signal exponential function (equation 4.10) with a rate constant of $4.1 \pm 0.3 \times 10^6 \text{ s}^{-1}$ (k_{obs} , 263 ns). A biexponential function would be required to fit the transient absorption traces if $k_{\text{ET}} > k_{\text{q}}'$. One rate constant would match the luminescence decay constant, k_{lum} , corresponding to the quenching process; the second rate constant would represent k_{ET} from equation 4.18. The transient traces only require a single exponential to obtain a good fit. Furthermore, values of k_{obs} are within experimental error of k_{lum} ($4 \times 10^6 \text{ s}^{-1}$).

The observations at 460 nm are mirrored in traces at 500 nm. The initial rise is due to the formation of $^*[\text{Ru}-(\text{XY})_2-\text{G}]^{2+}$. The second, slower absorption increase is due to the formation of $[\text{Ru}^{\text{II}}-(\text{XY})_2-\text{G}^+]^{3+}$, with a small fraction of the signal due to MV^+ . Just as the case at 460 nm, the trace fits well using only a single exponential function with a rate constant of $5 \pm 0.3 \times 10^6 \text{ s}^{-1}$. This rate constant is not significantly higher

than the luminescence decay constant, k_{lum} , to attribute it to anything but the quenching process. Therefore, the conclusion for $[\text{Ru}(\text{XY})_2\text{-G}]^{2+}$ in the presence of 5 mM MV^{2+} , is the intramolecular electron transfer reaction (equation 4.18) proceeds at a faster rate than the quenching process and, therefore, k_{obs} is due to quenching only.

Figure 4.5 shows the transient difference spectra of $[\text{Ru}(\text{XY})_2\text{-G}]^{2+}$ with 5 mM MV^{2+} , produced by compiling single-wavelength data between 330 and 570 nm. The formation of $^*[\text{Ru}(\text{XY})_2\text{-G}]^{2+}$, subsequent quenching, and intramolecular electron transfer are clearly observable in the transient difference spectra. Initially (20 ns after excitation), absorption increases at 360 and 510 nm indicate the formation of $^*[\text{Ru}(\text{XY})_2\text{-G}]^{2+}$. The difference spectra evolve to a combination of reduced quencher, MV^+ , and $[\text{Ru}^{\text{II}}(\text{XY})_2\text{-G}^+]^{3+}$. The relatively sharp band at 390 nm, the absorption red of 500 nm, and some residual absorption in the MLCT region are all characteristic of MV^+ . The two isosbestic points at 380 and 510 nm indicate the transition from excited state to ground state products is a two-state process. The transient spectra also indicate that the flash-quench intermediate, $[\text{Ru}^{\text{III}}(\text{XY})_2\text{-G}]^{3+}$, does not build up to appreciable levels.

The relative short donor-acceptor distance in $[\text{Ru}(\text{XY})_2\text{-G}]^{2+}$ allows for the possibility of an excited-state short circuit reaction. In this process, the excited-state is deactivated via an intramolecular electron transfer (k_{es}) that could possibly contribute to the observed difference spectra (equation 4.20).



As previously discussed, the lifetime of $^*[\text{Ru}(\text{XY})_2\text{-G}]^{2+}$ in the absence of quencher (760 ns) is shorter than the model complex $[\text{Ru-XY-TMS}]^{2+}$ (909 ns). While excited-

state intramolecular electron transfer could account for the shortened lifetime of $^*[Ru-(XY)_2-G]^{2+}$, the calculated rate constant, k_{es} , would only be on the order of $1 \times 10^5 \text{ s}^{-1}$. Therefore, the excited-state electron transfer reaction is too slow to compete with quenching. The Stern-Volmer analysis also indicates that quenching is the major excited state decay pathway. The difference spectrum does not show the characteristically strong absorbance for Ru^I , further excluding equation 4.20.

Figure 4.6 further demonstrates that at early times ($< 100 \text{ ns}$) the difference spectrum agrees well with the excited-state difference spectrum of $^*[Ru-(XY)_2-G]^{2+}$. Figure 4.7 is an overlay of the MV^+ spectrum, produced from spectroelectrochemistry experiments, and shows increased absorption in the region of 500 nm at long times ($> 1 \text{ }\mu\text{s}$) indicative of G^+ formation. All of these factors indicate that reaction 4.20 is not a major contributor to the observed transient traces.

4.11 Electron Transfer of $[Ru-(XY)_2-G]^{2+}$ (High Quencher Concentrations)

The most straightforward approach to isolate and measure k_{ET} is to increase the rate of the quenching process. The quenching reaction is bimolecular and with increased quencher concentrations, the apparent rate constant, k_q' , will exceed the instrument limit of $1 \times 10^8 \text{ s}^{-1}$. The flash-quench experiments were repeated with 10, 40, and 80 mM of MV^{2+} ; greater concentrations would cause too much interference from bimolecular recombination reactions (equation 4.5 and 4.7).

Figures 4.8 and 4.9 show the single-wavelength transient absorption traces at 460 and 500 nm for $[Ru-(XY)_2-G]^{2+}$ in the presence of 0, 5, 10, and 80 mM of MV^{2+} . The trace for 40 mM MV^{2+} was omitted for clarity and essentially matches the 80 mM trace. Table 4.1 summarizes the observed rate constants, k_{obs} , as a function of

quencher concentration. In the absence of quencher, the transient absorption traces at 460 and 500 nm both fit to single exponential functions that match, within experimental error, the luminescence decay rate, k_{lum} , (1.32×10^6 , 1.34×10^6 , $1.28 \times 10^6 \text{ s}^{-1}$ respectively). With 80 mM of MV^{2+} , the trace at 460 nm shows a very rapid rise to a positive ΔOD . This is assigned to the rapid quenching (equation 4.4) of the excited state followed by intramolecular electron transfer to form $[\text{Ru}^{\text{II}}-(\text{XY})_2-\text{G}^+]^{3+}$ (equation 4.18). The sub-sequent decay corresponds to the back reaction between $[\text{Ru}-(\text{XY})_2-\text{G}]^{2+}$ and MV^+ (equation 4.5). Both quenching and k_{ET} occur faster than the 10 ns instrument response and are convoluted into the fast rise.

The same situation is observed at 500 nm, where $[\text{Ru}^{\text{II}}-(\text{XY})_2-\text{G}^+]^{3+}$ and, to a lesser extent, MV^+ absorbs. The presence of the excited state followed by quenching (equation 4.4) and ground state electron transfer (equation 4.18) to form $[\text{Ru}^{\text{II}}-(\text{XY})_2-\text{G}^+]^{3+}$ is evident with 5 mM MV^{2+} . Quencher concentrations above 10 mM display only the back reaction between $[\text{Ru}^{\text{II}}-(\text{XY})_2-\text{G}^+]^{2+}$ and MV^+ (equation 4.5). The initial formation of the excited-state (equation 4.3), quenching (equation 4.4), and ground-state intramolecular electron transfer (equation 4.18) are all convoluted in the initial rise. Whether the kinetics for the process in equation 4.18 are faster than the limit of the flash-quench method is unclear, but the traces in Figures 4.8 and 4.9 clearly show that k_{ET} is faster than the instrument response of 10 ns. Therefore, a lower limit of $1 \times 10^8 \text{ s}^{-1}$ can be placed on k_{ET} for $[\text{Ru}-(\text{XY})_2-\text{G}]^{2+}$.

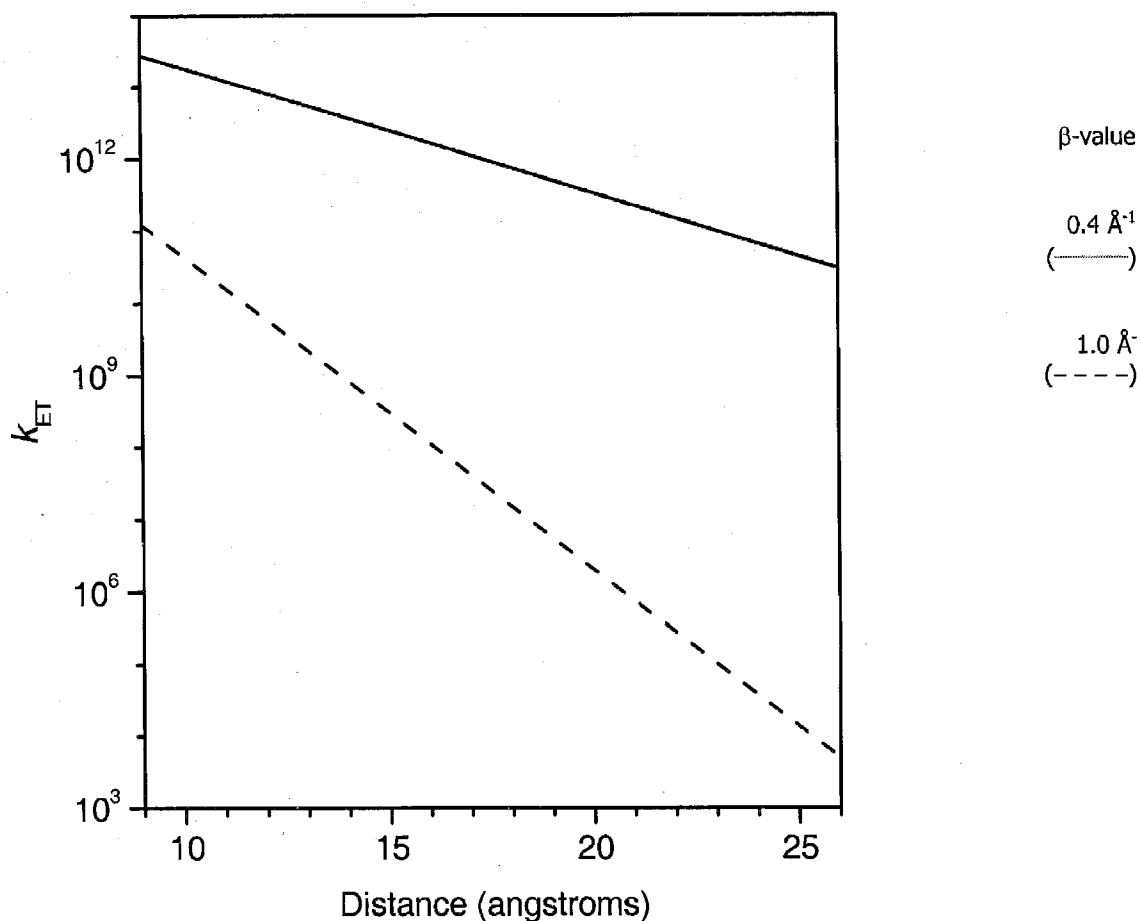


FIGURE 4.2 – Estimated $[\text{Ru}-(\text{XY})_2\text{-G}]^{2+}$ Electron Transfer Rates

Calculated β -plot for $[\text{Ru}-(\text{XY})_2\text{-G}]^{2+}$ based on an estimation of k_0 ($1 \times 10^{15} \text{ s}^{-1}$). The distance axis displays the estimated range for donor-acceptor separation. The two sets of data illustrate the effect of β on the rates of electron transfer.

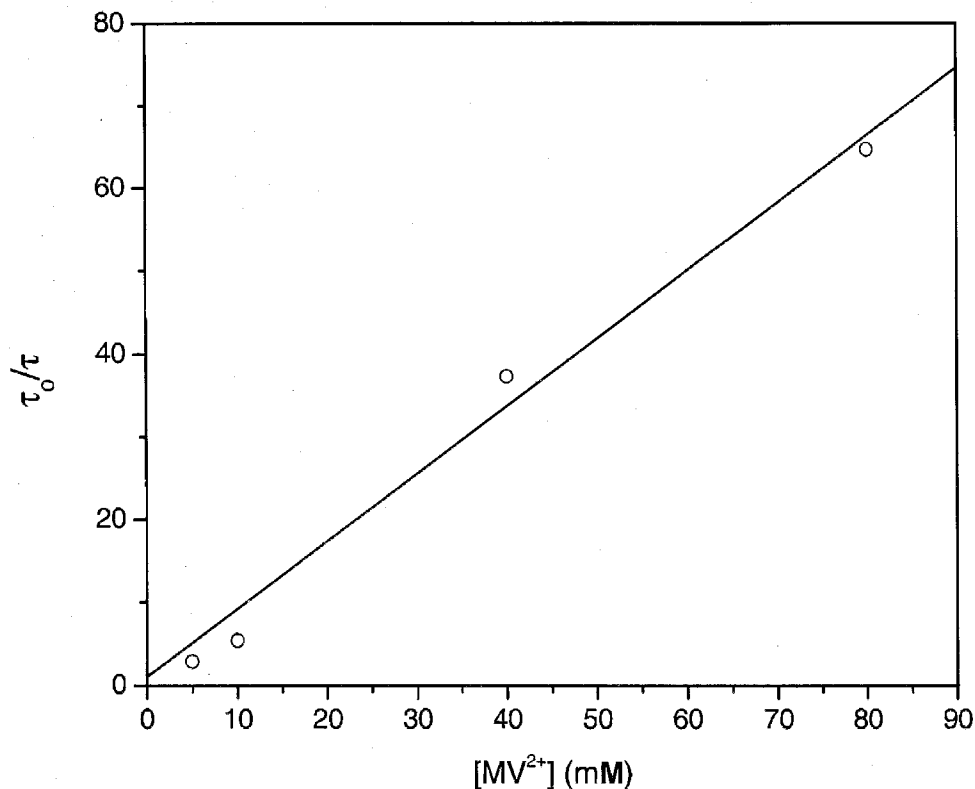
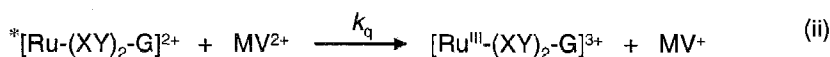
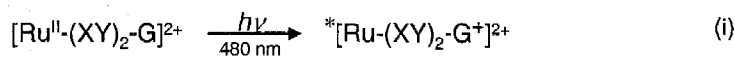


FIGURE 4.3 – Stern-Volmer Analysis of $[\text{Ru}(\text{XY})_2\text{-G}]^{2+}$

Stern-Volmer plot of $[\text{Ru}(\text{XY})_2\text{-G}]^{2+}$ quenching by MV^{2+} . τ_0/τ was determined from fitting luminescence decay traces to monoexponential functions. τ_0 , 1.32 μs , is the lifetime of $[\text{Ru}(\text{XY})_2\text{-G}]^{2+}$ in absence of quencher, while τ is the lifetime with quencher. Linear least squares regression, forcing an intercept of 1, gives a k_q of $1.1 \times 10^9 \text{ M}^{-1} \text{ s}^{-1}$ with a regression coefficient, R^2 , of 0.99.



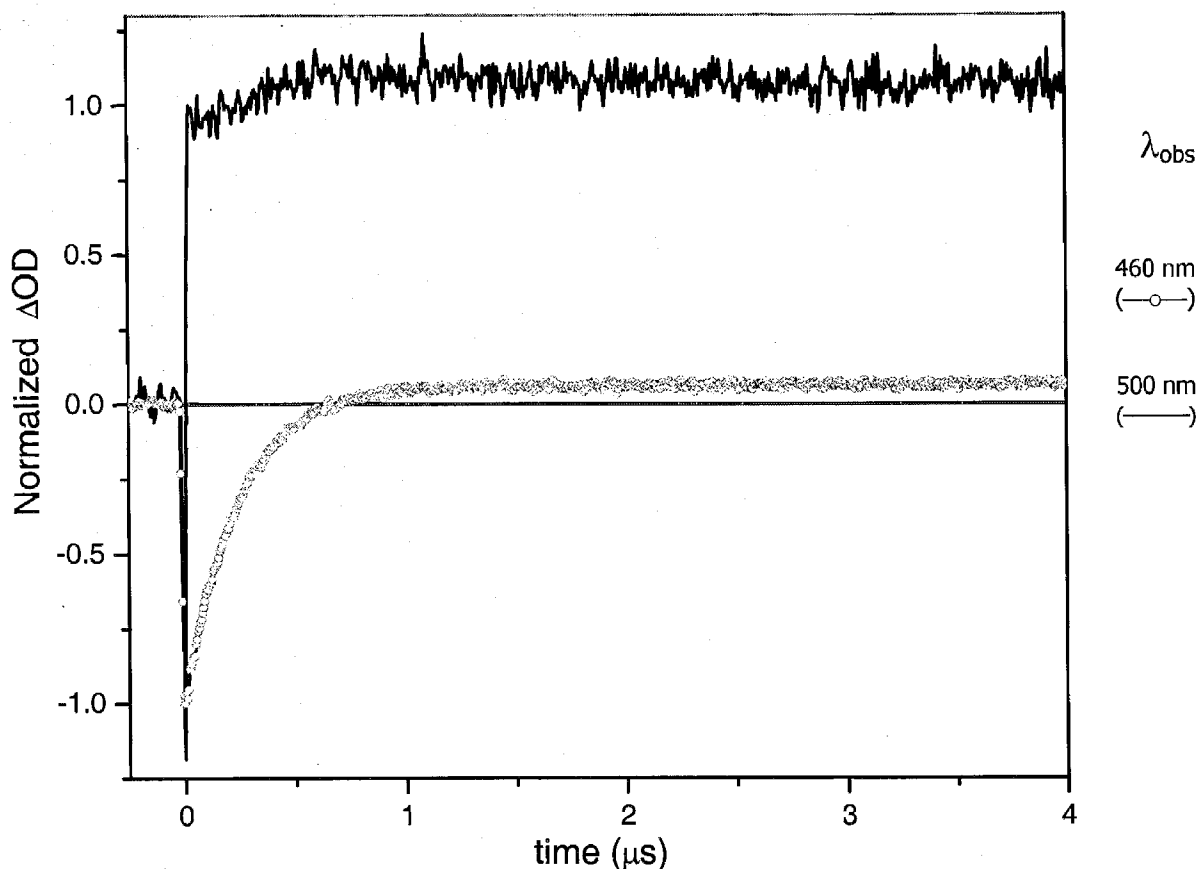
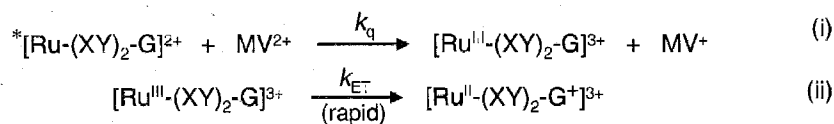


FIGURE 4.4 – Transient Absorption of $[\text{Ru}(\text{XY})_2\text{-G}]^{2+}$ with 5 mM MV^{2+}

Transient absorption traces of $[\text{Ru}(\text{XY})_2\text{-G}]^{2+}$ (with 5 mM MV^{2+}) at 460 nm. The initial, fast decrease (460 nm) or rise (500 nm) was normalized to 1. The ΔOD at 460 and 500 nm is due to the quenching reaction (i) followed by rapid intramolecular electron transfer (ii, k_{ET} , $[\text{Ru}^{\text{III}}(\text{XY})_2\text{-G}]^{3+} \rightarrow [\text{Ru}^{\text{II}}(\text{XY})_2\text{-G}^+]^{3+}$). k_{obs} , from exponential fits, are $4.1 \pm 0.3 \times 10^6 \text{ s}^{-1}$ at 460 nm and $5 \pm 0.3 \times 10^6 \text{ s}^{-1}$.



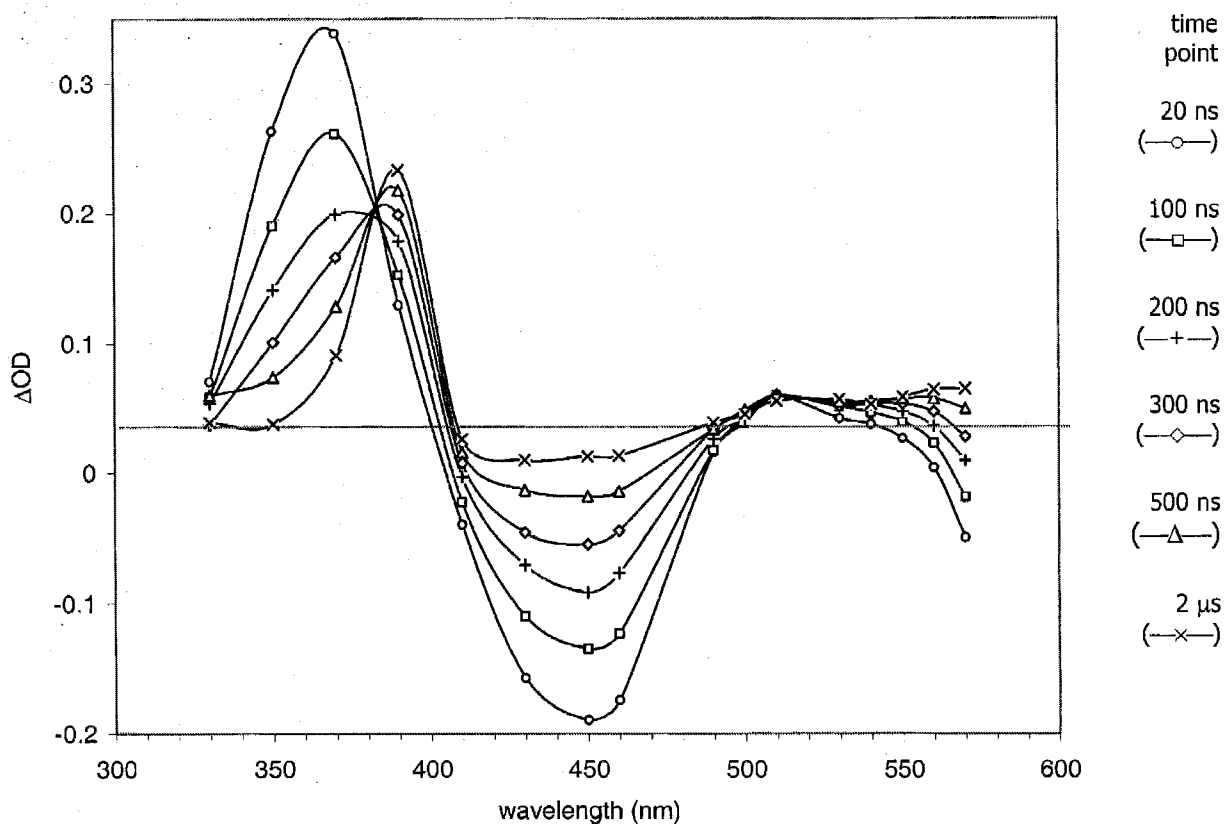
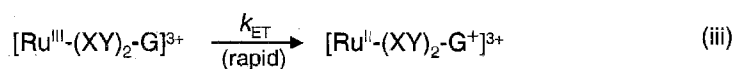
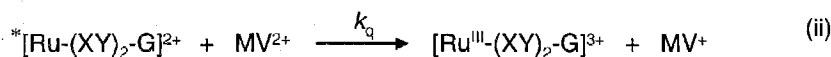
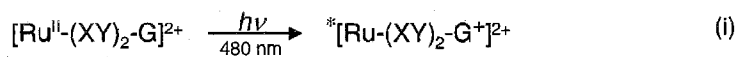


FIGURE 4.5 – Transient Difference Spectra of $[\text{Ru}(\text{XY})_2\text{-G}]^{2+}$ with 5 mM MV^{2+}

Transient difference spectra of $[\text{Ru}(\text{XY})_2\text{-G}]^{2+}$ in the presence of 5 mM MV^{2+} . Time zero is set to sample excitation. The initial species present is assigned to $^*[\text{Ru}(\text{XY})_2\text{-G}]^{2+}$ with characteristic absorption features at 360 nm and 510 nm (equation i). The spectra then evolve to the formation of $[\text{Ru}^{\text{II}}(\text{XY})_2\text{-G}^+]^{3+}$ and MV^+ (equation ii and iii).



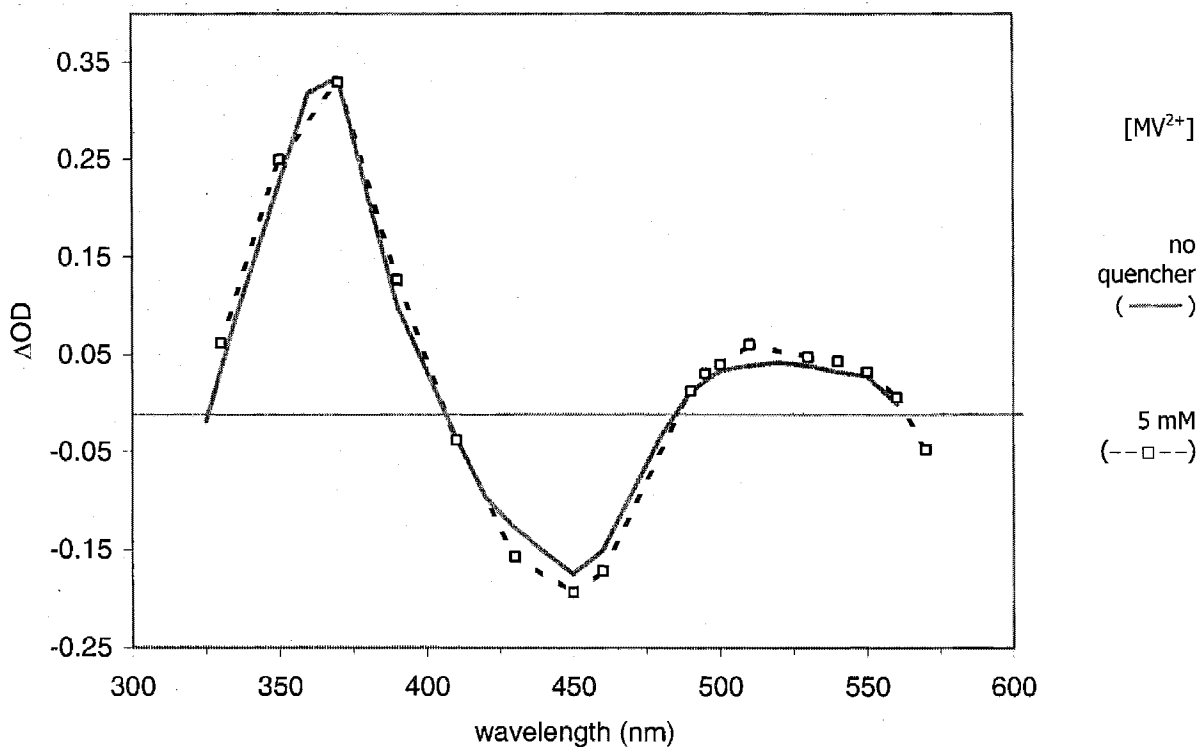


FIGURE 4.6 – Comparison of $[\text{Ru}-(\text{XY})_2\text{-G}]^{2+}$ Transient Difference Spectra

Comparison of $^*[\text{Ru}-(\text{XY})_2\text{-G}]^{2+}$ difference spectrum in the absence of quencher to the difference spectrum of $[\text{Ru}-(\text{XY})_2\text{-G}]^{2+}$ in the presence of 5 mM MV^{2+} . The traces are taken 20 ns after the laser pulse. $^*[\text{Ru}-(\text{XY})_2\text{-G}]^{2+}$ was normalized at 370 nm to the ΔOD of the trace with quencher. The band at 520 nm corresponds to excited state formation.

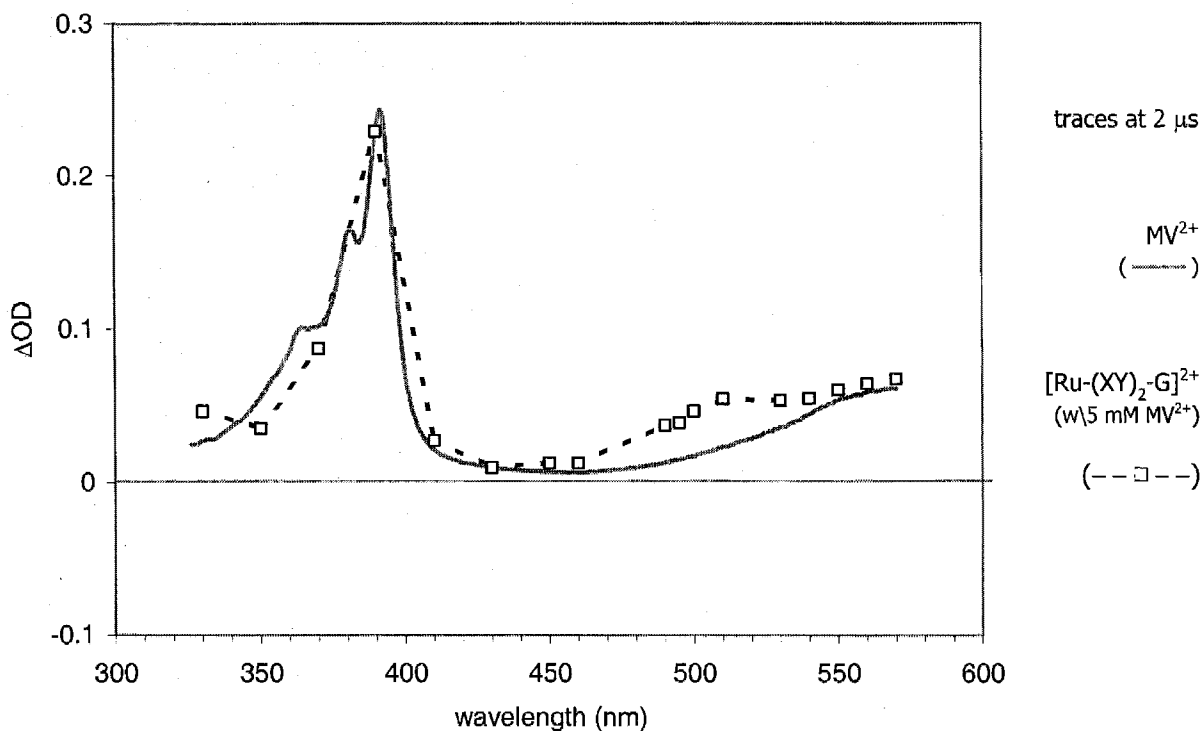


FIGURE 4.7 – Comparison of MV^+ and $[Ru^{II}-(XY)_2-G^+]^{3+}$ Transient Spectra

Comparison of reduced quencher, MV^+ , to the difference spectrum of $[Ru-(XY)_2-G]^{2+}$ in the presence of 5 mM MV^{2+} . The MV^+ spectrum is from spectroelectrochemistry experiments. The traces are taken 2 μ s after the laser pulse. MV^+ was normalized at 390 nm to the ΔOD of the difference spectrum. The extra absorbance at 520 nm, relative to MV^+ , is indicative of $[Ru^{II}-(XY)_2-G^+]^{3+}$ formation.

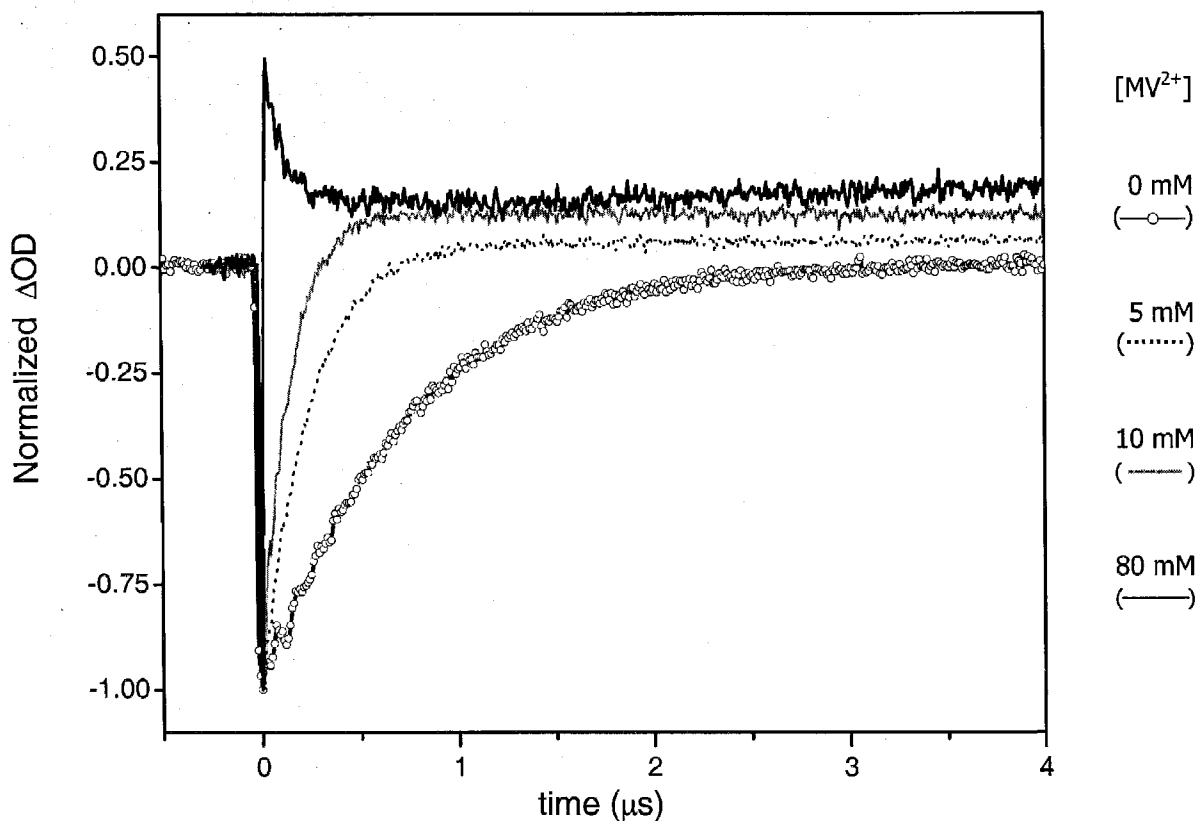
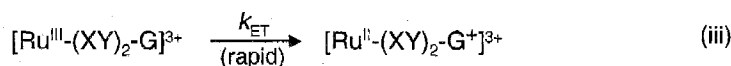
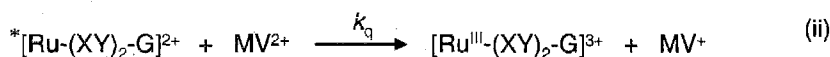
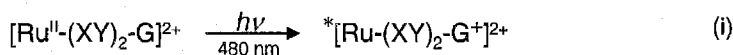


FIGURE 4.8 – Transient Absorption Spectra of $[\text{Ru}-(\text{XY})_2-\text{G}]^{2+}$ under Flash-Quench Conditions at 460 nm

Normalized transient absorption spectrum of $[\text{Ru}-(\text{XY})_2-\text{G}]^{2+}$ with varying amounts of MV^{2+} quencher from 0 to 80 mM. The traces were taken with excitation at 480 nm and recorded at 460 nm, corresponding to the MLCT band. The trace for 40 mM MV^{2+} was omitted for clarity, but essentially matches the 80 mM trace. The traces show the formation of $^*[\text{Ru}-(\text{XY})_2-\text{G}]^{2+}$ (equation i) followed by quenching (equation ii), and rapid electron transfer to form $[\text{Ru}^{\text{II}}-(\text{XY})_2-\text{G}^+]^{3+}$ (equation iii).



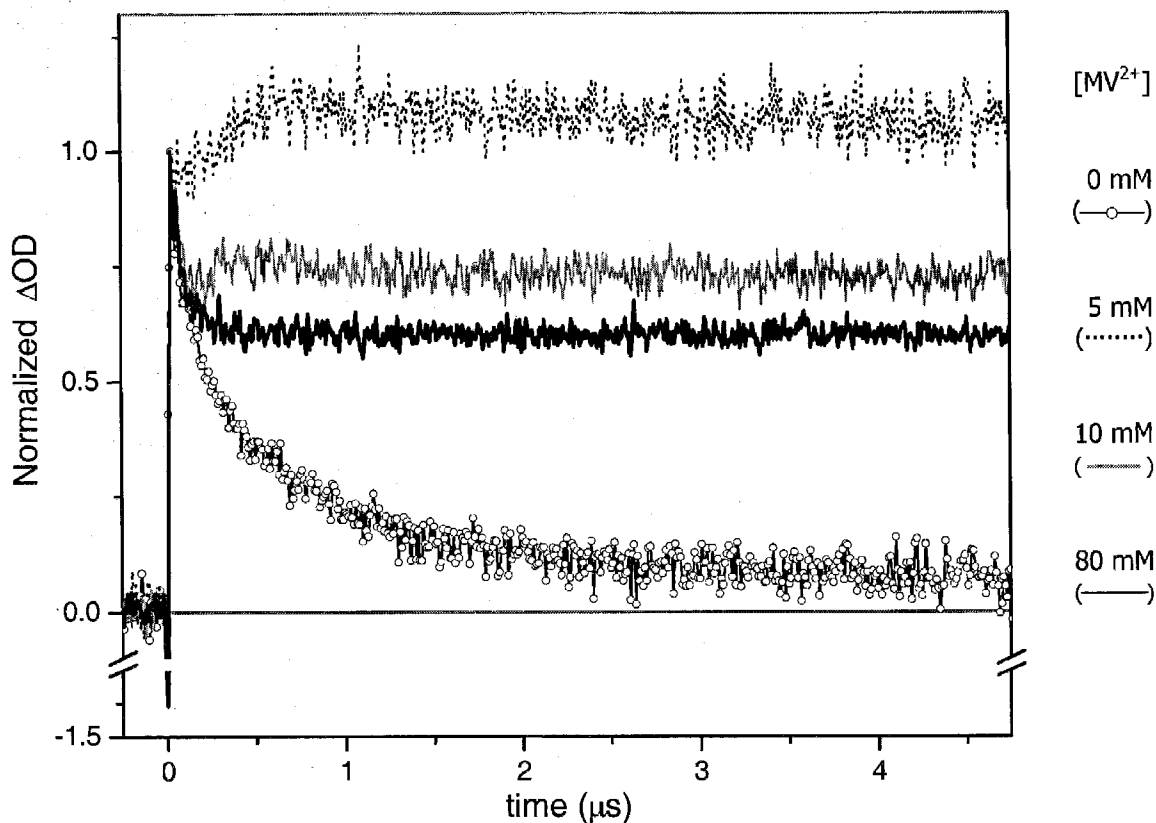


FIGURE 4.9 – Transient Absorption Spectra of $[\text{Ru}(\text{XY})_2\text{-G}]^{2+}$ under Flash-Quench Conditions at 500 nm

Normalized transient absorption spectrum of $[\text{Ru}(\text{XY})_2\text{-G}]^{2+}$ with varying amounts of MV^{2+} quencher from 0 to 80 mM. The traces were taken with excitation at 480 nm and recorded at 500 nm, corresponding to G^+ absorption. The trace for 40 mM MV^{2+} was omitted for clarity, but essentially matches the 80 mM trace. The traces show the formation of $^*[\text{Ru}(\text{XY})_2\text{-G}]^{2+}$ (equation i) followed by quenching (equation ii), and rapid electron transfer to form $[\text{Ru}^{\text{II}}(\text{XY})_2\text{-G}^+]^{3+}$ (equation iii).

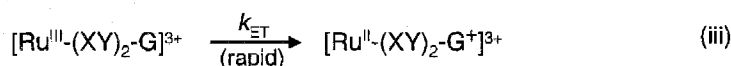
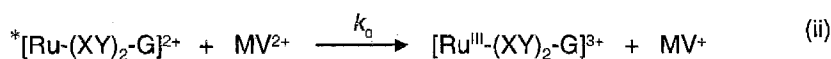
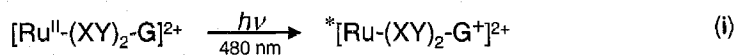


TABLE 4.1 – Observed Kinetics for $[\text{Ru}(\text{XY})_2\text{-G}]^{2+}$ Under Flash-Quench Conditions

$[\text{MV}^{2+}]$ (mM)	$k_{\text{lum}}^{\text{a}}$ (s^{-1})	$k_{\text{obs}460}^{\text{b}}$ (s^{-1})	$k_{\text{obs}500}^{\text{b}}$ (s^{-1})	$k_{\text{obs}}^{\text{c}}$ (s^{-1})
0	1.3×10^6	1.3×10^6	1.3×10^6	1.3×10^6
5	3.8×10^6	4.1×10^6	5.0×10^6	4.6×10^6
10	7.1×10^6	7.1×10^6	7.9×10^6	7.5×10^6
40	4.9×10^7	4.3×10^7	2.3×10^7	3.3×10^6
80	1.1×10^8	$\sim 1 \times 10^8^{\text{d}}$	$\sim 1 \times 10^8^{\text{d}}$	$\sim 1 \times 10^8^{\text{d}}$

^a k_{lum} is the luminescence decay rate measured at 620 nm.

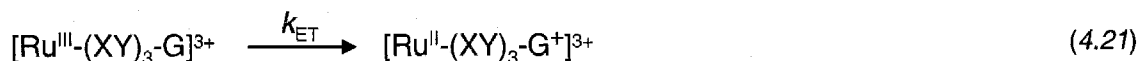
^bRate constant observed at indicated wavelength from exponential fits of transient absorption data. The kinetics at 460 nm are diagnostic for changes in the ruthenium MLCT band due to reactant consumption. Formation of the electron transfer product, $[\text{Ru}^{\text{II}}(\text{XY})_2\text{-G}^+]^{3+}$, has a spectroscopic handle at 500 nm.

^cAverage of k_{obs} at 460 and 500 nm.

^dThere were insufficient data points to get a reasonable fit. The k_{obs} is estimated based on comparing the rise time to the luminescence decay.

4.12 Electron Transfer of $[\text{Ru}(\text{XY})_3\text{-G}]^{2+}$, General Considerations

The flash quench and time-resolved laser spectroscopy were used to measure the rate constant, k_{ET} , for the ground state reaction highlighted in equation 4.21.



To get an accurate measurement, k_{ET} must be within the limits of the flash-quench method, $\sim 1 \times 10^9 \text{ s}^{-1}$ with MV^{2+} as the quencher, and the instrument response, $1 \times 10^8 \text{ s}^{-1}$. Because of these experimental constraints, it was important to examine the effect of varying quencher concentrations on the observed kinetics.

Both the donor-bridge-acceptor and quencher species have significant aromatic character and may be prone to stacking interactions that can interfere with the quenching reaction, cage escape to form $[\text{Ru}^{\text{III}}(\text{XY})_3\text{-G}]^{3+}$, or the observed electron transfer kinetics. A Stern-Volmer analysis is diagnostic of any behavior that deviates from the expected quenching process in Scheme 4.1. Figure 4.10 shows the Stern-Volmer plot for quenching of $[\text{Ru}(\text{XY})_3\text{-G}]^{2+}$ with MV^{2+} and yields a k_{q} of $1.2 \times 10^9 \text{ M}^{-1} \text{ s}^{-1}$, with a regression coefficient, R^2 , of 0.98. The linearity of the plot in Figure 4.10 and lack of discrepancy between the experimental and reported values of k_{q} indicate that the quenching proceeds as described in Scheme 4.1.

4.13 Electron Transfer Reactions of $[\text{Ru}(\text{XY})_3\text{-G}]^{2+}$

Under flash-quench conditions, k_{ET} was determined from fitting single-wavelength transient absorption traces to a biexponential function (equation 4.11). One

kinetic phase corresponds to the quenching process (k_q , equation 4.4) with a rate constant equal to the luminescence decay rate, k_{lum} ; the second phase corresponds to k_{ET} . The presence and assignment of two kinetic phases are predicated on the apparent quenching rate constant, k_q' , being larger than k_{ET} . As was the case with $[Ru-(XY)_2-G]^{2+}$, if the quenching process cannot compete with the electron transfer reaction, $[Ru^{III}-(XY)_3-G]^{3+} \rightarrow [Ru^{II}-(XY)_3-G^+]^{3+}$ (equation 4.21), the transient spectra will display monoexponential kinetics with a rate constant equal to the excited-state decay rate, k_{lum} . Unlike $[Ru-(XY)_2-G]^{2+}$, k_{ET} for $[Ru-(XY)_3-G]^{2+}$ is an order of magnitude slower than the maximum apparent quenching rate ($k_q' = 1 \times 10^8 \text{ s}^{-1}$) that can be achieved.

Figure 4.11 shows the single-wavelength transient absorption spectra of $[Ru-(XY)_3-G]^{2+}$ at 460 nm under flash-quench conditions. The traces for samples containing 5 and 12 mM MV^{2+} can be fit to monoexponential functions with rate constants matching the luminescence decay rate, k_{lum} (Table 4.2). Based on the previous discussion, in this quencher concentration regime the observed rate constant, k_{obs} , corresponds to the quenching process k_q' . Furthermore, this analysis places a lower limit of $6 \times 10^6 \text{ s}^{-1}$ on k_{ET} . The upper limit for the MV^{2+} concentration is between 80 and 100 mM. While solubility is not an issue, at higher concentrations of MV^{2+} the back reaction between $[Ru^{II}-(XY)_3-G^+]^{3+}$ or $[Ru^{III}-(XY)_3-G]^{3+}$ and MV^+ (equation 4.5 and 4.7) dominate the transient spectra and complicate their analysis.

A sample with 47 mM MV^{2+} gave a luminescence decay rate of $5.1 \times 10^7 \text{ s}^{-1}$. Analysis and fitting of single-wavelength kinetics at 460 nm reveal two distinct phases. The first phase is assigned to the quenching process with a rate constant of $3.9 \times 10^7 \text{ s}^{-1}$. The second phase has a rate constant of $9.3 \times 10^6 \text{ s}^{-1}$ and is attributed to k_{ET} (Table 4.3). Increasing quencher concentration by 2-fold had the expected effect of doubling

k_{lum} but did not appreciably change k_{ET} . Averaging over all of the transient traces taken at 460 nm with 47 mM MV^{2+} or more gives a k_{ET} of $8.9 \times 10^6 \text{ s}^{-1}$.

The same trends at 460 nm are observed at 500 nm for $[\text{Ru}(\text{XY})_3\text{-G}]^{2+}$ (Figure 4.12). The observed ΔOD at 500 nm has contributions from excited state formation, quenching, the electron transfer product $[\text{Ru}^{\text{II}}(\text{XY})_3\text{-G}^+]^{3+}$, and the back reaction with MV^+ (equation 4.5). Fitting to a three-exponential decay function, with a phase to account for quenching, k_{ET} , and the back reaction (k_{CR} , equation 4.5) would not be accurate; the back reaction is a bimolecular process that is not correctly described by an exponential decay function. An alternative kinetic analysis involves numerically solving a series of differential equations that represent all of the possible reactions for this system, shown Scheme 4.2 and 4.3.

Using the commercial software package MATLAB,¹⁶⁶ concentration versus time profiles were generated for the species: $*[\text{Ru}(\text{XY})_3\text{-G}]^{2+}$, $[\text{Ru}^{\text{II}}(\text{XY})_3\text{-G}]^{2+}$, $[\text{Ru}^{\text{III}}(\text{XY})_3\text{-G}]^{3+}$, $[\text{Ru}^{\text{II}}(\text{XY})_3\text{-G}^+]^{3+}$, $[\text{Ru}^{\text{III}}(\text{XY})_3\text{-G}^+]^{4+}$, MV^{2+} , MV^+ (The formation of $*[\text{Ru}(\text{XY})_3\text{-G}]^{2+}$ was omitted from the kinetic analysis; an approximation for the $*[\text{Ru}(\text{XY})_3\text{-G}]^{2+}$ concentration was used as part of the initial conditions). Using the measured extinction coefficients, or model compounds to estimate unknown coefficients, ΔOD versus time profiles were created. The parameters, k_{lum0} , k_{ET} , k_{Q} , k_{CR} , k_{BR1} , k_{BR2} , k_{BR3} , k_{BM1} , and k_{BM1} were optimized (using MATLAB's optimization functions) to fit the experimental data. The method accurately fit the experimental data, producing reasonable values for k_{ET} . Using a combination of fitting to biexponential functions (equation 4.11) and using the above kinetic analysis, k_{ET} for $[\text{Ru}(\text{XY})_3\text{-G}]^{2+}$, as measured at 500 nm, had an average value of $9.4 \times 10^6 \text{ s}^{-1}$ (Figure 4.13).

4.14 Electron Transfer Kinetics of $[\text{Ru}-(\text{XY})_3-\text{G}]^{2+}$

The data at 500 nm corroborate the conclusions drawn from data collected at 460 nm: For low concentrations of MV^{2+} ($< 12 \text{ mM}$), the observed rate constant corresponds to the quenching reaction and $k_{\text{ET}} > k_{\text{q}}'$. Raising the quencher concentration to greater than 45mM sufficiently increased the quenching reaction so that $k_{\text{ET}} < k_{\text{q}}'$. Using a combination of analysis techniques, including fitting to biexponential functions and utilizing Schemes 4.2 and 4.3, k_{ET} can be measured for samples with 47mM or more quencher. Combining the measured rate constants at or near 460 and 500 nm yields an overall average value of $9.0 \pm 0.3 \times 10^6 \text{ s}^{-1}$ for the k_{ET} of $[\text{Ru}-(\text{XY})_3-\text{G}]^{2+}$.

4.15 $[\text{Ru}-(\text{XY})_3-\text{G}]^{2+}$ Flash-Quench Transient Difference Spectra

Transient difference spectra from time zero to 2 μs (Figure 4.14) were collected to identify species present during the course of the reaction. In the first 100 ns after sample excitation, the main spectral feature is a broad bleach centered at approximately 450 nm. The bleach corresponds to $\text{Ru}^{\text{II}} \rightarrow \text{Ru}^{\text{III}}$, consistent with excited formation followed by quenching (equation 4.3 and 4.4). As early as 20 ns after excitation, the growth of a peak at 390 nm indicates MV^+ formation. The quenching process and ground state electron transfer, $[\text{Ru}^{\text{III}}-(\text{XY})_3-\text{G}]^{3+} \rightarrow [\text{Ru}^{\text{II}}-(\text{XY})_3-\text{G}^+]^{3+}$ (k_{ET} , equation 4.21), is completed by 250 ns.

Broad red absorption ($> 480 \text{ nm}$) is possibly due to $*[\text{Ru}-(\text{XY})_3-\text{G}]^{2+}$, $[\text{Ru}^{\text{II}}-(\text{XY})_3-\text{G}^+]^{3+}$, and or MV^+ . $*[\text{Ru}-(\text{XY})_3-\text{G}]^{2+}$ can be ruled out for difference spectra after 50 ns, which corresponds to five excited-state lifetimes. To distinguish the electron transfer product $[\text{Ru}^{\text{II}}-(\text{XY})_3-\text{G}^+]^{3+}$ from reduced quencher, the transient

difference spectrum at 2 μ s was overlayed with the MV^+ spectrum, generated from spectroelectro-chemistry experiments (Figure 4.15). The additional absorbance between 460 and 530 nm, when compared to the normalized MV^+ spectrum, is due to the aromatic amine radical cation of $[Ru^{II}-(XY)_3-G^+]^{3+}$. The normalized MV^+ spectrum gives a calculated $[MV^+]$ of 6 μ M; this value is reasonable considering the initial concentration of $[Ru-(XY)_3-G]^{2+}$ is 20 μ M and a yield of 25% or less flash-quench product is expected. Normalizing to 540 nm represents an upper limit for the concentration of MV^+ and a lower limit for the amount of $[Ru^{II}-(XY)_3-G^+]^{3+}$. Constructing such a plot (Figure 4.16) shows essentially the same features as Figure 4.15.

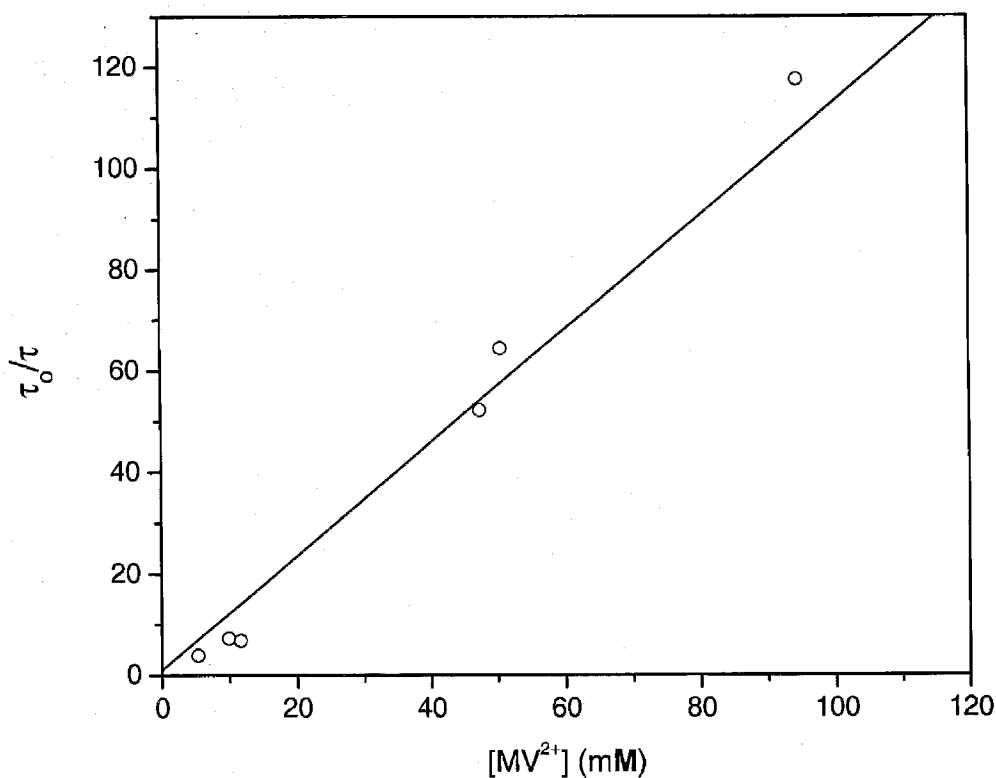
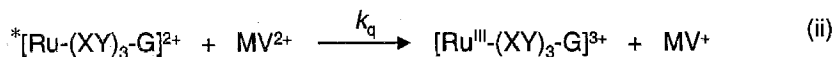
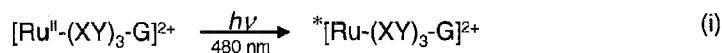


FIGURE 4.10 – Stern-Volmer Analysis of $[\text{Ru}-(\text{XY})_3\text{-G}]^{2+}$ Quenching by MV^{2+}

Stern-Volmer plot of $[\text{Ru}-(\text{XY})_3\text{-G}]^{2+}$ quenching by MV^{2+} . τ_0/τ was determined from fitting luminescence decay traces to monoexponential functions. τ_0 , 1.0×10^{-6} s, is the lifetime of $[\text{Ru}-(\text{XY})_3\text{-G}]^{2+}$ in absence of quencher, while τ is the lifetime with quencher. Linear least-squares regression, forcing an intercept of 1, gives a k_q of $1.2 \times 10^9 \text{ M}^{-1} \text{ s}^{-1}$ with a regression coefficient, R^2 , of 0.98.



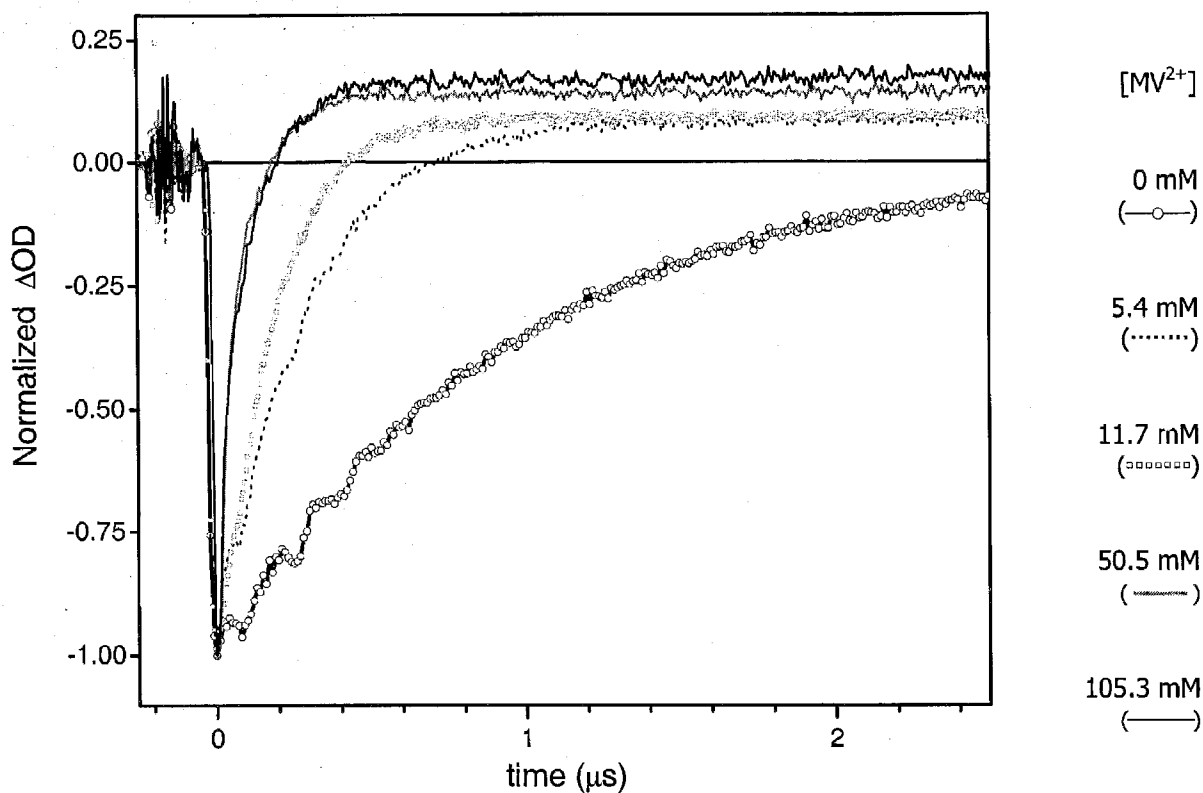


FIGURE 4.11 – $[\text{Ru}(\text{XY})_3\text{-G}]^{2+}$ Quencher Concentration Dependent Transient Absorption Traces

Normalized transient absorption spectrum of $[\text{Ru}(\text{XY})_3\text{-G}]^{2+}$ with varying amounts of MV^{2+} quencher from 0 to 105.3 mM. The traces were taken with excitation at 480 nm and recorded at 460 nm, corresponding to the region of the MLCT band. The traces show the formation of $^*[\text{Ru}(\text{XY})_3\text{-G}]^{2+}$ (equation i) followed by quenching (equation ii). The recovery is assigned to the electron transfer reaction (equation iii).

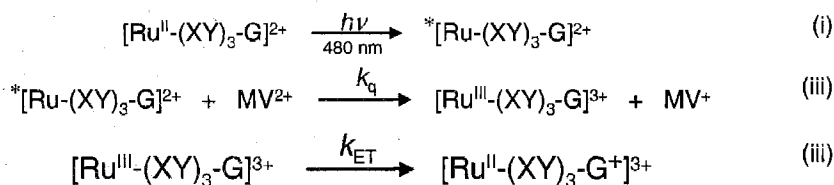


TABLE 4.2 – $[\text{Ru}-(\text{XY})_3\text{-G}]^{2+}$ Electron Transfer Kinetics under Flash-Quench Conditions ($k_{\text{ET}} > k_{\text{q}}'$)^a

$[\text{MV}^{2+}]$ (mM)	$k_{\text{lum}}^{\text{b}}$ (s^{-1})	$k_{\text{obs}460}^{\text{c}}$ (s^{-1})	$k_{\text{obs}500}^{\text{c}}$ (s^{-1})
0	9.8×10^5	1.0×10^6	9.3×10^5
5.4	3.8×10^6	3.5×10^6	3.0×10^6
9.9	7.1×10^6	6.3×10^6	4.5×10^6
11.7	6.6×10^6	5.5×10^6	5.7×10^6

^aThe electron transfer rates for $[\text{Ru}-(\text{XY})_3\text{-G}]^{2+}$ under flash-quench conditions do not reveal k_{ET} in this concentration regime (< 12 mM). Rather, k_{obs} is related to the apparent quenching rate constant, k_{q}' .

^b k_{lum} is the luminescence decay rate measured at 620 nm.

^cRate constant obtained at the indicated wavelength from exponential fits of transient absorption data. The kinetics at 460 nm are diagnostic for changes in the ruthenium MLCT band due to reactant consumption. Formation of the electron transfer product, $[\text{Ru}^{\text{II}}-(\text{XY})_3\text{-G}^+]^{3+}$, has a spectroscopic handle at 500 nm.

TABLE 4.3 – $[\text{Ru}-(\text{XY})_3\text{-G}]^{2+}$ Electron Transfer Kinetics
under Flash-Quench Conditions ($k_{\text{ET}} < k_{\text{q}}'$)^a

$[\text{MV}^{2+}]$ (mM)	$k_{\text{lum}}^{\text{a}}$ (s^{-1})	$k_{\text{ET}460}^{\text{b}}$ (s^{-1})	$k_{\text{ET}500}^{\text{b}}$ (s^{-1})	k_{ET}^{c} (s^{-1})
47.4	5.1×10^7	9.3×10^6	9.2×10^6	9.2×10^6
50.5	6.3×10^7	9.1×10^6	8.3×10^6	8.9×10^6
94.5	$1.2 \times 10^8^{\text{b}}$	8.5×10^6	9.0×10^6	8.7×10^6
105	$1.1 \times 10^8^{\text{b}}$	8.6×10^6	1.1×10^7	9.4×10^6

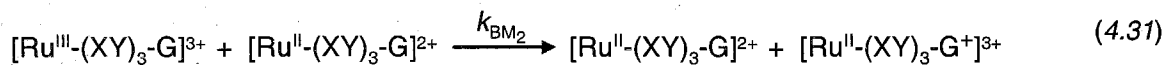
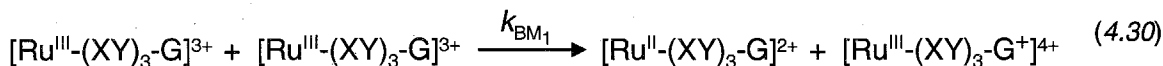
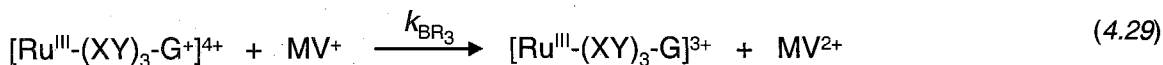
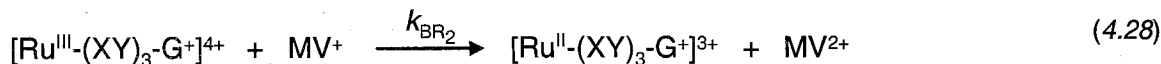
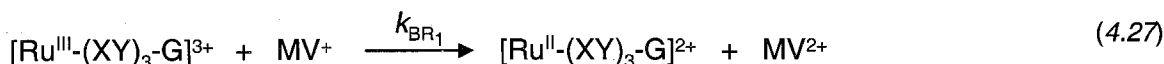
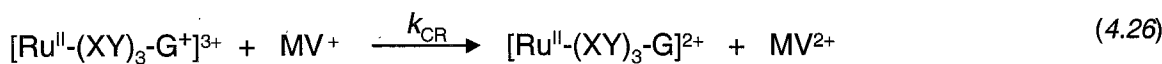
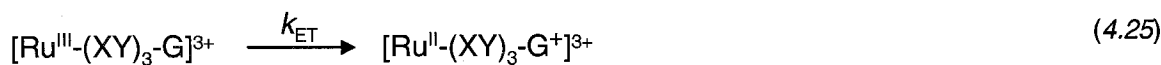
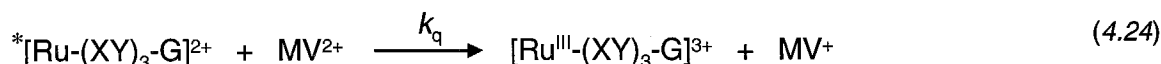
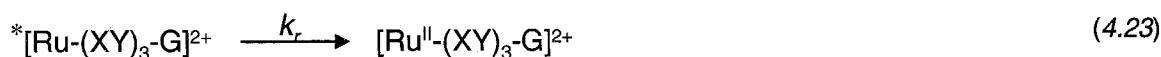
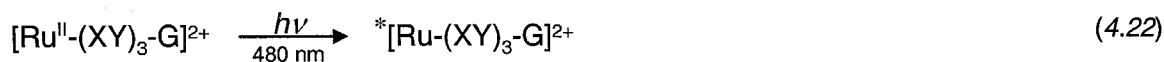
^a k_{lum} is the luminescence decay rate measured at 620 nm.

^bRate constant observed at the indicated wavelength from exponential fits of transient absorption data. The kinetics at 460 nm are diagnostic for changes in the ruthenium MLCT band due to reactant consumption. Formation of the electron transfer product, $[\text{Ru}^{\text{II}}-(\text{XY})_3\text{-G}^{+}]^{3+}$, has a spectroscopic handle at 500 nm.

^cAverage of rates from several traces in at or near 460 and 500 nm.

Scheme 4.2

Relevant Reactions for Measuring the Electron Transfer Kinetics of
 $[\text{Ru}-(\text{XY})_3-\text{G}]^{2+}$ Under Flash-Quench Conditions



Scheme 4.3

Kinetic Analysis of the Electron Transfer Mechanism
for $[\text{Ru}(\text{XY})_3\text{-G}]^{2+}$ from Scheme 2

$$\frac{\partial}{\partial t} [\text{*Ru}^{\text{II}}(\text{XY})_3\text{-G}] = -k_r [\text{*Ru}(\text{XY})_3\text{-G}] - k_q [\text{*Ru}(\text{XY})_3\text{-G}][\text{MV}^{2+}] \quad (4.32)$$

$$\begin{aligned} \frac{\partial}{\partial t} [\text{Ru}^{\text{II}}(\text{XY})_3\text{-G}] = & k_r [\text{*Ru}(\text{XY})_3\text{-G}]^{2+} + k_{\text{CR}} [\text{Ru}^{\text{II}}(\text{XY})_3\text{-G}^+][\text{MV}^+] + \\ & k_{\text{BR}_1} [\text{Ru}^{\text{III}}(\text{XY})_3\text{-G}][\text{MV}^+] + k_{\text{BM}_1} [\text{Ru}^{\text{III}}(\text{XY})_3\text{-G}][\text{Ru}^{\text{III}}(\text{XY})_3\text{-G}] \end{aligned} \quad (4.33)$$

$$\begin{aligned} \frac{\partial}{\partial t} [\text{Ru}^{\text{III}}(\text{XY})_3\text{-G}] = & k_q [\text{*Ru}(\text{XY})_3\text{-G}][\text{MV}^{2+}] - k_{\text{ET}} [\text{Ru}^{\text{III}}(\text{XY})_3\text{-G}] - \\ & k_{\text{BR}_1} [\text{Ru}^{\text{III}}(\text{XY})_3\text{-G}][\text{MV}^+] - k_{\text{BM}_1} [\text{Ru}^{\text{III}}(\text{XY})_3\text{-G}][\text{Ru}^{\text{III}}(\text{XY})_3\text{-G}] - \\ & k_{\text{BM}_2} [\text{Ru}^{\text{III}}(\text{XY})_3\text{-G}][\text{Ru}^{\text{II}}(\text{XY})_3\text{-G}] + k_{\text{BR}_3} [\text{Ru}^{\text{III}}(\text{XY})_3\text{-G}^+][\text{MV}^+] \end{aligned} \quad (4.34)$$

$$\begin{aligned} \frac{\partial}{\partial t} [\text{Ru}^{\text{II}}(\text{XY})_3\text{-G}^+] = & k_{\text{ET}} [\text{Ru}^{\text{III}}(\text{XY})_3\text{-G}] - k_{\text{CR}} [\text{Ru}^{\text{II}}(\text{XY})_3\text{-G}^+][\text{MV}^+] + \\ & k_{\text{BR}_2} [\text{Ru}^{\text{III}}(\text{XY})_3\text{-G}^+][\text{MV}^+] + k_{\text{BM}_2} [\text{Ru}^{\text{III}}(\text{XY})_3\text{-G}][\text{Ru}^{\text{II}}(\text{XY})_3\text{-G}] \end{aligned} \quad (4.35)$$

$$\begin{aligned} \frac{\partial}{\partial t} [\text{Ru}^{\text{III}}(\text{XY})_3\text{-G}^+] = & -k_{\text{BR}_2} [\text{Ru}^{\text{III}}(\text{XY})_3\text{-G}^+][\text{MV}^+] - k_{\text{BR}_3} [\text{Ru}^{\text{III}}(\text{XY})_3\text{-G}^+][\text{MV}^+] + \\ & k_{\text{BM}_1} [\text{Ru}^{\text{III}}(\text{XY})_3\text{-G}][\text{Ru}^{\text{III}}(\text{XY})_3\text{-G}] \end{aligned} \quad (4.36)$$

$$\begin{aligned} \frac{\partial}{\partial t} [\text{MV}^{2+}] = & -k_q [\text{*Ru}(\text{XY})_3\text{-G}][\text{MV}^{2+}] + k_{\text{CR}} [\text{Ru}^{\text{II}}(\text{XY})_3\text{-G}^+][\text{MV}^+] + \\ & k_{\text{BR}_1} [\text{Ru}^{\text{III}}(\text{XY})_3\text{-G}][\text{MV}^+] + k_{\text{BR}_2} [\text{Ru}^{\text{III}}(\text{XY})_3\text{-G}^+][\text{MV}^+] + \\ & k_{\text{BR}_3} [\text{Ru}^{\text{III}}(\text{XY})_3\text{-G}^+][\text{MV}^+] \end{aligned} \quad (4.37)$$

$$\begin{aligned} \frac{\partial}{\partial t} [\text{MV}^+] = & k_q [\text{*Ru}(\text{XY})_3\text{-G}][\text{MV}^{2+}] - k_{\text{CR}} [\text{Ru}^{\text{II}}(\text{XY})_3\text{-G}^+][\text{MV}^+] - \\ & k_{\text{BR}_1} [\text{Ru}^{\text{III}}(\text{XY})_3\text{-G}][\text{MV}^+] - k_{\text{BR}_2} [\text{Ru}^{\text{III}}(\text{XY})_3\text{-G}^+][\text{MV}^+] - \\ & k_{\text{BR}_3} [\text{Ru}^{\text{III}}(\text{XY})_3\text{-G}^+][\text{MV}^+] \end{aligned} \quad (4.38)$$

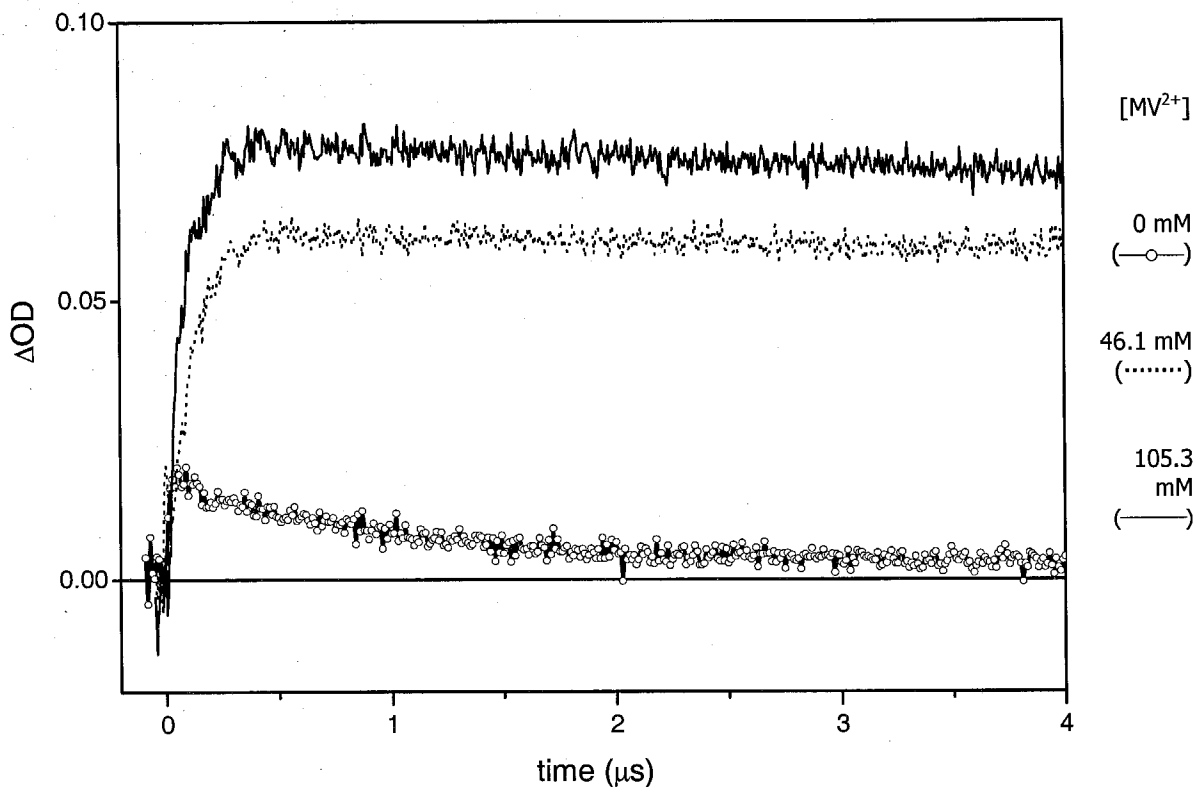
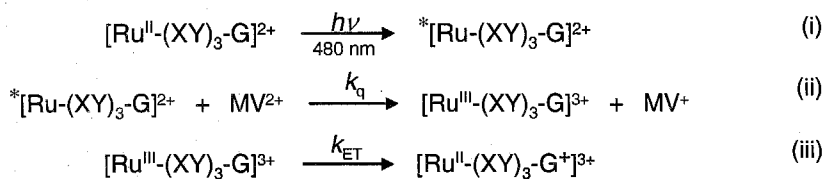


FIGURE 4.12 – $[\text{Ru}(\text{XY})_3\text{-G}]^{2+}$ Quencher Concentration Dependent Transient Absorption

Transient absorption spectra of $[\text{Ru}(\text{XY})_3\text{-G}]^{2+}$ with 0 to 80 mM MV^{2+} . Samples were excited at 480 nm and traces were recorded at 500 nm, which correspond to $[\text{Ru}^{\text{II}}(\text{XY})_3\text{-G}^+]^{3+}$ absorption, and to a lesser extent, MV^+ . The traces were corrected for stray laser light and excited-state emission. The initial, rapid rise is assigned to $^*[\text{Ru}(\text{XY})_3\text{-G}]^{2+}$ (equation i) followed by quenching (equation ii). The second, slower rise is assigned to formation of $[\text{Ru}^{\text{II}}(\text{XY})_3\text{-G}^+]^{2+}$ (equation iii).



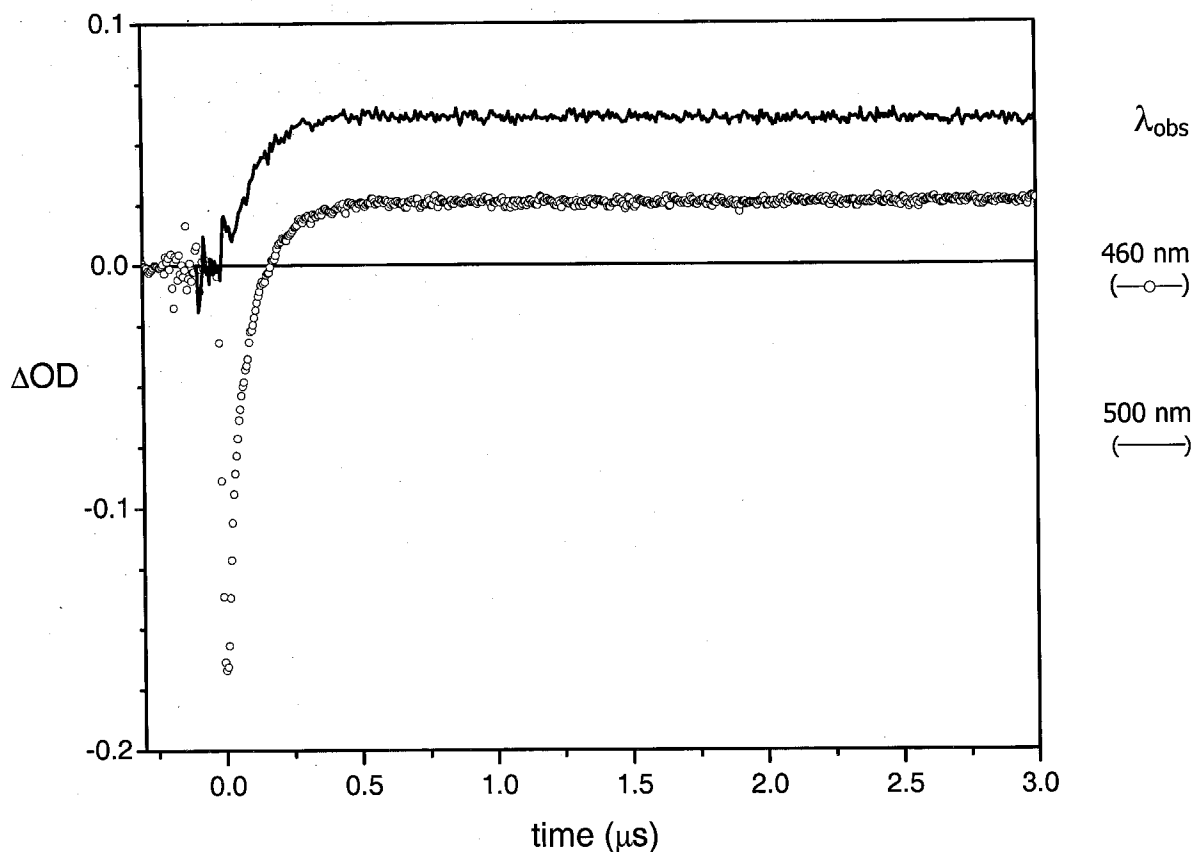
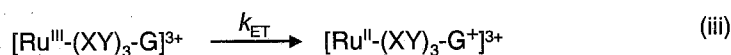
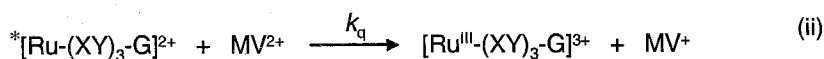
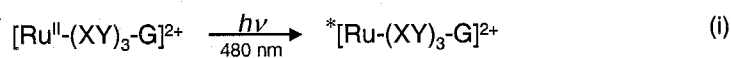


FIGURE 4.13 – $[\text{Ru}(\text{XY})_3\text{-G}]^{2+}$ Transient Absorption Traces under Flash-Quench Conditions

Single wavelength transient absorption spectra of $[\text{Ru}(\text{XY})_3\text{-G}]^{2+}$ with 47 mM MV^{2+} . The samples were excited with 480 nm light and the spectra recorded at 460 nm (monitors reactant consumption) and 500 nm (product formation). The spectrum at 500 nm was corrected for stray laser light and excited state emission. The average electron transfer rate constant, k_{ET} , is $8.9 \times 10^6 \text{ s}^{-1}$ at 460 nm and 9.4×10^6 at 500 nm.



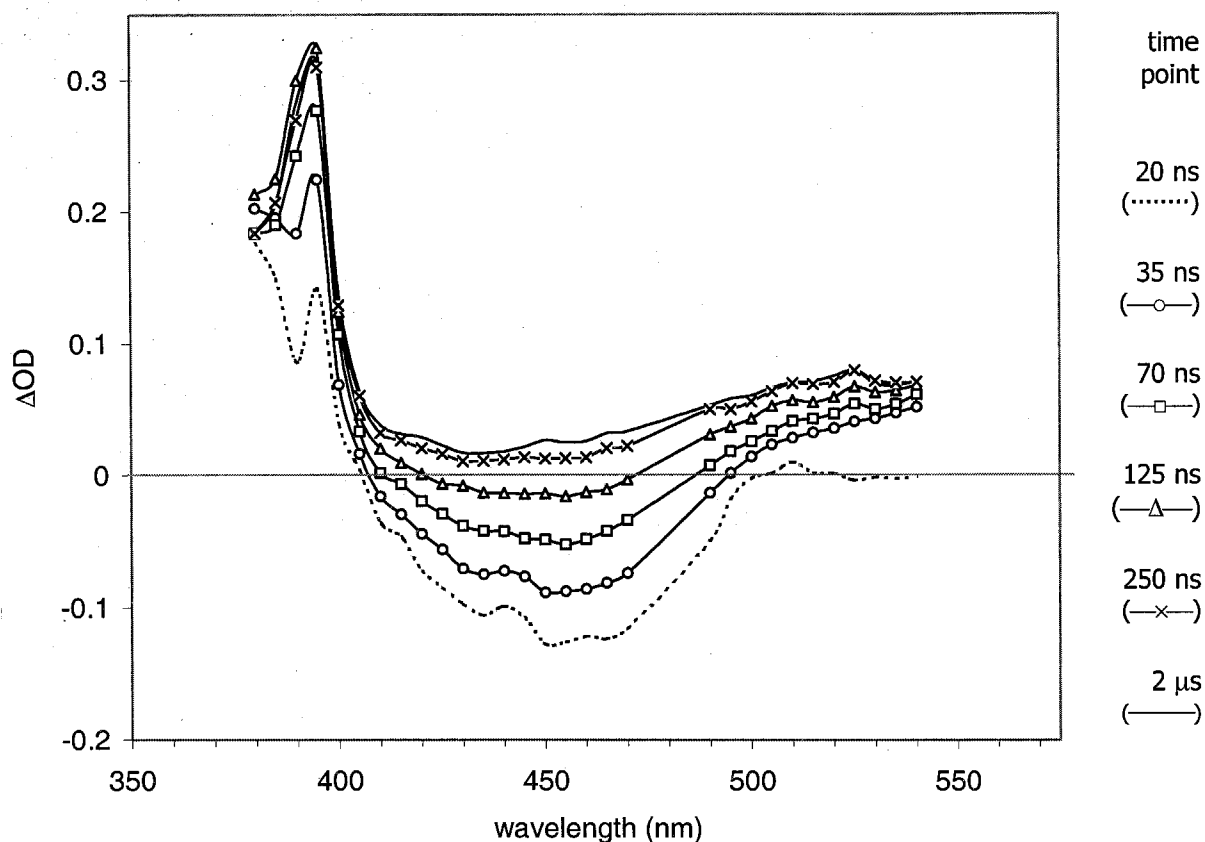
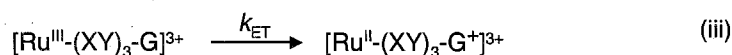
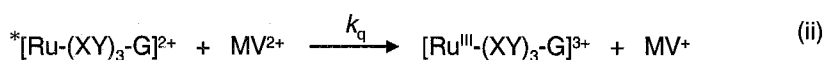
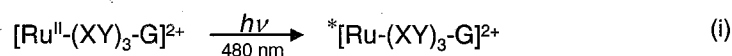


FIGURE 4.14 – $[\text{Ru}(\text{XY})_3\text{-G}]^{2+}$ Flash-Quench Transient Difference Spectra

Transient difference spectra of $[\text{Ru}(\text{XY})_3\text{-G}]^{2+}$ in the presence of 46 mM MV^{2+} . Time zero is set to sample excitation. Initially, MV^+ and $[\text{Ru}^{\text{III}}(\text{XY})_3\text{-G}]^{3+}$ are present, as indicated by the peak at 390 nm and the bleach of the MLCT band at 450 nm. The difference spectra show subsequent electron transfer (equation iii) highlighted by the recovery of the broad bleach at 450 nm and increased absorption at 500 nm.



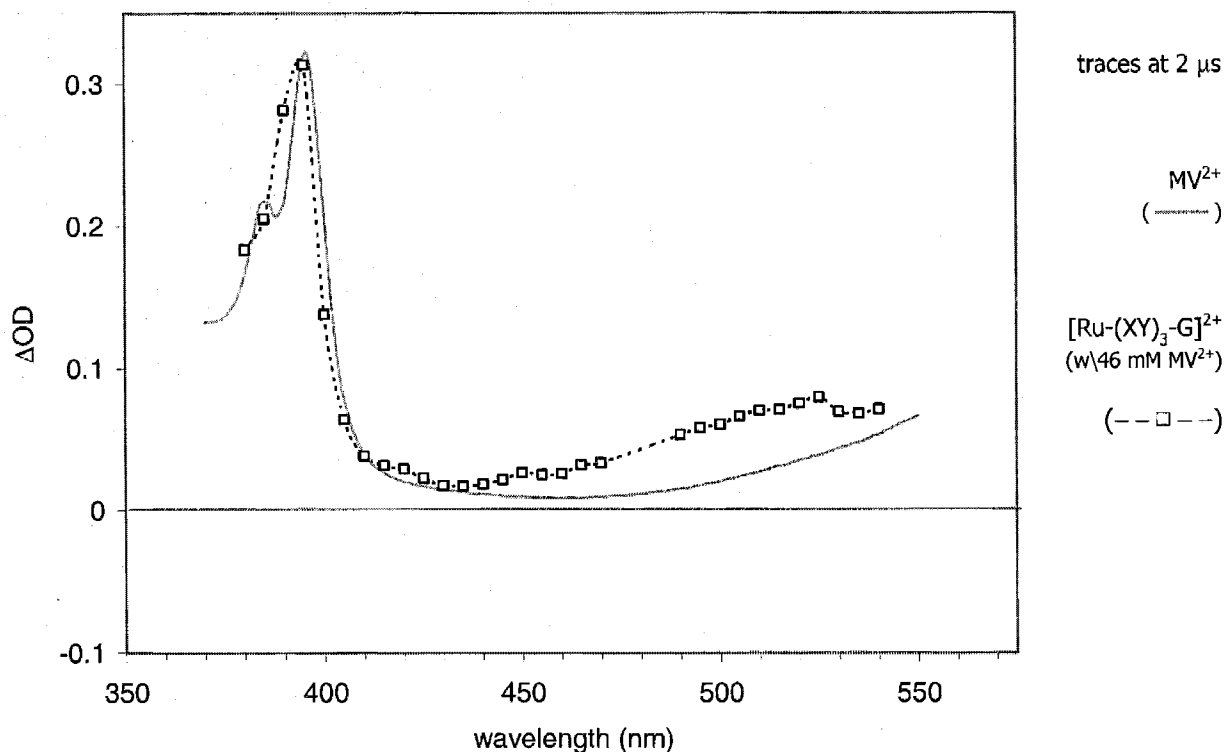
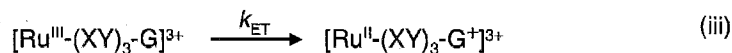
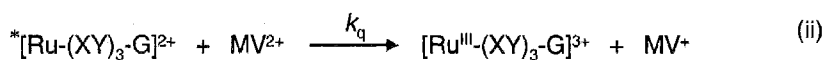
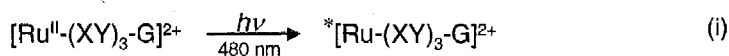


FIGURE 4.15 – Comparison of $[Ru-(XY)_3-G]^{2+}$ Electron Transfer Product and MV^+

Comparison of reduced quencher, MV^+ , to the difference spectrum of $[Ru-(XY)_3-G]^{2+}$ in the presence of 46 mM MV^{2+} . The MV^+ spectrum is from spectroelectrochemistry experiments. The difference spectrum was taken 2 μ s after the laser pulse. MV^+ was normalized at 390 nm to the ΔOD of the difference spectrum. The extra absorbance at 520 nm, relative to MV^+ , is indicative of $[Ru^{II}-(XY)_3-G^+]^{3+}$ formation.



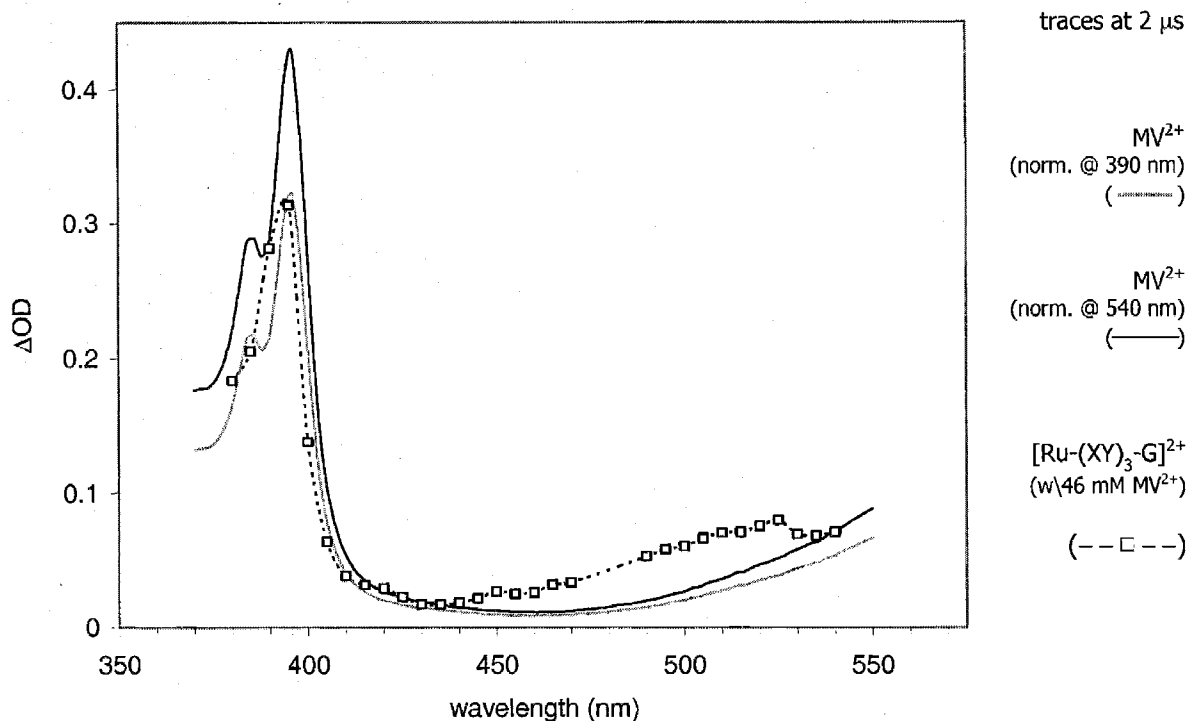
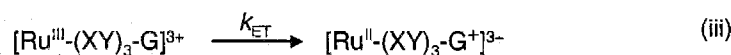
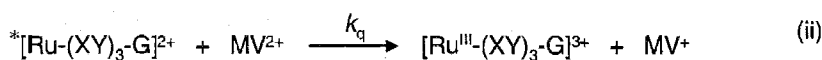
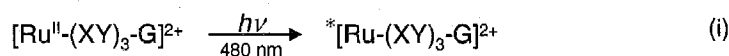


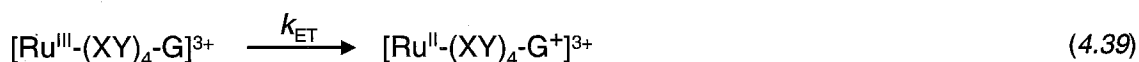
FIGURE 4.16 – Upper and Lower Limit for $[Ru^{II}-(XY)_3-G^+]^{2+}$

Comparison of reduced quencher, MV^+ , to the difference spectrum of $[Ru-(XY)_3-G]^{2+}$ in the presence of 46 mM MV^{2+} . The MV^+ spectrum is from spectroelectrochemistry experiments. The trace was taken 2 μ s after the laser pulse. MV^+ was normalized at 390 nm or 540 nm to the ΔOD of the difference spectrum. The extra absorbance at 520 nm, relative to MV^+ , is indicative of $[Ru^{II}-(XY)_3-G^+]^{3+}$ formation.



4.16 [Ru-(XY)₄-G]²⁺ Electron Transfer Kinetics

Measuring k_{ET} , as described in equation 4.39, was relatively straightforward for [Ru-(XY)₄-G]²⁺.



The length between the donor and acceptor is such that the electron transfer rate is slow enough to be well within the upper speed limits of the flash-quench method ($\sim 1 \times 10^9 \text{ s}^{-1}$) and the instrument response ($1 \times 10^8 \text{ s}^{-1}$). It was sufficiently rapid, however, that bimolecular reactions, $k_{\text{BM}1}$ and $k_{\text{BM}2}$ (equation 4.8 and 4.9) between [Ru^{II}-(XY)₄-G]³⁺ and [Ru-(XY)₄-G]²⁺ (and to a much lesser extent, [Ru^{III}-(XY)₄-G]³⁺) do not contribute significantly to the consumption of [Ru^{III}-(XY)₄-G]³⁺. The quencher concentration dependence measurements performed for [Ru-(XY)₂-G]²⁺ and [Ru-(XY)₃-G]²⁺ were not necessary for this complex.

A k_q of $1.5 \times 10^9 \text{ M}^{-1} \text{ s}^{-1}$ was extracted from the Stern-Volmer analysis, and is well within the range of reported quencher constants for methyl viologen in acetonitrile solution.¹⁶⁴ The lack of irregularity in the value of k_q suggests that photoexcitation of the samples results in the straightforward quenching of the excited state and formation of [Ru^{III}-(XY)₄-G]³⁺.

k_{ET} was measured with time-resolved transient absorption spectroscopy. Taken at single wavelengths, the samples were irradiated with 480 nm light and the absorbance changes as a function of time, out to 50 μs , were recorded (Figure 4.18). The observation wavelengths were chosen to monitor the consumption of the reactant, $[\text{Ru}^{\text{III}}-(\text{XY})_4-\text{G}]^{3+}$, and the formation of product, $[\text{Ru}^{\text{II}}-(\text{XY})_4-\text{G}^+]^{3+}$. Recovery of the MLCT absorption band is diagnostic for the reduction of ruthenium, $\text{Ru}^{\text{III}} \rightarrow \text{Ru}^{\text{II}}$, and occurs in the region of 460 nm. Formation of the product is indicated by oxidation of the aromatic amine moiety, $\text{G} \rightarrow \text{G}^+$. The radical cation has a spectroscopic handle at 500 nm in the form of an absorption increase.

The transient absorption traces were fit to biexponential decay functions (4.11). The faster kinetic phase was assigned to the quenching process and had a rate constant equal to k_{lum} . The second phase corresponded to the electron transfer reaction in equation 4.39 (k_{ET}), and was quencher and $[\text{Ru}-(\text{XY})_4-\text{G}]^{2+}$ concentration independent. k_{ET} determined at 460 nm, $1.0 \times 10^5 \text{ s}^{-1}$, and at 500 nm, $2.1 \times 10^5 \text{ s}^{-1}$, are within experimental error of each other. A value for k_{ET} , averaged over many wavelengths in the range of 340 to 520 nm, gives an electron transfer rate constant for $[\text{Ru}^{\text{III}}-(\text{XY})_4-\text{G}]^{3+} \rightarrow [\text{Ru}^{\text{II}}-(\text{XY})_4-\text{G}^+]^{3+}$ of $2 \pm 1 \times 10^5 \text{ s}^{-1}$.

4.17 $[\text{Ru}-(\text{XY})_4-\text{G}]^{2+}$ Transient Difference Spectra

Compiling the single-wavelength transient absorption traces into difference spectra (Figure 4.19) is useful for identifying the species present at any given reaction time point. During the early moments after excitation ($< 500 \text{ ns}$) there are three main spectral features consistent with $[\text{*Ru}-(\text{XY})_4-\text{G}]^{2+}$: an absorption increase at 360 nm, a bleach in the region of 460 nm, and increased absorption at 500 nm. At 1 μs , the

spectral features have completely shifted to the products of the flash quench, $[\text{Ru}^{\text{III}}-(\text{XY})_4-\text{G}]^{3+}$ and MV^+ . This is evident from the large absorption increase at 390 nm (indicative of MV^+), partial recovery of the bleach at 460 nm ($^*\text{Ru} \rightarrow \text{Ru}^{\text{III}}$), and the broad absorption red of 480 nm (also indicative of MV^+). Full recovery of the MLCT bleach at 460 nm ($\text{Ru}^{\text{III}} \rightarrow \text{Ru}^{\text{II}}$) and an absorption increase at 500 nm signal the formation of the electron transfer product $[\text{Ru}^{\text{II}}-(\text{XY})_4-\text{G}^+]^{2+}$ (equation 4.39). At much longer time the charge recombination reaction (k_{CR} , equation 4.5) is evident from the loss of absorption at 390 nm and red of 480 nm.

While an absorption increase at 500 nm is consistent with the formation of $[\text{Ru}^{\text{II}}-(\text{XY})_4-\text{G}^+]^{3+}$, other species including $^*[\text{Ru}-(\text{XY})_4-\text{G}]^{2+}$ and MV^+ absorb in the same region. The excited state species can be ruled out from any difference spectrum taken after five excited-state lifetimes or 1.5 μs . The extinction coefficients for MV^+ ($2.5 \times 10^3 \text{ M}^{-1}\text{cm}^{-1}$, appendix D) are smaller than $[\text{Ru}^{\text{II}}-(\text{XY})_n-\text{G}^+]^{3+}$ ($5.7 \times 10^3 \text{ M}^{-1}\text{cm}^{-1}$, appendix D) in the region around 500 nm. To confirm the existence of $[\text{Ru}^{\text{II}}-(\text{XY})_4-\text{G}^+]^{3+}$, the calculated MV^+ spectrum (derived from spectroelectrochemical experiments) was compared to the difference spectrum at 45 μs (Figure 4.20).

Normalizing the MV^+ trace to the $[\text{Ru}-(\text{XY})_4-\text{G}]^{2+}$ difference spectrum represents an upper limit for the MV^+ concentration. The calculated concentration of $[\text{MV}^+]$ (which is equal to the concentration of $[\text{Ru}^{\text{II}}-(\text{XY})_4-\text{G}^+]^{3+}$) was 1.4 μM , a reasonable Figure given a starting concentration of $[\text{Ru}-(\text{XY})_4-\text{G}]^{2+}$ of 20 μM . The comparison between MV^+ and the observed difference spectrum clearly indicates the absorption increase in the vicinity of 500 nm is largely due to $[\text{Ru}^{\text{II}}-(\text{XY})_4-\text{G}^+]^{3+}$.

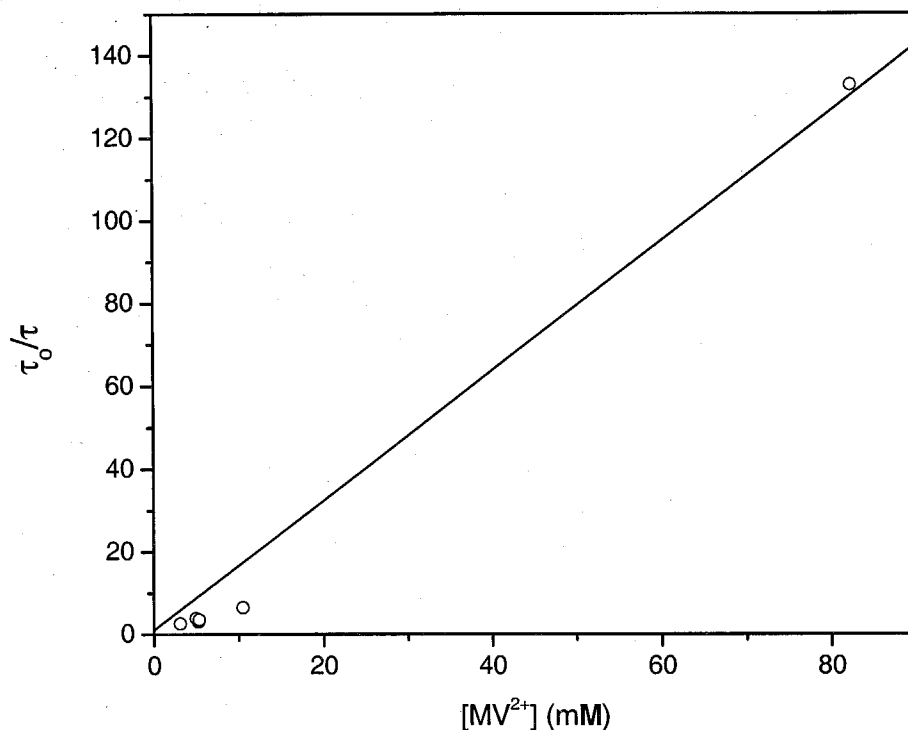
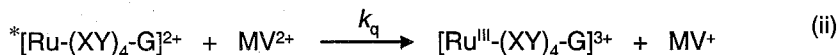
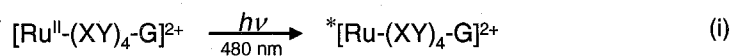


FIGURE 4.17 – Stern-Volmer Analysis of $[\text{Ru}(\text{XY})_4\text{-G}]^{2+}$ Quenching with MV^{2+}

Stern-Volmer plot of $[\text{Ru}(\text{XY})_4\text{-G}]^{2+}$ quenching by MV^{2+} . τ_0/τ was determined from fitting luminescence decay traces to monoexponential functions. τ_0 , 1.1×10^{-6} s, is the lifetime of $[\text{Ru}(\text{XY})_4\text{-G}]^{2+}$ in the absence of quencher, while τ is the lifetime with quencher. Linear least squares regression, forcing an intercept of 1, gives a k_q of $1.5 \times 10^9 \text{ M}^{-1} \text{ s}^{-1}$ with a regression coefficient, R^2 , of 0.98.



(iii)

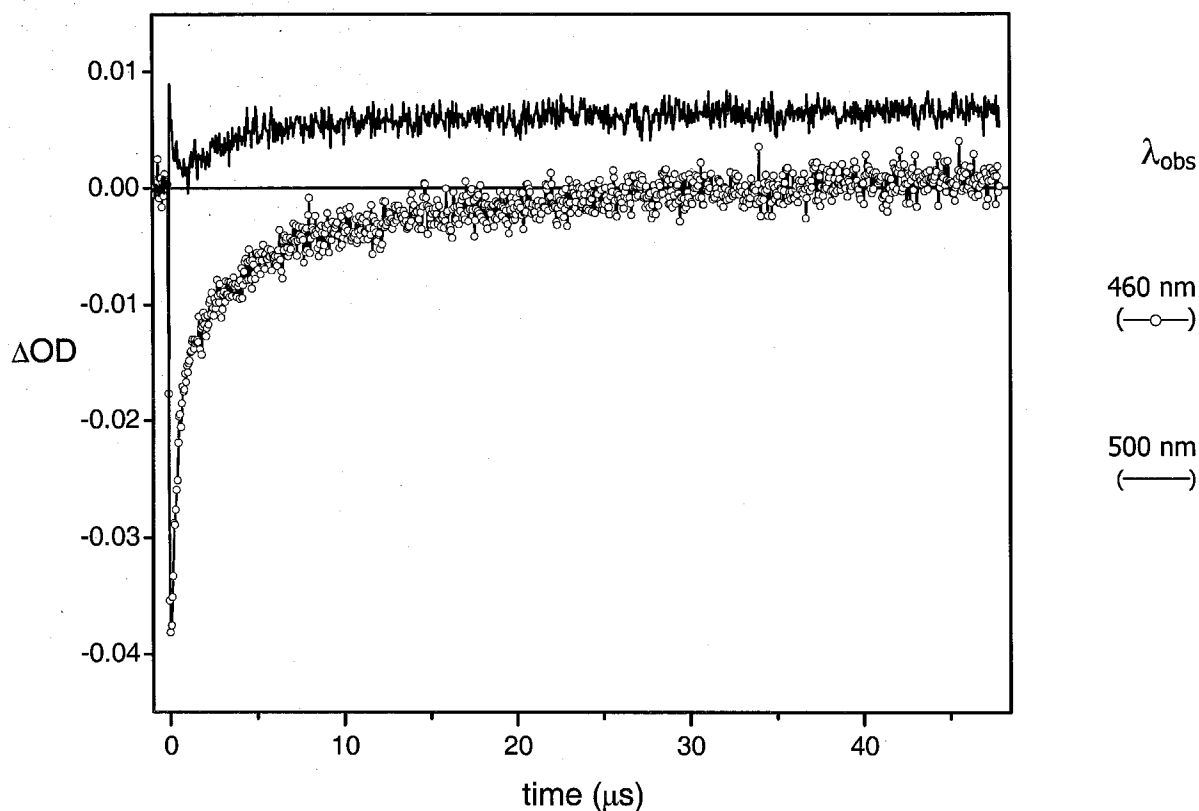
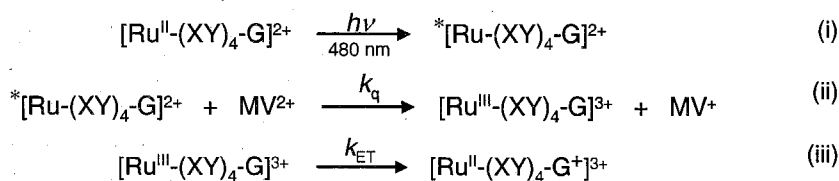


FIGURE 4.18 – $[\text{Ru}(\text{XY})_4\text{-G}]^{2+}$ Transient Absorption Under Flash-Quench Conditions

Single-wavelength transient absorption spectra of $[\text{Ru}(\text{XY})_4\text{-G}]^{2+}$ with 5.3 mM MV^{2+} . The samples were excited with 480 nm light and the spectra recorded at 460 nm (monitoring reactant consumption) and 500 nm (product formation). The electron-transfer rate constant, k_{ET} , is $1.0 \times 10^5 \text{ s}^{-1}$ at 460 nm and 2.1×10^5 at 500 nm.



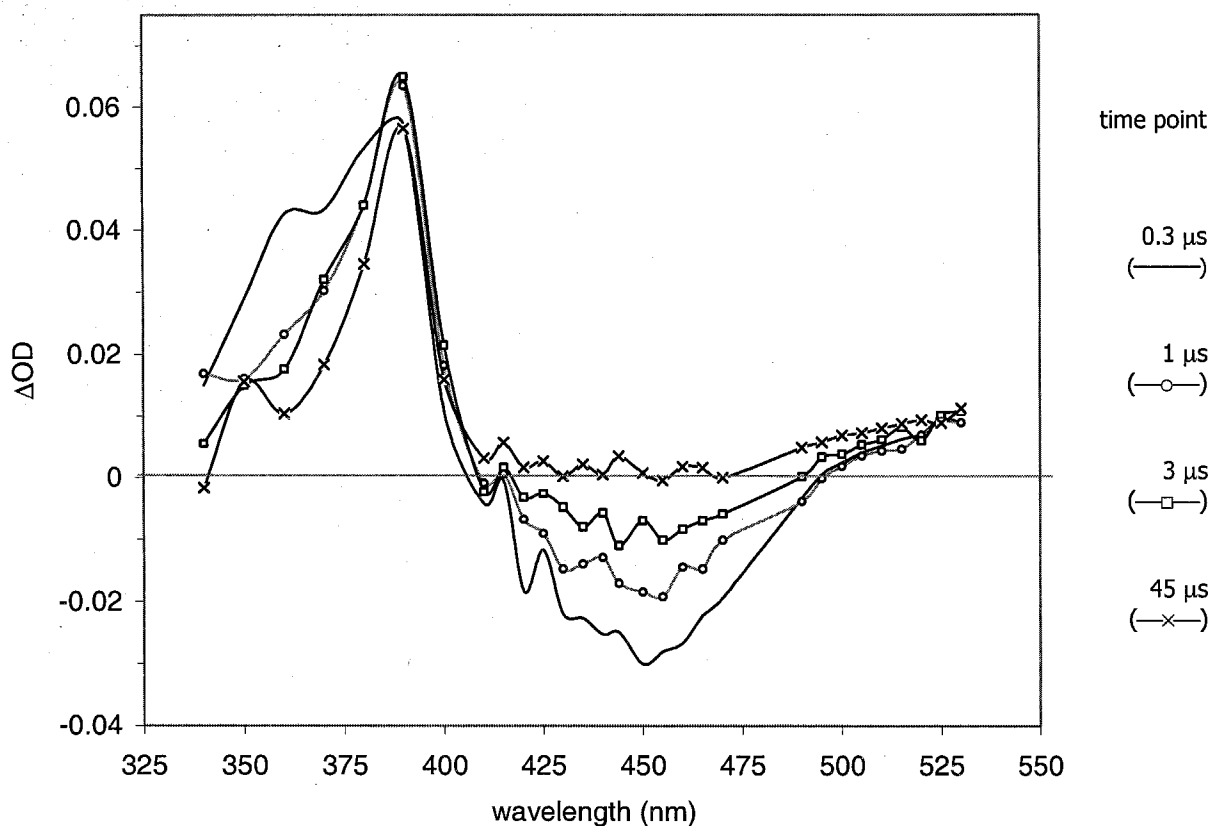
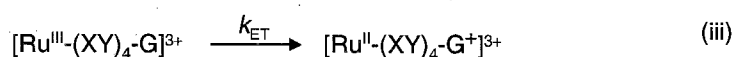
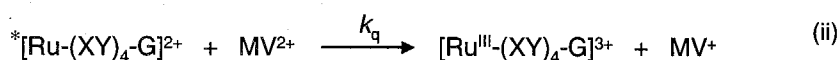
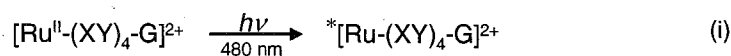


FIGURE 4.19 – $[\text{Ru}(\text{XY})_4\text{-G}]^{2+}$ Transient Difference Spectra Under Flash-Quench Conditions

Transient difference spectra of $[\text{Ru}(\text{XY})_4\text{-G}]^{2+}$ in the presence of 46 mM MV^{2+} . Time zero is the arrival of the laser pulse. Initially there is MV^+ and $[\text{Ru}^{\text{III}}(\text{XY})_3\text{-G}]^{3+}$, as indicated by the peak at 390 nm and the bleach of the MLCT band at 450 nm. Subsequent electron transfer (equation iii) is highlighted by the recovery of the broad bleach at 450 nm and increased absorption at 500 nm.



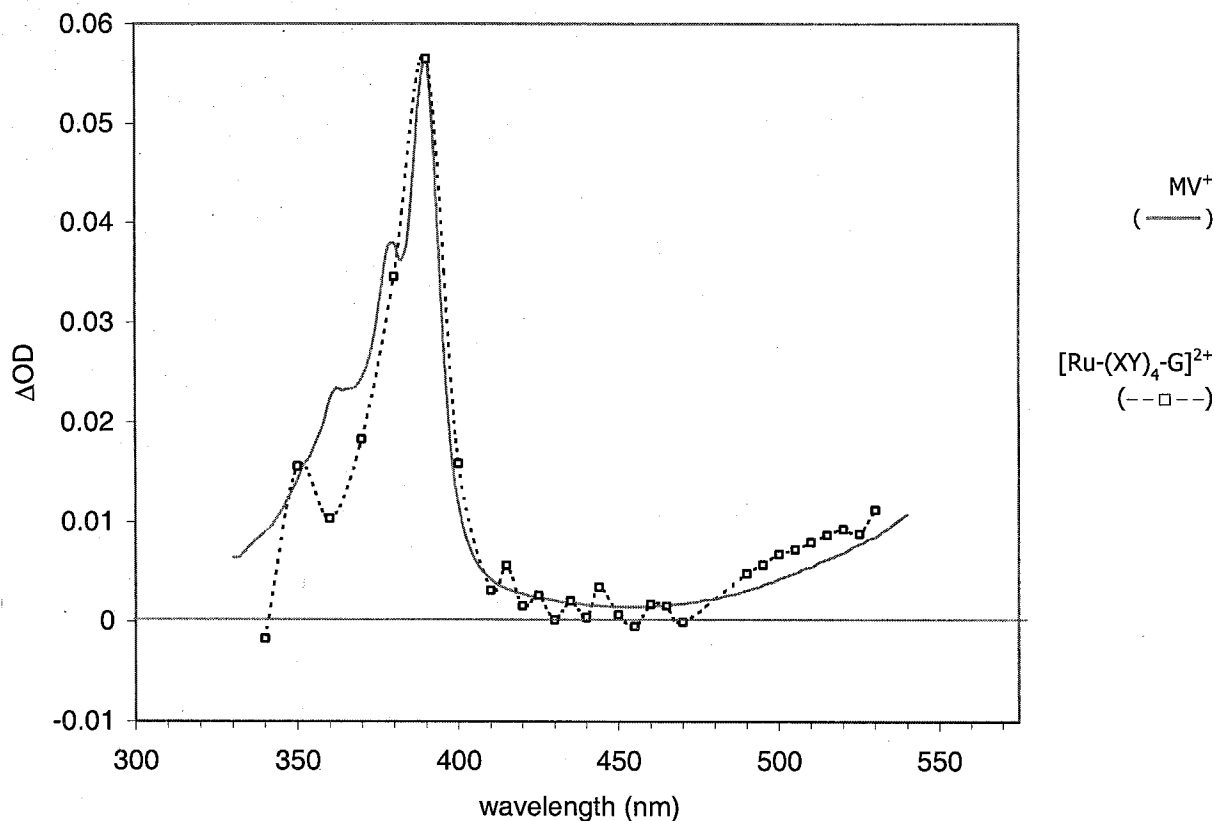
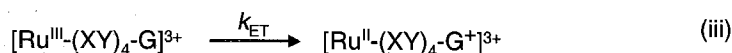
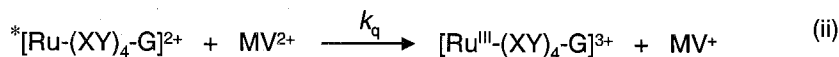
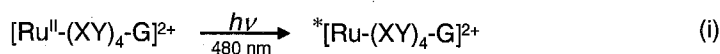


FIGURE 4.20 – Comparison of MV^+ to $[Ru-(XY)_4-G]^{2+}$
 $(Ru^{III}-G \rightarrow Ru^{II}-G^+)$ Electron Transfer Products

Comparison of reduced quencher MV^+ to the difference spectrum of $[Ru-(XY)_4-G]^{2+}$ in the presence of 5.3 mM MV^{2+} . The MV^+ spectrum is from spectroelectrochemistry experiments. The trace was taken 45 μs after the laser pulse. MV^+ was normalized at 390 nm to the ΔOD of the difference spectrum. The extra absorbance at 520 nm, relative to MV^+ , is indicative of $[Ru^{II}-(XY)_4-G^+]^{3+}$ formation.

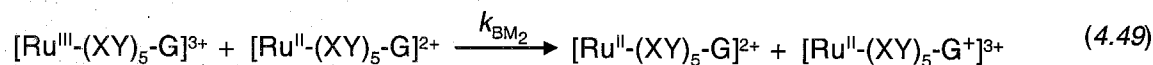
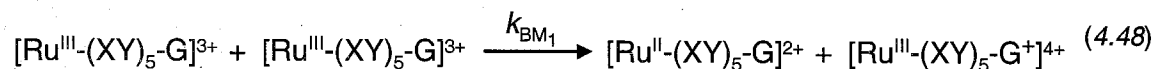
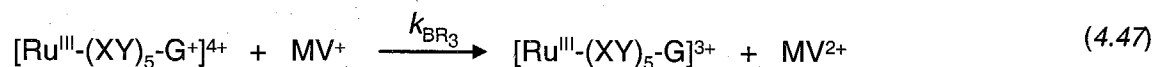
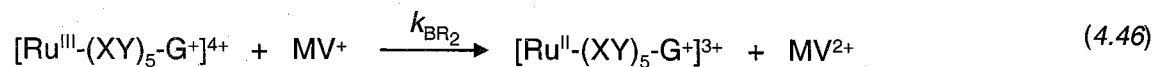
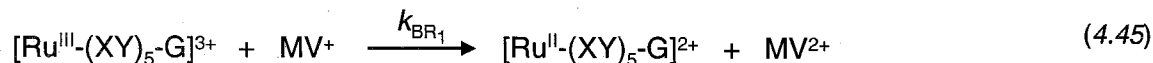
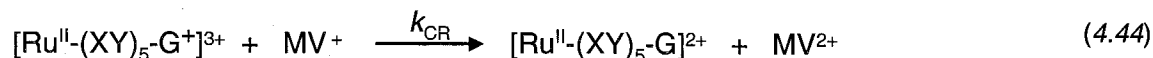
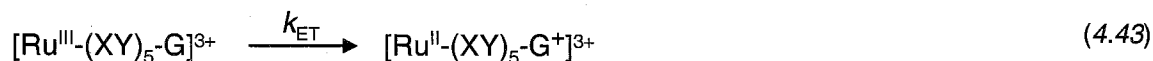
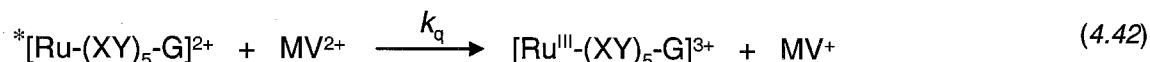
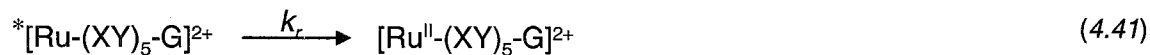
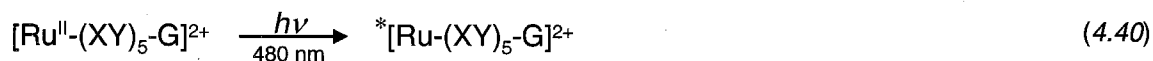


4.18 [Ru-(XY)₅-G]²⁺ Electron Transfer Experimental Methods and Analysis

The electron transfer reactions pertinent to measuring k_{ET} for [Ru-(XY)₅-G]²⁺ are outlined in Scheme 4.4.

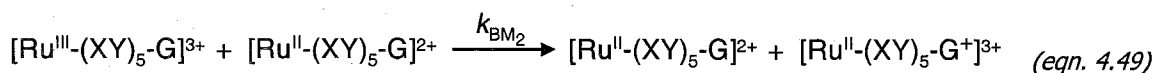
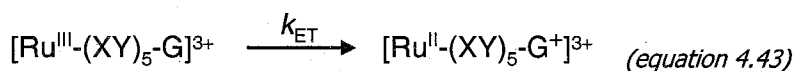
Scheme 4.4

Relevant Reactions for Measuring the Electron Transfer Kinetics of
[Ru-(XY)₅-G]²⁺ Under Flash-Quench Conditions



Of the competing reactions for consumption of the electron transfer reactant $[\text{Ru}^{\text{III}}-(\text{XY})_5-\text{G}]^{3+}$, the bimolecular reaction in equation 4.49 is the most problematic. When the electron transfer reaction proceeds more slowly than this bimolecular reaction, the observed rate constant, from time-resolved transient absorption measurements, is not solely due to k_{ET} . Because the reaction in equation in 4.49 is bimolecular, directly comparing k_{BM_2} to k_{ET} is not possible. Likewise, extracting k_{ET} from k_{obs} is not as straightforward as fitting transient absorption data to exponential functions. Due to the small concentration (1–3 μM) of reactants, the other bimolecular reactions, k_{BR_1} and k_{BM_1} , consume orders of magnitude less $[\text{Ru}^{\text{III}}-(\text{XY})_5-\text{G}]^{3+}$ than k_{ET} and k_{BM_2} . Therefore, the other bimolecular reactions are negligible and ignored for this analysis.

To determine k_{ET} , k_{obs} was measured as a function of $[\text{Ru}-(\text{XY})_5-\text{G}]^{2+}$ concentration. k_{obs} refers to the rate constant derived from fitting single-wavelength transient absorption traces, taken under flash-quench conditions, to exponential decay functions (equation 4.10 – 4.12). The major pathways for forming the electron transfer product, $[\text{Ru}^{\text{II}}-(\text{XY})_5-\text{G}^+]^{3+}$, are equations 4.43 and 4.49,



Based on these two reactions, a equation for product formation can be written,

$$\frac{\partial}{\partial t} [\text{Ru}^{\text{II}}-(\text{XY})_5-\text{G}^+] = k_{\text{ET}} [\text{Ru}^{\text{III}}-(\text{XY})_5-\text{G}] + k_{\text{BM}_2} [\text{Ru}^{\text{III}}-(\text{XY})_5-\text{G}][\text{Ru}^{\text{II}}-(\text{XY})_5-\text{G}] \quad (4.50)$$

Typical yields of the flash-quench product, $[\text{Ru}^{\text{III}}-(\text{XY})_5\text{-G}]^{3+}$, were 5 to 10%. The initial concentration of the donor-bridge-acceptor complex ranged from 0.9 μM to 80 μM . In general, a factor of 10 to 20 more $[\text{Ru}^{\text{II}}-(\text{XY})_5\text{-G}]^{2+}$ was present than $[\text{Ru}^{\text{III}}-(\text{XY})_5\text{-G}]^{3+}$. Therefore, equation 4.50 can be simplified by invoking pseudo-first-order conditions with respect to $[\text{Ru}^{\text{II}}-(\text{XY})_5\text{-G}]^{2+}$,

$$\frac{\partial}{\partial t} [\text{Ru}^{\text{II}}-(\text{XY})_3\text{-G}^+] = k_{\text{ET}} [\text{Ru}^{\text{III}}-(\text{XY})_5\text{-G}] + k' [\text{Ru}^{\text{III}}-(\text{XY})_5\text{-G}] \quad (4.51)$$

where,

$$k' = k_{\text{BM2}} [\text{Ru}^{\text{II}}-(\text{XY})_5\text{-G}] \quad (4.52)$$

Equation 4.52 can then be written in terms of one observable rate constant, k_{obs} , that is the sum of all first-order processes that produce $[\text{Ru}^{\text{II}}-(\text{XY})_5\text{-G}^+]^{3+}$,

$$\frac{\partial}{\partial t} [\text{Ru}^{\text{II}}-(\text{XY})_3\text{-G}^+] = k_{\text{obs}} [\text{Ru}^{\text{III}}-(\text{XY})_5\text{-G}] \quad (4.53)$$

where,

$$k_{\text{obs}} = k' + k_{\text{ET}} \quad (4.54)$$

Rewriting equation 4.54 gives a linear relationship between k_{obs} , k_{BM2} , and k_{ET} (equation 4.55). A plot of k_{obs} versus $[\text{Ru}-(\text{XY})_5\text{-G}]^{2+}$ concentration gives a y-intercept of k_{ET} .

$$k_{\text{obs}} = k_{\text{BM2}} [\text{Ru}-(\text{XY})_5\text{-G}]^{2+} + k_{\text{ET}} \quad (4.55)$$

4.19 [Ru-(XY)₅-G]²⁺ Electron Transfer Kinetics

Unlike [Ru-(XY)₂-G]²⁺ and [Ru-(XY)₃-G]²⁺, there are no concerns over the electron transfer reaction for [Ru-(XY)₅-G]²⁺ being faster than the flash quench or instrumentation upper speed limit. Figure 4.21 consists of single-wavelength transient absorption traces of a ~2 μM sample of [Ru-(XY)₅-G]²⁺ with 5 mM MV²⁺. The traces were fit to biexponential functions; the first rate constant matched k_{lum} and was assigned to the quenching reaction. The second, slower kinetic phase was labeled k_{obs} , and had a value of $7.5 \times 10^3 \text{ s}^{-1}$ at 460 nm and $5.7 \times 10^3 \text{ s}^{-1}$ for 500 nm. Changes to the MLCT band occur in the vicinity of 460 nm and represent consumption of the reactant, [Ru^{III}-(XY)₅-G]³⁺. The formation of product, [Ru^{II}-(XY)₅-G⁺]³⁺ is characterized by absorption at 500 nm. Based on the previous discussion, it is not accurate to call the observed rate constant k_{ET} .

The intrusion of a bimolecular electron transfer reaction (k_{BM2} , equation 4.49) is evident from the [Ru-(XY)₅-G]²⁺ concentration dependence of k_{obs} (Figure 4.22). For a given [Ru-(XY)₅-G]²⁺ concentration, k_{obs} was obtained by averaging at least two different wavelengths—one was in the region of the MLCT band (450 nm) and the other accounted for absorption due to [Ru^{II}-(XY)₅-G⁺]³⁺ formation (500 nm). The concentration of [Ru-(XY)₅-G]²⁺ was estimated by converting measured steady-state absorbances. [Ru-(XY)₃-G]²⁺, [Ru-XY-TMS]²⁺, and [Ru(bpy)₃]²⁺ were used as model complexes to estimate extinction coefficients for [Ru-(XY)₅-G]²⁺. The use of an estimation for the [Ru-(XY)₅-G]²⁺ concentration does not affect the determination of k_{ET} .

From equation 4.55, k_{ET} is the y-intercept of the plot in Figure 4.22; whether the actual absorbance values, estimates of $[\text{Ru}(\text{XY})_5\text{-G}]^{2+}$ concentrations based on steady-state sample absorbances, or the actual concentrations are used only affects the slope and not the intercept of the plot. A linear least-squares regression of the data in Figure 4.22 yields a k_{ET} for $[\text{Ru}(\text{XY})_5\text{-G}]^{2+}$ of $6 \pm 1 \times 10^3 \text{ s}^{-1}$ (with an R^2 of 0.99).

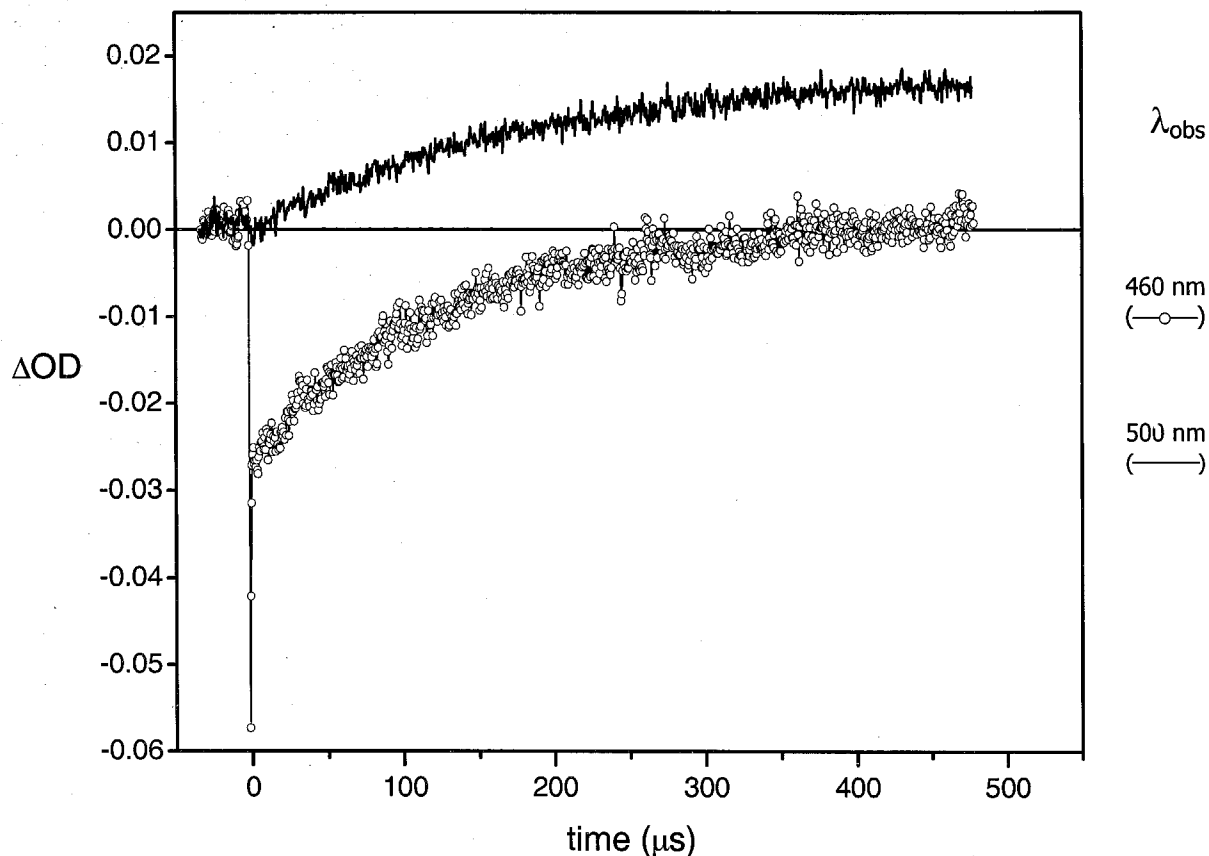
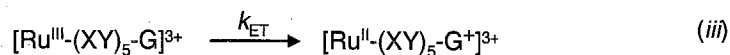
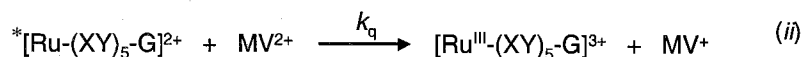
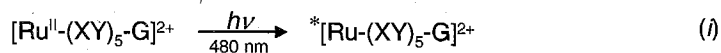


FIGURE 4.21 – $[\text{Ru}(\text{XY})_5\text{-G}]^{2+}$ Transient Absorption Spectra under Flash-Quench Conditions

Single wavelength transient absorption spectra of $[\text{Ru}(\text{XY})_5\text{-G}]^{2+}$ with 5 mM MV^{2+} . The samples were excited with 480 nm light and the spectra recorded at 460 nm (monitoring reactant consumption) and 500 nm (product formation). The observed rate constant, k_{obs} , was $7.5 \times 10^3 \text{ s}^{-1}$ at 460 nm and 5.7×10^3 at 500 nm.



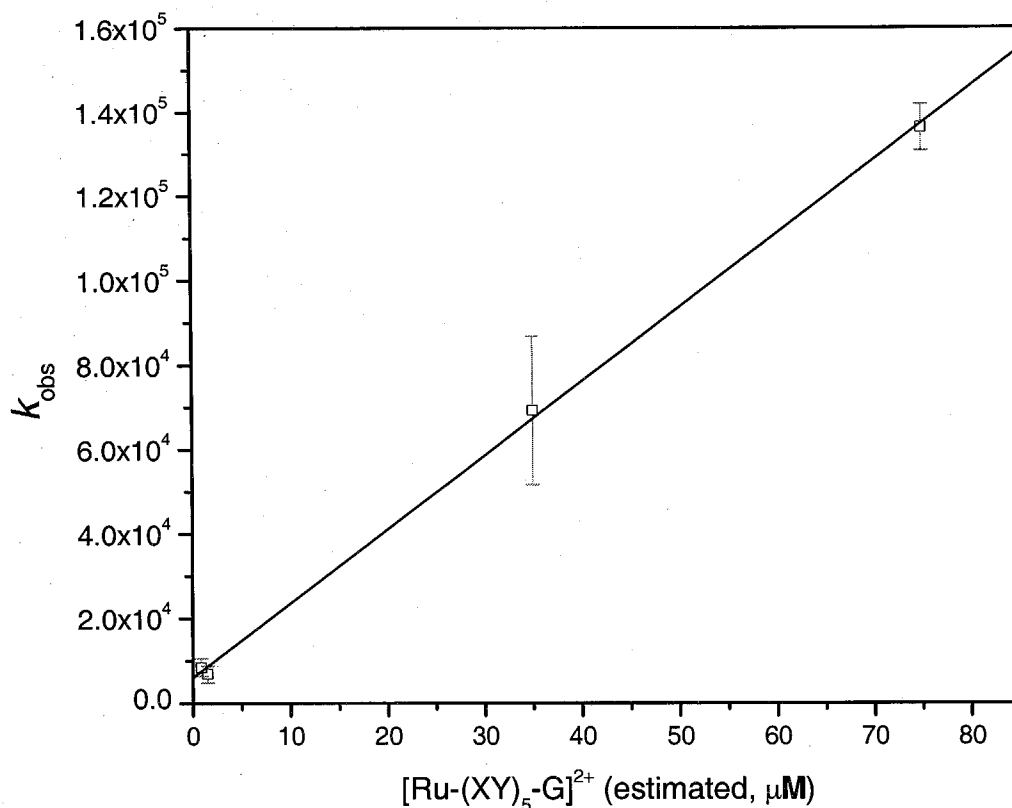
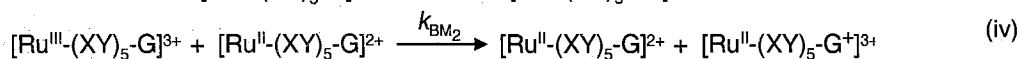
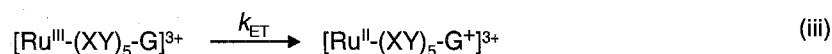
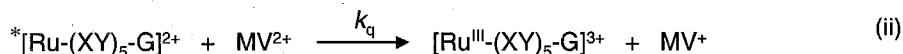
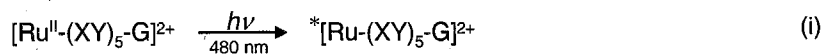


FIGURE 4.22 – Concentration Dependence of $[\text{Ru}-(\text{XY})_5\text{-G}]^{2+}$ Rates

Concentration dependence of k_{obs} on $[\text{Ru}-(\text{XY})_5\text{-G}]^{2+}$. k_{obs} was determined from exponential fits of single-wavelength transient absorption spectra taken over several observation wavelengths that are indicative of reaction progress. The concentration of $[\text{Ru}-(\text{XY})_5\text{-G}]^{2+}$ was calculated based on converting absorbances using estimates for the extinction coefficient. k_{obs} represents both the electron transfer reaction (equation iii) and the bimolecular reaction (equation iv).



DISCUSSION

4.20 [Ru-(XY)_n-G]²⁺ Electron Transfer Kinetics Summary

The flash-quench method¹²⁹ was utilized to measure the electron transfer rate constant, k_{ET} , for the donor-bridge-acceptor series [Ru-(XY)_n-G]²⁺, where n= 2 to 5 (equation 4.56, Scheme 4.1).

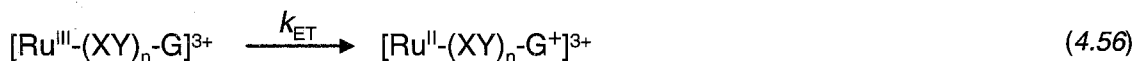


Table 4.4 (summarized below) lists the electron transfer rate constants, k_{ET} . For each complex, the electron transfer rate was measured at several wavelengths. The main criterium for determining k_{ET} was the rate of product formation should match the rate of reactant consumption. Spectral changes at 460 nm are diagnostic for [Ru^{III}-(XY)_n-G]³⁺ consumption and product formation ([Ru^{II}-(XY)_n-G⁺]³⁺) was monitored at 500 nm.

TABLE 4.4 (Summarized)

[Ru-(XY) _n -G] ²⁺ Electron Transfer Kinetics under Flash-Quench Conditions	
compound	k_{ET}^a (s ⁻¹)
[Ru-(XY) ₂ -G] ²⁺	$> 1 \times 10^8$ ^b
[Ru-(XY) ₃ -G] ²⁺	$9.0 \pm 0.3 \times 10^6$
[Ru-(XY) ₄ -G] ²⁺	$2 \pm 1 \times 10^5$
[Ru-(XY) ₅ -G] ²⁺	$6 \pm 1 \times 10^3$

^a k_{ET} was determined using the flash-quench method. k_{ET} was measured at several wavelengths and averaged to obtain the values shown.

^bThe rate constant for [Ru-(XY)₂-G]²⁺ is faster than the instrument response.

It was not possible to measure the rate constant for [Ru-(XY)₂-G]²⁺ due to limitations of the flash-quench method and instrumentation. The observed rate constant, k_{obs} , tracked with the quenching process (k_q , equation 4.4) up to the highest, experimentally possible quencher concentration, 80 mM MV²⁺. This amount of quencher yielded a response-limited luminescence decay constant, k_{lum} , of 1×10^8 s⁻¹. While the flash-quench method will support higher concentrations of quencher, k_{ET} is faster than the instrument response. Therefore, a lower limit on the electron transfer rate constant is placed at 1×10^8 s⁻¹. Transient difference spectra confirmed the formation of [Ru^{II}-(XY)₂-G⁺]³⁺ rather than the excited state product, [Ru^I-(XY)₂-G⁺]²⁺.

For low concentrations of MV^{2+} (< 12 mM), the observed rate constant for $[Ru-(XY)_3-G]^{2+}$ was also limited by the quenching process. Quencher concentration studies yielded a k_{ET} of $9.0 \pm 0.3 \times 10^6 \text{ s}^{-1}$ for $[Ru-(XY)_3-G]^{2+}$ when $[MV^{2+}]$ was greater than 47 mM. Above this point, k_{ET} did not vary with quencher concentration. Transient difference spectrum confirmed the formation of $[Ru^{II}-(XY)_3-G^+]^{3+}$, the product of the electron transfer reaction.

Measuring the rate constant for $[Ru-(XY)_4-G]^{2+}$ was relatively straightforward and yielded a k_{ET} of $2 \pm 1 \times 10^5 \text{ s}^{-1}$. As with the two previous complexes, transient difference spectra confirmed the formation of the electron transfer product, $[Ru^{II}-(XY)_4-G^+]^{3+}$. Competition from bimolecular electron transfer reactions (k_{BM2} , equation 4.49) required the extrapolation of k_{ET} for $[Ru-(XY)_5-G]^{2+}$. The observed rate constant, k_{obs} , was measured with varying concentrations of $[Ru-(XY)_5-G]^{2+}$. Applying pseudo-first-order conditions, a plot of k_{obs} versus $[Ru-(XY)_5-G]^{2+}$ concentration yielded a k_{ET} of $6 \pm 1 \times 10^3 \text{ s}^{-1}$. Figure 4.23 is a schematic of how the rate constants for the series of donor-bridge-acceptor complexes compare with the limits of the instrument, flash-quench method, and competing bimolecular reactions.

4.21 Experimental Considerations for Determining β

To evaluate and characterize electron transfer through phenylene bridges, it is essential to experimentally determine the distance decay constant, β . For a given donor-acceptor pair, β is the best experimental means to assess and compare the efficiency of electron transfer mediated through a bridge. Chemical factors, such as geometry, orientation, electronic structure, and redox potential, affect β . Factors not

related to the tunneling medium, such as driving force and reorganizational energy (λ), do not affect β , however. Literature reports demonstrate that β values tend to track and cluster based on chemical motif.^{165,167,168} The ability to use β as a means to compare the electron transfer properties and efficiencies of different chemical structures is an extremely powerful tool.

Experimentally determining β requires three key pieces: (1) a series of donor-bridge-acceptor complexes that have a consistent donor-acceptor pair, a bridge that can be systematically varied in length, and is experimentally amenable to measuring k_{ET} , (2) measured values of k_{ET} for the series of complexes, and (3) known distances between the donor and acceptor. The first piece, the design and synthesis of a donor-bridge-acceptor system was discussed in chapter 2. The majority of this chapter thus far has dealt with piece number 2. The third piece requires knowledge of not just the geometries of the complexes but also an understanding of the electronic structure of the donor, bridge, and acceptor.

4.22 Donor-Acceptor Distances

Electron transfer reactions are redox process and, as such, involve the formation or consumption of oxidized or reduced species. The localization or delocalization of charge on the donor or acceptor can change dramatically upon oxidation or reduction. Reduction of ruthenium polypyridyl complexes from $Ru^{III} \rightarrow Ru^{II}$ largely affects the metal center and not the ancillary ligands.¹⁶⁹ The aromatic amine donor, ethynyl-G, is oxidized during the course of the electron transfer reaction. Judging by the redox potential, the radical cation originates from the amine functionality. There is significant delocalization

over the aromatic ring and adjoining acetylene moiety, however, which could result in the radical cation having significant density closer to the bridge. These factors affect the endpoints for the donor-acceptor distance.

Besides determining where the donor and acceptor are localized, there is the issue of how to calculate the distance: through bond or through space. The variability of β -values for different chemical structures implies through bond distances are more accurate than through space. The bipyridine ligand, xylene bridge, and aromatic amine donor have significant aromatic character and electron delocalization. The method for measuring the tunneling distance through an aromatic ring, either using a circuitous route along the bonds or a straight path through the center, has a big impact on β . For these complexes, a hybrid model is required in which aromatic and highly delocalized structures are calculated using the through space distance while the through bond method is used everywhere else. (Figure 4.24).

An X-ray crystal structure of the complexes would provide useful structural information, but attempts to crystallize $[\text{Ru}-(\text{XY})_n-\text{G}]^{2+}$ were unsuccessful. The combination of a relatively "greasy" organic tail and a charged metal complex made crystallization difficult. The attempts were further hampered by a lack of sufficient material. While crystal structures would provide very accurate bond lengths, it is insufficient data for calculating electron tunneling distances because of redox localization and electronic coupling issues previously discussed. In the absence of DFT calculations, an approach to determining tunneling distances is to evaluate all plausible tunneling pathways to create an upper and lower bound for β . This method will be discussed followed by the choice of the most reasonable electron tunneling path.

Representative bond lengths for aromatic rings, carbon-carbon bonds between adjacent rings, the bipyridine ligand, and the donor were calculated using molecular modeling. Figure 4.25 shows all of the pertinent bonds and Table 4.5 lists the lengths from calculations, and from a crystal structure of TMS-(XY)₂-TMS. Eight pathways that are relevant to electron tunneling were identified and labeled 'a' through 'h' as depicted in Figure 4.26. Table 4.6 lists the donor-acceptor distances, r , as a function of n (number of xylene units), using the segment lengths in Table 4.5. The calculated tunneling distances vary from 8.68 Å to 43.09 Å along the series $n = 2$ to 5.

4.23 Electron Transfer Distance Decay Constant – β

Taking the rate constants from Table 4.4 and the distances from Table 4.6, a series of β -plots were constructed (Figure 4.27). Utilizing equation 4.57, β and the close contact electron transfer rate constant, k_0 , can be determined from linear least squares regression of the plots in Figure 4.27.

$$k_{\text{ET}} = k_0 e^{-\beta r} \quad (\text{equation 4.19})$$

$$\ln k_{\text{ET}} = \ln k_0 - \beta r \quad (4.57)$$

The variations among the distances calculated in Table 4.6 stem from either assuming a through bond versus a hybrid tunneling pathway or from the differences in endpoints for the donor-acceptor. β is derived from the slope of the plots in Figure 4.27 and is only affected by changes to the tunneling distance of an individual xylene

monomer. Therefore, two β -values come out of this analysis: 0.64 \AA^{-1} for the through bond pathway and 0.84 \AA^{-1} for the hybrid pathway. k_0 is not affected by the different tunneling pathway models but does vary with changing endpoints. Table 4.7 summarizes the k_0 values for pathways 'a' through 'h'. Typical values for k_0 are on the order of 10^{13} to 10^{15} ; based on these trends, pathway b, c, through bond d, and hybrid h are ruled out.

The field of eight possible tunneling pathways can be narrowed further. A given tunneling pathway can be assessed by examining the intersection of the through bond and hybrid β -lines. The distance, r , at which this occurs reveals the suitability of a tunneling pathway. The close contact rate constant, k_0 , is based on $r = 0 \text{ \AA}$, a situation that is not chemically realistic. A more appropriate metric is the closest approach distance (analogous to van der Waals contact distance), r_0' (Figure 4.28). Given that ruthenium is buried within the core of the octahedral polypyridyl framework, if the donor were free in solution, it would not be able to achieve a close contact distance of 0 \AA . Rather, the minimum separation between the donor and acceptor is referred to as the closest approach distance.

The presence of the bipyridine ligands and similar obstructions on the donor yield a closest approach distance of 3 to 7 \AA for $[\text{Ru}(\text{XY})_n\text{-G}]^{2+}$. The closest approach distance is only a function of the donor-acceptor chemical structures and electronic properties, not β or the bridge. The β -plots in Figure 4.27 represent one pathway using two different models: through bond or hybrid. The intersection of these two lines gives the closest approach distance (Table 4.8). This analysis rules out pathways a, b, c, and f as having an r_0' that is too small.

The analysis of k_0 and r_0' leaves the following viable pathways: hybrid d, e, g, and through bond h. Hybrid pathway g is the most reasonable based on the chemical nature of the donor, bridge, and acceptor, k_0 , and r_0' . Pathway g localizes the acceptor on the ruthenium, and the donor on the closest edge. The distance was calculated using the hybrid method, which takes into account the aromatic nature of the phenylene bridging ligand. Therefore, based on the measured electron transfer rates combined with the estimated donor-acceptor distances (Figure 4.29), the β -value for $[\text{Ru}(\text{XY})_n\text{-G}]^{2+}$ is 0.84 \AA^{-1} .

4.24 Conformational Effects on Electron Transfer

Several reports have established the role of chemical structure on electron transfer rates.¹⁷⁰⁻¹⁷⁴ For long distances ($> 10 \text{ \AA}$), the intervening medium must be involved to facilitate electron transfers. The distance decay constant, β , is an experimentally measurable property that connects chemical structure to electron transfer efficiency. A survey of literature reports reinforces the connection between β and chemical structure.

β -values tend to cluster based on different chemical groups: aliphatics, aromatic oligomers, and highly conjugated π -systems. For the most part, aliphatic compounds (including hydrocarbons and proteins) have β -values around 1 \AA^{-1} .^{167,175-179} Highly conjugated systems, such as alkenes or phenylethynylenes, typically have β -values less than 0.2 \AA^{-1} .^{168,180} Phenylene oligomers have β 's around 0.4 \AA^{-1} .^{7,165} The clustering of β -values can be understood by taking an electronic coupling view of chemical structure. Aliphatic compounds, made solely of a sigma-bonded network, are highly localized and

prove to be inefficient media for electron transfer reactions. Highly delocalized π -systems, such as alkenes or phenylethynylenes, are on the other end of the electron transfer spectrum. This class of compounds exhibits extended electronic delocalization and is well suited for rapid, long-range electron transfer.

Oligomeric aromatic compounds, which include the substituted phenylenes in this thesis, fall in between weakly coupled aliphatics and highly conjugated π -systems. The individual rings of a phenylene oligomer would fall into the highly conjugated category. The interconnections between rings are sigma bonds, however. Numerous studies place the tilt angle of adjacent rings somewhere between 25 and 50°. ¹³⁵⁻¹³⁸ Any orientation that places the rings out of planarity reduces the electron tunneling efficiency.

Compared to other types of bridges, there are only a limited number of reports on aromatic oligomers. ^{5-13,100,101} Many of the reports are based on phenylethynylene oligomers ¹³⁰⁻¹³³ that fall into the highly conjugated chemical group. The most notable reports of aromatic oligomers as electron transfer media are from De Cola ⁷ and McLendon ^{165,173}. De Cola studied a series of donor-bridge-acceptor complexes consisting of Ru/Os or Os/Os donor-acceptor pairs with phenylene oligomers ($n = 3$ to 7) as bridges. The phenylene bridges of the Os/Os complexes were unsubstituted and gave a ground state electron transfer β of 0.36 Å⁻¹. The bridge of the Ru/Os complexes were also unsubstituted phenylenes, except for the center ring which was functionalized with two hexyl groups for solubility. That series of complexes also had a ground state β of 0.36 Å⁻¹. McLendon used unsubstituted phenylene in their study of Zn/Fe diporphyrin donor-bridge-acceptor complexes, and reported an excited-state electron transfer β of 0.4 Å⁻¹.

The β for $[\text{Ru}(\text{XY})_n\text{-G}]^{2+}$ is twice that of the systems reported by De Cola and McLendon. Because β is an exponential decay constant, small changes in its value translate into large effects on k_{ET} . A β that is double the typical values reported in the literature must be due to a significant difference between $[\text{Ru}(\text{XY})_n\text{-G}]^{2+}$ and the other systems. The major difference between $[\text{Ru}(\text{XY})_n\text{-G}]^{2+}$ and the systems from De Cola and McLendon is the ring substituents. The individual rings of the bridge in $[\text{Ru}(\text{XY})_n\text{-G}]^{2+}$ are all identical, based on 2,5-dimethylbenzene. The literature systems are either unsubstituted or only contain one substituted ring.

Substituents can affect the electronic properties of an aromatic ring that manifest through changes in redox potentials, NMR chemical shifts, absorption spectra, and many other physical quantities. The lack of variation across the series $[\text{Ru}(\text{XY})_n\text{-G}]^{2+}$ would make any substituent-induced electronic effects on the bridge negligible. Rather, the presence of methyl substituents causes a structural and conformational bridge effect; the result is a β for $[\text{Ru}(\text{XY})_n\text{-G}]^{2+}$ that is double the expected value. The addition of substituents, ortho to the phenylene axis, causes the twist angle to increase significantly. For $[\text{Ru}(\text{XY})_n\text{-G}]^{2+}$, an orthogonal conformation of the xylene rings is consistent with the high β -value.

There is a strong dependence of the coupling through phenylenes on twist angle. A 0° twist angle would place all of the rings in the same plane and create a highly delocalized π -system. β 's for such a bridge would be $< 0.2 \text{ \AA}^{-1}$. Intermediate twist angles would attenuate the electronic coupling and lead to a β of $\sim 0.4 \text{ \AA}^{-1}$. At 90° most, if not all, inter-ring conjugation is lost and the electronic communication between rings is through sigma bonds and second-order effects only. As a consequence, a 90° twist angle would yield a β closer to 1 \AA^{-1} rather than 0.4 \AA^{-1} . Both De Cola and McLendon's

systems should have twist angles within the normal range of 22 to 50°, thus consistent with a β of $\sim 0.4 \text{ \AA}^{-1}$. Calculations and information obtained from a crystal structure of TMS-(XY)₂-TMS (Figure 4.30) show that the twist angle is 90°.

The connection between chemical structure and β is an incredibly useful research tool. Novel materials can be designed to have certain electron transfer properties, using β -values as a guide. β is also a means for comparing the efficiency of xylene oligomers in this study to other bridges.

TABLE 4.4 – $[\text{Ru}(\text{XY})_n\text{-G}]^{2+}$ Electron Transfer Kinetics
 $[\text{Ru}^{\text{III}}(\text{XY})_n\text{-G}]^{3+} \rightarrow [\text{Ru}^{\text{II}}(\text{XY})_n\text{-G}^+]^{3+}$

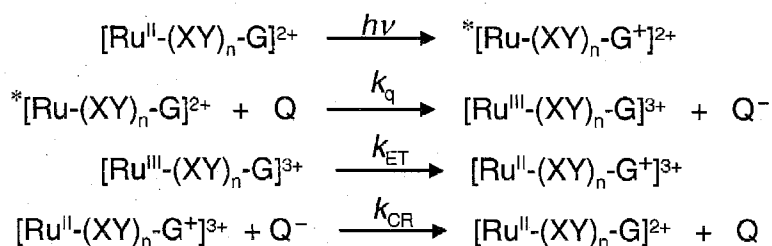
compound	k_{ET}^{a} (s^{-1})	$r_{\text{min}}^{\text{b}}$ (\AA)	$r_{\text{max}}^{\text{b}}$ (\AA)	r^{c} (\AA)
$[\text{Ru}(\text{XY})_2\text{-G}]^{2+}$	$> 1 \times 10^8^{\text{d}}$	8.7	26.0	17.6
$[\text{Ru}(\text{XY})_3\text{-G}]^{2+}$	$9.0 \pm 0.3 \times 10^6$	13.0	31.7	22.0
$[\text{Ru}(\text{XY})_4\text{-G}]^{2+}$	$2 \pm 1 \times 10^5$	17.4	37.4	26.3
$[\text{Ru}(\text{XY})_5\text{-G}]^{2+}$	$6 \pm 1 \times 10^3$	21.7	43.1	30.6

^a k_{ET} was determined using the flash-quench method as outlined in the Scheme above. k_{ET} was measured at several wavelengths and averaged to obtain the values shown.

^b r is the donor-acceptor electron tunneling distance. The minimum or lower limit for r is based on an estimate for the shortest tunneling distance, utilizing the phenylene bridge only. Maximum r is the through-bond distance from ruthenium to the nitrogen of the donor.

^c Most probable electron tunneling distance.

^d The rate constant for $[\text{Ru}(\text{XY})_2\text{-G}]^{2+}$ is faster than the instrument response.



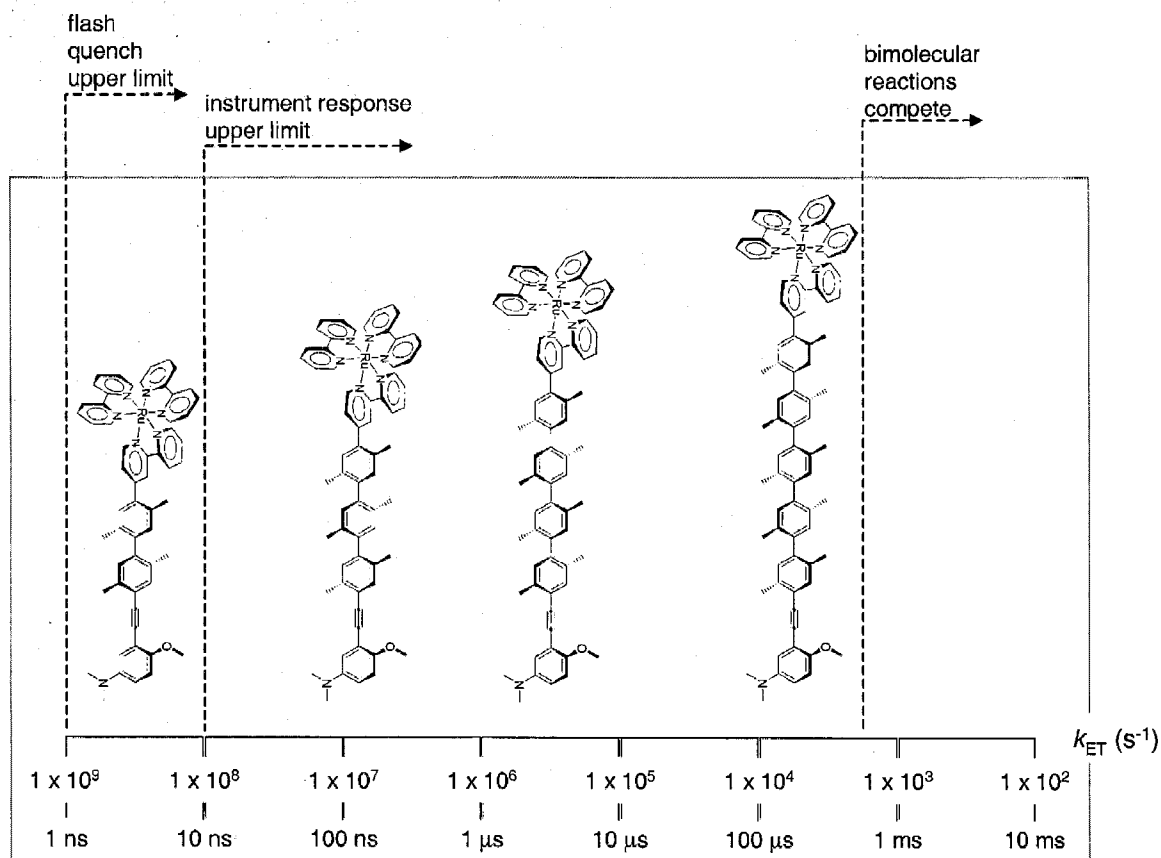
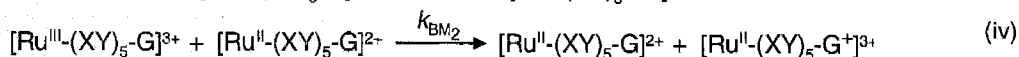
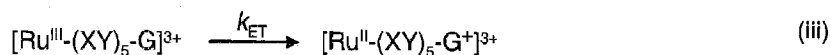
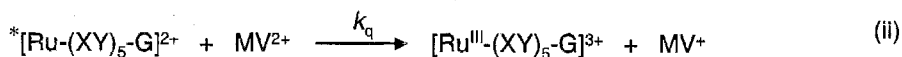
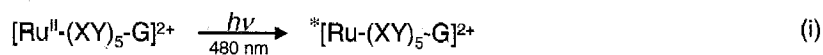


FIGURE 4.23 – $[\text{Ru}-(\text{XY})_n-\text{G}]^{2+}$ Electron Transfer Landscape

Schematic showing the ordering of electron transfer rates for $[\text{Ru}-(\text{XY})_n-\text{G}]^{2+}$. The placement of the donor-bridge-acceptor complexes is based on the rates in Table 4.4. The flash quench and instrument response upper limits represent the maximum rate that can be measured. Bimolecular electron transfer reactions begin to compete efficiently with intramolecular electron transfer (equation iii) at the point indicated. These limits are based on the previously described flash-quench method and laser flash photolysis instrument.



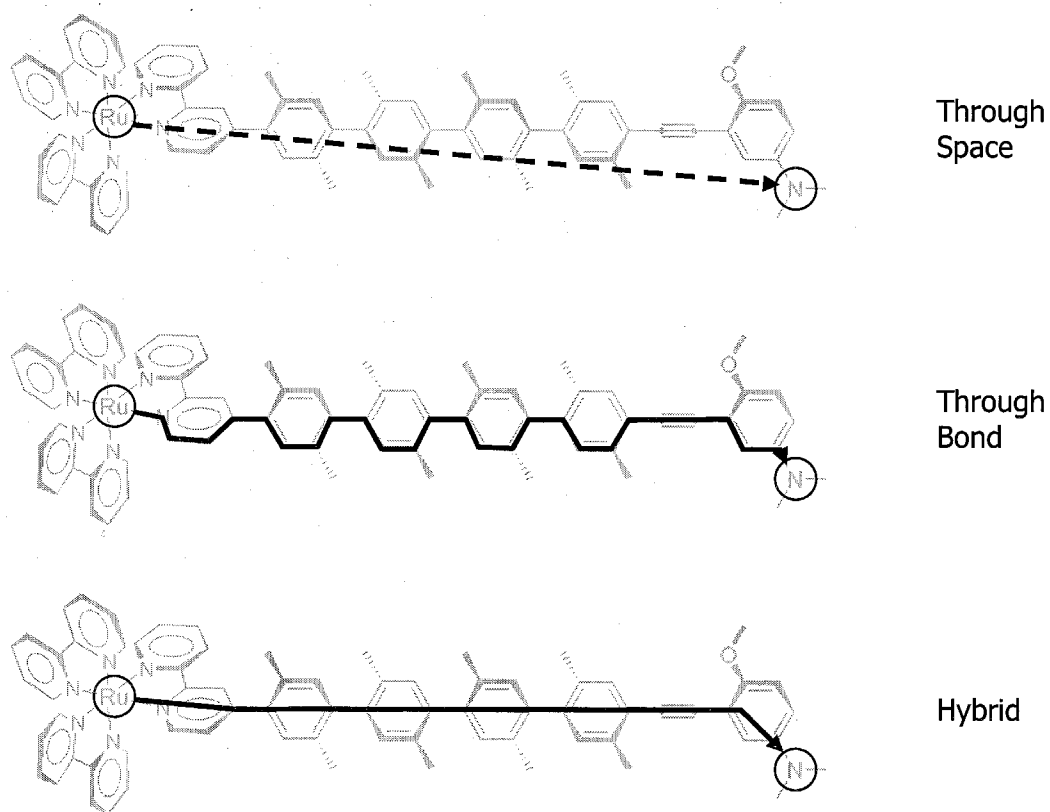


FIGURE 4.24 – Electron Tunneling Pathways

Three models for calculating donor-acceptor distances: Through-space uses the straight line-of-sight distance; Through-bond follows the most direct route through the most favorable bonds; Hybrid is a combination of the through space model, used when dealing with aromatic or highly delocalized structures, but follows the through-bond model everywhere else.

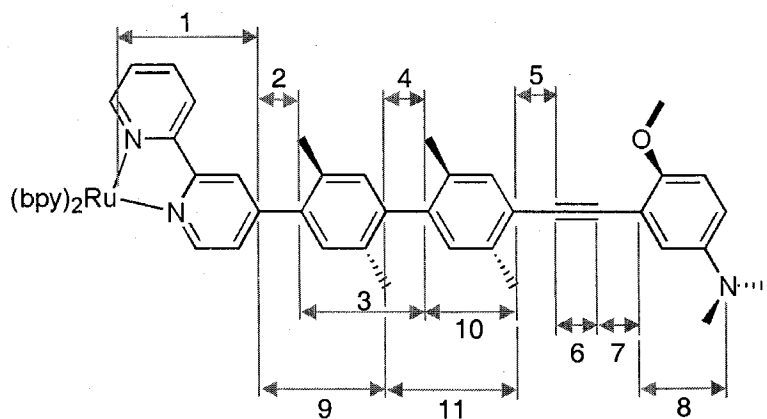


FIGURE 4.25 – Tunneling Segments

Schematic of tunneling segments of $[Ru-(XY)_n-G]^{2+}$ based on the through bond and hybrid methods.

TABLE 4.5 – Tunneling Segment Lengths

Segment ^a	Through-Bond (Å)	Hybrid (Å)	X-ray Structure (Å)
1	6.26	4.87	
2	1.49	1.49	
3	5.70	4.34	
4	1.49	1.49	1.51 ^b
5	1.43	1.43	
6	1.2	1.2	
7	1.43	1.43	
8	4.27	3.77	
9	5.7	4.34	
10	4.21	2.85	2.83 ^c
11	5.7	4.34	4.35 ^c

^aSee Figure 4.25 for legend.^bthrough-bond^chybrid

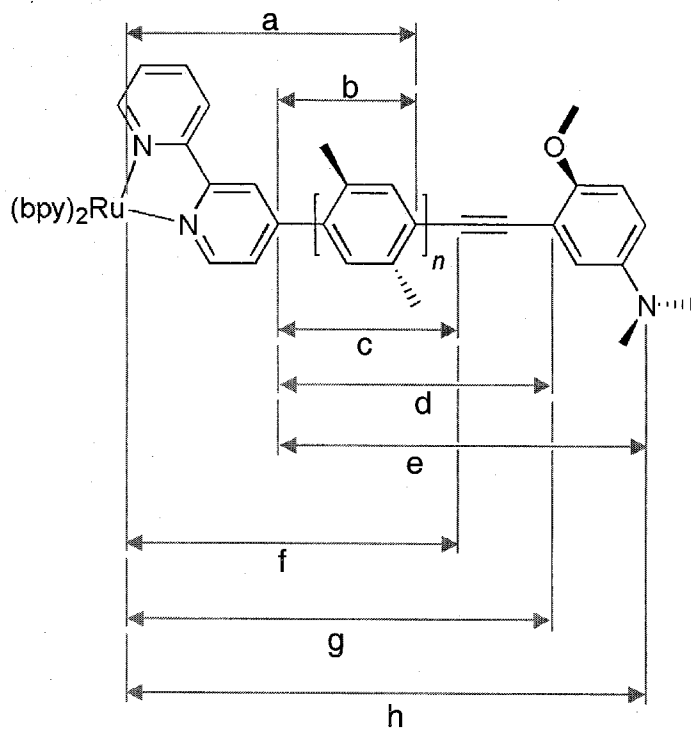


FIGURE 4.26 – $[\text{Ru}(\text{XY})_n\text{-G}]^{2+}$ Electron Tunneling Pathways

Schematic showing the relevant electron tunneling pathways for $[\text{Ru}(\text{XY})_n\text{-G}]^{2+}$.

TABLE 4.6 – Electron Tunneling Distances

Calculated donor-acceptor distances based on segments defined in Figure 4.25 and distances in Table 4.5 for pathways shown in Figure 4.26. For each complex (denoted by the number of xylyl rings, *n*), the donor-acceptor distance was calculated using the through-bond model ("bond") and the hybrid model ("hybrid").

n	a		b		c		d	
	bond	hybrid	bond	hybrid	bond	hybrid	bond	hybrid
2	17.66	13.55	11.4	8.68	12.83	10.11	15.46	12.74
3	23.36	17.89	17.1	13.02	18.53	14.45	21.16	17.08
4	29.06	22.23	22.8	17.36	24.23	18.79	26.86	21.42
5	34.76	26.57	28.50	21.7	29.93	23.13	32.56	25.76

n	e		f		g		h	
	bond	hybrid	bond	hybrid	bond	hybrid	bond	hybrid
2	19.73	16.51	19.09	14.98	21.72	17.61	25.99	21.38
3	25.43	20.85	24.79	19.32	27.42	21.95	31.69	25.72
4	31.13	25.19	30.49	23.66	33.12	26.29	37.39	30.06
5	36.83	29.53	36.19	28.00	38.82	30.63	43.09	34.40

FIGURE 4.27 – $[\text{Ru}(\text{XY})_n\text{-G}]^{2+}$ β -Plots

Each plot is labeled with a pathway from Figure 4.26. For each pathway, β was calculated from linear regression using either the through-bond (\circ) or hybrid (\square) distance models.

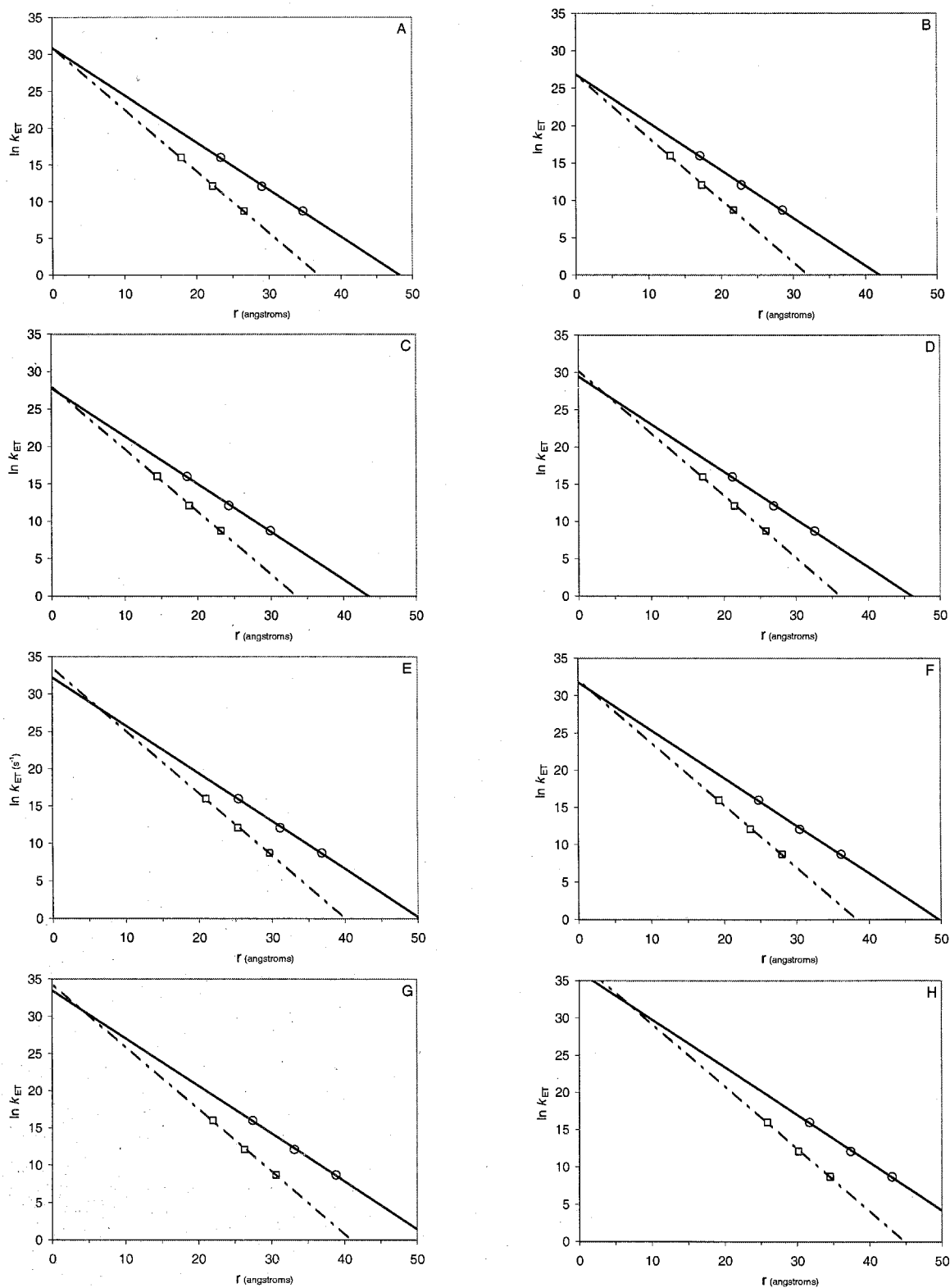


TABLE 4.7 – $[\text{Ru}(\text{XY})_n\text{-G}]^{2+}$ Close Contact
Electron Transfer Rates, k_0

Pathway ^a	k_0 (s^{-1})	
	Through-Bond	Hybrid ^b
a	2.6×10^{13}	2.8×10^{13}
b	4.7×10^{11}	4.7×10^{11}
c	1.2×10^{12}	1.6×10^{12}
d	6.3×10^{12}	1.4×10^{13}
e	9.7×10^{13}	3.8×10^{14}
f	6.4×10^{13}	9.3×10^{13}
g	3.5×10^{14}	8.5×10^{14}
h	5.3×10^{15}	2.3×10^{16}

^aSee Figure 4.26 for legend.

^bSee text for description of hybrid model.

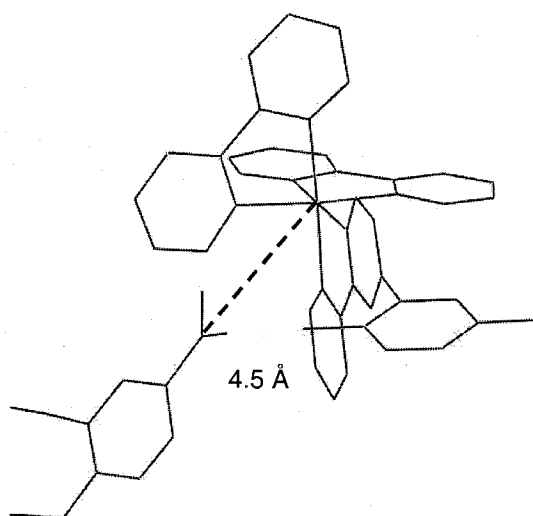


FIGURE 4.28 – Closest Approach Distance, r_o'

This cartoon illustrates the closest approach distance for untethered ethynyl-G and a ruthenium polypyridyl complex with a xylene-functionalized bipyridine ligand. The 4.5 Å distance labeled in the Figure is the closest approach distance, r_o' , for this donor-acceptor pair. It represents the shortest distance the two can come without incurring major steric clash.

TABLE 4.8 – $[\text{Ru}(\text{XY})_n\text{-G}]^{2+}$ Closest Approach Distances, r_o'

Pathway ^a	r_o' (Å)
a	0.4
b	0.0
c	1.4
d	4.1
e	6.8
f	1.9
g	4.5
h	7.3

^aSee Figure 4.26 for legend.

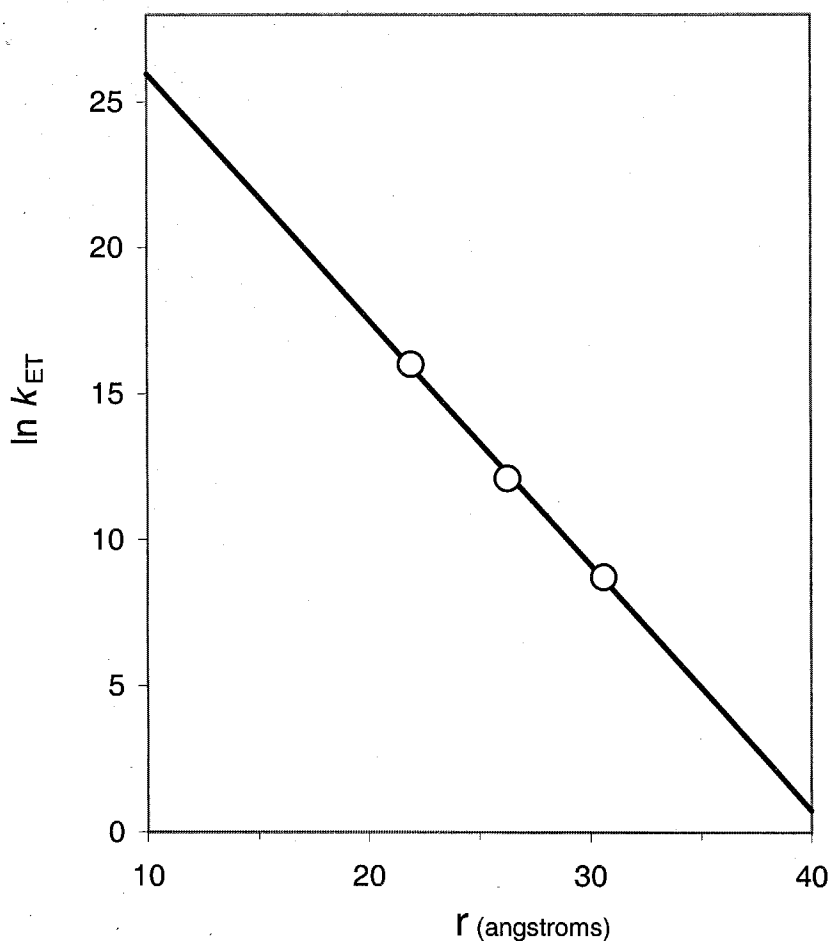
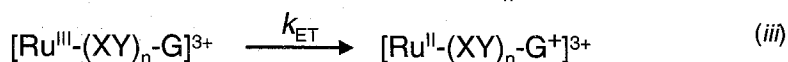
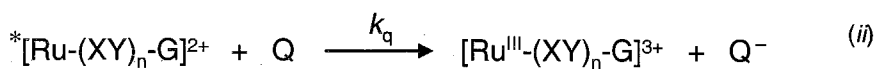


FIGURE 4.29 – Distance Dependence of $[\text{Ru}(\text{XY})_5\text{-G}]^{2+}$ Electron Transfer Rates (β – Plot)

β -plot of $[\text{Ru}(\text{XY})_n\text{-G}]^{2+}$ for the ground state intramolecular electron transfer in equation iii. k_{ET} was determined experimentally as listed in Table 4.4. The donor-acceptor separation, r , was estimated from pathway g (Figure 4.26), using the hybrid tunneling distance model. The slope (β) of the line, obtained from linear least squares regression, is 0.84 \AA^{-1} with an intercept (k_0) of 8.5×10^{14} and a R^2 of 0.99.



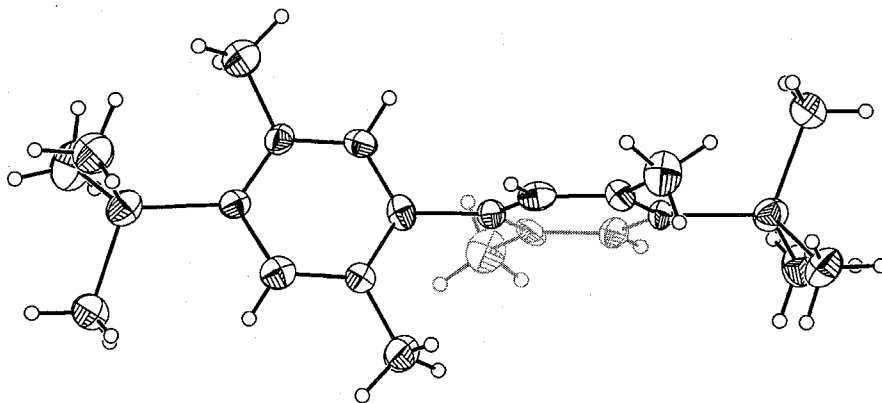


FIGURE 4.30 – TMS-(XY)₂-TMS X-ray Crystal Structure

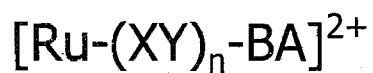
X-ray crystal structure of TMS-(XY)₂-TMS (2,2',5,5'-tetramethyl-4,4'-di(trimethylsilyl)-1,1'-biphenyl). The crystals were grown from layered solutions of methanol over dichloromethane. The twist angle is 87.2°; the ring-ring separation is 1.51 Å⁻¹.

CONCLUSION

Based on the β for $[\text{Ru}-(\text{XY})_n-\text{G}]^{2+}$ (0.84 \AA^{-1}), the twist angle for xylene oligomers, and comparisons with other systems, a connection can be made between the conformation of the bridge and electron transfer efficiency. The higher than expected β -value for $[\text{Ru}-(\text{XY})_n-\text{G}]^{2+}$ is due to the near-orthogonal twist angle conformation of the xylene bridge. The conformational bridge effects cause the electronic coupling in $[\text{Ru}-(\text{XY})_n-\text{G}]^{2+}$ to be more sigma-coupled than π -coupled. The lack of distance dependence in the redox potentials and steady-state absorption spectra, coupled with a β -value that suggests a more aliphatic-type electronic coupling, and crystallographic and computational evidence showing orthogonal rings, all support the conclusion that the conformation of the bridge, characterized by the twist angle, affects the electronic coupling between the donor and acceptor, the electron transfer rates, and distance decay constant β .

Chapter 5

SYNTHESIS,
CHARACTERIZATION, and
ELECTRON TRANSFER REACTIONS OF
NANOCRYSTALLINE TiO_2 SOLAR CELL DYES –



INTRODUCTION

5.1 Nanocrystalline TiO_2 Solar Cells

Solar cells operate on the basic premise of using light to generate a charge-separated state. Current is produced by directing the recombination process through an external circuit. Silicon semiconductors are the typical material for solar cells, but recently an alternative has emerged based on nanocrystalline TiO_2 . These solar cells have potential advantages over silicon including cheaper materials costs and greater design flexibility.¹⁸¹

Gratzel reported the first solar cell utilizing nanocrystalline TiO_2 .^{77,78} This is a wide band-gap semiconductor (3.2 eV) that absorbs ultraviolet light. The basic layout of the cell (Figure 5.1) involved coating a conducting electrode with TiO_2 particles. Upon excitation, valence band electrons are promoted to the conduction band and migrate out of the semiconductor to the electrode substrate. The charge then migrates through an external circuit and regenerates the cell, through the help of a redox couple. Nanocrystalline TiO_2 solar cells are often constructed with a dye that coats the semiconductor

particles. The dye acts as a sensitizer, increasing the spectral response of the solar cell into the visible and near-infrared.

Many fundamental questions are unresolved about the details of how TiO_2 solar cells operate. For example, the best performing combination of dye and electrolyte is $(\text{COOH}_2\text{-bpy})_2\text{Ru}(\text{NCS})_2$ and I^-/I_3^- .^{77,78,182} No other combination has been found that produces better results, nor is there any understanding on how to rationally design dyes for TiO_2 solar cells. Because each step in the solar energy conversion process involves an electron transfer reaction (intramolecular, intermolecular, and interfacial), fundamental studies were undertaken utilizing the donor-bridge-acceptor complex $[\text{Ru}(\text{XY})_n\text{-BA}]^{2+}$ (where $n = 0$ to 2 ; $\text{BA} = 4\text{-ethynyl-benzoic acid}$) to understand charge injection and recombination dye-sensitized nanocrystalline TiO_2 solar cells.

5.2 Electron Transfer Reactions in Nanocrystalline TiO_2 Solar Cells

Many of the electron transfer reactions in TiO_2 solar cells are interfacial (Figure 5.2). The solar energy conversion process begins with light absorption to form the dye excited state, k_1 . The excited state then injects an electron into the TiO_2 conduction band, k_3 , via an interfacial reaction. As the injected electron migrates through the TiO_2 , the I^-/I_3^- redox couple reduces the dye in a bimolecular electron transfer reaction, k_5 . The redox couple is then cycled back to the starting state at the counter electrode with formerly injected, TiO_2 electrons.

Less than ideal solar conversion efficiencies stem from (1) less than unity absorption of incident light, (2) less than unity injection from the excited dye into the TiO_2 , (3) rapid back reaction between the injected electron and the oxidized dye, k_6 , and

(4) and rapid interfacial, bimolecular electron transfer between the solution redox couple and injected TiO_2 surface electrons, k_7 . Preventing the non productive back reactions (k_6 and k_7) is major theme of this study.

5.3 Application of $[\text{Ru}-(\text{XY})_n-\text{BA}]^{2+}$ to Studying TiO_2 Solar Cells

The donor-bridge-acceptor complexes, $[\text{Ru}-(\text{XY})_n-\text{R}]^{2+}$ discussed in Chapter 2 were modified for use in nanocrystalline TiO_2 solar cells. Instead of using a donor for the R group, 4-ethynyl-benzoic acid (BA) was attached to the complex to make $[(\text{bpy})_2\text{Ru}(\text{bpy}-(\text{XY})_n-\text{BA})](\text{PF}_6)_2$ (abbreviated $[\text{Ru}-(\text{XY})_n-\text{BA}]^{2+}$, $n = 0$ to 2, Figure 5.3). The carboxyl group forms ester bonds with TiO_2 surface hydroxyl groups. Several experiments based on attaching this dye to TiO_2 (Figure 5.4) all focus on the effect of the dye being held away from the surface of the TiO_2 particle through a xylene oligomer linker. The distance dependence for electron injection, orientational effects on cell performance, charge recombination between TiO_2 and the oxidized dye, and dye regeneration by the electrolyte are all possible studies.

Interfacial electron transfer reactions are often difficult to study. Lack of information on the species involved, ambiguous concentrations, and lack of experimental methods all hamper fundamental studies. The approach taken in this chapter is to study the regeneration reaction, k_5 , between $[\text{Ru}-(\text{XY})_n-\text{BA}]^{2+}$ and I^- in homogenous solution. Using the flash-quench method, we can carefully control the reaction conditions, allowing us to analyze the kinetics.

EXPERIMENTAL

5.4 Methods and Materials

The same methods and materials for synthesis of the complexes, sample preparation, and instrumentation in Chapters 2 and 3 were used for this study. Three novel ligands and the associated dyes were synthesized as described in the next section. The preparation of precursors 4-iodobipyridine, bpy-XY-I, and bpy-(XY)₂-I are detailed in Chapter 2 (section 2.12). Electron-transfer studies were carried using the flash-quench method in conjunction with time-resolved spectroscopy.

5.5 Synthetic Procedures

4-TMS-BA (4-trimethylsilylethynyl-benzoic acid) – Using the general Sonogashira coupling cross-coupling method (section 2.13), 4-iodobenzoic acid (16 mmol) was reacted with trimethylsilylacetylene (1.5 equiv.), Pd(PPh₃)₂Cl₂ (2.5 mol %) and CuI (5

mol%) to produce the crude product after 1 day of sonication at room temperature. A silica gel column was used to purify the crude reaction mixture, eluting with 50:2 CH₂Cl₂:MeOH to afford a yellowish-white solid. (1.32g, 38%) MS (CI) [M]⁺ 218 (calc. 218.33), [M - CH₃]⁺ 203 (calc. 203.3) m/z.

4-ethynyl-BA (4-ethynyl-benzoic acid) – 4-trimethylsilylethynyl-benzoic acid (1.44 mmol) was dissolved in a solvent mixture of 1:1.4 THF:MeOH (23 mL:17 mL) and bubble degassed with argon. A solution of 5N NaOH (1.8 equiv.) was added dropwise with a syringe. The reaction mixture was stirred at room temperature for 2 hours. HCl (1 M) was added to the reaction mixture until a pH of 1 was achieved. The organics were extracted with Et₂O (3 x 50 mL). The solvent was removed with rotary evaporation and the crude product purified with a silica gel column using 50:2 CH₂Cl₂:MeOH as the eluant to yield a yellowish-white solid. (152 mg, 78%) MS (CI) [M]⁺ 146 (calc. 146.1), [M - OH]⁺ 129 (calc. 129.1) m/z, [M - COOH]⁺ 101 (calc. 101.1) m/z,.

bpy-(XY)₀-BA (4-(4'-ethynyl-benzoic acid)-2,2'-bipyridine) – General Sonogashira cross-coupling method was used with 4-iodobipyridine (0.355 mmol), 4-ethynyl-BA (1.2 equiv.), 10 mL of Et₂NH₂, Pd(PPh₃)₂Cl₂ (2.5 mol %), and CuI (5 mol %). The reaction was sonicated at room temperature for 21 hours. The crude reaction residue was loaded onto a silica gel column and eluted with 5:1 CH₂Cl₂:MeOH. (52 mg, 49%) MS (APCI) [M+H]⁺ 301.1 (calc. 301.1).

[Ru-(XY)₀-BA](PF₆)₂ ([bpy]₂Ru^{II}(bpy-(XY)₀-BA)(PF₆)₂) – Using the general ruthenium metalation method, bpy-(XY)₀-BA (0.17 mmol), Ru(bpy)Cl₂ (1.2 equiv), 20 mL EtOH, and

4 mL of CHCl_3 were gently refluxed for 20 hours. The product was purified on silica gel and collected with a mixture of 2.5:20:80 saturated aqueous $\text{KNO}_3\text{:H}_2\text{O:CH}_3\text{CN}$ as the final eluant. Concentrating and metathesizing to the hexafluorophosphate salt produced a red solid. (28 mg, 16%) MS (ESI) $[\text{M}]^{2+}$ 357.3 (calc. 357.1), $[\text{M} - \text{H}]^+$ 712.9 (calc. 713.1) m/z.

bpy-(XY)₁-BA (4-(2,5-dimethyl-4-(4-ethynylbenzoic acid)-2,2'-bipyridine) – General Sonogashira cross-coupling method was used with bpy-XY-I (0.74 mmol), 4-ethynyl-BA (1.2 equiv.), 10 mL of Et_2NH_2 , $\text{Pd}(\text{PPh}_3)_2\text{Cl}_2$ (2.5 mol %), and CuI (5 mol %). The reaction was sonicated at room temperature for 22 hours. The crude reaction residue was loaded onto a silica gel column and eluted with 50:5 $\text{CH}_2\text{Cl}_2\text{:MeOH}$. (230 mg, 77%) MS (APCI) $[\text{M}+\text{H}]^+$ 405.1 (calc. 405.5).

[Ru-(XY)₁-BA](PF₆)₂ ($[(\text{bpy})_2\text{Ru}^{\text{II}}(\text{bpy}-(\text{XY})_1\text{-BA})(\text{PF}_6)_2]$) – Using the general ruthenium metalation method, bpy-(XY)₁-BA (0.06 mmol), $\text{Ru}(\text{bpy})\text{Cl}_2$ (1.2 equiv), 10 mL EtOH, and 2 mL of CHCl_3 were gently refluxed for 20 hours. The product was purified on silica gel and collected with a mixture of 2.5:20:80 saturated aqueous $\text{KNO}_3\text{:H}_2\text{O:CH}_3\text{CN}$ as the final eluant. Concentrating and metathesizing to the hexafluorophosphate salt produced a red solid. (14.5 mg, 22%) MS (ESI) $[\text{M}]^{2+}$ 409.2 (calc. 409.1).

bpy-(XY)₂-BA (4-(4'-(4-ethynylbenzoic acid)-2,2',5,5'-tetramethyl-1,1'-biphenyl-4-yl - 2,2'-bipyridine) – General Sonogashira cross-coupling method was used with bpy-(XY)₂-I (0.16 mmol), 4-ethynyl-BA (1.2 equiv.), 10 mL of Et_2NH_2 , $\text{Pd}(\text{PPh}_3)_2\text{Cl}_2$ (2.5 mol %), and CuI (5 mol %). The reaction was sonicated at room temperature for 1 day. The crude

reaction residue was loaded onto a silica gel column and eluted with 25:8 CH₂Cl₂:MeOH. (21.2 mg, 26%) MS (APCI) [M+H]⁺ 509 (calc. 509).

[Ru-(XY)₂-BA](PF₆)₂ ([Ru(bpy)₂(bpy-(XY)₂-BA)](PF₆)₂) – Using the general ruthenium metalation method, bpy-(XY)₂-BA (0.04 mmol), Ru(bpy)Cl₂ (1.2 equiv), 10 mL EtOH, and 2 mL of CHCl₃ were gently refluxed overnight. The product was purified on silica gel and collected with a mixture of 2.5:20:80 saturated aqueous KNO₃:H₂O:CH₃CN as the final eluant. Concentrating and metathesizing to the hexafluorophosphate salt produced a red solid. (21 mg, 22%) MS (ESI) [M]²⁺ 461.3 (calc. 461.1), [M - PF₆]⁺ 1067.1 (calc. 1067.2) m/z.

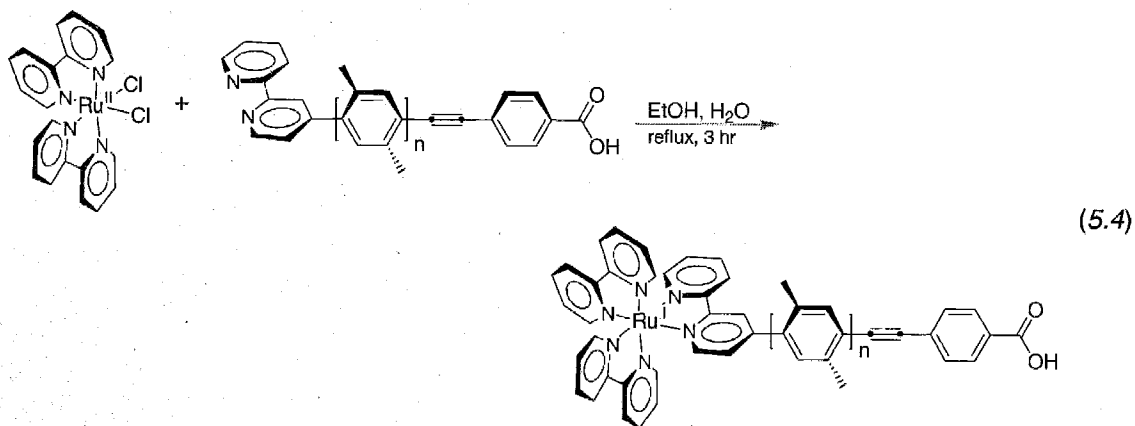
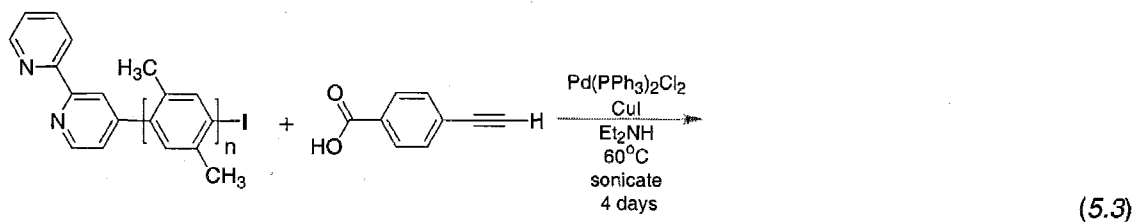
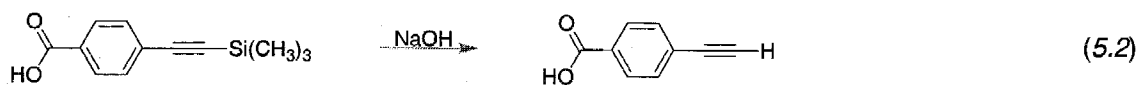
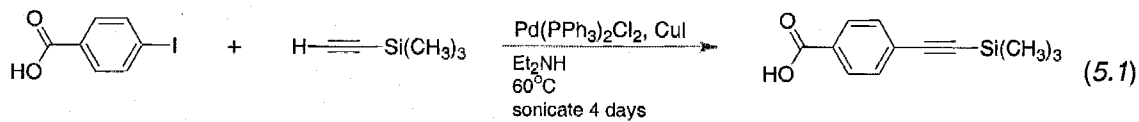
RESULTS and DISCUSSION

5.6 Synthesis of $[\text{Ru}-(\text{XY})_n-\text{BA}]^{2+}$

The synthesis of the dye series $[\text{Ru}-(\text{XY})_n-\text{BA}]^{2+}$ was based on a modification to $[\text{Ru}-(\text{XY})_n-\text{G}]^{2+}$, where the donor was replaced with 4-ethynyl-benzoic acid (BA). The synthetic route (Scheme 5.1) started with preparing the precursor, 4-ethynyl-benzoic acid. This was achieved through Sonogashira¹⁵⁰ cross coupling of commercially available 4-iodobenzoic acid with trimethylsilylacetylene (equation 5.1). Deprotection of the TMS group with base afforded 4-ethynylbenzoic acid (equation 5.2). The ligand was then made via Sonogashira cross-coupling between the benzoic acid and $\text{bpy}-(\text{XY})_n-\text{I}$ (equation 5.3). The final complex was assembled by refluxing $(\text{bpy})_2\text{RuCl}_2$ with $\text{bpy}-(\text{XY})_n-\text{BA}$, followed by metathesis to the hexafluorophosphate salt to give the final product as a red solid (equation 5.4).

SCHEME 5.1

General Synthetic Route to $[\text{Ru}(\text{XY})_n\text{-BA}]^{2+}$



5.7 UV-visible Absorption spectra of $[\text{Ru}-(\text{XY})_n-\text{BA}]^{2+}$

The UV-visible absorption spectra of $[\text{Ru}-(\text{XY})_n-\text{BA}]^{2+}$ (Figure 5.5) show three main features: The bipyridine $\pi \rightarrow \pi^*$ transition has an intense peak at 290 nm, followed by a peak around 326 nm that is assigned to the ethynylbenzoic acid moiety, and finally broad absorption center in the region of 460 nm corresponding to the MLCT band. The position and/or intensity of the absorption bands shift as the number of xylene spacers changes (Table 5.1). The bipyridine band $\pi \rightarrow \pi^*$ transition has the same position but decreases intensity across the series (from $n = 0$ to $n = 2$). The same is true for the ethynylbenzoic acid band at 326 nm. The MLCT band for $[\text{Ru}-(\text{XY})_1-\text{BA}]^{2+}$ and $[\text{Ru}-(\text{XY})_2-\text{BA}]^{2+}$ remain in the same position while $[\text{Ru}-(\text{XY})_0-\text{BA}]^{2+}$ has red-shifted by 4 nm. The intensity of the MLCT band also decreases with length.

The red-shift of the MLCT band in $[\text{Ru}-(\text{XY})_0-\text{BA}]^{2+}$ indicates a greater degree of electronic coupling between the metal center and ethynylbenzoic acid. Because the MLCT band does not shift between $[\text{Ru}-(\text{XY})_1-\text{BA}]^{2+}$ and $[\text{Ru}-(\text{XY})_2-\text{BA}]^{2+}$, the effect is effectively shut off once a xylene ring is introduced between the ruthenium and ethynylbenzoic acid. The enhanced coupling in $[\text{Ru}-(\text{XY})_0-\text{BA}]^{2+}$ can be explained by examining the structure of the bpy-(XY)₀-BA ligand. The free rotation of the alkyne linker allows for good electronic communication between the aromatic ring of the benzoic acid and the ring of the bipyridine. This creates a somewhat delocalized π -system leading to the red shift.

5.8 Electrochemistry of $[\text{Ru}-(\text{XY})_n-\text{BA}]^{2+}$

Any variation in the electronic coupling or structure of $[\text{Ru}-(\text{XY})_n-\text{BA}]^{2+}$, as the number of xylene rings increases, is not apparent in the redox potentials of the $\text{Ru}^{\text{II/III}}$ couple (Figure 5.6, Table 5.2). For all three complexes, the same potential of 1.6 V (vs. Ag/AgCl) was measured for the metal center. Considering the small shift observed in the UV-visible absorption spectra, it is likely that any perturbations to the metal center $[\text{Ru}-(\text{XY})_0-\text{BA}]^{2+}$ are too weak to be detected by cyclic voltammetry methods.

5.9 Photophysics of $[\text{Ru}-(\text{XY})_n-\text{BA}]^{2+}$

The excited-state lifetimes were measured using time-resolved luminescence decay spectroscopy (Figure 5.7, Table 5.3). As was the case with UV-visible absorption data, there is a clear demarcation between the lifetimes for $[\text{Ru}-(\text{XY})_0-\text{BA}]^{2+}$ (2.3 μs) and $[\text{Ru}-(\text{XY})_n-\text{BA}]^{2+}$ ($n = 1$ or 2, 1.1 μs). The enhanced lifetime of $[\text{Ru}-(\text{XY})_0-\text{BA}]^{2+}$ is likely an effect of greater electronic coupling between the metal center and the benzoic acid modified ligand. $[\text{Ru}-(\text{XY})_n-\text{BA}]^{2+}$ ($n = 1$ and 2) have the same lifetime, and are slightly longer than the model compounds $[\text{Ru}(\text{bpy})_3]^{2+}$ and $[\text{Ru}-\text{XY}-\text{TMS}]^{2+}$.

5.10 Regeneration of $[\text{Ru}^{\text{II}}-(\text{XY})_n-\text{BA}]^{2+}$ with Iodide

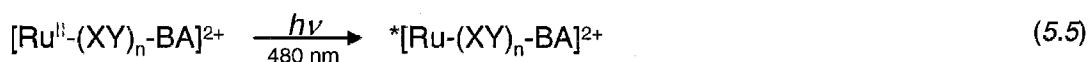
An electron transfer method (Scheme 5.2) was devised to mimic the dye regeneration process (k_5) in homogenous fluid solution. Utilizing the flash-quench method,¹²⁹ the $[\text{Ru}-(\text{XY})_n-\text{BA}]^{2+}$ dye is excited with a laser pulse and then oxidatively quenched with

methyl viologen (MV^{2+}). This process generates $[Ru^{III}-(XY)_n-BA]^{3+}$, which then reacts with iodide in solution to regenerate $[Ru^{II}-(XY)_n-G]^{2+}$ and produce I^{\bullet} . The final step completes the cycle by regenerating the quencher and iodide.

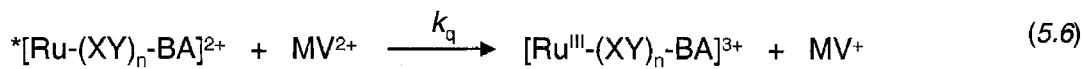
Scheme 5.2

Dye Regeneration in Homogenous Fluid Solution

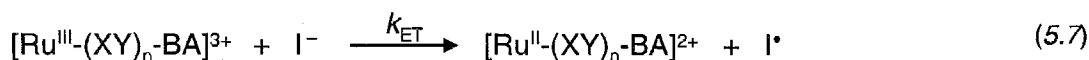
Excited state formation via excitation into the MLCT band,



Excited state quenching,



Bimolecular dye regeneration,



Quencher charge recombination,



Figure 5.8 shows the transient absorption traces recorded at 450 nm for a sample of $[Ru-(XY)_0-BA]^{2+}$ with varying amounts of lithium iodide (from 0 to 200 μM). The traces were fit to biexponential decay functions to obtain the rate constants. In the absence of iodide, regeneration of $[Ru^{II}-(XY)_n-BA]^{2+}$ occurs through a reaction between $[Ru^{III}-(XY)_n-BA]^{3+}$ and reduced quencher. This process takes several hundred micro-

seconds to complete under these experimental conditions (12 mM MV²⁺). As iodide is added, [Ru^{II}-(XY)_n-BA]²⁺ is regenerated via a bimolecular reaction between [Ru^{III}-(XY)_n-BA]²⁺ and I⁻. Increasing the concentration of iodide increases the observed rate constant for [Ru^{II}-(XY)₁-G]²⁺ regeneration.

The regeneration of [Ru^{II}-(XY)_n-BA]²⁺ with iodide can be treated with pseudo first-order kinetics. The concentration of iodide (minimum amount was 20 μM) is at least a factor of 10 larger than the estimated amount of [Ru^{III}-(XY)_n-BA]²⁺. In general, the rate of regeneration is given by,

$$\frac{\partial}{\partial t} [\text{Ru}^{\text{II}}\text{-(XY)}_n\text{-BA}] = k_{\text{obs}} [\text{Ru}^{\text{III}}\text{-(XY)}_n\text{-BA}], \quad (5.9)$$

where

$$k_{\text{obs}} = k_5 [\text{I}^-] \quad (5.10)$$

Fitting the transient absorption data to a biexponential function yields a fast phase corresponding to quenching. k_{obs} was obtained from the second kinetic phase. A plot of k_{obs} versus iodide concentration gives a slope equal to the second order rate constant for regeneration, k_5 .

The reaction between [Ru^{III}-(XY)_n-BA]²⁺ and iodide was repeated for all three dyes and pseudo-first-order plots (Figure 5.9) were generated to extract k_5 . The same k_5 of $1.5 \times 10^{10} \text{ M}^{-1}\text{s}^{-1}$ was measured for all three dyes. The differences among the dyes that led to variation in the UV-visible absorption spectra and excited-state lifetimes do not affect the regeneration by iodide in homogenous solutions. There appears to be no substantial difference in the reactivity among the members of [Ru^{III}-(XY)_n-BA]³⁺ towards regeneration by iodide.

CONCLUSION

A series of dyes based on the $[\text{Ru}^{\text{II}}-(\text{XY})_n-\text{R}]^{2+}$ framework were designed and synthesized to study the electron transfer reactions of nanocrystalline TiO_2 solar cells. This study demonstrates the versatility of the $[\text{Ru}^{\text{II}}-(\text{XY})_n-\text{R}]^{2+}$ scaffold discussed in chapters 2 and 3. UV-visible absorption, electrochemical, and photophysical characterizations of the dye series, $[\text{Ru}-(\text{XY})_n-\text{BA}]^{2+}$, indicate small differences exist among the dyes. The flash-quench method was coupled with a ground-state bimolecular electron-transfer reaction to study the regeneration of $[\text{Ru}^{\text{II}}-(\text{XY})_n-\text{BA}]^{2+}$ by iodide. The kinetics experiments demonstrate no difference in the reactivity among the members of $[\text{Ru}^{\text{III}}-(\text{XY})_n-\text{BA}]^{2+}$. Future studies will focus on measuring the distance dependence for charge injection and recombination of the dyes bound to TiO_2 particles.

FIGURES and TABLES

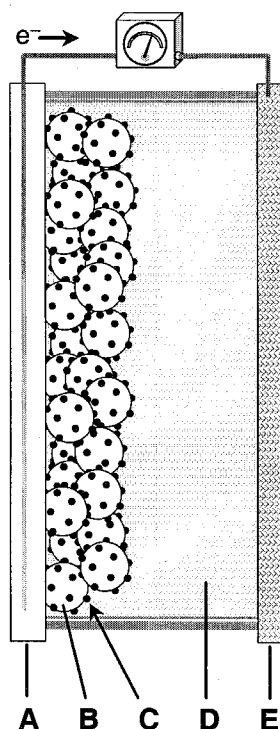


FIGURE 5.1 – Schematic of Nanocrystalline TiO_2 Solar Cells

(A) Conducting transparent electrode; (B) Nanocrystalline TiO_2 particles; (C) Dye covalently bound to the TiO_2 particles; (D) Electrolyte solution, typically containing a mixture of I^- and I_3^- ; (E) Counter electrode.

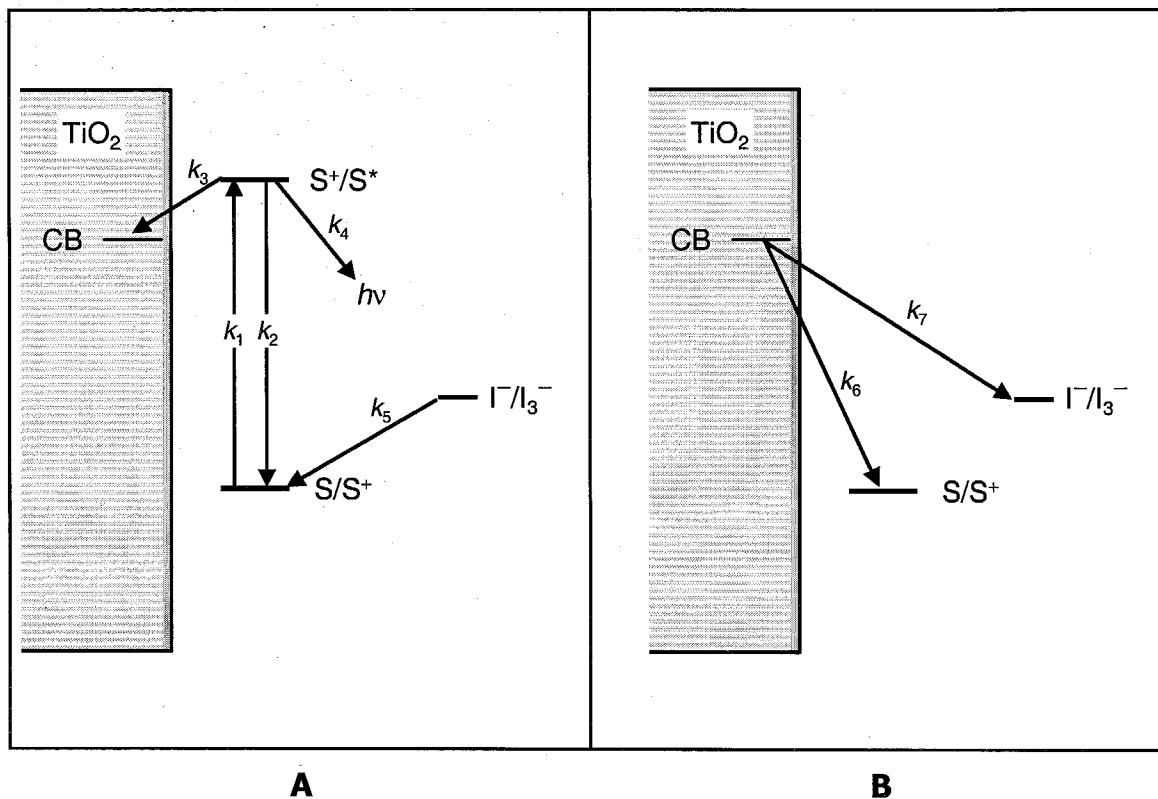


FIGURE 5.2 – Electron Transfer Reactions of Nanocrystalline TiO_2 Solar Cells

Electron-transfer reactions of a nanocrystalline TiO_2 solar cell. (A) Photoexcitation of the dye sensitizer (S) produces the excited state (S^*) with a rate constant of k_1 . k_2 and k_4 represent the non-radiative and radiative excited-state decay pathways. Electron injection into the TiO_2 conduction band is represented by k_3 . Upon injecting an electron, the I^-/I_3^- redox couple fills the hole left on the dye, denoted by process k_5 . (B) Possible efficiency loss steps include the back reaction between the injected conduction band electron and the oxidized dye, k_6 . Reaction between the injected conduction band electron and the I^-/I_3^- redox couple at the semiconductor surface, k_7 is another major loss pathway.

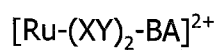
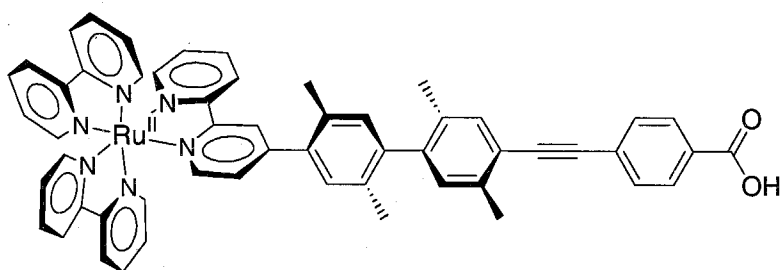
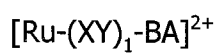
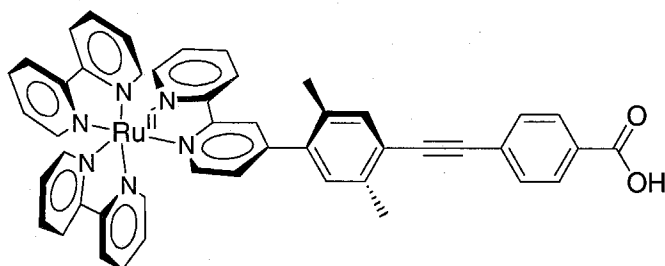
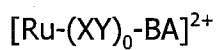
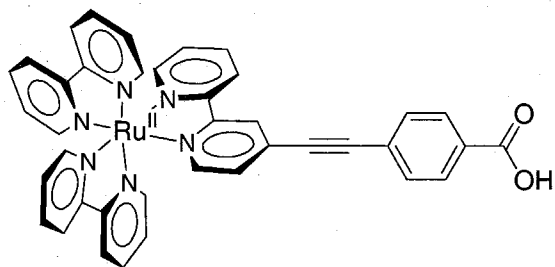


FIGURE 5.3 – $[\text{Ru}-(\text{XY})_n\text{-BA}]^{2+}$

Series of dyes for studying electron transfer process in nanocrystalline TiO_2 solar cells.

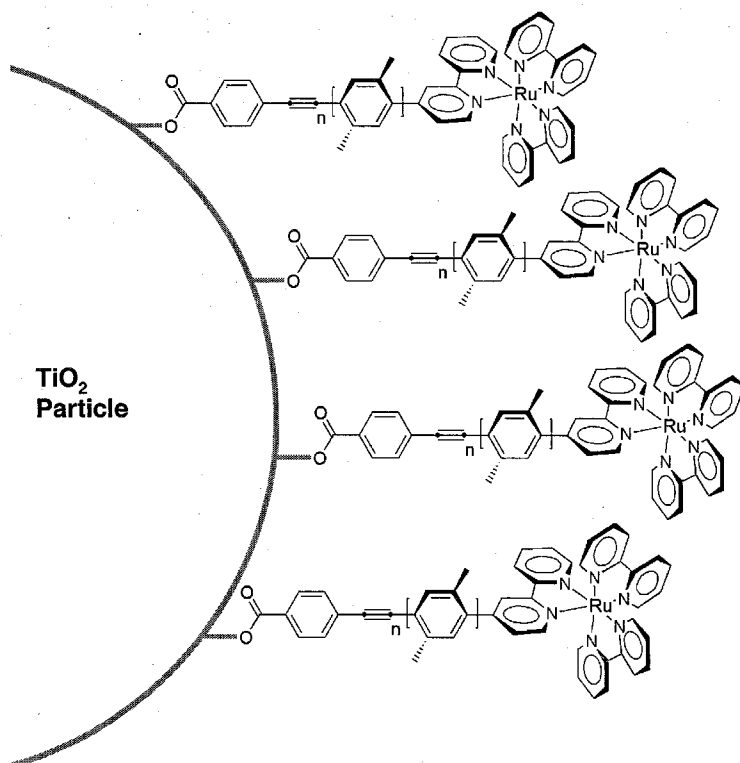


FIGURE 5.4 – $[\text{Ru}-(\text{XY})_n\text{-BA}]^{2+}$ Bound to TiO_2

Idealized schematic of $[\text{Ru}-(\text{XY})_n\text{-BA}]^{2+}$ bound to TiO_2 shows the placement of the ruthenium chromophore removed from the surface of the particle.

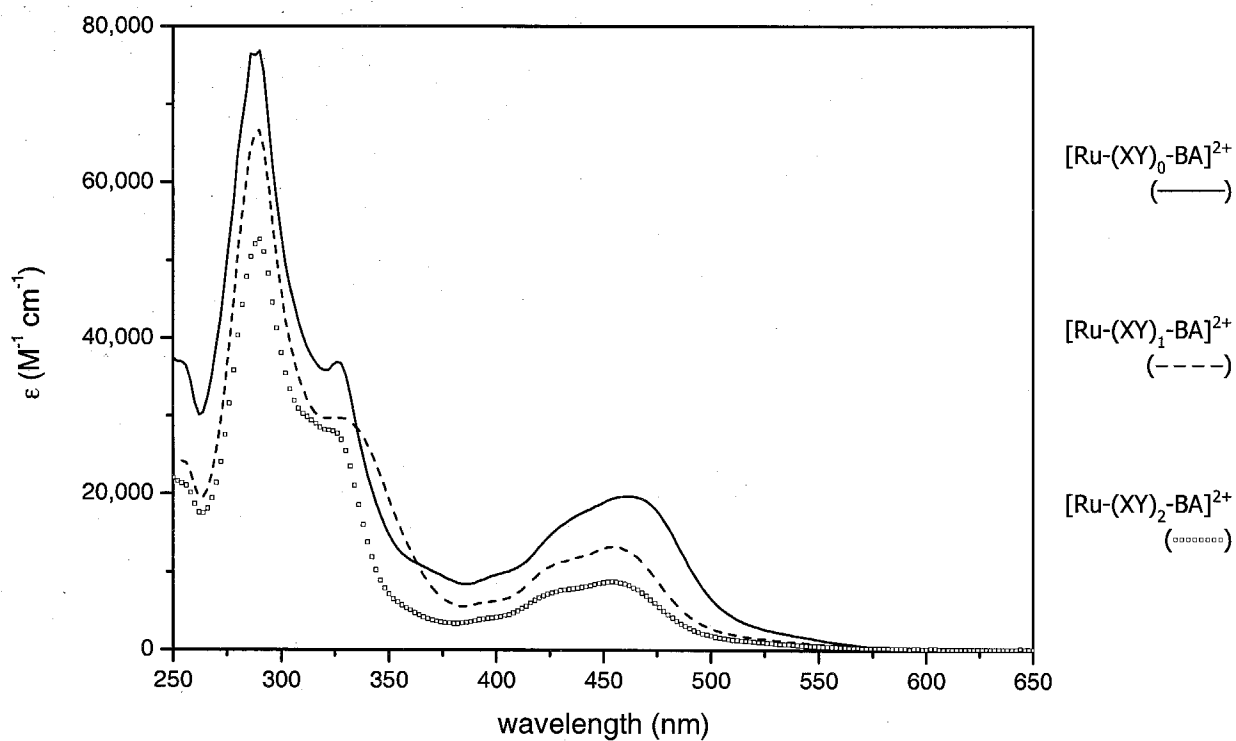


FIGURE 5.5 – $[\text{Ru}-(\text{XY})_n-\text{BA}]^{2+}$ UV-visible Absorption Spectra

The traces in the Figure above show the UV-visible absorption spectra of $[\text{Ru}-(\text{XY})_n-\text{BA}]^{2+}$ (where $n = 0$ to 2) in acetonitrile.

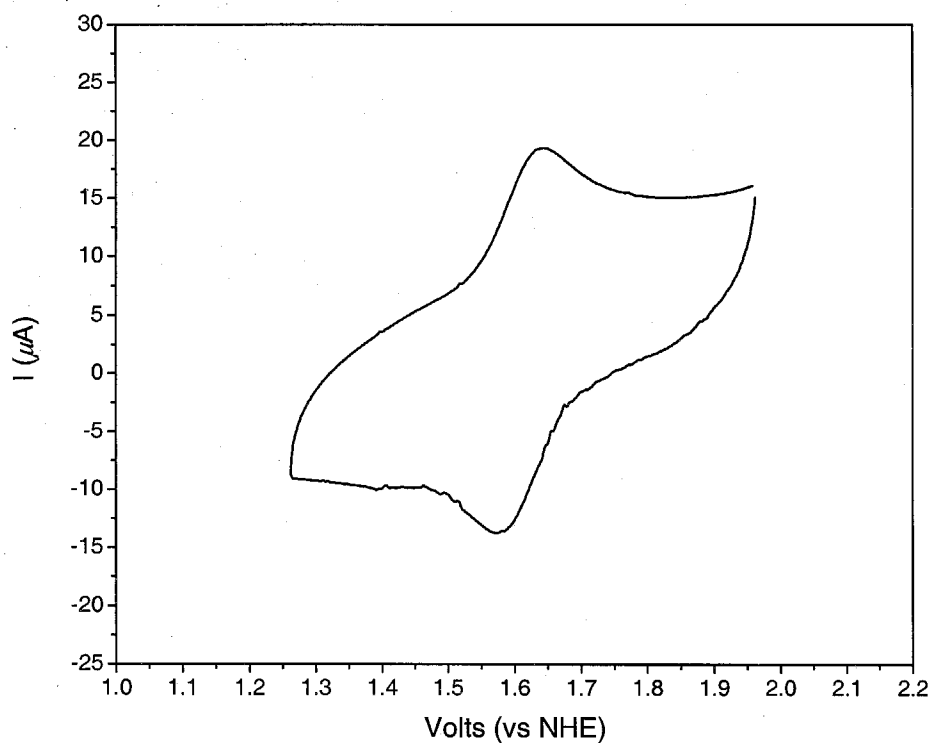


FIGURE 5.6 – $[\text{Ru}(\text{XY})_0\text{-BA}]^{2+}$ Cyclic Voltammogram ($\text{Ru}^{\text{II/III}}$)

The cyclic voltammogram of $[\text{Ru}(\text{XY})_0\text{-BA}]^{2+}$ shows a reversible couple with a potential of 1.6 V (vs. NHE), which corresponds to the couple $\text{Ru}^{\text{II/III}}$.

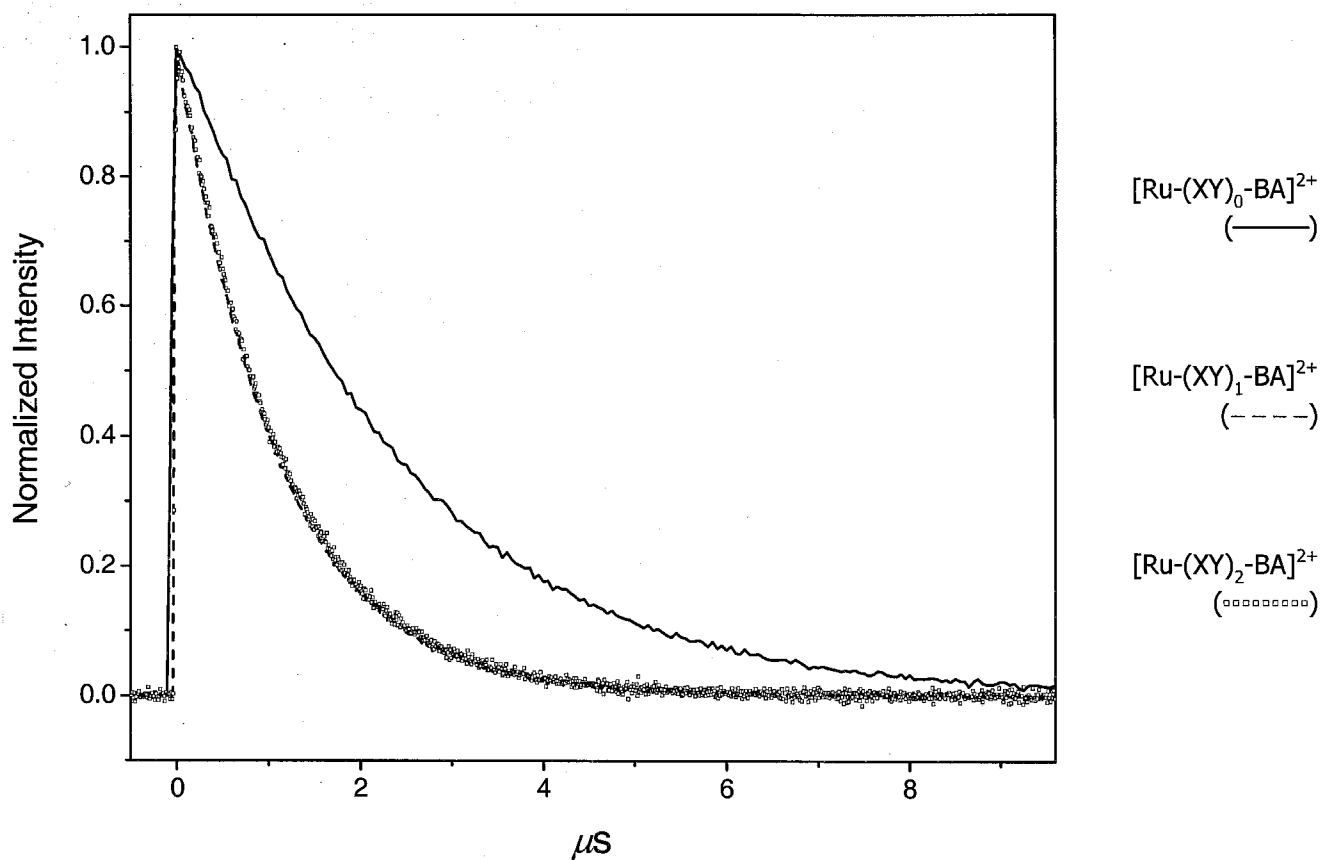


FIGURE 5.7 – $[\text{Ru}-(\text{XY})_n-\text{BA}]^{2+}$ Excited State Lifetimes

The excited state lifetimes of $[\text{Ru}-(\text{XY})_n-\text{BA}]^{2+}$ were measured in deaerated acetonitrile solution using time-resolved luminescence decay instrumentation.

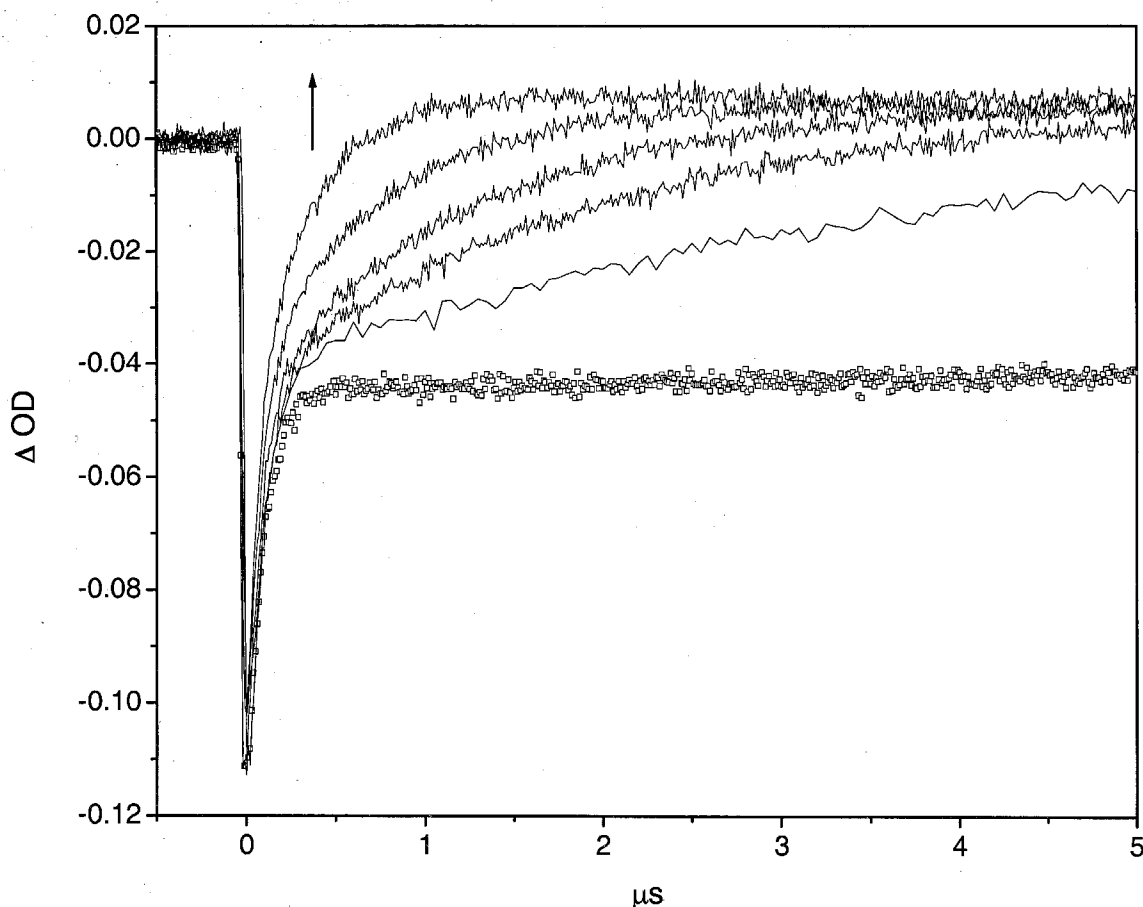


FIGURE 5.8 – $[\text{Ru}-(\text{XY})_0\text{-BA}]^{2+}$ Regeneration with Iodide

Transient absorption traces of $[\text{Ru}-(\text{XY})_0\text{-BA}]^{2+}$ recorded at 450 nm with 12 mM MV^{2+} . Rate constants were obtained by fitting the traces to biexponential decay functions. The initial trace, with no iodide (oooooo), has a fast phase that corresponds to the quenching process and a much longer phase for the back reaction with quencher. As the concentration of iodide is increased from 20 μM to 200 μM , the rate constant for the second phase increases (arrow indicates direction of change as the iodide concentration increases).

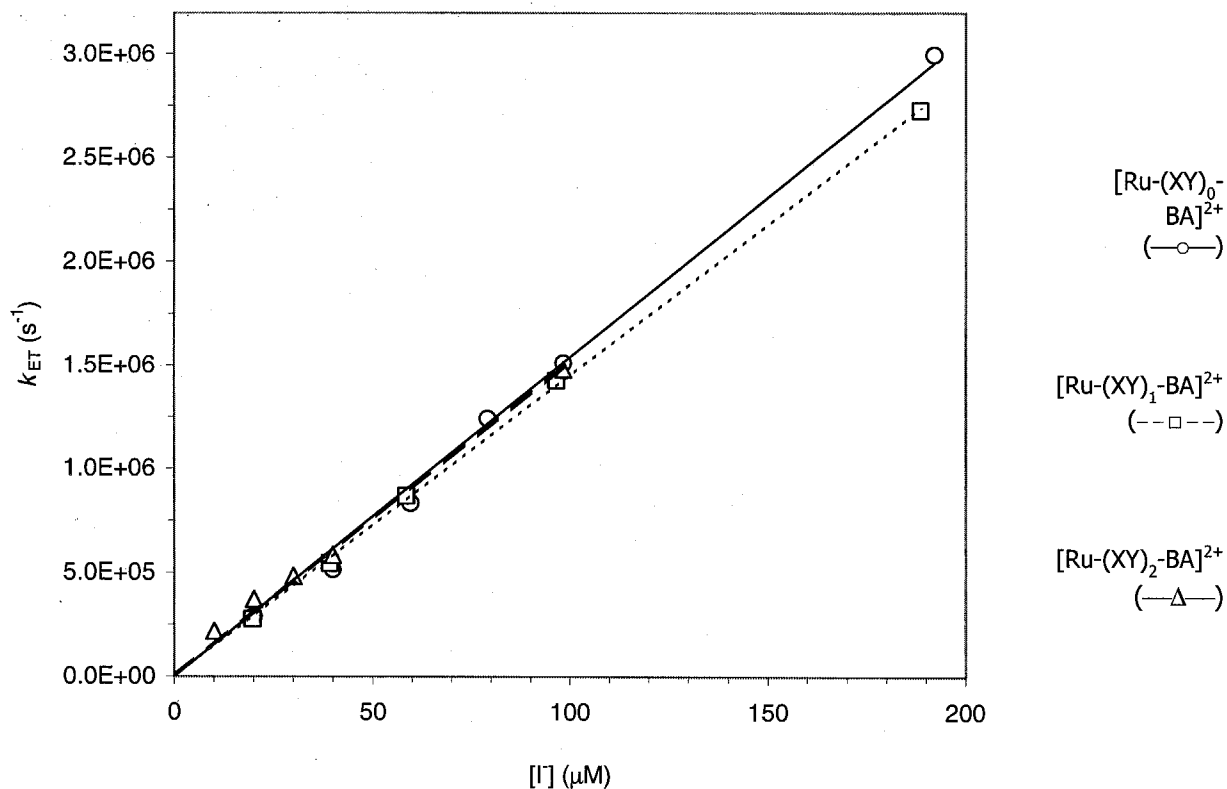


FIGURE 5.9 – $[\text{Ru}-(\text{XY})_n\text{-BA}]^{2+}$ Regeneration with Iodide
Pseudo-First-Order Plots

Pseudo-first-order plots of observed electron-transfer rate versus iodide concentration for dyes 1-3. The second-order rate constant, determined from linear regression analysis, is the same for all three dyes, $1.5 \times 10^{10} \text{ s}^{-1}\text{M}^{-1}$.

TABLE 5.1 – Summary of $[\text{Ru}-(\text{XY})_n\text{-BA}]^{2+}$
UV-Visible Absorption Spectra

compound	Ru MLCT nm (epsilon $\text{M}^{-1} \text{cm}^{-1}$)	$\pi \rightarrow \pi^*$ nm (epsilon $\text{M}^{-1} \text{cm}^{-1}$)
$[\text{Ru}(\text{bpy})_3]^{2+}$	450 (12,600)	288 (67,600)
$[\text{Ru-XY-TMS}]^{2+}$	450 (17,600)	288 (87,000)
$[\text{Ru}-(\text{XY})_0\text{-BA}]^{2+}$	460 (19,600)	290 (76,800) 326 (36,900)
$[\text{Ru}-(\text{XY})_1\text{-BA}]^{2+}$	454 (13,200)	290 (66,700) 326 (29,700)
$[\text{Ru}-(\text{XY})_2\text{-BA}]^{2+}$	454 (8,790)	290 (52,700) 320 (28,200)

TABLE 5.2 – Summary of $[\text{Ru}(\text{XY})_n\text{-BA}]^{2+}$
Redox Potentials

Compound	$\text{Ru}^{\text{II/III}} E^{\circ}$ (V) ^a
$[\text{Ru}(\text{bpy})_3]^{2+}$	1.63 ^a
$[\text{Ru-XY-TMS}]^{2+}$	1.62 ^a
$[\text{Ru}(\text{XY})_0\text{-BA}]^{2+}$	1.6 ^b
$[\text{Ru}(\text{XY})_1\text{-BA}]^{2+}$	1.6 ^b
$[\text{Ru}(\text{XY})_2\text{-BA}]^{2+}$	1.6 ^b

^aThese potentials are referenced to NHE by taking the potentials originally referenced to Ag/AgCl and adding 298 mV.

^bReported vs. NHE by using the ferrocene/ferrocenium couple in acetonitrile as a reference.

TABLE 5.3 – Summary of $[\text{Ru}(\text{XY})_n\text{-BA}]^{2+}$
Excited State Lifetimes

compound	τ_0 (μs)
$[\text{Ru}(\text{bpy})_3]^{2+}$	0.91
$[\text{Ru}\text{-XY-TMS}]^{2+}$	0.91
$[\text{Ru}(\text{XY})_0\text{-BA}]^{2+}$	2.3
$[\text{Ru}(\text{XY})_1\text{-BA}]^{2+}$	1.1
$[\text{Ru}(\text{XY})_2\text{-BA}]^{2+}$	1.1

Appendix A

CUSTOM GLASSWARE

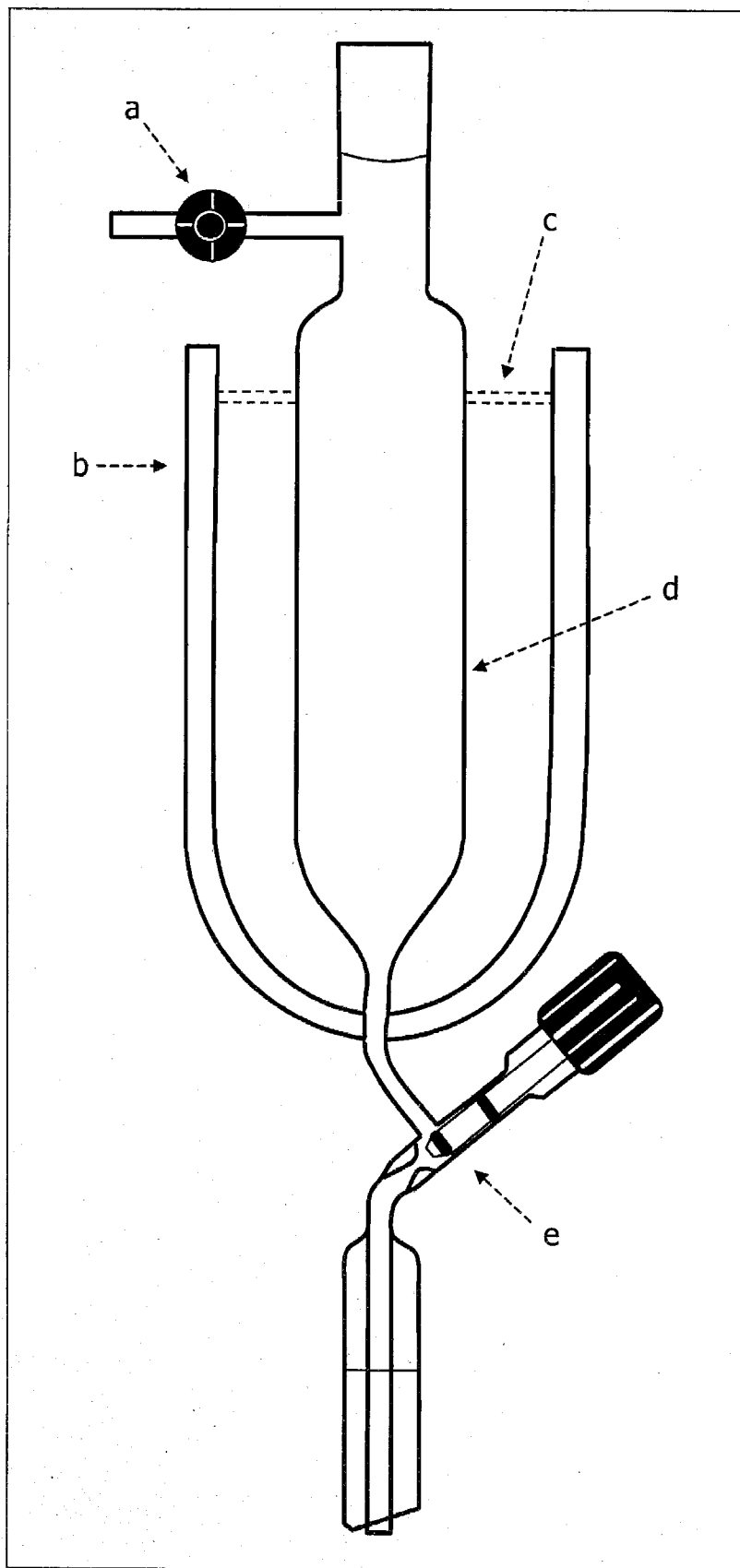
LOW TEMPERATURE ADDITION FUNNEL

Low-Temperature Addition Funnel

The funnel in Figure A.1 was designed to add large quantities of air- or water-sensitive liquids to a reaction flask. The key features are (1) a 250 mL-capacity addition funnel, (2) a Teflon needle-valve stopcock with a minimum flow rate of 0.1 mL/min (Ace Glass), (3) a low-temperature jacket with an evacuated interior (4), and a pressure equalizing valve.

Typical Use

A two- or three-neck round bottom flask is fitted with the addition funnel and a septum. A needle is placed through the septum and attached to a Schlenk Line. The addition funnel is sealed at the top with a rubber septum as well. The funnel is flushed with argon by opening the needle valve, adding a bubbler to valve **a**, and introducing argon through the needle in the round bottom flask. Once flushed, the needle valve can be sealed and liquid added to the funnel through the top septum. Pressure is relieved in the funnel through the bubbler on valve **a**. The funnel can be cooled with a mixture of dry ice/acetone (or similar). As the liquid is added dropwise, the pressure is equalized in the reaction flask by adding a bubbler, through a needle in the septum, and maintaining argon flow. The funnel is equalized by introducing a low-pressure flow of argon through the funnel's septum and leaving valve **a** open and connected to a bubbler.

**FIGURE A.1**

Addition Funnel
with a
Low-Temperature Jacket
and Needle Valve

This funnel was designed for low-temperature additions of air-sensitive liquids. The funnel (d) has a 250 mL capacity and is fitted with a needle valve (e), capable of a minimum flow rate of 0.1 mL/min (Ace Glass). The interior of the low-temperature jacket (b) is evacuated. Two support bars (c) were added symmetrically around the funnel. The Teflon stopcock (a) is provide to equalize pressure.

Design by
Randy Villahermosa

Appendix B

OPTICALLY TRANSPARENT THIN LAYER (OTTL)

SPECTROELECTROCHEMICAL CELL

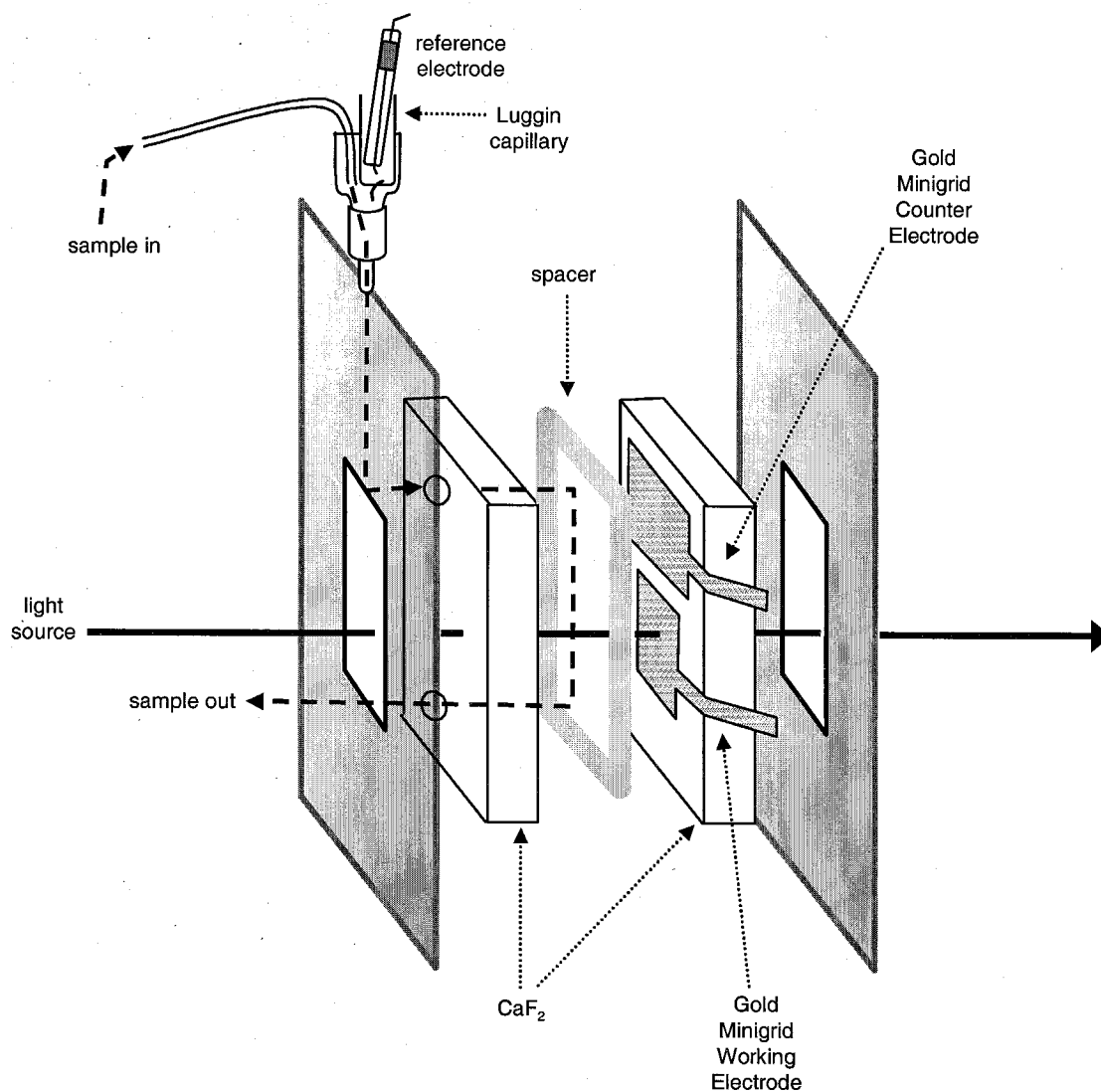


FIGURE B.1 – Optically Transparent Thin Layer (OTTL) Spectroelectrochemical Cell

This cell was used to record spectroelectrochemical traces. The chassis is taken from an infrared flow cell. The windows are made of organic-solvent resistant CaF_2 . The reference electrode is placed in the sample inlet using a Luggin capillary made from Pt wire. The working and counter electrodes are made from gold minigrid. Light is direct through the working electrode to collect absorption spectra.

Appendix C

NANOSECOND

LASER FLASH PHOTOLYSIS

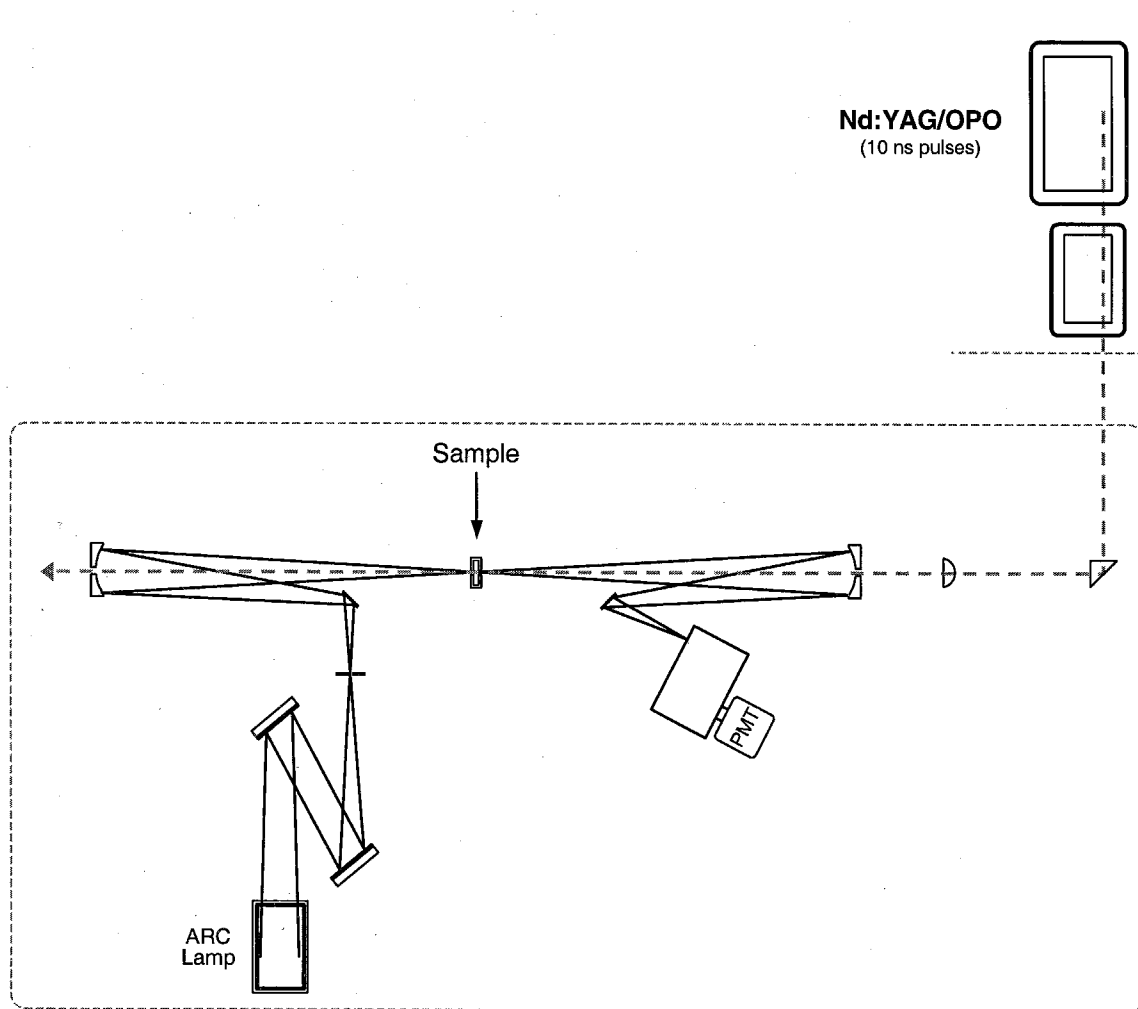


FIGURE C.1 – Nanosecond Laser Flash Photolysis Schematic

The nanosecond laser flash photolysis instrument used to measure luminescence decay and transient absorption trace is outlined above. The laser path (broken line) is aligned co-linear with the probe (solid line). The excitation source is a YAG-pumped OPO laser and the probe is a broadband arc lamp. The optics are arranged for 1:1 imaging of the sample on the photomultiplier tube (PMT) detector.

Appendix D

SPECTROSCOPIC HANDLES

METHYL VIOLOGEN (MV^{2+}) SPECTRA

$[Ru-(XY)_n-G]^{2+}$ HANDLES

TMS-ethynyl-G HANDLES

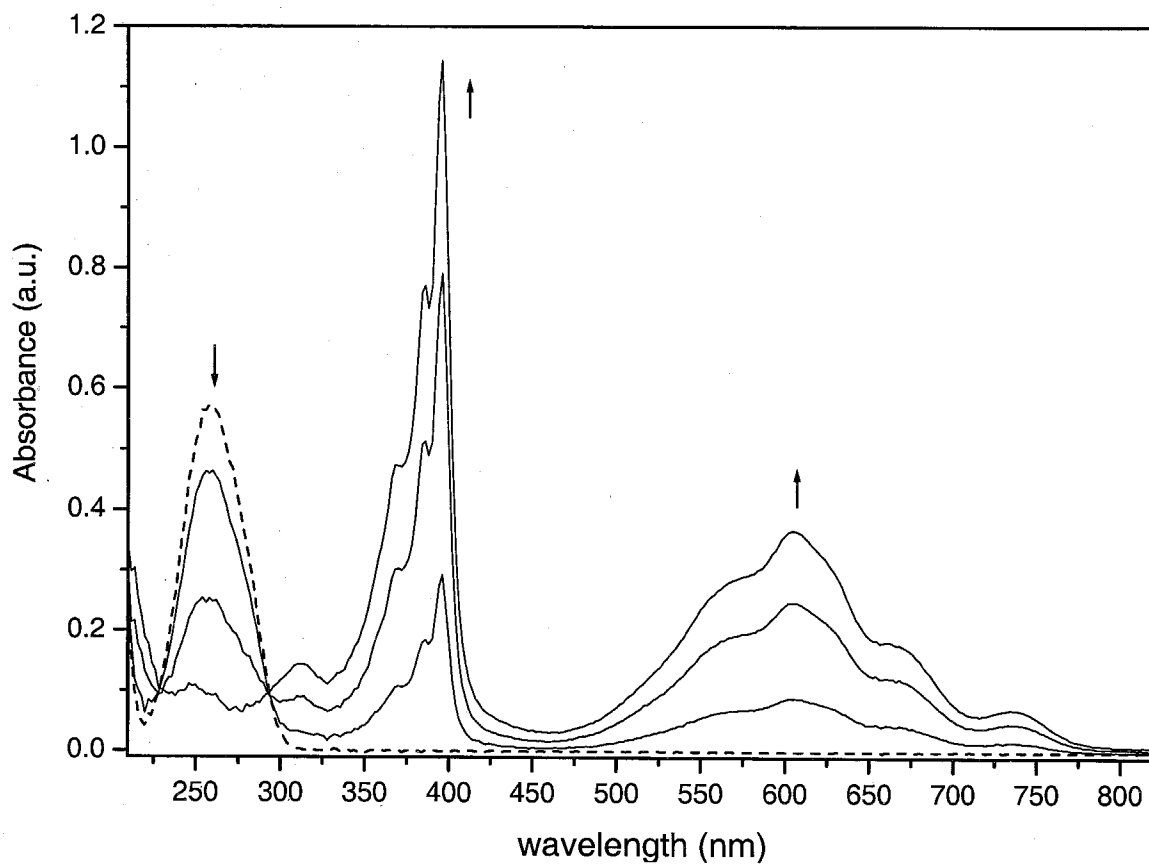


FIGURE D.1 – Methyl Viologen (MV^{2+})
Spectroelectrochemical Traces

The bulk electrolysis of MV^{2+} to MV^+ at -0.5 V (vs. Ag/AgCl) was performed in acetonitrile with 0.1 M TBAH, using the cell in appendix B. UV-visible absorption traces were taken at regular intervals, starting with the initial spectrum (broken line). The arrows indicate direction of change. Reduction of the sample, via electrolysis at 0 V, fully recovers the initial spectrum, indicating the cycle $MV^{2+} \rightarrow MV^+ \rightarrow MV^{2+}$ is completely reversible.

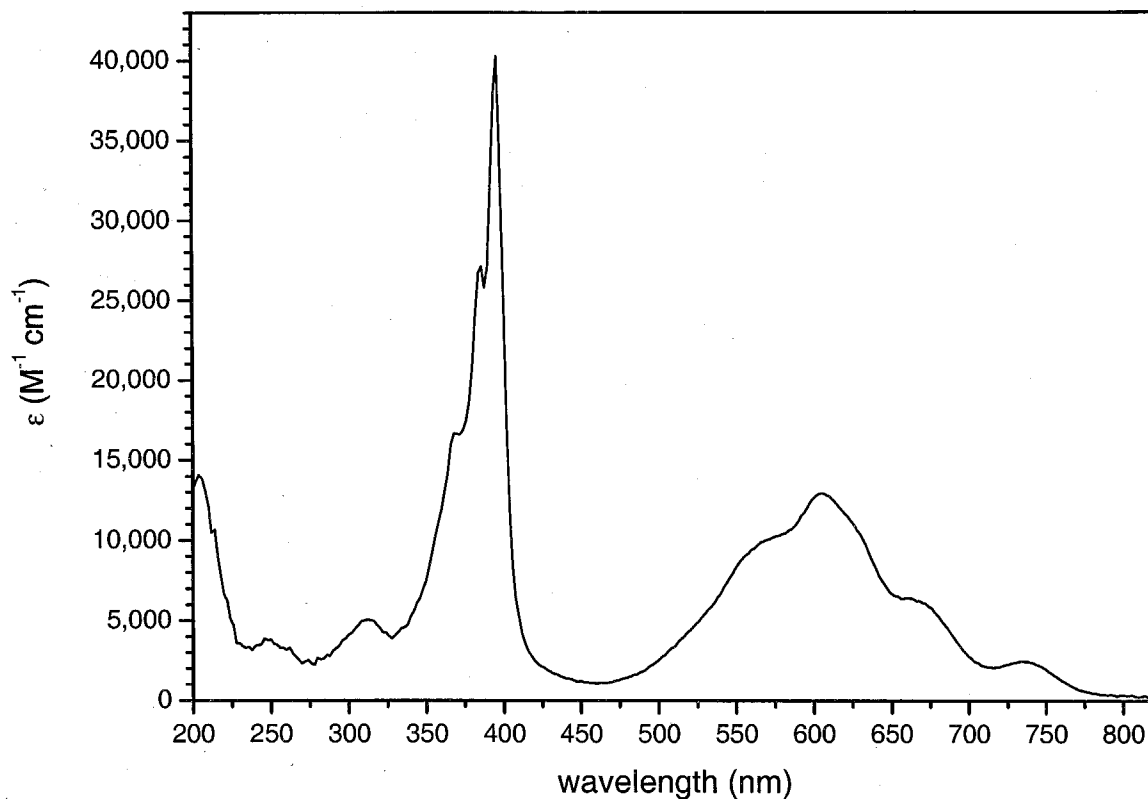


FIGURE D.2 – Methyl Viologen Cation (MV⁺)
UV-visible Absorption

Bulk electrolysis at -0.5 V (vs. Ag/AgCl) was performed in acetonitrile with 0.1 M TBAH, using the cell in appendix B. The electrolysis was considered complete when less than 2% of the initial current was passed to the working electrode. The extinction coefficients for the Figure above were calculated based on the assumption that the reduction of MV²⁺ to MV⁺ was complete.

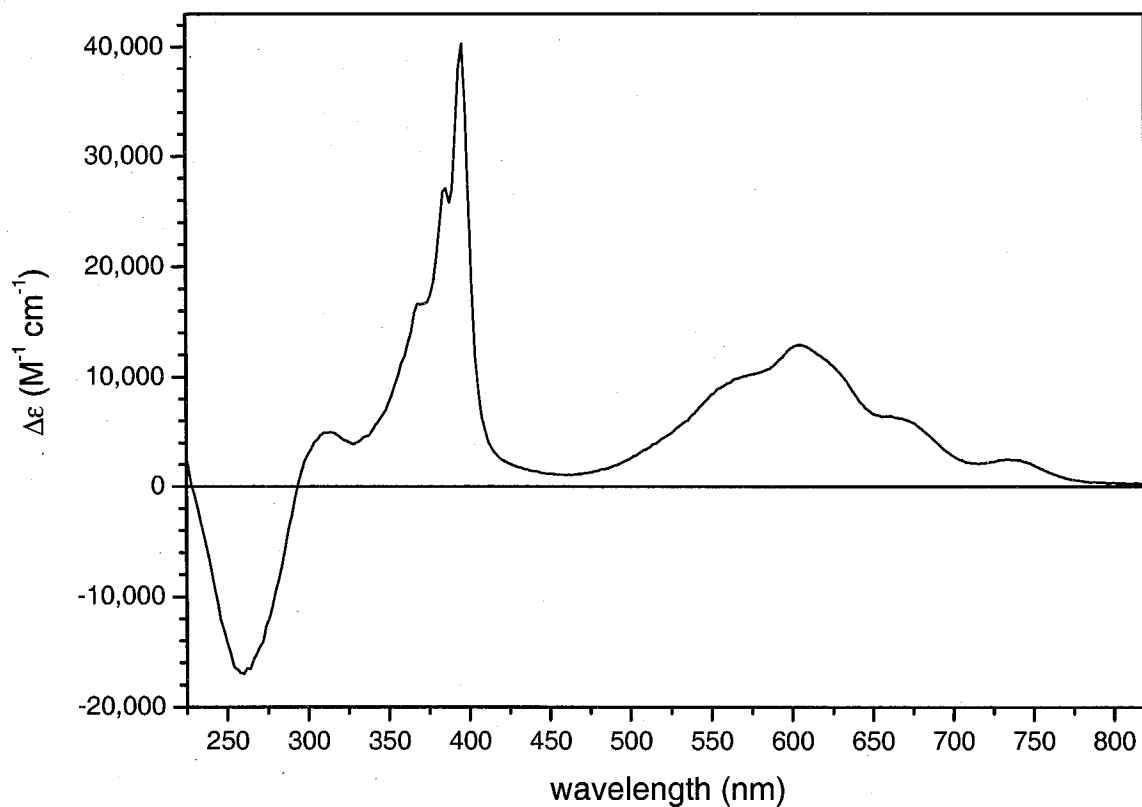


FIGURE D.3 – $MV^+ - MV^{2+}$ Difference Spectrum

Difference spectrum for $MV^+ - MV^{2+}$, calculated from the spectroelectrochemical traces in Figure D.1. The electrolysis was considered complete when less than 2% of the initial current was passed to the working electrode. The extinction coefficients for the Figure above were calculated based on the assumption that the reduction of MV^{2+} to MV^+ was complete.

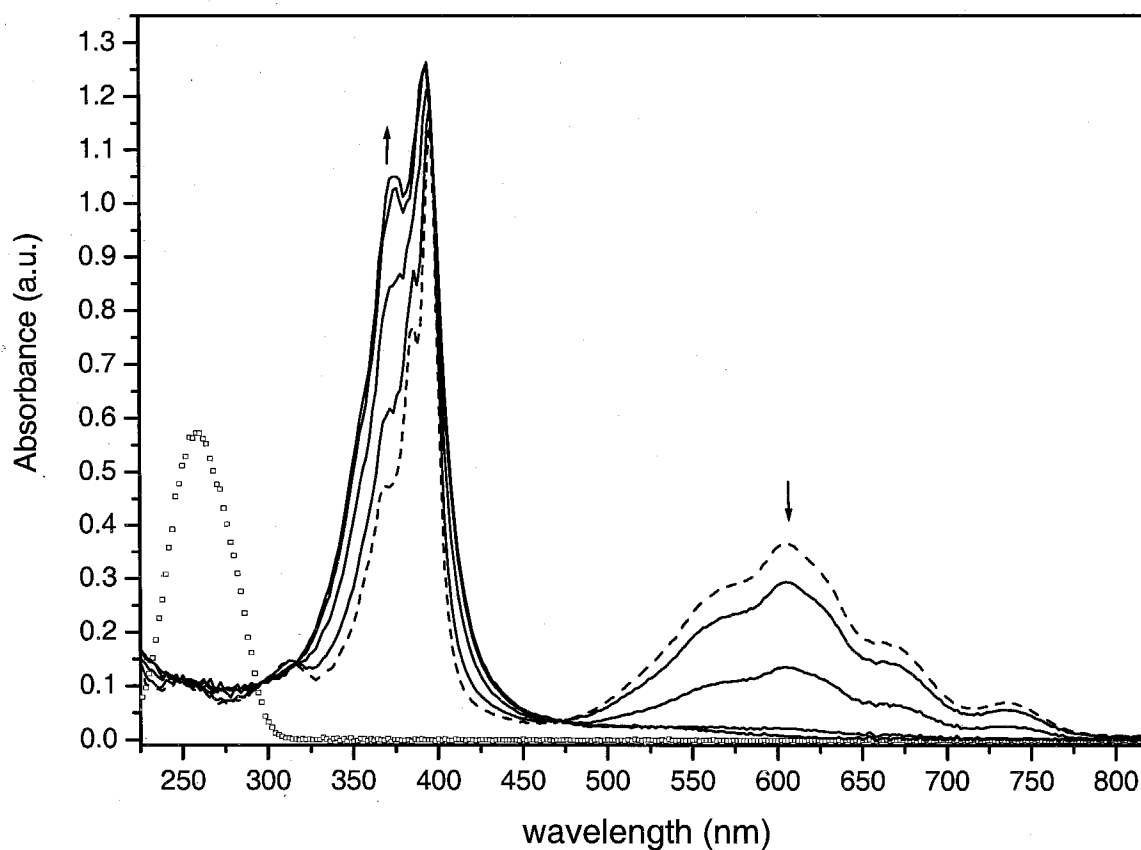


FIGURE D.4 – Methyl Viologen (MV)
Spectroelectrochemical Traces

The initial spectrum (MV^{2+}), prior to electrolysis, shows a single peak at 260 nm (□□□□□□). Bulk electrolysis of MV^{2+} to MV^+ at -0.5 V (vs. Ag/AgCl), performed in acetonitrile with 0.1 M TBAH using the cell in appendix B, yields a spectrum with strong absorption at 396 nm and 606 nm (----). Bulk electrolysis of the same sample at -1.2 V generates the remaining traces. Spectra were taken at regular intervals, with the arrows indicating direction of change. The second electrolysis is assigned to $MV^+ \rightarrow MV$ (neutral). Reduction of the sample, via electrolysis at 0 V, fully recovers the initial spectrum, indicating the process was completely reversible.

TABLE D.1 – Spectroscopic Handles

Compound	λ (ϵ) ^a [nm ($M^{-1}cm^{-1}$)]
$[Ru^{II}-(XY)_3-G]^{2+}$	460 (1.2×10^4) ^b 500 (2.4×10^3)
$[Ru^{III}-(XY)_3-G^+]^{4+}$	460 (5.3×10^3) 500 (5.7×10^3)
TMS-ethynyl-G	346 (4.3×10^3) ^b 460 (2.1×10^2) 500 (1.5×10^2) 520 (1.3×10^2)
TMS-ethynyl-G ⁺	460 (9.6×10^2) 500 (1.6×10^3) 520 (1.8×10^3) ^b
MV ²⁺	396 (0) 460 (0) 500 (0) 606 (0)
MV ⁺	396 (4.0×10^4) ^b 460 (1.0×10^3) 500 (2.5×10^3) 606 (1.3×10^4) ^b

^aPeak positions and extinction coefficients determined from spectroelectrochemical experiments. The calculation of ϵ is based on the assumption that the electrolysis was complete and fully reversible.

^bAbsorption band maximum.

REFERENCES

1. Paddon-Row, M. N.; Shephard, M. J.; Jordan, K. D. *J. Am. Chem. Soc.* **1993**, *115*, 3312-3313.
2. Jensen, K. K.; vanBerlekom, S. B.; Kajanus, J.; Martensson, J.; Albinsson, B. *J. Phys. Chem. A* **1997**, *101*, 2218-2220.
3. Kilsa, K.; Kajanus, J.; Macpherson, A.; Martensson, J.; Albinsson, B. *J. Am. Chem. Soc.* **2001**, *123*, 3069-3080.
4. Kilsa, K.; Kajanus, J.; Martensson, J.; Albinsson, B. *J. Phys. Chem. B* **1999**, *103*, 7329-7339.
5. De Cola, L.; Belser, P. *Coordination Chemistry Reviews* **1998**, *177*, 301-346.
6. Balzani, V.; Barigelletti, F.; Belser, P.; Bernhard, S.; DeCola, L.; Flamigni, L. *J. Phys. Chem.* **1996**, *100*, 16786-16788.
7. Schlicke, B.; Belser, P.; Cola, L. D.; Sabbioni, E.; Balzani, V. *J. Am. Chem. Soc.* **1999**, *121*.
8. Hammarstrom, L.; Barigelletti, F.; Flamigni, L.; Armaroli, N.; Sour, A.; Collin, J.-P.; Sauvage, J.-P. *J. Am. Chem. Soc.* **1996**, *118*, 11972-11973.
9. Barigelletti, F.; Flamigni, L.; Guardigli, M.; Juris, A.; Beley, M.; Chodorowski-Kimmes, S.; Collin, J.-P.; Sauvage, J.-P. *Inorg. Chem.* **1996**, 136-142.
10. Barigelletti, F.; Flamigni, L.; Balzani, V.; Collin, J.-P.; Sauvage, J.-P.; Sour, A.; Constable, E. C.; Thompson, A. M. W. C. *J. Am. Chem. Soc.* **1994**, *114*, 7692-7699.
11. Indelli, M. T.; Scandola, F.; Collin, J.-P.; Sauvage, J.-P.; Sour, A. *Inorg. Chem.* **1996**, *35*, 303-312.

12. Barigelletti, F.; Flamigni, L.; Balzani, V.; Collin, J.-P.; Sauvage, J.-P.; Sour, A.; Constable, E. C.; Thomson, A. M. W. C. *Coord. Chem. Rev.* **1994**, *132*, 209-214.
13. Staab, H. A.; Kratzer, B.; Quazzotti, S. *Eur. J. Org. Chem.* **1998**, 2149-2160.
14. Weber, K.; Hockett, L.; Creager, S. *J. Phys. Chem. B* **1997**, *101*, 8286-8291.
15. Sengupta, B.; Curtiss, L. A.; Miller, J. R. *J. Chem. Phys.* **1996**, *104*, 9888.
16. Winkler, J. R.; Di Bilio, A. J.; Farrow, N. A.; Richards, J. H.; Gray, H. B. *Pure and Applied Chemistry* **1999**, *71*, 1753-1764.
17. Babini, E.; Bertini, I.; Borsari, M.; Capozzi, F.; Luchinat, C.; Zhang, X. Y.; Moura, G. L. C.; Kurnikov, I. V.; Beratan, D. N.; Ponce, A.; Di Bilio, A. J.; Winkler, J. R.; Gray, H. B. *J. Am. Chem. Soc.* **2000**, *122*, 4532-4533.
18. Gray, H. B.; Winkler, J. R. *J. Inorg. Biochem.* **1999**, *74*, 27-27.
19. Skov, L. K.; Pascher, T.; Winkler, J. R.; Gray, H. B. *J. Am. Chem. Soc.* **1998**, *120*, 1102-1103.
20. Gray, H. B.; Winkler, J. R. *Journal of Electroanalytical Chemistry* **1997**, *438*, 43-47.
21. Balzani, V. *Electron Transfer in Chemistry*; Balzani, V., Ed.: New York, 2001; Vol. 3.
22. Berglund, J.; Pascher, T.; Winkler, J. R.; Gray, H. B. *J. Am. Chem. Soc.* **1997**, *119*, 2464-2469.
23. Langen, R.; Chang, I. J.; Germanas, J. P.; Richards, J. H.; Winkler, J. R.; Gray, H. B. *Science* **1995**, *268*, 1733-1735.
24. Casimiro, D. R.; Richards, J. H.; Winkler, J. R.; Gray, H. B. *J. Phys. Chem.* **1993**, *97*, 13073-13077.
25. Casimiro, D. R.; Wong, L. L.; Colon, J. L.; Zewert, T. E.; Richards, J. H.; Chang, I. J.; Winkler, J. R.; Gray, H. B. *J. Am. Chem. Soc.* **1993**, *115*, 1485-1489.
26. Casimiro, D. R.; Winkler, J. R.; Richards, J. H.; Gray, H. B. *Photosynthesis Research* **1992**, *34*, 166-166.
27. Gray, H. B.; Winkler, J. R. *Pure and Applied Chemistry* **1992**, *64*, 1257-1262.
28. Winkler, J. R.; Gray, H. B. *Chemical Reviews* **1992**, *92*, 369-379.
29. Wuttke, D. S.; Bjerrum, M. J.; Winkler, J. R.; Gray, H. B. *Science* **1992**, *256*, 1007-1009.
30. Tamao, K.; Miyaura, N. *Topics in Current Chemistry* **2002**, *219*, 1-9.
31. Frost, C. G. *Rodd's Chemistry of Carbon Compounds (2nd Edition)* **2001**, *5*, 315-350.
32. Chemler, S. R.; Trauner, D.; Danishefsky, S. J. *Angewandte Chemie, International Edition* **2001**, *40*, 4544-4568.

33. Suzuki, A. *ACS Symposium Series* **2001**, 783, 80-93.
34. Bo, Z.; Schluter, A. D. *Chemistry--A European Journal* **2000**, 6, 3235-3241.
35. Balzani, V. *Electron Transfer in Chemistry*; Balzani, V., Ed.: New York, 2001; Vol. 1-5.
36. Newton, M. D. *Electron Transfer: Theoretical Models and Computational Implementation*; Balzani, V., Ed.; Wiley-VCH: New York, 2001; Vol. 1.
37. Marcus, R. A. *Angew. Chem. Int. Ed. Engl.* **1993**, 32, 1111-1121.
38. Marcus, R. A.; Sutin, N. *Biochem. et Biophys. Act.* **1985**, 811, 265-322.
39. Creager, S.; Yu, C. J.; Bamdad, C.; O'Connor, S.; MacLean, T.; lam, E.; Chong, Y.; Olsen, G. T.; Luo, J.; Gozin, M.; Kayyem, J. F. *J. Am. Chem. Soc.* **1999**, 121, 1059-1064.
40. Tour, J. M.; Rawlett, A. M.; Kozaki, M.; Yao, Y.; Jagessar, R. C.; Dirk, S. M.; Price, D. W.; Reed, M. A.; Zhou, C.-W.; Chen, J.; Wang, W.; Campbell, I. *Chemistry--A European Journal* **2001**, 7, 5118-5134.
41. Tanaka, S.; Yamashita, Y. *Synthetic Metals* **1999**, 101, 532-533.
42. Hall, L. E.; Reimers, J. R.; Hush, N. S.; Silverbrook, K. *J. Chem. Phys.* **2000**, 112, 1510-1521.
43. Tour, J. M. *Polymer News* **2000**, 25, 329-336.
44. Ratner, M. A.; Davis, B.; Kemp, M.; Mujica, V.; Roitberg, A.; Yaliraki, S. *Annals of the New York Academy of Sciences* **1998**, 852, 22-37.
45. Whitesides, G. M.; Mathias, J. P.; Seto, C. T. *Science* **1991**, 254, 1312-19.
46. Heath, J. R.; Kuekes, P. J.; Snider, G. S.; Williams, R. S. *Science* **1998**, 280, 1716-1721.
47. Heath, J. R. *Accounts of Chemical Research* **1999**, 32, 388-388.
48. Heath, J. R. *Pure and Applied Chemistry* **2000**, 72, 11-20.
49. Kohlman, R. S.; Zibold, A.; Tanner, D. B.; Ihas, G. G.; Ishiguro, T.; Min, Y. G.; MacDiarmid, A. G.; Epstein, A. J. *Physical Review Letters* **1997**, 78, 3915-3918.
50. Pease, A. R.; Jeppesen, J. O.; Stoddart, J. F.; Luo, Y.; Collier, C. P.; Heath, J. R. *Accounts of Chemical Research* **2001**, 34, 433-444.
51. Reed, M. A.; Zhou, C.; Muller, C. J.; Burgin, T. P.; Tour, J. M. *Science* **1997**, 278, 252-254.
52. Whitesides, G. M.; Mathias, J. P.; Seto, C. T. *Science* **1991**, 254, 1312-1319.
53. Ward, M. D. *Chemistry and Industry* **1997**, 16, 640-645.
54. Mirkin, C. A.; Ratner, M. A. *Annu. Rev. Phys. Chem.* **1992**, 43, 719-754.
55. Reimers, J. R.; Hall, L. E.; Hush, N. S.; Silverbrook, K. *Annals of the New York Academy of Sciences* **1998**, 852, 38-53.

56. Emberly, E. G.; Kirczenow, G. *Annals of the New York Academy of Sciences* **1998**, 852, 54-67.
57. Seminario, J. M.; Tour, J. M. *Annals of the New York Academy of Sciences* **1998**, 852, 68-94.
58. Metzger, R. M.; Cava, M. P. *Annals of the New York Academy of Sciences* **1998**, 852, 95-115.
59. Launay, J. P.; Coudret, C. *Annals of the New York Academy of Sciences* **1998**, 852, 116-132.
60. Reed, M. A.; Zhou, C.; Deshpande, M. R.; Muller, C. J.; Burgin, T. P.; Jones, L.; Tour, J. M. *Annals of the New York Academy of Sciences* **1998**, 852, 133-144.
61. Weiss, P. S.; Bumm, L. A.; Dunbar, T. D.; Burgin, T. P.; Tour, J. M.; Allara, D. L. *Annals of the New York Academy of Sciences* **1998**, 852, 145-168.
62. Anantram, M. P.; Han, J.; Govindan, T. R. *Annals of the New York Academy of Sciences* **1998**, 852, 169-177.
63. Srivastava, D.; Saini, S.; Menon, M. *Annals of the New York Academy of Sciences* **1998**, 852, 178-187.
64. Persson, S. H. M.; Olofsson, L.; Hedberg, L.; Sutherland, D.; Olsson, E. *Annals of the New York Academy of Sciences* **1998**, 852, 188-196.
65. Tour, J. M.; Reinerth, W. A.; Jones, L.; Burgin, T. P.; Zhou, C. W.; Muller, C. J.; Deshpande, M. R.; Reed, M. A. *Annals of the New York Academy of Sciences* **1998**, 852, 197-204.
66. Mullen, K.; Rabe, J. P. *Annals of the New York Academy of Sciences* **1998**, 852, 205-218.
67. Gourdon, A.; Tang, H. *Annals of the New York Academy of Sciences* **1998**, 852, 219-229.
68. Kawai, T. *Annals of the New York Academy of Sciences* **1998**, 852, 230-242.
69. Joachim, C.; Bergaud, C.; Pinna, H.; Tang, H.; Gimzewski, J. K. *Annals of the New York Academy of Sciences* **1998**, 852, 243-256.
70. Wada, Y. *Annals of the New York Academy of Sciences* **1998**, 852, 257-276.
71. Manassen, Y.; Shachal, D. *Annals of the New York Academy of Sciences* **1998**, 852, 277-289.
72. Matsushige, K.; Yamada, H.; Tada, H.; Horiuchi, T.; Chen, X. Q. *Annals of the New York Academy of Sciences* **1998**, 852, 290-305.
73. Fujihira, M. *Annals of the New York Academy of Sciences* **1998**, 852, 306-329.
74. Wolf, H. C.; Gomez, U.; Port, H. *Annals of the New York Academy of Sciences* **1998**, 852, 330-338.
75. Aviram, A.; Roland, P. *Annals of the New York Academy of Sciences* **1998**, 852, 339-348.

76. Allara, D. L.; Dunbar, T. D.; Weiss, P. S.; Bumm, L. A.; Cygan, M. T.; Tour, J. M.; Reinerth, W. A.; Yao, Y.; Kozaki, M.; Jones, L. *Annals of the New York Academy of Sciences* **1998**, *852*, 349-370.
77. Gratzel, M. *Cattech* **1999**, *3*, 4-17.
78. Vlachopoulos, N.; Liska, P.; Augustynski, J.; Gratzel, M. *J. Am. Chem. Soc.* **1988**, *110*, 1216-1220.
79. Nitzan, A.; Jortner, J. *J. Phys. Chem. B* **2000**, *104*, 5661-5665.
80. Fox, L. S.; Kozik, M.; Winkler, J. R.; Gray, H. B. *Science* **1990**, *247*, 1069.
81. Dibilio, A. J.; Hill, M. G.; Bonander, N.; Karlsson, B. G.; Villahermosa, R. M.; Malmstrom, B. G.; Winkler, J. R.; Gray, H. B. *J. Am. Chem. Soc.* **1997**, *119*, 9921-9922.
82. McCleskey, T. M.; Winkler, J. R.; Gray, H. B. *J. Am. Chem. Soc.* **1992**, *114*, 6935-6937.
83. Newton, M. D. *J. Phys. Chem.* **1988**, *92*, 3049-3056.
84. Balabin, I. A.; Onuchic, J. N. *J. Phys. Chem.* **1996**, *100*, 11573-11580.
85. Nishino, M.; Saito, K.; Miyashita, S. *Physical Review B: Condensed Matter and Materials Physics* **2002**, *65*, 014403/1-014403/7.
86. Kurnikov, I. V.; Zusman, L. D.; Kurnikova, M. G.; Farid, R. S.; Beratan, D. N. *J. Am. Chem. Soc.* **1997**, *119*, 5690-5700.
87. Lee, M.; Shephard, M. J.; Risser, S. M.; Priyadarshy, S.; Paddon-Row, M. N.; Beratan, D. N. *J. Phys. Chem. A* **2000**, *104*, 7593-7599.
88. Skourtis, S. S.; Beratan, D. N.; Onuchic, J. N. *Chem. Phys.* **1993**, *176*, 501-20.
89. Onuchic, J. N.; Beratan, D. N. *J. Am. Chem. Soc.* **1987**, *109*, 6771-8.
90. Beratan, D. N.; Hopfield, J. J. *J. Chem. Phys.* **1984**, *81*, 5753-9.
91. Beratan, D. N.; Onuchic, J. N.; Hopfield, J. J. *J. Chem. Phys.* **1985**, *83*, 5325-9.
92. McConnell, H. M. *J. Chem. Phys.* **1961**, *35*, 508-515.
93. Onipko, A. *Chem. Phys. Lett.* **1998**, *292*, 267-272.
94. Curtiss, L. A.; Naleway, C.; Miller, J. R. *Chem. Phys.* **1993**, *176*, 387-405.
95. naleway, C. A.; Curtiss, L. A.; Miller, J. R. *J. Phys. Chem.* **1991**, *95*, 8434-8437.
96. Hayes, R. T.; Wasielewski, M. R.; Gosztola, D. *J. Am. Chem. Soc.* **2000**, *122*, 5563-5567.
97. Collin, J.-P.; Guillerez, S.; Sauvage, J.-P.; Barigelletti, F.; Cola, L. D.; Flamigni, L.; Balzani, V. *Inorg. Chem.* **1991**, *30*, 4230-4238.

98. Pullen, S. H.; Studer-Martinez, S. L.; Edington, M. D.; Harris, A. L.; Long, A.; Baldwin, S. W.; Staen, H. A.; Simon, J. D. *J. Phys. Chem. A* **1999**, *103*, 10220-10225.
99. Broo, A.; Zerner, M. C. *Chem. Phys.* **1995**, *196*, 423-436.
100. Schlicke, B.; De Cola, L.; Belser, P.; Balzani, V. *Coordination Chemistry Reviews* **2000**, *208*, 267-275.
101. Bredas, J. L.; Heeger, A. J. *Chem. Phys. Lett.* **1994**, *217*, 507-512.
102. Williams, R. J. P. *J. Biol. Inorg. Chem.* **1997**, *2*, 373-377.
103. Winkler, J. R.; Gray, H. B. *J. Biol. Inorg. Chem.* **1997**, *2*, 399-404.
104. Paulson, B.; Pramod, K.; Eaton, P.; Closs, G.; Miller, J. R. *J. Phys. Chem.* **1993**, *97*, 13042-13045.
105. Calcaterra, L. T.; Closs, G. L.; Miller, J. R. *J. Am. Chem. Soc.* **1983**, *105*, 670-671.
106. Clayton, A. H. A.; Ghiggino, K. P.; Lawson, J. M.; Paddon-Row, M. N. *J. Photochem. Photobiol. A: Chem.* **1994**, *80*, 323-331.
107. Skourtis, S. S.; Beratan, D. N. *J. Biol. Inorg. Chem.* **1997**, *2*, 378-386.
108. Farver, O.; Pecht, I. *J. Biol. Inorg. Chem.* **1997**, *2*, 387-392.
109. Moser, C. C.; Page, C. C.; Chen, X.; Dutton, P. L. *J. Biol. Inorg. Chem.* **1997**, *2*, 393-398.
110. Johnson, M. D.; Miller, J. R.; Green, N. S.; Closs, G. L. *J. Phys. Chem.* **1989**, *93*, 1173.
111. Paulson, B. P.; Curtiss, L. A.; Bal, B.; Closs, G. L.; Miller, J. R. *J. Am. Chem. Soc.* **1996**, *118*, 378-387.
112. Dunn, A. R.; Dmochowski, I. J.; Bilwes, A. M.; Gray, H. B.; Crane, B. R. *PNAS* **2001**, *98*, 12420-12425.
113. Dmochowski, I. J.; Crane, B. R.; Wilker, J. J.; Winkler, J. R.; Gray, H. B. *PNAS* **1999**, *96*, 12987-12990.
114. Wilker, J. J.; Dmochowski, I. J.; Dawson, J. H.; Winkler, J. R.; Gray, H. B. *Angewandte Chemie-International Edition* **1999**, *38*, 90-92.
115. Wagenknecht, H. A.; Rajski, S. R.; Pascaly, M.; Stemp, E. D. A.; Barton, J. K. *J. Am. Chem. Soc.* **2001**, *123*, 4400-4407.
116. Rajski, S. R.; Barton, J. K. *Journal of Biomolecular Structure & Dynamics* **2000**, 285-291.
117. Nunez, M. E.; Rajski, S. R.; Barton, J. K. *Methods in Enzymology*, 2000; Vol. 319, pp 165-188.
118. Stemp, E. D. A.; Barton, J. K. *Inorganic Chemistry* **2000**, *39*, 3868-3874.
119. Wagenknecht, H. A.; Stemp, E. D. A.; Barton, J. K. *Biochemistry* **2000**, *39*, 5483-5491.

120. Nunez, M. E.; Barton, J. K. *Current Opinion in Chemical Biology* **2000**, *4*, 199-206.
121. Rajski, S. R.; Jackson, B. A.; Barton, J. K. *Mutat. Res.-Fundam. Mol. Mech. Mutagen.* **2000**, *447*, 49-72.
122. Nunez, M. E.; Hall, D. B.; Barton, J. K. *Chemistry & Biology* **1999**, *6*, 85-97.
123. Kelley, S. O.; Barton, J. K. *Science* **1999**, *283*, 375-381.
124. Dandliker, P. J.; Holmlin, R. E.; Barton, J. K. *Science* **1997**, *275*, 1465-1468.
125. Kuciauskas, D.; Freund, M. S.; Gray, H. B.; Winkler, J. R.; Lewis, N. S. *J. Phys. Chem. B* **2001**, *105*, 392-403.
126. Sauve, G.; Cass, M. E.; Coia, G.; Doig, S. J.; Lauermann, I.; Pomykal, K. E.; Lewis, N. S. *J. Phys. Chem. B* **2000**, *104*, 6821-6836.
127. Sauve, G.; Cass, M. E.; Doig, S. J.; Lauermann, I.; Pomykal, K.; Lewis, N. S. *J. Phys. Chem. B* **2000**, *104*, 3488-3491.
128. Tan, M.X.; Laibinis, P.E.; Nguyen, S.T.; Kesselman, J.M.; Stanton, C.E.; Lewis, N.S. *Prog. In Inorg. Chem.* **1994**, *41*, 21.
129. Chang, I. J.; Gray, H. B.; Winkler, J. R. *J. Am. Chem. Soc.* **1991**, *113*, 7056-7057.
130. Hsung, R. P.; Chidsey, C. E. D.; Sita, L. R. *Organomet.* **1995**, *14*, 4808-4815.
131. Tzalis, D.; Tor, Y. *Chem. Commun.* **1996**, 1043-1044.
132. Barrett, A. G. M. *J. Org. Chem.* **1988**, *53*, 1815-1817.
133. Yu, C. J.; Chong, Y.; Kayyem, J. F.; Gozin, M. *J. Org. Chem.* **1999**, *64*, 2070-2079.
134. Jones, L.; Pearson, D. L.; Schumm, J. S.; Tour, J. M. *Pure and Applied Chemistry* **1996**, *68*, 145-148.
135. Bates, R.; Camou, F.; Kane, V.; Mistra, P.; Suvannachut, K.; White, J. *J. Org. Chem.* **1989**, *54*, 311.
136. Suzuki, N. *Bull. Chem. Soc. Jpn.* **1959**, *32*, 1340.
137. Schmid, E.; Brosa, B. *J. Chem. Phys.* **1972**, *56*, 6267.
138. Brock, C. *Acta Crystallogr. Sect. B* **1980**, *36*, 86.
139. Pasco, S. T.; Baker, G. L. *Syn. Met.* **1997**, *84*, 275-276.
140. Davis, W. B.; Ratner, M. A.; Wasielewski, M. R. *J. Am. Chem. Soc.* **2001**, *123*, 7877-7886.
141. Pappenfus, T. M.; Mann, K. R. *Inorg. Chem.* **2001**, *40*, 6301-6307.
142. Kalyanasundaram, K.; Neumann-Spallart, M. *Chem. Phys. Lett.* **1982**, *88*, 7-12.

143. Sassoon, R. E.; Gershuni, S.; Rabani, J. *J. Phys. Chem.* **1992**, *96*, 4692-4698.
144. Zhu, Y.; Schuster, G. B. *J. Am. Chem. Soc.* **1993**, *115*, 2190-2199.
145. Bock, C. R.; Connor, J. A.; Gutierrez, A. R.; Meyer, T. J.; Whitten, D. G.; Sullivan, B. P.; Bagle, J. K. *J. Am. Chem. Soc.* **1979**, *101*, 4815-4824.
146. Miedlar, K.; Das, P. K. *J. Am. Chem. Soc.* **1982**, *104*, 7462-7469.
147. Huang, S.; Tour, J. M. *J. Am. Chem. Soc.* **1999**, *121*, 4908-4909.
148. Miyaura, N.; Suzuki, A. *Chemical Reviews* **1995**, *95*, 2457-2483.
149. Miyaura, N.; Yanagi, T.; Suzuki, A. *Syn. Comm.* **1981**, *11*, 513-519.
150. Sonogashira, K.; Takahashi, S. *J. Syn. Org. Chem. Jpn.* **1993**, *51*, 1053-1063.
151. Watanabe, T.; Miyaura, N. *Synlett* **1992**, *3*, 207-210.
152. Ziener, U.; Godt, A. *J. Org. Chem.* **1997**, *62*, 6137-6143.
153. Sprecher, M.; Breslow, R.; Uziel, O.; Link, T. M. *OPPI Briefs* **1994**, *26*, 696.
154. Hino, T.; Hasegawa, A.; Liu, J.-J.; Nakagawa, M. *Chem Pharm. Bull* **1990**, *38*, 59-64.
155. Beley, M.; Collin, J.-P.; Sauvage, J.-P. *Inorg. Chem.* **1993**, *32*, 4539-4543.
156. Senko, M. *IspPro*; 3.0 ed.; MS/MS Software: Sunnyvale, 1998.
157. Mullen, K.; Wegner, G. *Electronic Materials: The Oligomeric Approach*; Wiley-VCH: New York, 1998.
158. Steckhan, E.; Kuwana, T. *Berichte der Bunsen-Gesellschaft* **1974**, *78*, 253.
159. Borsarelli, C. D.; Braslavsky, S. E. *J. Phys. Chem. A* **1999**, *103*, 1719-1727.
160. DeLaive, P. J.; Lee, K. T.; Sprintschnik, H. W.; Abruna, H.; Meyer, T. J.; Whitten, D. G. *J. Am. Chem. Soc.* **1977**, *99*, 7094-7097.
161. young, R. C.; Meyer, T. J.; Whitten, D. G. *J. Am. Chem. Soc.* **1976**, *98*, 286-287.
162. Delaive, P. J.; Lee, J. T.; Abruna, J.; Sprintschnik, H. W.; Meyer, T. J.; Whitten, D. G. *Adv. Chem. Ser.* **1977**, *168*, 28-43.
163. Demtroder, W. *Laser Spectroscopy*; 2nd ed.; Springer, 1996, pp 594-647.
164. Hoffman, M. Z.; Bolletta, F.; Moggi, L.; Hug, G. L. *J. Phys. Chem. Ref. Data* **1989**, *18*, 219.
165. Helms, A.; Heiler, D.; McLendon, G. **1992**, *114*, 6227-6238.
166. MathWorks *MATLAB*; 5.3.0.10183 (R11) ed.; MathWorks: Natick, 1999.
167. *Distance Dependencies of Electron-Transfer Reactions*; Elsevier: Amsterdam, 1988.

168. Joachim, C.; Launay, J. P.; Woitellier, S. *Chem. Phys.* **1990**, *147*, 131-141.
169. Kalyanasundaram, K. *Photochemistry of Polypyridine and Porphyrin Complexes*; Academic Press: San Diego, 1992.
170. Sakata, Y.; Nakashima, S.; Goto, Y.; Tatemitsu, H.; Misumi, S. *J. Am. Chem. Soc.* **1989**, *111*, 8979-8981.
171. Takahashi, O.; Kikuchi, O. *J. Chem. Phys.* **1994**, *100*, 1350.
172. Sakata, Y.; Tsue, H.; Goto, Y.; Misumi, S.; Asahi, T.; Nishikawa, S.; Okada, T.; Mataga, N. *Chem. Lett. Japan* **1991**, 1307-1310.
173. Helms, A.; Heiler, D.; McLendon, G. *J. Am. Chem. Soc.* **1991**, *113*, 4325-4327.
174. Cave, R. J.; Siders, P.; Marcus, R. A. *J. Phys. Chem.* **1986**, *90*, 1436-1444.
175. Warman, J. M.; Smit, K. J.; Haas, M. P. D.; Jonker, S. A.; Paddon-Row, M. N.; Oliver, A. M.; Kroon, J.; Oevering, H.; Verhoeven, J. W. *J. Phys. Chem.* **1991**, *95*, 1979-1987.
176. Smalley, J. F.; Feldberg, S. W.; Chidsey, C. E. D.; Linford, M. R.; Newton, M. D.; Liu, Y. *J. Phys. Chem.* **1995**, *99*, 13141-13149.
177. Closs, G. L.; Miller, J. R. *Science* **1988**, *240*, 440-447.
178. Paddon-Row, M. N.; Oliver, A. M.; Warman, J. M.; Smith, K. J.; Haas, M. P. d.; Oevering, H.; Verhoeven, J. W. *J. Phys. Chem.* **1988**, *92*, 6958-6962.
179. Lawson, J. M.; Craig, D. C.; Paddon-Row, M. N.; Kroon, J.; Verhoeven, J. W. *J. Phys. Chem.* **1989**, *92*, 6958-6962.
180. Benniston, A. C.; Goulle, V.; Harriman, A.; Lehn, J. M.; Marczinke, B. *J. Phys. Chem.* **1994**, *98*, 7798-7804.
181. Oregan, B.; Gratzel, M. *Nature* **1991**, *353*, 737-740.
182. Hamnett, A.; Dare-Edwards, M. P.; Wright, R. D.; Seddon, K. R.; Goodenough, J. B. *J. Phys. Chem.* **1979**, *83*, 3280-90.